Springer Proceedings in Physics 256

Vinod Kumar Jain
Sunita Rattan
Abhishek Verma *Editors*

Recent Trends in Materials and Devices

Proceedings of ICRTMD 2019

Springer

Springer Proceedings in Physics

Volume 256

Indexed by Scopus

The series Springer Proceedings in Physics, founded in 1984, is devoted to timely reports of state-of-the-art developments in physics and related sciences. Typically based on material presented at conferences, workshops and similar scientific meetings, volumes published in this series will constitute a comprehensive up-to-date source of reference on a field or subfield of relevance in contemporary physics. Proposals must include the following:

- name, place and date of the scientific meeting
- a link to the committees (local organization, international advisors etc.)
- scientific description of the meeting
- list of invited/plenary speakers
- an estimate of the planned proceedings book parameters (number of pages/articles, requested number of bulk copies, submission deadline).

More information about this series at http://www.springer.com/series/361

Vinod Kumar Jain · Sunita Rattan ·
Abhishek Verma
Editors

Recent Trends in Materials and Devices

Proceedings of ICRTMD 2019

Springer

Editors
Vinod Kumar Jain
Amity Institute of Advanced Research and Studies (Materials and Devices)
Amity University
Noida, Uttar Pradesh, India

Abhishek Verma
Amity Institute of Advanced Research and Studies (Materials and Devices)
Amity University
Noida, Uttar Pradesh, India

Sunita Rattan
Amity Institute of Applied Science
Amity University
Noida, Uttar Pradesh, India

ISSN 0930-8989 ISSN 1867-4941 (electronic)
Springer Proceedings in Physics
ISBN 978-981-15-8624-8 ISBN 978-981-15-8625-5 (eBook)
https://doi.org/10.1007/978-981-15-8625-5

This Springer imprint is published by the registered company Springer Nature Singapore Pte Ltd.
The registered company address is: 152 Beach Road, #21-01/04 Gateway East, Singapore 189721, Singapore

Preface

Today, the global challenges are too complex to be addressed with the traditional disciplinary boundaries. To tackle these intricate challenges, interdisciplinary research is the only solution. From research funders to journal editors, policymakers to think tanks—all seem to agree that the future of research lies outside firm disciplinary boundaries. The field of materials and devices intrinsically is a perfect example for the same, which is generating an efficient outcome.

"International Conference on Recent Trends in Materials and Devices" (ICRTMD) was organized at Amity University Uttar Pradesh, Noida, India, from 18 to 19 December 2019, with the aim to provide a common forum for eminent scientists, technologists, entrepreneurs and scholars from different disciplines to interact and collaborate to solve scientific challenges. The purpose and objective of this meeting was also to share the vast knowledge and latest investigations with the scientific industrial community and how to include in the production to get more efficient devices or system. The conference also provided an opportunity for the participants to interact and develop collaborative partnership.

The book *Recent Trends in Materials and Devices* is a collection of recent scientific contributions from different veins of semiconductors, composites, polymeric materials, energy generation, energy harvesting, devices and the other related technologies. The contributions have been made by various researchers and eminent scientist, who presented their papers in this International Conference. The chapters include various latest and significant topics, i.e. **semiconductor materials & devices, smart materials, polymeric materials, sensors, photovoltaics, solar thermal energy storage, optoelectronics, nanotechnology/nanomaterials and other emerging technologies**. The book gives the cutting-edge technologies and other significant aspects related to material synthesis, optimization, characterization and device fabrication.

It includes the latest findings of eminent scientists and researchers discussing the thermophysical properties of nanoparticle-enhanced phase change materials for thermal energy storage; fabrication of in-line PERT bifacial solar cells, concept of agrivoltaics; graphene nano-material, amicable approach for nclear reactors; nanofibers for antimicrobial wound dressing; optoelectronic properties of iridium

(III) complexes; liquid crystal display materials; synthesis and characterization of nanoalloy for thermal applications; water purification using graphene-functionalized nanoparticles; nano-composites; nano-material-based sensors; bio-sensor; preparation and characterization of influenza virosomes; photonic crystals; rheological properties of magneto-rheological fluid; nonlinear optical susceptibilities of a piezoelectric semiconductor; modelling & simulations; and a many more.

These contributory papers provided new insights, thought-provoking ideas and exchange of scientific solutions. We are sure that all the latest results and findings reported here will be useful to the young researchers or scientists working in these areas and will serve as an important document for all those associated with research and development in materials and its usage.

We are immensely grateful to all the eminent speakers who delivered the talks and contributed the rich and dense programme of the conference. We are also thankful to all the members of the team ICRTMD 2019 who worked with full commitment and provided their guidance and support.

The editors wish to place on record our profound gratitude to Dr. Ashok K. Chauhan, Chief Patron—ICRTMD 2019 and Founder President, Amity University, Noida, for his continuous guidance and encouragement to organize this important conference. Editors are also highly thankful to Prof. (Dr.) Balvinder Shukla, Vice Chancellor, Amity University, for her tremendous support, in making this conference a success event. Our sincere thanks and gratitude goes to all Co-Chairpersons—Dr. Sangeeta Tiwari, Dr. R. S. Pandey, Dr. Prakriti Rai, Dr. Dheeraj Pawar, Dr. Christine J., Dr. Suman; and Secretaries—Dr. Rohit Verma, Dr. Deepshikha Gupta, Dr. Kuldeep Chaudhary; and all the members of International Conference on the Recent Trends in Materials and Devices, 2019 (*jointly organized by Amity Institute for Advanced Research and Studies* (*AIARS*) *and Amity Institute of Applied Sciences* (*AIAS*), *Amity University, Noida*), for their support in organizing this conference.

Noida, India

Vinod Kumar Jain
Sunita Rattan
Abhishek Verma

Contents

Contributors

Navshad Alam Department of Applied Science, BNCET, Affiliated to Dr. A.P.J. Abdul, Kalam Technical University, Lucknow, India

Rohit Babu Aniyery Amity Institute of Applied Sciences, AUUP, Noida, India

Tania Banerjee University of Delhi, New Delhi, India

A. M. Biradar CSIR—National Physical Laboratory, New Delhi, India

Vishal Singh Chandel Department of Applied Science, BNCET, Affiliated to Dr. A.P.J. Abdul, Kalam Technical University, Lucknow, India;
Department of APSH, Rajkiya Engineering College, Affiliated to Dr. A.P.J. Abdul, Kalam Technical University, Lucknow, India

N. Chandra Department of Physics, University of Allahabad, Allahabad, India

Sonal Chauhan Amity Institute of Applied Sciences, Amity University, Noida, Uttar Pradesh, India

Roman Dabrowski Institute of Applied Sciences and Chemistry, Military University of Technology, Warsaw, Poland

Subhra Das Solar Engineering Department, Amity School of Engineering & Technology, Amity University Haryana, Gurgaon, India

Ravindra Dhar Centre of Material Sciences, Institute of Interdisciplinary Studies, University of Allahabad, Allahabad, India

Hrishikesh Dhasmana Amity Institute of Renewable and Alternative Energy, Amity Institute of Advanced Research and Studies (Materials and Devices), Amity University, Noida, Uttar Pradesh, India

S. K. Dhawan Division of Materials Physics and Engineering, National Physical Laboratory, New Delhi, India

Mohd. Adil Faizi Amity Institute of Renewable and Alternative Energy, Amity University, Noida, Uttar Pradesh, India

Jyoti Gahlawat Department of Physics, Baba Mastnath University, Rohtak, Haryana, India

Aakarti Garg Department of Applied Physics, Amity Institute of Applied Sciences, Amity University Uttar Pradesh, Noida, India

Jampana Gayathri Amity Institute of Renewable and Alternative Energy and Amity Institute of Advanced Research and Studies (Materials and Devices), Amity University, Noida, Uttar Pradesh, India

Ajay Gupta Amity Center for Spintronic Materials, Amity University UP, Noida, India

Anita Gupta Amity Institute of Applied Sciences, AUUP, Noida, India

Jyoti Gupta Amity Institute of Applied Science/Amity University, Noida, Uttar Pradesh, India

Neeraj Gupta Amity Institute of Advanced Research and Studies (Materials and Devices), Amity University, Noida, Uttar Pradesh, India

V. K. Jain Amity Institute of Renewable and Alternative Energy, Amity Institute of Advanced Research and Studies (Materials and Devices), Amity University, Noida, Uttar Pradesh, India

Praveen Kumar Kaicker Shriram Institute for Industrial Research, New Delhi, Delhi, India

C. V. Kannan Mundra Solar PV Limited, Mundra, Gujrat, India

Jyoti Kapil Department of Physics, AIAS, Amity University, Noida, Uttar Pradesh, India

Ch. Kartikeshwar Patro Department of Applied Physics, Amity Institute of Applied Sciences, Amity University Uttar Pradesh, Noida, India

Isha Katyal Amity Center for Spintronic Materials, Amity University UP, Noida, India

H. Kaur Department of Applied Sciences, PEC University of Technology, Chandigarh, India

Tahira Khatoon Department of Physics, Integral University, Lucknow, India

Adarsh Kumar Department of Physics, Amity Institute of Applied Sciences, Amity University Noida, Noida, UP, India

Amit Kumar School of Engineering and Technology, Central University of Haryana, Mahendergarh, Haryana, India

Anil Kumar Department of Chemistry, Lovely Professional University, Phagwara, India

Avshish Kumar Amity Institute of Advanced Research and Studies (Materials and Devices), Amity University, Noida, Uttar Pradesh, India

Deepak Kumar Department of Chemistry, Lovely Professional University, Phagwara, India

Ramesh Kumar Virology Section, Department of Microbiology, All India Institute of Medical Sciences (AIIMS), New Delhi, India

Satendra Kumar Department of Applied Physics, Amity Institute of Applied Sciences, Amity University Uttar Pradesh, Noida, India

Shivani A. Kumar Amity Institute of Applied Sciences, Amity University, Noida, India

Varun Kumar Amity Institute of Advanced Research and Studies (Materials and Devices), Amity University, Noida, Uttar Pradesh, India

Vivek Kumar Amity Institute of Advanced Research and Studies (Materials and Devices), Amity University, Noida, Uttar Pradesh, India

Arti Maan Shriram Institute for Industrial Research, New Delhi, Delhi, India

Sudip Majumder Amity School of Applied Sciences, Gurgaon, India

Akansha Mehra Amity Institute of Advanced Research and Studies (Materials & Devices), Amity University, Noida, UP, India

Harish Mudila Department of Chemistry, Lovely Professional University, Phagwara, India

Suman Nagpal Amity Institute of Advanced Research and Studies (Materials & Devices), Amity University, Noida, UP, India

Omita Nanda Amity Institute of Renewable and Alternative Energy and Amity Institute of Advanced Research and Studies (Materials and Devices), Amity University, Noida, Uttar Pradesh, India

Rajiv Narang Department of Cardiology, All India Institute of Medical Sciences (AIIMS), New Delhi, India

Safiya Nisar Amity Institute of Applied Sciences, Amity University, Noida, Uttar Pradesh, India

Yash Pal Mundra Solar PV Limited, Mundra, Gujrat, India

Ariba Parveen Department of Physics, Aligarh Muslim University, Aligarh, India

Ashish Pathak DMRL, Hyderabad, Telangana, India

Ch. Kartikeshwar Patro Department of Applied Physics, Amity Institute of Applied Sciences, Amity University Uttar Pradesh, Noida, India

H. Prakash Department of Physics, University of Allahabad, Allahabad, India

Jai Prakash Department of Physics, Aligarh Muslim University, Aligarh, India

R. Prakash Department of Physics, University of Allahabad, Allahabad, India

V. Raghavendra Reddy UGC-DAE Consortium for Scientific Research, University Campus, Indore, India

Bhuvneshwar Rai Shriram Institute for Industrial Research, New Delhi, Delhi, India

Rashmi Material Science Programme, IIT Kanpur, Kanpur, India

Sunita Rattan Amity Institute of Applied Science/Amity University, Noida, Uttar Pradesh, India;
Amity Institute of Applied Sciences, Amity University, Noida, Uttar Pradesh, India

Astha Sachdeva Department of Anthropology, University of Delhi, New Delhi, India

Mahima Sachdeva INO, Tata Institute of Fundamental Research, Mumbai, India

Vyas Maharshi Sandipkumar Amity Institute of Renewable and Alternative Energy, Amity University, Noida, Uttar Pradesh, India

Anita Sangwan Department of Physics, Singhania University, Jhunjhunu, Rajasthan, India

Kanchan Saxena Amity Institute of Renewable and Alternative Energy and Amity Institute of Advanced Research and Studies (Materials and Devices), Amity University, Noida, Uttar Pradesh, India

Bharti Sharma Department of Analytical Chemistry, CSIR-NPL, New Delhi, India

Kavita Sharma Amity Center for Spintronic Materials, Amity University UP, Noida, India

Virender Sharma Mundra Solar PV Limited, Mundra, Gujrat, India;
Amity Institute of Renewable and Alternative Energy, Amity University, Noida, Uttar Pradesh, India

Pramila Shukla Department of Physics, AIAS, Amity University, Noida, Uttar Pradesh, India

D. P. Singh School of Physics and Materials Science, Thapar Institute of Engineering & Technology, Patiala, India

Mahender Singh Department of Physics, Singhania University, Jhunjhunu, Rajasthan, India

Manjeet Singh Department of Physics, Government College Matanhail, Jhajjar, Haryana, India

Nahar Singh Department of Analytical Chemistry, CSIR-NPL, New Delhi, India

Navneet Singh Department of Physics, Rajiv Gandhi Government College for Women, Bhiwani, Haryana, India

Prachi Singhal Amity Institute of Applied Science/Amity University, Noida, Uttar Pradesh, India

Ricardo B. Smith Nuclear and Energy Research Institute (IPEN/CNEN—SP), São Paulo, Brazil

Alok Kumar Srivastava Defence Materials and Stores Research and Development Establishment, Kanpur, India

Ritu Srivastava Center for Organic Electronics, OLED Lab, Physics of Energy Harvesting Division, National Physical Laboratory, New Delhi, India

Sanjeev K. Srivastava Department of Physics, Amity Institute of Applied Sciences, Amity University Uttar Pradesh, Noida, India

Suman Amity Institute of Advanced Research and Studies (Materials and Devices), Amity University, Noida, Uttar Pradesh, India

Anjali Tyagi Amity Institute of Applied Sciences, AUUP, Noida, India

Vinay Tyagi Shriram Institute for Industrial Research, New Delhi, Delhi, India

Abhishek Verma Amity Institute of Renewable and Alternative Energy, Amity Institute of Advanced Research and Studies (Materials and Devices), Amity University, Noida, Uttar Pradesh, India;
Advanced Research and Studies (Materials and Devices), Amity Institute, Amity University, Noida, Uttar Pradesh, India

Rohit Verma Department of Applied Physics, Amity Institute of Applied Sciences, Amity University Uttar Pradesh, Noida, India

Heena Yadav Amity School of Applied Sciences, Gurgaon, India

Chapter 1
Improved Thermal Conductivity and Energy Storage Properties of Graphitized Carbon Black Based Magnesium Nitrate Hexahydrate Composite

Neeraj Gupta, Amit Kumar, Hrishikesh Dhasmana, Avshish Kumar, Vivek Kumar, Abhishek Verma, S. K. Dhawan, and V. K. Jain

Abstract Latent heat thermal energy storage (LHTES) using phase change materials (PCMs) are an effective way to store energy. Here we demonstrated the effect of carbon nano-material include graphitized carbon black on the thermal conductivity and energy storage properties of magnesium nitrate hexahydrate (MNH), an inorganic salt hydrate phase change material. The MNH-carbon nanocomposite was prepared using melt mixing method by dispersing the carbon nano-material at a mass fraction of 0.5 wt% in MNH. The as-prepared composite was analyzed by scanning electron microscopy. The Fourier-transformed infrared (FTIR) confirmed no chemical interaction between the MNH and carbon nano-material in MNH-carbon nanocomposite. The thermal conductivity of the sample in the solid phase was measured using the transient hot-wire method and found that the thermal conductivity of MNH-carbon nanocomposite increased by 62.5% with respect to pristine MNH. The energy storage properties include charging and discharging was also analyzed by a conventional heating system, which confirmed that the presence of carbon nano-material enhances the heat transfer rates. The result implies that the materials used in this study could be used as a potential candidate for thermal energy storage.

N. Gupta · H. Dhasmana · A. Kumar · V. Kumar · A. Verma · V. K. Jain
Amity Institute of Advanced Research and Studies (Materials and Devices), Amity University, Noida, Uttar Pradesh 201303, India

A. Kumar (✉)
School of Engineering and Technology, Central University of Haryana, Jant-Pali, Mahendergarh, Haryana 123031, India
e-mail: kumaramit@cuh.ac.in

S. K. Dhawan
Division of Materials Physics and Engineering, National Physical Laboratory, New Delhi, India

V. K. Jain et al. (eds.), *Recent Trends in Materials and Devices*, Springer Proceedings in Physics 256, https://doi.org/10.1007/978-981-15-8625-5_1

1.1 Introduction

The rapid depletion of fossil-based energy resources and the increase of environmental pollution, renewable energy utilization have been an area of interest for research and development. Solar radiation is one of the most important sources of energy. Solar energy is available during day time; hence its application requires an efficient thermal energy storage system to store the energy for later use. Latent heat thermal energy storage (LHTES) using phase change material (PCMs) is getting popular because it offers a much higher storage density and constant operating temperature [1]. PCMs are those materials that can absorb and release a large amount of thermal energy at their phase transition temperature. Owing to their excellent energy storage property, PCMs have been utilized in the fields of smart textile, surplus heat management, building, and solar energy harvesting [2–6]. According to the different phase forms and chemical nature, PCMs are divided into two types, organic and inorganic. Compared with organic PCMs, inorganic salt hydrate has huge advantages in LHTES, such as high latent heat and thermal conductivity, lower price, and incombustibility [7, 8]. However, the inherently low conductivity of salt hydrates limits the efficiency of thermal energy storage system and their application in actual engineering [9, 10]. To solve the above problem, several techniques have been proposed, such as the uses of heat pipes and fins, macro-encapsulation and microencapsulation, dispersion of high conductivity materials [11–13]. The dispersion of high thermally conductive material such as nanoparticles is one of the best ways to enhance the thermal conductivity of PCMs is currently of great interest and receiving attention [14–16]. Harikrishnan and kalaiselvam [17] added the 2 wt% of CuO nanoparticles in oleic acid, the pristine PCM. It was found that by adding the nanoparticles, thermal conductivity significantly improved by 98.66%. Zeng et al. [18] prepared the PCM-nanocomposite by dispersing copper nanowires (11.9 vol%) into tetradecyl alcohol. It was interesting to find that the thermal conductivity reached 2.86 W m^{-1} K^{-1}, nine times higher that of pure tetradecyl alcohol. Said et al. [19] study the performance of the air conditioning system using rubitherm commercial (SP24E) as the base PCM and PCM mixed with nanoparticles. It was found that the heat transfer characteristics of the composite increased in comparison to the pristine PCM.

Besides metallic and metallic oxide nanoparticles, carbon-based nano-materials have received great attention, to enhance the thermal conductivity of PCMs, because of their extremely high thermal conductivity (e.g. 3000–6600 W m^{-1} K^{-1}). For instance, wang et al. [20] dispersed the 2 wt% of MWCNT into the paraffin, the thermal conductivity increased by 35% and 40% in solid and liquid states, respectively. Hashempur et al. [21] used the surfactant to stabilize the MWCNTs in the butyl sterate as the PCM matrix to improve its thermal properties. The thermal conductivity increased from 0.16 to 0.185 W m^{-1} K^{-1} at 50 °C. Sahan et al. [22] used the MWCNTs and activated carbon to form the composite with the paraffin. Their finding shows that the thermal conductivity of the AC/paraffin and MWCNTs/paraffin composites increased by 17.2% and 38.5%, respectively. Li et al. [23] measured the

thermal conductivity of paraffin by dispersed the nano graphite at 10 wt%. The thermal conductivity reached 0.9362 W m^{-1} K^{-1}, which was 7.41 times higher in comparison to raw PCM. Colla et al. [24] prepared the nano-enhanced PCMs by embedded the carbon black nanoparticles into the paraffin. It was found that the thermal conductivity enhances to more than 25%. This article presents the preparation and thermal characterization of MNH-carbon nanocomposite for solar thermal application using magnesium nitrate hexahydrate and carbon nano-material includes graphitized carbon black. The main aim of this research work is to form the nano-enhanced composite with desirable property, especially with high thermal conductivity for the effective utilization of solar thermal energy systems. The chemical and thermal properties of prepared MNH-carbon nanocomposite were characterized by SEM, FTIR, and thermal conductivity measurement. The heat transfer properties of the MNH-carbon nanocomposite were further analyzed by measuring its melting and solidification cycle with respect to base PCM using a conventional heating system.

1.2 Experimental Description

1.2.1 Materials and Method

Magnesium nitrate hexahydrate (MNH), an inorganic salt hydrate PCM was purchased from Alfa-Aesar. Carbon nano-material (graphitized carbon black) was procured from Sigma Aldrich. All the materials were used directly as received without any further purification.

1.2.2 Preparation of MNH-Carbon Nanocomposite

The MNH-carbon nanocomposite was prepared using the melt-blending method [25]. In this method, MNH was heated above its melting point i.e. 89 °C to ensure its melting. The carbon nano-material was added to the molten MNH and mixed thoroughly by using a mechanical stirrer for 20 min and then ultrasonicated to obtained the homogenous dispersion of carbon nano-material in MNH matrix for the formulate of stable MNH-carbon nanocomposite. The optimal mass fraction 0.5 wt% carbon nano-material was used for the preparation of MNH-carbon nanocomposite.

1.2.3 Characterization Techniques

The morphology analysis of the material was done using Zeiss (EVO-18) scanning electron microscope (SEM). The SEM micrographs were used to observe the

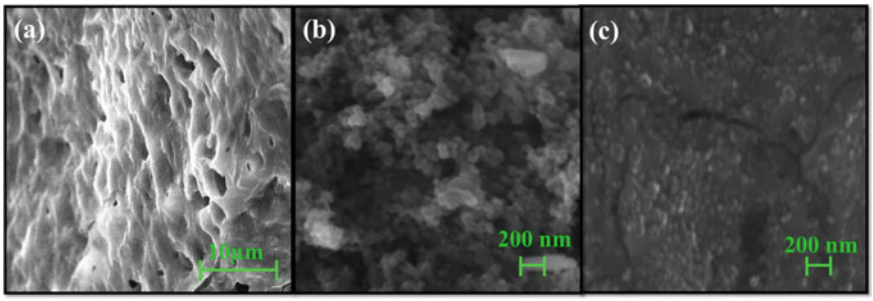

Fig. 1.1 SEM micrographs of **a** PCM (Magnesium nitrate hexahydrate) (MNH), **b** carbon nanomaterial (graphitized carbon black) and **c** MNH-carbon nanocomposite

dispersion of the carbon nano-material in the PCM matrix (MNH). The chemical interaction between MNH and carbon nano-material in MNH-carbon nanocomposite was investigated by using Fourier Transformed Infrared spectrophotometer (FTIR, VERTEX 70 BRUKER). Heat transfer characteristics were analyzed by carrying out the charging-discharging cycle of PCM-carbon nanocomposite with respected to pristine PCM using a conventional heating system [26]. The thermal conductivity of solid PCM-nanocomposite was measured by using a Linseis Transient Hot bridge-Thermal Conductivity Meter (THB6N43) under lab conditions.

1.3 Results and Discussion

1.3.1 SEM Analysis

The microstructure of the PCM, carbon nano-material (graphitized carbon black), and MNH-carbon nanocomposite are present in Fig. 1.1. It can be seen from Fig. 1.1a that pristine PCM characterized as a solid crystalline structure. The micrograph of carbon nano-material, as shown in Fig. 1.1b had a glossy structure and was used as a filler to increase the thermal conductivity of the base MNH matrix. The SEM image of MNH-carbon nanocomposite, as shown in Fig. 1.1c, which reveals that composite is homogeneous, and the carbon nano-material is well distributed over the surface of the MNH without any agglomeration.

1.3.2 FTIR Analysis

Figure 1.2 presents the FTIR spectrums of MNH and MNH-carbon nanocomposite. A series of absorption peaks can be observed in the FTIR spectrum of $Mg(NO_3)\cdot 6H_2O$ (MNH), as shown in Fig. 1.2a. For instance, the absorption peaks for N=O bending at

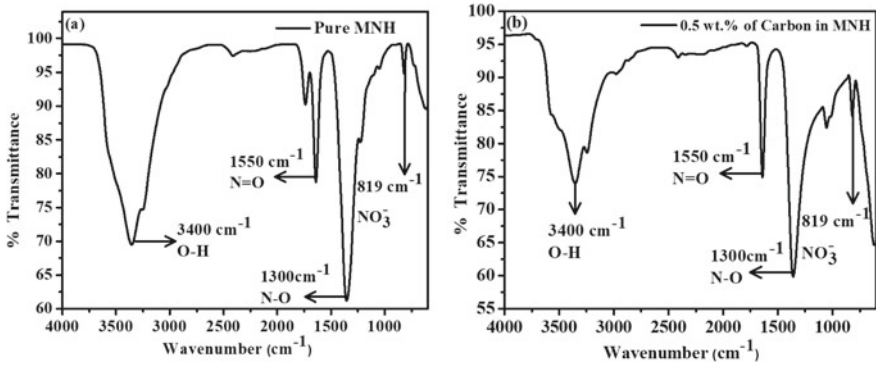

Fig. 1.2 FTIR spectra of **a** magnesium nitrate hexahydrate (MNH) and **b** MNH-carbon nanocomposite

1550 cm^{-1}, O–H stretching at 3400 cm^{-1}, a mixture of N–O stretching and bending of N=O at 1300 cm^{-1}, plus a sharp peak at 819 cm^{-1} for NO_3^- can be seen and are in well agreement with the reported literature [27]. In the spectrum of MNH-carbon nanocomposite as shown in Fig. 1.2b, no new shift or peaks is observed in comparison to pristine MNH. It means that no considerable chemical interaction between MNH and carbon nano-material, indicating that both the materials were merely physically mixed to form a stable MNH-carbon nanocomposite. Similar results were also reported by the other group, where they reported the simple physical interaction between the filler and the PCMs [28].

1.3.3 Meting and Solidification Experimental Results

The conventional heating system was used to evaluate the heat transfer characteristics of MNH and MNH-carbon nanocomposite by comparing their charging (melting) and discharging the solidification cycle. The melting cycle of MNH-carbon nanocomposite at a mass fraction of 0.5 wt% carbon nano-material and MNH, as shown in Fig. 1.3a. Both the MNH-carbon nanocomposite and MNH were kept at room temperature at the beginning of the melting cycle. The temperature of MNH-carbon nanocomposite and MNH were increased gradually by 2 °C/min until they reached their phase transition point. A drastic decrease in the melting time of MNH-nanocomposites at a mass fraction of 0.5 wt% carbon nano-material was observed. This shows the overall reduction of 5.8% in melting time for MNH-carbon nanocomposite was observed as compared to that of pristine MNH.

The solidification experiment on MNH-carbon nanocomposite and Pristine MNH was also performed as shown in Fig. 1.3b. The temperature of MNH and MNH-carbon nanocomposite was found to be at 120 °C at the initial stage of the solidification cycle. Both the materials were allowed to cool; naturally, the temperature of MNH-carbon

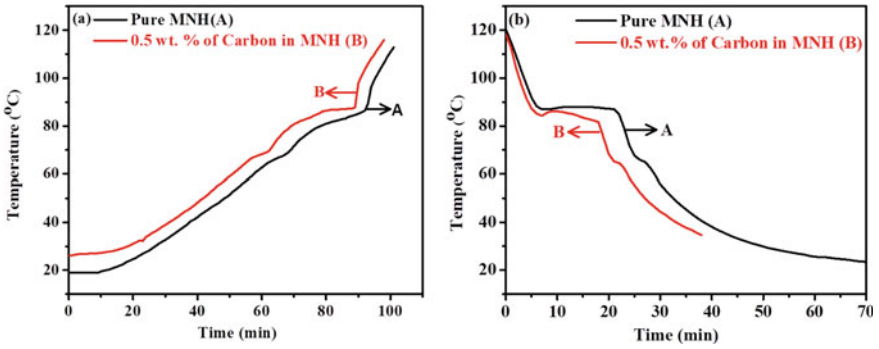

Fig. 1.3 **a** Melting curve of MNH and MNH-carbon nanocomposite at a mass fraction of 0.5 wt% nano-material and **b** solidification curves of MNH and MNH-carbon nanocomposite at a mass fraction of 0.5 wt% nano-material

nanocomposite at a mass fraction of 0.5 wt% nano-material and MNH decreased until they reached their respective solidification point. The results showed the overall reduction of 30% in solidification time for MNH-carbon nanocomposite is observed as compared to MNH, due to the enhancement in thermal conductivity of the material.

1.3.4 Thermal Conductivity

Thermal conductivity determines the speed of heat transfer with in the material. It is an important parameter for selecting phase change material for the thermal energy storage application. The main aim of this work is to analyze the effect of adding high conductivity carbon nano-materials on the effective thermal conductivity of inorganic salt hydrate PCMs. In nanocomposites, the heat transfer occurs due to the acoustic phonons with different frequencies. However, for the enhancement of thermal conductivity in nanocomposites, the interface resistance plays an important factor. Figure 1.4. describes the thermal conductivity results between the pristine MNH and MNH-carbon nanocomposite at a mass fraction of 0.5 wt% carbon nano-material. The results display that MNH-carbon nanocomposite has the thermal conductivity (0.66) W m^{-1} K^{-1} much higher than that of pristine MNH (0.4) W m^{-1} K^{-1}. The high thermal conductive network established by the filler in MNH matrix enhances the thermal conductivity of MNH-carbon nanocomposite. This enhancement in thermal conductivity decreases the phase transition time, i.e. (reduction in melting and solidification time), thereby providing a better solution for the proper functioning of the thermal energy storage system to respond to fast load variation.

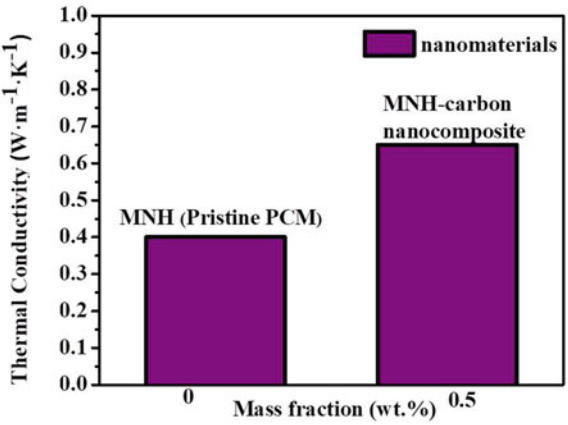

Fig. 1.4 Thermal conductivity curve of MNH and MNH-carbon nanocomposite at a mass fraction of 0.5 wt% nano-material

1.4 Conclusion

In this paper, MNH-carbon nanocomposite was prepared by the melt-mixing technique by adding carbon nano-material at a mass fraction of 0.5 wt% in MNH. The characterization results of SEM revealed that carbon nano-material is uniformly distributed in the MNH matrix without any agglomeration. The FTIR analysis shows that carbon nano-material does not show any chemical interaction with the MNH matrix, as they are attached physically. The prepared MNH-carbon nanocomposite shows the rapid melting (charging rate increased to 5.8%) and solidification (discharging rate increased to 30%) for 0.5 wt% carbon nano-material as compared to Pristine MNH. The thermal conductivity of MNH-carbon nanocomposite enhances by 65% as compared to pristine PCM. Therefore MNH-carbon nanocomposite can be used as an effective material for the Latent heat thermal energy storage system.

Acknowledgements We thank Dr. Ashok K. Chauhan, founder president of Amity University, for his continuous support and also thanks to other members of the AIARS (M&D) group, Amity University, Noida, for their support.

References

1. E. Osterman, V. Tyagi, V. Butala, N.A. Rahim, U. Stritih, Review of PCM based cooling technologies for buildings. Energy Build. **49**, 37–49 (2012)
2. G.G. Han, H. Li, J.C. Grossman, Optically-controlled long-term storage and release of thermal energy in phase-change materials. Nature Commun. **8**(1), 1–10 (2017)
3. J.A. Turner, A realizable renewable energy future. Science **285**(5428), 687–689 (1999)
4. S. Mondal, Phase change materials for smart textiles–an overview. Appl. Therm. Eng. **28**(11–12), 1536–1550 (2008)

5. E. Solgi, R. Fayaz, B.M. Kari, Cooling load reduction in office buildings of hot-arid climate, combining phase change materials and night purge ventilation. Renew. Energy **85**, 725–731 (2016)
6. S.N. Gunasekara, R. Pan, J.N. Chiu, V. Martin, Polyols as phase change materials for surplus thermal energy storage. Appl. Energy **162**, 1439–1452 (2016)
7. A. Sharma, V.V. Tyagi, C. Chen, D. Buddhi, Review on thermal energy storage with phase change materials and applications. Renew. Sustain. Energy Rev. **13**(2), 318–345 (2009)
8. G. Li, B. Zhang, X. Li, Y. Zhou, Q. Sun, Q. Yun, The preparation, characterization and modification of a new phase change material: CaCl2 6H2O–MgCl2 6H2O eutectic hydrate salt. Sol. Energy Mater. Sol. Cells **126**, 51–55 (2014)
9. J. Khodadadi, L. Fan, H. Babaei, Thermal conductivity enhancement of nanostructure-based colloidal suspensions utilized as phase change materials for thermal energy storage: a review. Renew. Sustain. Energy Rev. **24**, 418–444 (2013)
10. Z.A. Qureshi, H.M. Ali, S. Khushnood, Recent advances on thermal conductivity enhancement of phase change materials for energy storage system: a review. Int. J. Heat Mass Transf. **127**, 838–856 (2018)
11. S. Motahar, N. Nikkam, A.A. Alemrajabi, R. Khodabandeh, M.S. Toprak, M. Muhammed, A novel phase change material containing mesoporous silica nanoparticles for thermal storage: a study on thermal conductivity and viscosity. Int. Commun. Heat Mass Transfer **56**, 114–120 (2014)
12. T. Khadiran, M.Z. Hussein, Z. Zainal, R. Rusli, Encapsulation techniques for organic phase change materials as thermal energy storage medium: a review. Sol. Energy Mater. Sol. Cells **143**, 78–98 (2015)
13. T.-u Rehman, H.M. Ali, M.M. Janjua, U. Sajjad, W.-M. Yan, A critical review on heat transfer augmentation of phase change materials embedded with porous materials/foams. Int. J. Heat Mass Transf. **135**, 649–673 (2019)
14. M. Kibria, M. Anisur, M. Mahfuz, R. Saidur, I. Metselaar, A review on thermophysical properties of nanoparticle dispersed phase change materials. Energy Convers. Manage. **95**, 69–89 (2015)
15. G.R. Dheep, A. Sreekumar, Influence of nano-materials on properties of latent heat solar thermal energy storage materials–a review. Energy Convers. Manage. **83**, 133–148 (2014)
16. H. Nazir, M. Batool, F.J.B. Osorio, M. Isaza-Ruiz, X. Xu, K. Vignarooban, P. Phelan, A.M. Kannan, Recent developments in phase change materials for energy storage applications: a review. Int. J. Heat Mass Transf. **129**, 491–523 (2019)
17. S. Harikrishnan, S. Kalaiselvam, Preparation and thermal characteristics of CuO–oleic acid nanofluids as a phase change material. Thermochim. Acta **533**, 46–55 (2012)
18. J.-L. Zeng, F.-R. Zhu, S.-B. Yu, L. Zhu, Z. Cao, L.-X. Sun, G.-R. Deng, W.-P. Yan, L. Zhang, Effects of copper nanowires on the properties of an organic phase change material. Sol. Energy Mater. Sol. Cells **105**, 174–178 (2012)
19. M. Said, H. Hassan, Effect of using nanoparticles on the performance of thermal energy storage of phase change material coupled with air-conditioning unit. Energy Convers. Manage. **171**, 903–916 (2018)
20. J. Wang, H. Xie, Z. Xin, Thermal properties of paraffin based composites containing multi-walled carbon nanotubes. Thermochim. Acta **488**(1–2), 39–42 (2009)
21. S. Hashempour, M.H. Vakili, Preparation and characterisation of nano enhanced phase change material by adding carbon nano tubes to butyl stearate. J. Exp. Nanosci. **13**(1), 188–198 (2018)
22. N. Şahan, M. Fois, H. Paksoy, The effects of various carbon derivative additives on the thermal properties of paraffin as a phase change material. Int. J. Energy Res. **40**(2), 198–206 (2016)
23. M. Li, A nano-graphite/paraffin phase change material with high thermal conductivity. Appl. Energy **106**, 25–30 (2013)
24. L. Colla, L. Fedele, S. Mancin, L. Danza, O. Manca, Nano-PCMs for enhanced energy storage and passive cooling applications. Appl. Therm. Eng. **110**, 584–589 (2017)
25. S.S. Narayanan, A. Kardam, V. Kumar, N. Bhardwaj, D. Madhwal, P. Shukla, A. Kumar, A. Verma, V. Jain, Development of sunlight-driven eutectic phase change material nanocomposite for applications in solar water heating. Res.-Efficient Technol. **3**(3), 272–279 (2017)

26. A. Kardam, S.S. Narayanan, N. Bhardwaj, D. Madhwal, P. Shukla, A. Verma, V. Jain, Ultrafast thermal charging of inorganic nano-phase change material composites for solar thermal energy storage. RSC Adv. **5**(70), 56541–56548 (2015)
27. M. Graham, E. Shchukina, P.F. De Castro, D. Shchukin, Nanocapsules containing salt hydrate phase change materials for thermal energy storage. J. Mater. Chem. A **4**(43), 16906–16912 (2016)
28. B. Xu, J. Zhou, Z. Ni, C. Zhang, C. Lu, Synthesis of novel microencapsulated phase change materials with copper and copper oxide for solar energy storage and photo-thermal conversion. Sol. Energy Mater. Sol. Cells **179**, 87–94 (2018)

Chapter 2
Effect of Additional Heat Treatment in Fabrication Line of n-PERT Bifacial Solar Cell to Improve the Surface Passivation

Virender Sharma, C. V. Kannan, Yash Pal, Hrishikesh Dhasmana, Amit Kumar, Abhishek Verma, and V. K. Jain

Abstract This work presents optimization of preannealing step at the end of the existing process line of Silicon solar cell device fabrication and compared it with regularly processed n-Passivated Emitter Rear Total (n-PERT) bifacial solar cell. For preannealing purpose, rapid thermal process (RTP) treatment of the device has been performed in the temperature range of 500–900 °C for 20 min duration in the existing process line. The electrical evaluations of the devices are performed via I–V measurements which are depicting variation in respective solar cell output parameters such as open circuit voltage, short circuit current and fill factor with annealing temperature. An optimized heat treatment of RTP at 700 °C suggests appreciable improvement of 0.31% in the device efficiency with improvement in other solar cell parameters such as short circuit current and open circuit voltage by 51.6 mA and 4.8 mV respectively. The measured cell parameters are analysed in detail with the variation of RTP temperature and suggest that additional heat treatment at the end of process line can results into device improvement with the increase of annealing temperature upto 700 °C, via reduction of bulk recombination in the base region without much affecting junction properties in the crystalline Si solar cell. However, high temperature (>700 °C) annealing in the device fabrication line is deteriorating device parameters as well as its efficiency which can be attributed to depletion of hydrogen in passivating layer and degradation of p–n junction properties.

V. Sharma · C. V. Kannan · Y. Pal
Mundra Solar PV Limited, Mundra, Gujrat, India

V. Sharma · H. Dhasmana (✉) · A. Kumar · A. Verma · V. K. Jain
Amity Institute of Renewable and Alternative Energy, Amity University, Noida, Uttar Pradesh 201303, India
e-mail: hdhasmana@amity.edu

H. Dhasmana · A. Kumar · A. Verma · V. K. Jain
Amity Institute for Advanced Research and Studies (Materials and Devices), Amity University, Noida, Uttar Pradesh 201303, India

V. K. Jain et al. (eds.), *Recent Trends in Materials and Devices*, Springer Proceedings in Physics 256, https://doi.org/10.1007/978-981-15-8625-5_2

2.1 Introduction

Photo generation and thereby photovoltaic phenomenon into silicon (Si) based p–n junction device involves process of converting sunlight directly into electricity. The photovoltaic generation of electric energy by solar cells from incident solar irradiation energy is an important part of the renewable energy concept. This aims to reduce global warming by replacing fossil energy sources by renewable ones. By the end of 2018, an accumulated PV power installation is nearly 480 GW with nearly 95% share of crystalline silicon [1]. Hence, crystalline silicon cells are the workhorse of a multibillion dollar photovoltaic (PV) industry. Way back in 1950s with the first monocrystalline single junction solar cells made for space applications had an efficiency of about 6% and known as oldest type of solar cells [2]. Since then, by many years of continuous research and development, the efficiency of silicon solar cells have been improved to a record level of 26.7%/22.3% for mono-Si/multi-Si [3]. In recent past, the major efforts amongst research community are driven towards reducing the cost of Si solar cell device via enhancing efficiency and adopting low cost process. Since silicon material is abundant, nontoxic and related device fabrication technology is well matured, therefore, silicon wafer-based solar cells are currently dominating this dynamic photovoltaic market. Single junction Si solar cells have relatively simple device architecture. They consist of an electrically contacted large area p−n junction, which is equipped with a top grid contact so that the semiconductor material can be illuminated [4, 5]. Amongst different type of wafer based solar cell, *p*-type (typically boron doped) silicon solar cells have dominated all industrial development for decades due to its relative insensitivity to the degradation caused by exposure to cosmic rays [6]. For today's industrial mass production for terrestrial electricity generation, a typical state of the art *p*-type c-silicon solar cell with a homogeneous emitter and full aluminium back surface field (Al-BSF) has an efficiency of ∼19% with the standard silicon nitride passivation and screen printed silver paste metallization on the front [7]. But during field application of these solar cells, Light Induced Degradation (LID) due to boron oxygen complex formation in base region of solar cell affects working efficiency of the device [8]. Therefore, a lot of research has been conducted in the field of *n*-type (typically phosphorus doped) silicon based solar cells. It provides several advantages over *p*-type which includes better tolerance to common impurities (e.g., iron) [9], high bulk lifetime with negligible LID. Thus, *n* type silicon solar cells with high efficiency with better surface passivation features can be potentially more cost effective than *p* type silicon based cells during their field applications. There has been continuous development to achieve cost-efficient processes such as wafer surface passivation [10, 11], laser opening [12] and screen-printed aluminium local back surface field [13]. Based on surface passivation concept, various solar cell structures such as Passivated Emitter Rear Contact (PERC), Passivated Emitter Rear Locally Diffused (PERL), Passivated Emitter Rear Totally (PERT) etc. are suggested for fabricating high efficiency Si solar cells [14, 15]. Out of these solar cell technologies, n-type silicon based PERT solar cell has provided advantage of fabricating high efficiency bifacial solar cell which

involves process optimization in cost effective manner. It has been reported that employing a pre-firing annealing process at low temperature and/or short duration modulates the lifetime and suppresses the effect of Light and Elevated Temperature Induced Degradation (LeTiD) in mc-Si lifetime test structures and improves the bulk and surface lifetime [16]. Since bifacial Si solar cell involves silicon nitride layer on both front and rear side of the device therefore annealing effect can be beneficial for enhancing efficiency of the device via increase of hydrogen atom diffusion into Si surface and bulk. There are seldom reports available on thermal annealing of n-PERT bifacial Si solar cell. This paper presents thermal annealing effect on n-PERT bifacial solar cell via I–V study of the device in the temperature range of 500–900 °C. All the related device parameter are compared and analysed accordingly with respect to change in annealing temperature. The electrical evaluation of the device was carried out by measuring I–V curve by cetisPV, a complete class AAA rated high-precision tester system for the IV measurement of solar cells under standard test condition such as solar irradiance of 1000 w/m^2 (AM 1.5 spectrum) at device temperature of 25 °C.

2.2 Experimental Section

The n-type monocrystalline CZ Si wafers of area 15.735 × 15.735 cm^2 with resistivity range of 0.3–2.1 Ω cm with a thickness of 170 μm were used in the fabrication of n-PERT solar cell. The wafer was polished using alkaline solution with an industrial wet bench. A rear emitter of n-type was formed by the phosphorous diffusion using Phosphorous Oxychloride ($POCl_3$) as source dopant. The measured post diffusion sheet resistance on p-type wafers using four point probe method was approximately 110 Ω/sq of rear emitter. The rear Antireflection Coating (ARC) SiN_x was deposited at temperature of 450 °C by Plasma-Enhanced Chemical Vapour Deposition (PECVD) in Centrotherm cPLASMA tube furnace PECVD tool. After rear ARC, the front surface of wafer was anisotropically textured by an industrial-type alkaline texturing process line. The front emitter of solar cell was designed by the boron diffusion using Boron Bromide (BBr_3) as source dopant. The measured median sheet resistance was found to be approximately 80 Ω/sq. After Boron diffusion, wafers were isolated using $HF/HNO_3/H_2O$ chemicals. The front ARC (SiNx) was deposited by PECVD on this emitter layer. After front ARC deposition, the samples were annealed in industrial tube furnace at different temperatures ranging from 500 to 900 °C for 20 min to analyse the impact of thermal annealing on cell efficiency. After completing end process step of device (with and without annealing), electrical contacts (front and back) are screen printed on both side of the device and co-firing is performed with standard heat cycle. The flow chart of process line is shown in Fig. 2.1.

The adopted device architecture of this n-type bifacial solar cell based on PERT technology is shown in Fig. 2.2.

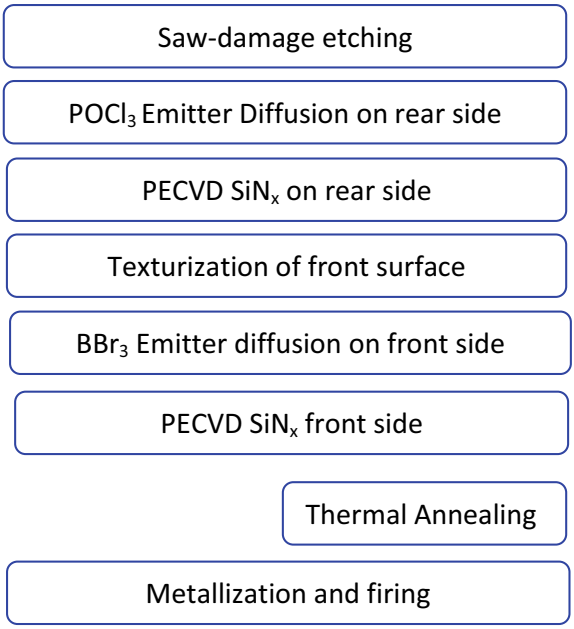

Fig. 2.1 Flow diagram of process line of n-PERT Bifacial solar cell

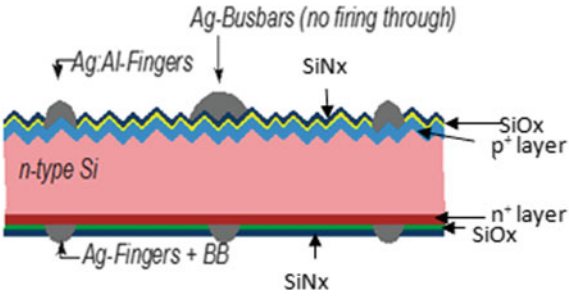

Fig. 2.2 Device architecture of n-PERT Si Bifacial solar cell

2.3 Results and Discussions

The I–V curve of any solar cell can be derived from its equivalent circuit diagram of one diode model for bulk crystalline solar cell structure [17]. The associated I–V (current density–voltage) equation for this model is given below (2.1) with the assumptions that there is negligible recombination existing in p–n junction region of solar cell.

$$J = J_{\mathrm{L}} + J_{\mathrm{o}}\left(e^{q(V+\mathrm{AJR_s})/\mathrm{nKT}} - 1\right) - q(V + \mathrm{AJR_s})/\mathrm{AR_{sh}} \tag{2.1}$$

where I, $I_{L,}$ $I_{o,}$ V, n, R_s, R_{sh} and K are net current, illumination current, reverse saturation current, terminal voltage, ideality factor, series resistance, shunt resistance and Boltzmann constant, respectively.

This equation determines ultimate shape of I–V curve under standard test conditions. The measured I–V graph of various fabricated devices with thermal treatment (thermal annealing at 500, 600, 700, 800 and 900 °C for 20 min duration) and untreated n-PERT Si solar cell devices are shown in Fig. 2.3. This I–V measurement of respective n-PERT solar cell gives solar cell output parameters, such as I_{SC}, V_{OC} and fill factor (F.F) with respect to different solar cell treatment conditions and accordingly determines the efficiency of the device under standard test conditions.

The figure clearly reflects improvement in solar cell parameters such as $V_{oc,}$ $I_{sc,}$ Fill Factor (F.F) and hence efficiency (η) of device with the increase of annealing temperature upto 700 °C and then device degrades with the increase of annealing temperature upto 900 °C. The extracted solar cell parameters, such as $V_{oc,}$ $I_{sc,}$ F.F and η from above I–V measurement, with respect to thermal annealing temperature are shown in Figs. 2.4, 2.5, 2.6 and 2.7, respectively.

Figure 2.4 depicts V_{oc} study of n-PERT solar cell with thermal heat treatment. A negligible change in V_{oc} upto thermal annealing temperature of 600 °C is observed and afterwards a maximum enhancement of 4.5 mV in V_{oc} from 658.2 mV (for without annealing solar cell) to 662.7 mV is observed This output cell parameter open circuit voltage (V_{oc}) i.e. maximum voltage across output terminal of a solar cell can be further analysed from following equation

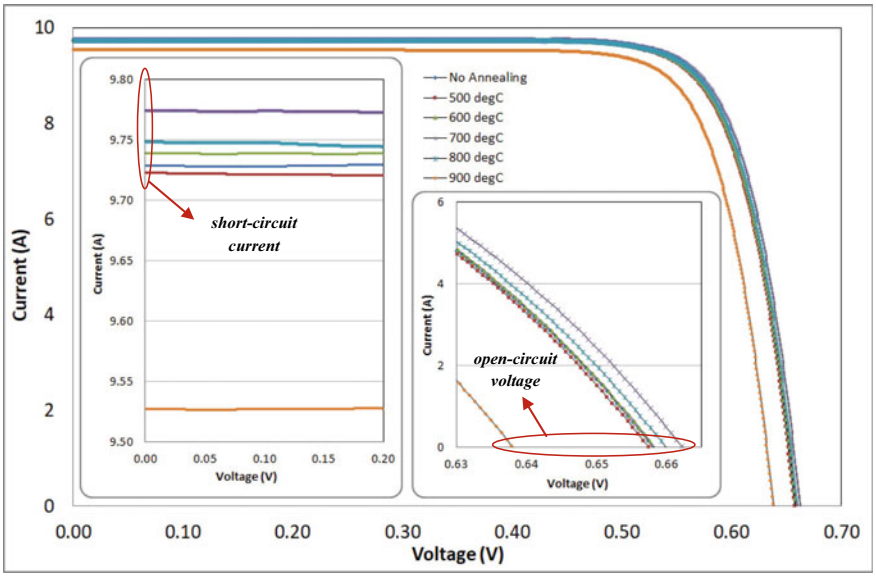

Fig. 2.3 I–V measurement of fabricated various n-PERT bifacial solar cells with additional thermal annealing along with controlled devices (without annealing solar cell)

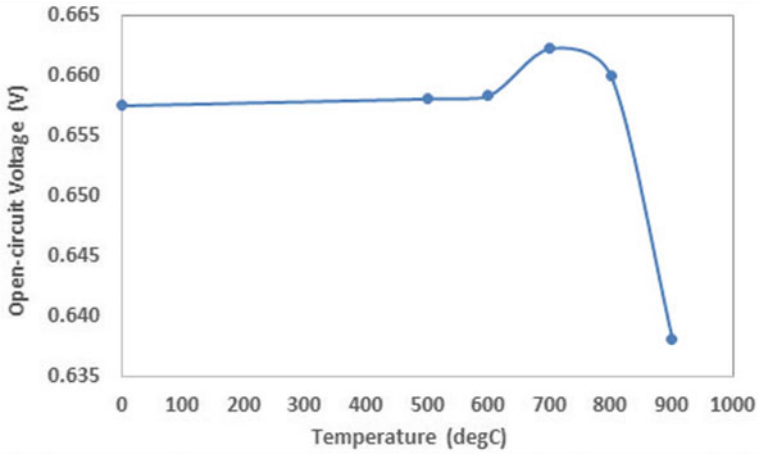

Fig. 2.4 Open circuit voltage variation of n-PERT solar cell with respect to annealing temperature

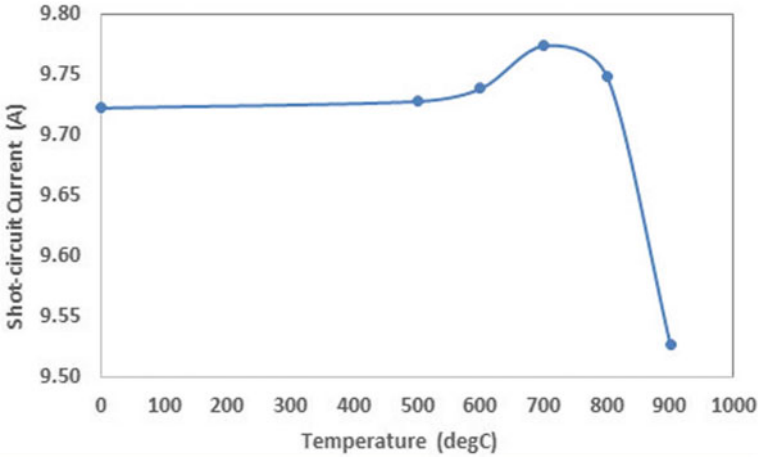

Fig. 2.5 Variation of short circuit current with the variation in thermal annealing temperature of n-PERT solar devices

$$V_{\mathrm{oc}} = \frac{\mathrm{KT}}{q}\mathrm{In}\left(\frac{I_{\mathrm{sc}}}{I_{\mathrm{o}}} + 1\right) \tag{2.2}$$

The (2.2) shows that V_{oc} extremely sensitive to I_{o} under standard test conditions and lower I_{o} is absolute necessity for enhancing V_{oc}. With the given device architecture shown in Fig. 2.2, total of I_{o} value can be subdivide into three associated parameters and are given by

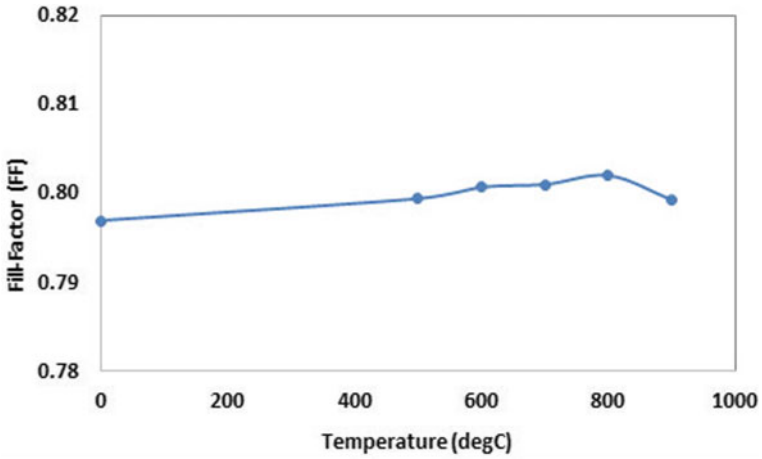

Fig. 2.6 Fill factor variation with thermal annealing temperature of n-PERT solar cell

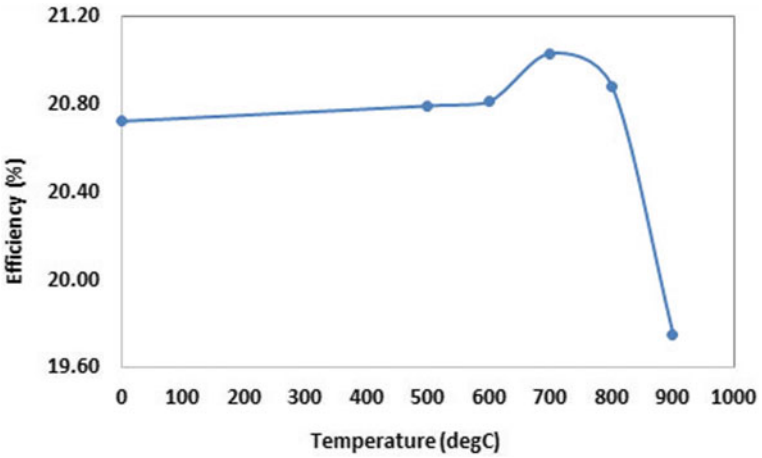

Fig. 2.7 Efficiency variation with thermal annealing temperature in n-PERT solar cell

$$I_o = I_{oe,f} + I_{ob,bulk} + I_{oe,b} \tag{2.3}$$

where, $I_{oe,f}$, $I_{ob,bulk}$ and $I_{oe,b}$ represents reverse saturation current from front emitter side, reverse saturation current from bulk base region, reverse saturation current from rear emitter side. These reverse saturation current densities measures leakage (or recombination) current of minority carriers in the p–n junction; which is the result of carrier recombination in near neutral regions on either side of the junctions. Both $I_{oe,f}$ and $I_{oe,b}$ depend largely on filling metallic contact properties, emitter passivation and emitter contact layer reverse saturation current. These two parameters in our case

do not much get affected because dependent parameters are not much sensitive to additional heat treatment as compare to parameter $I_{ob,bulk}$ [18]. This parameter $I_{ob,bulk}$ can be expressed by

$$I_{ob,bulk} = \frac{qn_i^2 W}{N_D \tau_p} \tag{2.4}$$

where, q, n_i, W, N_D and τ_p are electron charge, intrinsic carrier concentration, wafer thickness, donor concentration in base region and minority charge carrier life time respectively. Thus for minimization of $I_{ob,bulk}$ value, higher minority charge carrier life time is absolute necessity in the bulk region which can be observed by reducing bulk recombination in the device.

The thermal annealing temperature dependent short circuit current variations extracted from measured I–V graph (Fig. 2.3) are shown in Fig. 2.5. The figure clearly shows appreciable change of 40.8 mA in I_{SC} due to thermal annealing treatment at 700 °C with respect to untreated device. On further increasing annealing temperature, device performance degrades on account of device parameter I_{SC}. This behaviour can be analysed by studying dependent parameters of I_{SC} of solar cell which can be given by

$$I_{SC} = qG\left(L_n + L_p + W\right) \tag{2.5}$$

where G,L_n and L_p are generation rate, diffusion length of electron and hole respectively. Since G, A and W are same for all treated and untreated n-PERT solar cell, therefore minority charge carrier diffusion length of holes i.e. L_p in base region largely determine improvement in this parameter. This diffusion length (L_p) can be given by

$$L_p = \sqrt{D_p \tau_p} \tag{2.6}$$

where, D_p is diffusion coefficient of holes in the device.

So, parameter I_{SC} depends on minority charge carrier life time and on increasing minority charge carrier lifetime, diffusion length increases which shows enhancement in short circuit current. Enhancing minority charge carrier lifetime clearly reflects reduction in bulk recombination phenomenon in the device.

The variation of Fill factor of n-PERT solar cell with respect to increase in thermal annealing temperature is shown in Fig. 2.6. The figure shows negligible improvement in FF with increase of annealing temperature upto 700 °C. This variation of FF in device can be further analysed by equation given by

$$FF = \frac{v_{OC} - \ln(v_{OC} + 0.72)}{v_{OC} + 1} \tag{2.7}$$

where $v_{OC} = \frac{V_{OC}}{KT/q}$ is normalized open circuit voltage to thermal voltage. Literature [17] suggests that for $V_{OC} \geq 650$ mV of devices, FF variation of solar cell with respect to open circuit voltage increase shows almost saturation.

The variations in measured efficiency of n-PERT solar cell are shown in Fig. 2.7. The figure clearly shows efficiency increment with thermal annealing temperature upto 700 °C and then afterwards it shows degradation with the increase in temperature upto 900 °C. This variation in the device with thermal annealing treatment can be further validated by equation given below:

$$\eta = \frac{\text{FF} \times I_{SC} \times V_{OC}}{P_{in} \times A} \tag{2.8}$$

where, P_{in} is incident solar irradiance over A area of the device. Herein, P_{in} and A are same for all treated and untreated n-PERT solar cells. Thus equation clearly shows that efficiency of devices is dependent on output solar cell parameter, such as FF, I_{SC} and V_{OC}. The additional optimized heat treatment (thermal annealing at 700 °C for 20 min) is enhancing device performance by 0.31% due to thermal treatment and is indicated by improvement in solar cell output parameters such as V_{OC}, I_{SC} and FF, which is responsible for reducing bulk recombination in the base region of the device.

Thus device performance continuously improves on increasing annealing temperature upto 700 °C and starts to deteriorate afterwards. This behaviour of n-PERT solar cell to thermal annealing heat cycle with increase of temperature can be attributed to improved hydrogen passivation upto certain temperature and thereafter hydrogen start depleting itself because of high temperature treatment. Moreover, high annealing temperature close to diffusion temperature of front and rear emitter can degrade junction properties in solar cell.

2.4 Conclusions

The potential of incorporating optimized thermal heat treatment for enhancing n-PERT solar cell performance via measuring I–V curves of the devices has been studied. Our in-house developed industrial relevant electron-selective (thermal-SiOx/C-Si(n+)) and hole selective (thermal-SiOx/C–Si(p+)) passivated contacts into double-sided passivated contact solar cells along with passivated (SiN_x) layer on front and rear emitter sides are able to produce high efficiency (>20%) crystalline Si solar cell in n-type CZ wafers. The n-PERT solar cells are thermally annealed at different temperature of 500, 600, 700, 800 and 900 °C at the end of process line, just before metallization of the device. The effect of thermal treatment in the I–V characteristics of all the respective devices are analysed and discussed in detail. The measured I–V curves indicate improvement in solar cell parameters and show maximum enhancement of 51.6 mA and 4.8 mV in short circuit current and open

circuit voltage, respectively of the device due to optimized heat treatment (thermal annealing at 700 °C for 20 min). This has resulted into an improvement of 0.31% in the efficiency of solar cell. The I–V measurements of these devices are further analysed with respective device equations which indicates that reduction in bulk recombination due to additional optimized heat treatment in the device is responsible for enhancing device performance. The drop on efficiency above annealing temperature of 700 °C is presumably due to the depletion of hydrogen available in wafer for passivation and deterioration of diffused junction properties as annealing temperature reaching close to diffusion temperatures of front and rear emitter in n-PERT Si bifacial solar cell.

References

1. Future of Solar Photovoltaic, Deployment, investment, technology, grid integration and socio-economic aspects, Nov 2019, IRENA
2. https://en.wikipedia.org/wiki/Solar_cell#History_of_solar_ cells
3. M.A. Green, Y. Hishikawa, E.D. Dunlop, D.H. Levi, J. Hohl-Ebinger, M. Yoshita, A.W.Y. Ho-Baillie, Solar cell efficiency tables (version 53) Progress in Photovoltaics. Res. Appl. **27**, 3–12 (2019)
4. S.M. Sze, K.K. Ng, *Physics of Semiconductor Devices* (Wiley−Interscience, Hoboken, 2007)
5. A. Muller, M. Ghosh, R. Sonnenschein, P. Woiditsch, Silicon for photovoltaic applications. Mater. Sci. Eng. B **134**, 257–262 (2006)
6. G. Hahn, S. Joos, State of the art industrial crystalline silicon solar cells, in *Semiconductors and Semimetals*, 1st edn., vol. 90, eds. by G.P. Willeke, E.R. Weber (Academic, San Diego, CA, USA, 2014), pp. 1–62
7. P.K. Basu, K.D. Shetty, S. Vinodh, D. Sarangi, N. Palina, S. Duttagupta, F. Lin, Z. Du, J. Chen, B. Hoex, M.B. Boreland, A.G. Aberle, 19% Efficient inline-diffused large-area screen-printed Al-LBSF silicon wafer solar cells. Energy Procedia **27**, 444–448 (2012)
8. A. Wang, P.P. Altermatt, M. Green, J.P. Rakotoniaina, O. Breitenstein, High efficiency PERT cells on n-type silicon substrates, in *29th IEEE Photovoltaic Specialists Conference*, May 2002, pp. 218–221
9. S.W. Glunz, S. Rein, J.Y. Lee, W. Warta, Minority carrier lifetime degradation in boron doped Czochralski silicon. J. Appl. Phys. **90**(5), 2397–2404 (2001)
10. D. Macdonald, L.J. Geerligs, Recombination activity of interstitial iron and other transition metal point defects in p-and n-type crystalline silicon. Appl. Phys. Lett. **85**(18), 4061–4063 (2004)
11. A.G. Aberle, Overview on SiN surface passivation of crystalline silicon solar cells. Solar Energy Mater. Solar Cells **65**, 239–248 (2001)
12. G. Dingemans, W.M.M. Kessels, Status and prospects of Al_2O_3-based surface passivation schemes for silicon solar cells. J. Vac. Sci. Technol. A Vacuum Surf. Film **30**, 40802 (2012)
13. P. Engelhart, Laser processing for high-efficiency silicon solar cells. Proc. SPIE **7202**, 72020S–72020S-11 (2009)
14. S. Riegel, F. Mutter, T. Lauermann, B. Terheiden, G. Hahn, Review on screen printed metallization on p-type silicon. Energy Procedia **21**, 14–23 (2011)
15. A. Urueña1, M. Aleman, E. Cornagliotti, A. Sharma, J. Deckers, M. Haslinger, L. Tous, R. Russell, J. John, Y. Yao, T. Söderström, F. Duerinckx, J. Szlufcik, Beyond 22% large area n-type silicon solar cells with front laser doping and a rear emitter, in *30th EUPVSEC* (2015)
16. C. Sen, C. Chan, P. Hamer, M. Wright, U. Varshney, S. Liu, Annealing prior to contact firing: a potential new approach to suppress LeTID. Solar Energy Mater. Solar Cells **20**(15), 10993 (2019)

17. C.S. Solanki, *Solar Photovoltics* (PHI Learning Private Limited, New Delhi, 2009)
18. F. Feldmann, M. Bivour, C. Reichel, M. Hermle, S.W. Glunz, Passivated rear contacts for high-efficiency n-type Si solar cells providing high interface passivation quality and excellent transport characteristics. Solar Energy Mater. Solar Cells **120**, 270–274 (2014)

Chapter 3
Chitosan/Nanographiteplatlets (NGP)/Tungsten Trioxide (WO_3) Nanocomposites for Visible Light Driven Photocatalytic Applications

Jyoti Gupta, Prachi Singhal, and Sunita Rattan

Abstract Tungsten trioxide (WO_3) nanostructures have been one of the most important oxide nanostructures due to their unique properties and potential applications in optoelectronics such as dye-sensitized solar cell engineering, photocatalysis, water splitting, wastewater purification etc. Tungsten trioxide was a semiconductor material with a bandgap width of 2.5–2.8 eV that corresponds to the visible spectrum range. In the present work, Polymer/Nanographite platlets (NGP)/Tungsten trioxide (WO_3) nanocomposite films were prepared using solution blending followed by drop casting method. The morphological and structural characterization of polymer nanocomposites was carried out through Scanning Electron Microscopy (SEM), X-Ray Diffraction (XRD), Energy Dispersive Spectroscopy and Fourier Transform Infrared Spectroscopy (FTIR). The nanocomposites were evaluated for IV characteristics and optical properties through electrometer and UV spectroscopy respectively. The photocatalytic activities of pure Chitosan, Chi/NGP and Chi/NGP/WO_3 nanocomposites were explored for the photodegradation of methylene blue (MB) under visible light irradiation. The nanocomposite films proved to be the promising candidate for photocatalytic applications as they synergistically take advantage of all the three components, WO_3 as visible light responding nanostructured material, polymer for flexibility and faster charge transport through NGP. The nanocomposite material developed as photocatalyst is reusable and stable.

3.1 Introduction

Water pollution is a global environmental dispute which jeopardizes human health as well as affects our biodiversity. Dyes are the main by-product of industrial waste in water which badly affects the aquatic life and quality of water. Industrial waste water is produced by number of industries such as leather, paper, plastics and cosmetics which contains one of the harmful pollutants such as methylene blue, methyl orange

J. Gupta · P. Singhal · S. Rattan (✉)
Amity Institute of Applied Science/Amity University, Sector 125, Noida, Uttar Pradesh 201303, India
e-mail: srattan@amity.edu

V. K. Jain et al. (eds.), *Recent Trends in Materials and Devices*, Springer Proceedings in Physics 256, https://doi.org/10.1007/978-981-15-8625-5_3

and acid blue [1, 2]. Approximate 700,000 tons of dyes are discharged through water in which 15% of these are produced by textile industries [3, 4]. Methylene blue is used to tone up silk colors, to dye paper, in medicines and diagnostic procedures. Due to complex structure and hydrophilic nature of methylene blue, it can't be degraded by conventional process. Therefore, environment remediation is an immense need to get rid of pollutants from water and the photocatalytic degradation is one of the most important and ecofriendlly technique to degrade methylene blue. It is more effective rather than conventional process which produces no secondary pollutants. Many other complex organic compounds such as carbon dioxide and water can be oxidized into smaller molecular inorganic substances by photocatalytic degradation [5].

In past decade, various catalysts were used to degrade the methylene blue. Researchers had shown keen interest in semiconductor nanostructured materials and metal oxides for photocatalytic decomposition of pollutants in liquid phase [6–8].Tungsten trioxide, titanium dioxide, tungsten disulphide and graphene are the most promising candidates for decomposition of dyes. These have proven to be non-toxic, high chemically stable as well as low cost. In this paper, polymer, tungsten trioxide powder and graphene oxide nanocomposites films are used to degrade the methylene blue under visible light. WO_3 is n type semiconductor with low band gap. It has been widely used in gas sensing [9–12], lithium-ion batteries [13] smart windows [14, 15] and photocatalysis [16]. WO_3 has shown good response and high photocatalytic efficiency in visible light. Graphene, a monolayer of sp2-hybridized carbon atoms arranged in a two-dimensional lattice, has attracted tremendous attention in recent years owing to its exceptional thermal, mechanical, and electrical properties [17]. Graphene based semiconductor photocatalysts have shown prominent effect in environment and energy. Many researchers have shown their keen interest in graphene based nanocomposites because of exceptional thermal, mechanical and electrical properties. Graphene has played a role as an electron transfer medium in various nanocomposites such as graphene/TiO_2 photocatalyst and ZnO graphene composites proposed by Williams et al. [18] and Fan et al. [19] respectively. NGP/WO_3 nanocomposites can be prepared by so many methods such as electrochemical, hydrothermal [20], solvothermal [21]. In this work, Pure chitosan, Chitosan/Nanographite platelets (Chi/NGP) and Chitosan/Nanographite platelets/Tungsten trioxide (Chi/NGP/WO_3) nanocomposite films were synthesized to study the photocatalytic behavior in methylene blue upon visible light. Chi/NGP/WO_3 film was used as a photocatalyst, in which chitosan provides flexible, foldable and high stable matrix. Nanographite (NGP) was introduced with chitosan to provide an electron transfer medium which modified the semiconducting properties of WO_3 and chitosan.

3.2 Materials and Method

3.2.1 Materials

Acidified carbon graphite flakes (grade 1721) were supplied by Asbury. Sulfuric acid (98.08%), Hydrogen peroxide, Nitric acid (55%), HCl (3.6 wt%), Potassium permanganate, Methylene blue, Acetic Acid Glacial were purchased from Thermo fisher Scientific India Pvt. Ltd. All the Reagents of analytical grade were used in this experiment.

3.2.2 Preparation of Nanographite Platelets (NGP)

Graphene Oxide (GO) was synthesized from acidified graphite flakes according to Modified hummer's method. 50 ml of concentrated H_2SO_4 was dropped into 250 ml of three necked flask. This flask was kept into ice bath setup equipped with mechanical stirrer to maintain the temperature at 0 °C. 0.5 gm acidified graphite flakes were slowly added into H_2SO_4 under mechanical stirring to make the suspension for four hours and suspension turned into black. 3 gm $KMnO_4$ was slowly added into it under stirring for 1 h and maintained the temperature below 20 °C. Solution started turning into green color slowly then ice bath was removed and heated the solution upto 35 °C. 100 ml of deionized water was added to maintain temperature below 70 °C. Subsequently the suspension was diluted with 100 ml of deionized water also added 5 ml of H_2O_2 in the solution to quench the reaction. The suspension was centrifuged at 7000 rpm for twelve minutes and washed with HCl solution and then again washed with deionized water for four times until pH reached 6.

3.2.3 Synthesis of Pure Chitosan, Chi/NGP, Chi/NGP/WO_3 Films

1 gm chitosan flakes were added into the 50 ml of 2% acetic acid solution. 0.08 gm of tungsten trioxide and 0.3 gm of NGP were added into the prepared chitosan solution. The solution was ultrasonicated for 50 min for uniform distribution of nanofillers in the solution. After that, it was left on magnetic stirrer for overnight for complete dispersion of the particles. The solution had well dispersed particles and appropriate viscosity for casting the film then film was laid on the teflon plate. Teflon plate was kept in oven for about 20 h at 70 °C approximately and film was peeled off from teflon plate. Another film of same composition of chitosan (1 gm) and NGPs (0.3 gm) was synthesized using same procedure. In this series, pure chitosan film was also prepared by using 1 gm in 2% acetic acid solution. The synthesis process of

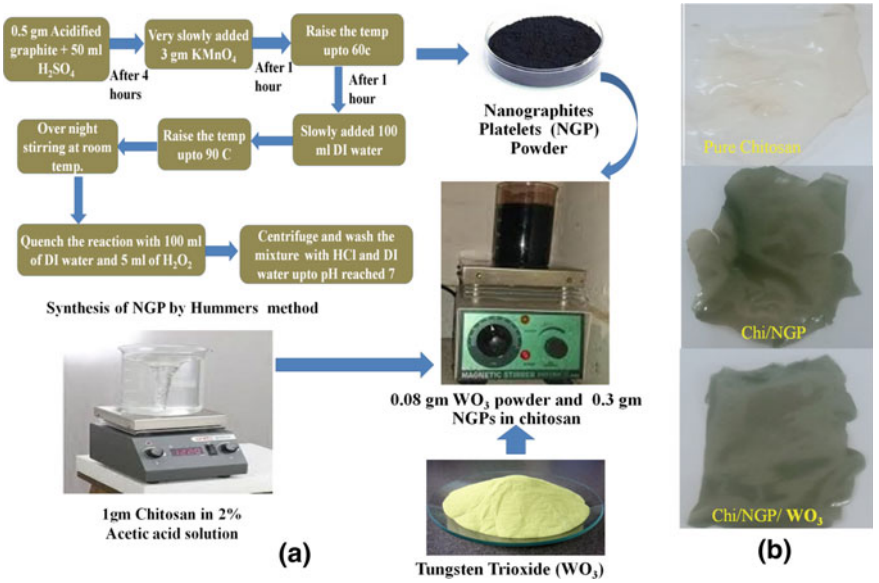

Fig. 3.1 (**a**) Schematic steps used for the synthesis of nanocomposite film of Pure Chitosan, Chi/NGP and Chi/NGP/WO_3, (**b**) The camera images of synthesized nanocomposite film of Pure Chitosan, Chi/NGP and Chi/NGP/WO_3

nanocomposite films were shown in Fig. 3.1. All three nanocomposite films were used for analysis of photocatalytic degradation of methylene blue.

3.3 Result and Discussion

3.3.1 Surface Morphology of Synthesized Chi/NGP and Chi/NGP/WO_3

The surface morphology of synthesized Chi/NGP and Chi/NGP/WO_3 nanocomposite films was analyzed by the SEM image that was conducted on ZEISS EVO Scanning Electron Microscope. Figure 3.2(a) has shown a large number of two dimensional nanosheets of graphene and the agglomeration of nanographite platelets. Figure 3.2(b) has shown the prominent image of nanographite platlets with rough surface and bend edges. The average size of Chi/NGP nanocomposite film was 150 nm. Nanographite platelets and nanorods of Chi/NGP/WO_3 structure were observed in Fig. 3.2(c) and (d) respectively at 10,000× magnification. Surface to volume ratio has increased in Chi/NGP/WO_3 nanocomposite film as compared to Chi/NGP film due to nanorods type structure. The adsorption of methylene blue has increased on the surface of Chi/NGP/WO_3 film because of this high surface to

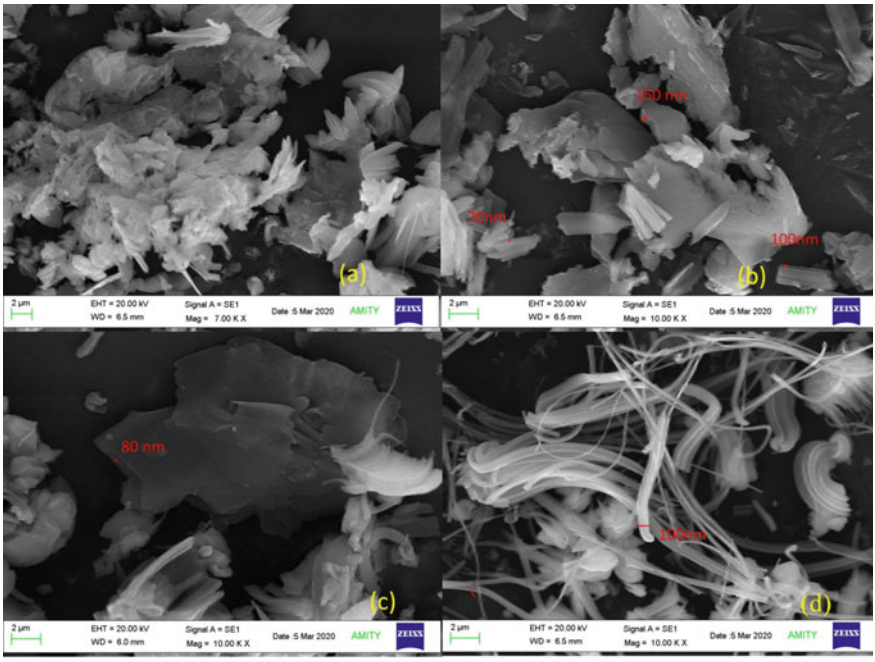

Fig. 3.2 **a** SEM image of Chi/NGP film at magnification of 7000×, **b** magnified SEM image of Chi/NGP film at 10000×, **c** SEM image of Chi/NGP/WO_3 film at magnification of 10,000×, **d** SEM image of Chi/NGP/WO_3 film at magnification of 10000×

volume ratio. The average size of synthesized Chi/NGP/WO_3 nanocomposite film was approximately 210 nm.

3.3.2 Elemental Composition of Synthesized Chi/NGPs and Chi/NGPs/WO_3

The energy dispersive X-ray spectrophotometry was equipped with SEM which indicated the elemental composition of synthesized film. Figure 3.3(a) and (b) indicated the elemental spectrum of Chi/NGP film and Chi/NGP/WO_3 film respectively. Small weight Percentage of Chlorine (2.54%) and Sulphor (5.96%) was also present in Chi/NGP film because of sulphuric acid and HCl which was used in synthesis of NGP. Weight percentage of Carbon (33.18%) and oxygen (41.14%) was present due to graphene. Figure 3.3(b) has indicated a very small weight percentage of tungsten (0.84%).

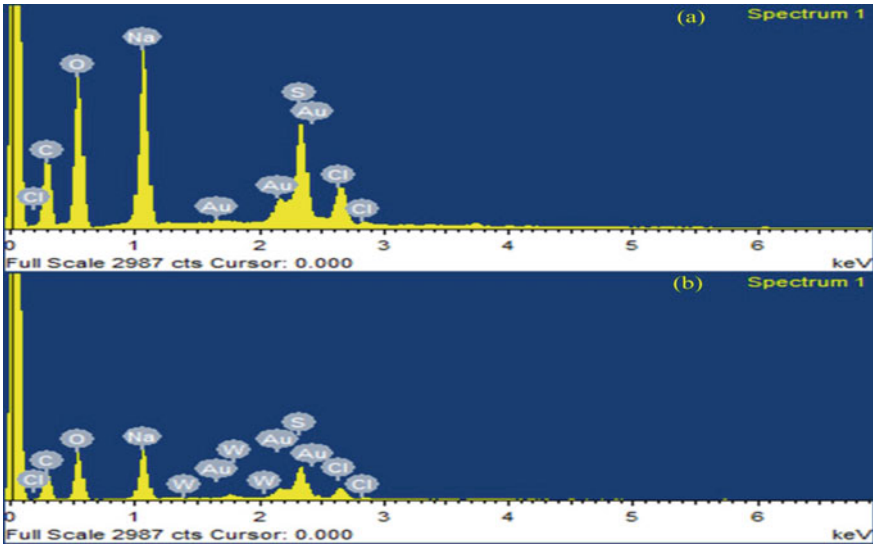

Fig. 3.3 **a** EDX spectrum image of Chi/NGP film. **b** EDX spectrum image of Chi/NGP/WO_3 film

3.3.3 Functional Group and Crystal Structure Analysis

The FTIR spectrum of synthesized film of Chi/NGP and Chi/NGP/WO_3 were shown in Fig. 3.4(a) and (b). The absorptoion band of nanographite platelets were shown by characteristic peaks at 3466.6 cm^{-1}, 3046.26 cm^{-1} and 1688.13 cm^{-1} ascribed to stretching of dissociative of O–H ions, stretching vibrations of C–H bond of aromatic ring and stretching of C=O (Carboxyl/Carbonyl roup) bond respectively. The characteristic peak of nanographite platelets at 1460.91 cm^{-1} was associated with the scissoring and bending of C–H bond. Absorption band at 1328.05 cm^{-1} in Chi/NGP nanocomposite film has demonstrated the O–H deformation (phenol group). The C–O bond vibrations of nanographite platelets was identified at 1140 cm^{-1}. Chi/NGP/WO_3 nanocomposite has shown the reduced height of peak at 1140 cm^{-1}due to reduction of graphene oxide. Different peaks were obtained at 848.10 cm^{-1} in Fig. 3.4(a) and (b). A broad characteristic peak were shown at 848.10 cm^{-1} in Chi/NGP/WO_3 nanocomposite film as compared to Chi/NGP which demonstrated the illustration of C–W bond. A small but discernible signal was shown at 716.33 cm^{-1} in Chi/NGP/ WO_3 as compared to the peak at 703.79 cm^{-1} in Chi/NGP which indicated the presence of W–O bond. The peak was obtained at 596.07 cm^{-1} demonstrated the the oxidation reaction and formation of W–O–W bond in Chi/NGP/WO_3 Nanocomposite film. The new peak was obtained at 439.21 cm^{-1} indicate the formation of new bond after the reaction NGP with WO_3.

The XRD pattern of synthesized Chi/NGP/WO_3 nanocomposite film was shown in Fig. 3.5. The diffraction peaks of planes as (002), (020), (101), (201), (121) and (102) were obtained at $2\theta = 21.150°$, 26.811°, 28.055°, 32.052°, 33.981° and 54.961°,

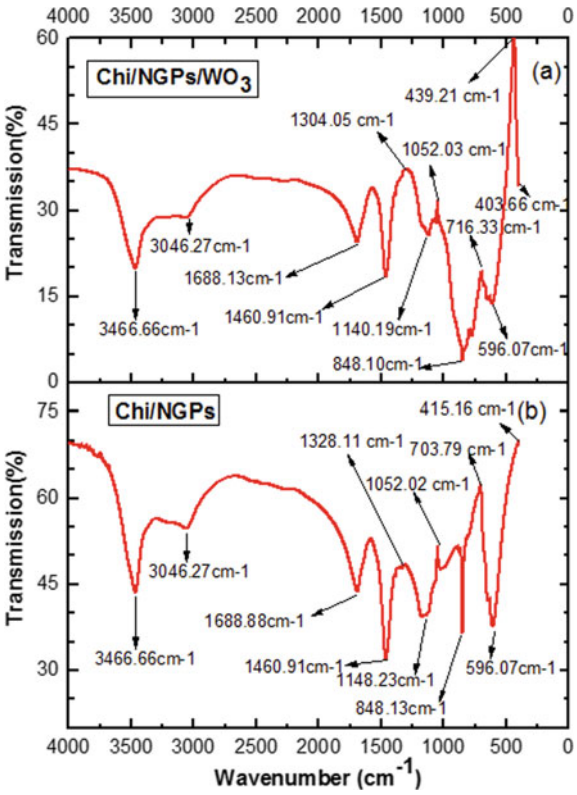

Fig. 3.4 **a** FTIR spectrum of Chi/NGP nanocomposite film, **b** FTIR spectrum of Chi/NGP/WO_3 nanocomposite film

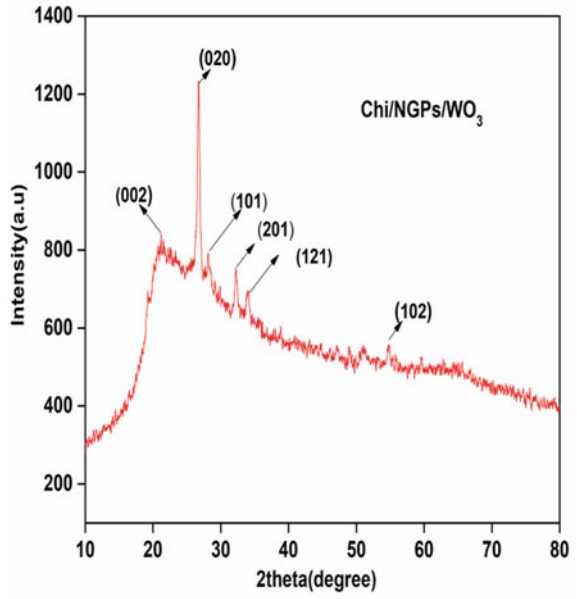

Fig. 3.5 XRD image of crystal structure of synthesized Chi/NGP/WO_3 nanocomposite film

respectively. The diffraction peaks at 21.150° and 26.811° were due chitosan and NGP respectively. The diffraction peaks at different 2θ values such as 28.055°, 32.052°, 33.981° and 54.961° were due to tungsten trioxide (WO_3). The crystal structure of the synthesized film was simple cubic. Average Size of Chi/NGP/WO_3 nanorod were given as 223.66 nm which was calculated by debye sherrer equation ($D = 0.9\lambda/\beta \cos \theta$) where as λ is the wavelentgh of (Cu(ka) = 1.540 A°) radiation, 2θ is bragg's angle and β is full width at half maximum intensity.

3.4 UV–Vis Photocatalytic Studies and UV–Vis Spectroscopy of Methylene Blue

The degradation experiment was performed in solar simulator equipped with xenon lamp light source and magnetic stirrer in dark wooden box. The degradation of methylene blue was analyzed by the adsorption of dye on the surface of nanocomposite films. Initially, the experiment was performed by pouring 10 μl of methylene blue in 15 ml of deionized water in 50 ml beaker. 250 mg of photocatalysts film of Chitosan/NGP/WO_3 was added in it under magnetic stirring in dark wooden box for 1 h to reach the adsorption. 5 ml of that adsorbed sampled were taken out for UV–Vis spectrometry. Now, light was kept on for 1 h for photocatalytic degradation of methylene blue. Lamp was fixed at 10 cm above the sample in equipped system. UV–Vis spectroscopy was performed for analysis of filtered sample after adsorption and photocatalytic phenomenon. Same process was repeated with pure chitosan and Chi/NGP nanocomposite films. The samples were filtered using Ran Disc PVDF syringes (0.45 μm) were purchased from Thermo fisher Scientific Pvt. Ltd. The maximum adsorption wavelength ($\lambda_{max} = 663.56$ nm) of prepared samples was determined using PerkinElmer Lambda 650S UV–Vis spectrometer in the range of 200–800 nm. The photocatalytic studies were performed with all three nanocomposite films such as pure chitosan, Chi/NGP and Chi/NGP/WO_3 by same procedure as shown in Fig. 3.6(a). Sample A_1, B_1 and C_1 have shown the degradation of pure methylene blue after adsorption on pure Chitosan, Chi/NGP and Chi/NGP/WO_3 nanocomposite film respectively for 1 h. In the same way, sample A_2, B_2 and C_2 have shown the photocatalytic degradation of methylene blue in the presence of UV–vis light by pure Chitosan, Chi/NGP, Chi/NGP/WO_3 nanocomposite films, respectively.

UV–Vis spectrophotometry was also plotted for pure methylene blue, adsorbed methylene blue and photocatalytic degraded methylene blue by all three nanocomposites film as shown in Fig. 3.6(b). Two absorption peaks of prepared sample were obtained at wavelength 290.779 nm and 663.56 nm. λ_{max} at 663.56 nm has shown the greater degradation of methylene blue after photocatalytic phenomenon. The absorbance of pure methylene blue in deionized water was 0.9567 a.u at 663.56 nm. The absorbance of sample A_1, B_1 and C_1 was calculated as 0.9525 a.u, 0.840 a.u and 0.765 a.u respectively upon adsorption of methylene blue. In this series, the absorbance value of methylene blue of sample A_2, B_2 and C_2 was also

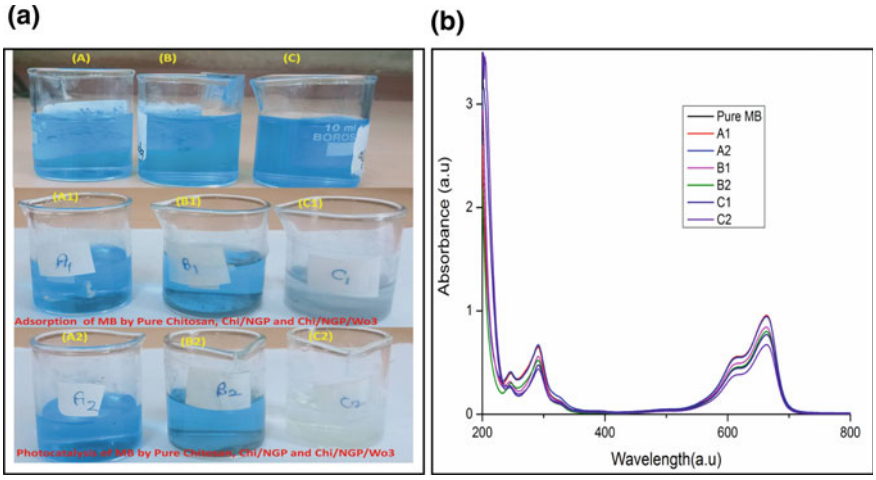

Fig. 3.6 **a** A_1, B_1 and C_1 are the camera images of degradation of methylene blue by adsorption process of 1 h. A_2, B_2 and C_2 are the camera images of photocatalytic degradation of methylene blue under visible light by pure chitosan, Chi/NGP and Chi/NGP/Wo_3 film respectively. **b** UV–Vis spectrum image of degradation of methylene blue after adsorption and photocatalytic phenomenon by pure Chitosan, Chi/NGP and Chi/NGP/WO_3 nanocomposite film

measured as 0.9440 a.u, 0.799 a.u and 0.6714 a.u respectively. These absorbance values at 663.56 nm have shown that methylene blue was highly degraded by Chi/NGP/WO_3 nanocomposite film after photocatalytic phenomenon. The performance of the photocatalyst was estimated by calculating its efficiency with respect to the initial absorbance before irradiation with light (A_i) and the final absorbance after the photocatalytic phenomenon (A_f) as given by (3.1).

$$\%\ \text{degradation efficiency} = \frac{A_i - A_f}{A_i} * 100 \tag{3.1}$$

Degradation efficiency of pure Chitosan, Chi/NGP and Chi/NGP/WO_3 nanocomposite film was 1.32%, 16.48% and 29.82%, respectively. These results have shown that methylene blue was highly degraded by Chi/NGP/WO_3 nanocomposite film under UV–Vis light.

3.5 Device Fabrication

Glass substrate were cleaned in soap solution, water, acetone, and isopropanol sequentially for 10–15 min each and dried for 2 h in an oven at 120 °C. Synthesized nanocomposite films of pure Chitosan, Chi/NGP and Chi/NGP/WO_3 were very flexible. The synthesized nanocomposite film of Chi/NGP/WO_3 was pasted on glass

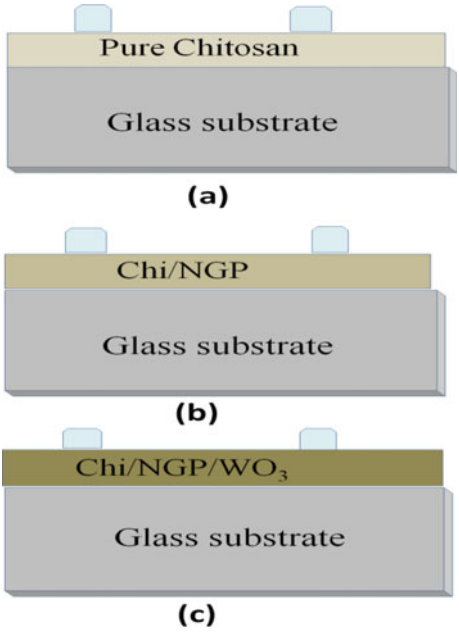

Fig. 3.7 (**a**) Pure chitosan device for IV characteristics, (**b**) Chi/NGP device for IV characteristics and (**c**) Chi/NGP/WO_3 device for IV characteristics

substrate for IV characteristics. Finally, silver (Ag) was thermally deposited through shadow mask by Trovato deposition unit to make contact on nanocomposite film. The distance between the contacts was approximately 0.5 cm. After the successful fabrication of device, it was kept in vacuum at 30 °C for dry. A similar fabrication was carried out for pure Chitosan and Chi/NGP nanocomposite device. The fabricated device was shown in Fig. 3.7.

3.6 I–V Characteristics

The IV characteristics of the fabricated devices were evaluated by Keithley 6517 A/B electrometer setup as shown in Fig. 3.8. I–V characteristics were plotted from −10 to 10 V and current was measured against the applied voltage. The sample of pure Chitosan film has shown very less conductivity because of very small current flows. Chi/NGP nanocomposite film has shown maximum current flow in the range of 0.0032 mA to 0.0030 at −10 V to 10 V, respectively, because of the electron transfer mechanism of nanographite platelets. Hence, nanogaraphite and chitosan composite film shows maximum conductivity of $3.13 \times 10^{-7}\ \Omega^{-1}\ cm^{-1}$. Here Chi/NGP/$WO_3$ nanocomposite film has conductivity approximately $2.32 \times 10^{-7}\ \Omega^{-1}\ cm^{-1}$.

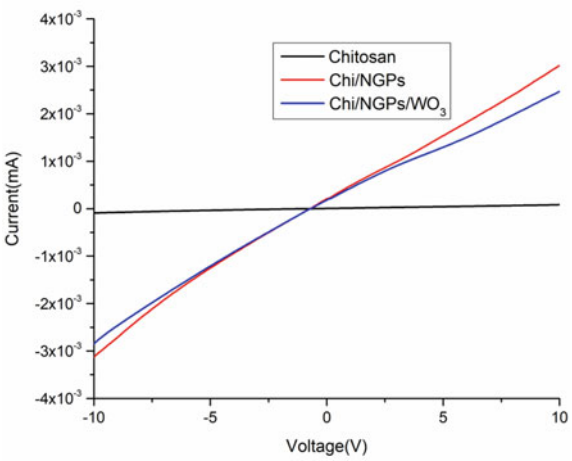

Fig. 3.8 I–V characteristics of pure Chitosan film, Chi/NGPs and Chi/NGP/WO3 nanocomposite film

3.7 Conclusion

Nanographite platelets are successfully synthesized by modified hummer's method with average size of 150 nm. Pure Chitosan, Chi/NGPs, Chi/NGPs/WO_3 nanocomposite films are successfully synthesized by using solution blending method at room temperature. SEM, XRD, FTIR, EDX confirm the successful synthesis of Chi/NGP, Chi/NGP/WO_3 nanocomposite films. UV–Vis spectroscopy shows that methylene blue solution is highly degraded by Chi/NGP/WO_3 nanocomposite film (29.82%) as compared to pure chitosan and Chi/NGP nanocomposite film. I–V characteristics have shown that conductivity of synthesized nanocomposites films lie in micro Siemens which indicates that synthesized nanocomposite film are highly conducting.

Conflict of Interest There is no conflict of interest.

Acknowledgements The corresponding authors acknowledge the Department of Science and Technology (DST) INDIA for financial assistance.

References

1. X. Yan, K. Ye, T. Zhang, C. Xue, D. Zhang, C. Ma, J. Wei and G. Yang, New J. Chem. **41**8482–8489 (2017)
2. M.B. Tahirand, M. Sagir, Sep. Purif. Technol. **209**, 94–102 (2019)
3. S.A. Ansari, M. Khan, O. Ansari, New J. Chem. **40**, 3000–3009 (2016)
4. S. Rayati, P. Nafarieh, M.M. Amini, New J. Chem. **42**, 6464–6471 (2018)
5. T. Ochiai, A. Fujishima, Photochem. Photobiol. **13**, 247–262 (2012)
6. Y.F. Wang, J.J. Tao, X.Z. Wang, Z. Wang, M. Zhang, H. Gang, Z.Q. Sun, Ceram. Int. **43**, 4866–4872 (2017)
7. Q. Xiang, J. Yu, M. Jaroniec, Chem. Soc. Rev. **41**, 782–796 (2012)

8. I.V. Lightcap, T.H. Kosel, P.V. Kamat, Nano Lett. **10**, 577–583 (2010)
9. B. Song, T.T. Wang, H.G. Sun, Q. Shao, J. Zhao, K. Song, L. Hao, L. Wang, Z. Guo, Dalton Trans. **46**, 15769–15777 (2017)
10. A. Marikutsa, L. Yang, M. Rumyantseva, M. Batuk, J. Hadermann, A. Gaskov, Sensor. Actuat. B-Chem. **277**, 336–346 (2018)
11. L. Hu, P. Hu, Y. Chen, Z. Lin, C. Qiu, Front. Chem. **6**, 452 (2018)
12. H. Zhang, W. Chen, H. Zhang, J. Nanoelectron. Optoelectron. **13**, 1141–1144 (2018)
13. X. Gu, F. Wu, B. Lei, J. Wang, Z. Chen, K. Xie, Y. Song, D. Sun, L. Sun, H. Zhou, J. Power Sources **320**, 231–238 (2016)
14. F. Malara, A. Cannavale, S. Carallo, G. Gigli, A.C.S. Appl, Mater. Inter. **6**, 9290–9297 (2014)
15. C.G. Granqvist, Thin Solid Films **564**, 1–38 (2014)
16. J. Guo, Y. Li, S. Zhu, Z. Chen, Q. Liu, D. Zhang, W.J. Moon, D.M. Song, RSC Adv. **2**, 1356–1363 (2012)
17. A.K. Geim, K.S. Novoselov, Nat. Mater. **6**, 183–191 (2007)
18. G. Williams, B. Seger, P.V. Kamat, ACS Nano **2**, 1487–1491 (2008)
19. H. Fan, X. Zhao, J. Yang, X. Shan, L. Yang, Y. Zhang, X. Li, M. Gao, Catal. Commun. **29**, 29–34 (2012)
20. M. Zhou, J. Yan, P. Cui, Mater. Lett. **89**, 258–261 (2012)
21. Y. Gui, J. Yuan, W. Wang, J. Zhao, J. Tian, B. Xie **7**, 4587–5460 (2014)

Chapter 4
Ciprofloxacin Loaded Chitosan/Alginate/PEO Nanofibers for Their Application in Antimicrobial Wound Dressing

Safiya Nisar, Sonal Chauhan, and Sunita Rattan

Abstract In the present work, biodegradable nanofibers of mucoadhesive polymers, Chitosan (CS) and Sodium Alginate (SA), along with polyethylene oxide (PEO) were fabricated and used for controlled release of a model drug, ciprofloxacin, for their possible wound healing application. The chemical structure of the nanofibers of CS/SA/PEO and drug containing nanofibers (CS/SA/PEO-CFX) were characterized by Fourier Transform Infrared Spectroscopy (FTIR). Surface wettability of the prepared nanofibers was verified using contact angle analysis. A considerable difference was found between CS/SA/PEO and drug containing CS/SA/PEO-CFX nanofibers with a contact angle of 62.326° and 72.66° respectively. The CS/SA/PEO and CS/SA/PEO-CFX fiber sheets were tested for their antibacterial activity against *Escherchia coli.* The results indicated that both CS/SA/PEO and CS/SA/PEO-CFX fibers exhibited a strong antimicrobial activity by inhibiting the bacterial growth. Such results showed that the prepared material can effectively be used for controlled release of antimicrobial drug, thus be used as a wound dressing material.

4.1 Introduction

In the recent years, researchers have shown an increasing interest in the development of biomaterials for wound dressing application [1]. In particular, for treatment of skin wounds, the most commonly used biomaterials are fibers and scaffolds due to the presence of the interconnected porous structure that makes them a favourable choice, as they allow an easy passage for gases and nutrients [2]. Other properties of fibers, which favor their applications in wound dressing are high absorbency, ability to swell, softness, increased surface area and their effective fabrication into various forms. Fibers synthesized from natural sources, particularly polysaccharides, have excellent properties of being biocompatible, non-toxic and bioactive, thus making them the best candidates for wound dressing.

S. Nisar · S. Chauhan · S. Rattan (✉)
Amity Institute of Applied Sciences, Amity University, Sector-125, Noida, Uttar Pradesh 201303, India
e-mail: srattan@amity.edu

V. K. Jain et al. (eds.), *Recent Trends in Materials and Devices*, Springer Proceedings in Physics 256, https://doi.org/10.1007/978-981-15-8625-5_4

Electrospinning offers a convenient and indispensable method to develop fibers with porous structure of varying diameters extending from micrometers to nanometers. Lately, electrospinning has gained popularity in formulation of various biomaterials for bone regeneration, tissue engineering and for developing wound dressing materials [3]. Electrospun chitosan (CS) fibers, as a biomaterial, is known to be non-toxic, biodegradable and biocompatible, which makes it perfect for the fabrication of wound dressing material. Chitosan is made by copolymerization of N-acetyl-D-glucosamine and D-glucosamine and is derived from chitin found in crustaceans [4]. Furthermore, chitosan nanofibers are known to promote cellular growth, also used as drug-delivery vehicle and the carrier of various kinds of nanoparticles [5]. Though, the chitosan nanofibers are tremendously useful, their poor mechanical strength limits their usage and application in medical industry. However, combination of chitosan with additional polymer may reinforce its strength, thus extend its applicability. Two biocompatible polymers like chitosan (CS) and sodium alginate (SA) form a great combination (CS/SA) in a biopharmaceutical viewpoint. Their easy availability and cost effectiveness further enhance their usage for numerous biological and biomedical purposes [6, 7]. In addition to that, CS/SA fibers are biodegradable, non-antigenic, mucoadhesive and bio-functional, all of which further support their usage in wound healing and wound dressing application [8]. One of the major advantages of this polyelectrolyte complex (CS/SA) is that its preparation involves the usage of aqueous system (water), thus, avoiding the usage of toxic organic solvents. However, the fibers obtained are insoluble in water and bear a great potential in biomedical applications mainly wound dressing [9].

During the present work, two natural biopolymers, cationic polymer (chitosan) and anionic polymer (alginate) were combined to form strong complexes through chemical interactions. A third high molecular weight polymer, viz., poly(ethylene oxide) (PEO), was further added to enhance spinning and hydrophilicity, in addition to the promotion of polymer chain entanglement, thus lowering their conductivity [10]. The fabricated fibers (CS/SA/PEO and CS/SA/PEO-CFX) were characterized through FTIR spectroscopy, scanning electron microscopy (SEM) and contact angle analysis. The fibers were further evaluated for antibacterial activity against *Escherchia coli* through zone of inhibition assay (in-vitro) for their potential application in wound dressing (Fig. 4.1).

4.2 Materials and Methods

4.2.1 Materials

Chitosan (75% deacetylation, Loba Chemie), Glacial Acetic acid (99–100%, Merck), Sodium Alginate (91%, Loba Chemie), Poly(ethylene oxide) (M_w ~ 900,000) were procured and used. Deionized water was used to prepare all the solutions.

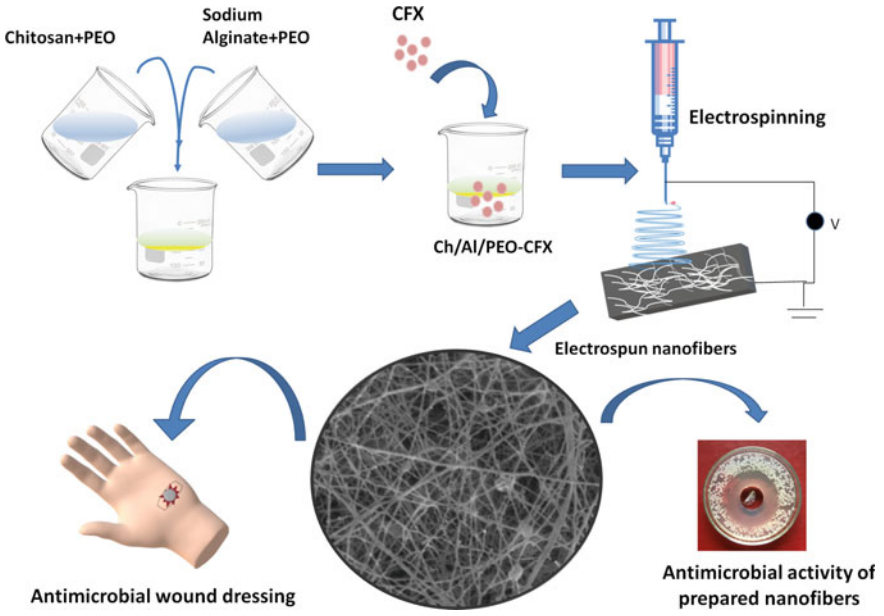

Fig. 4.1 Preparation of CS/SA/PEO and CS/SA/PEO-CFX Nanofibers for their potential application in antimicrobial wound dressing

4.2.2 Methods

The prepared CS/SA/PEO and CS/SA/PEO-CFX nanofibers were characterized using FTIR spectroscopy (Perkin Elmer Cetus Instruments, Norwalk). SEM micrographs of the fibers were taken using Zeiss Evo 18. The hydrophobicity of the prepared fibers was observed using Contact Angle Analyzer by SEO optics.

4.2.2.1 Preparation of CS/SA/PEO and CS/SA/PEO-CFX Solutions for Electrospinning

Solutions of chitosan 5% (w/w) in 1 M acetic acid and PEO 4% (w/w) were prepared in deionized water and the two were mixed in the ratio of 70:30. Then, to the above solution (chitosan/PEO) a solution of SA/PEO [2.4% SA/1.6% PEO (w/w)] was added in the ratio of 1:1 with the addition of 5% ethanol as a co-solvent. The solution was maintained under agitation for approximately 4 h, at room temperature. To one proportion of the above mixture, the ciprofloxacin drug solution was added (0.25 mg/ml) and stirred. To complete the homogenization the solutions were left to rest for 1 h before spinning to eliminate microbubbles.

4.2.2.2 Fabrication of CS/SA/PEO and Cs/SA/PEO/CFX Nanofibers

The prepared solutions, CS/SA/PEO (without drug) and CS/SA/PEO-CFX (with drug), were taken each in a 5 ml syringe. The fibers were collected on an aluminium foil that covered the rotating mandrel of the electrospinning unit at a distance of 15 cm. The flow-rate was maintained at 1 ml/h and the machine was operated at 20 kV. The prepared CS/SA/PEO and CS/SA/PEO-CFX fibers were dried at room temperature. The fibers were later washed once with 30 ml neutralization solution (3 M NaOH/MeOH) followed by washing with distilled water.

4.2.2.3 Antimicrobial Activity

Antimicrobial potential of the prepared fibers (CS/SA/PEO and CS/SA/PEO-CFX) was evaluated against *E. coli* by well diffusion assay by measuring the diameter of Zone of Inhibition (ZI) [11]. Soft nutrient agar plates were prepared using petri dishes of 90 mm diameter and *E. coli* was seeded as test organism. Wells of equal size (2 cm in diameter) were bored at the center of each agar plate. After placement of swollen CS/SA/PEO and CS/SA/PEO-CFX fibers (10 mg each) inside the wells, the plates were incubated at 35 °C for 16–18 h. Zones of inhibition (diameter) formed around the discs were measured in millimetres (cm).

4.3 Results and Discussions

4.3.1 Electrospinning and Morphology of CS/SA/PEO Nanofibers

The electrospinning technique of producing nano/microfibrous material from polymer solutions is though a versatile process but is affected by a number of factors, such as polymer molecular weight and chemical composition, solution parameters, processing conditions, and environmental parameters [12]. The conditions for the preparation of the CS/SA/PEO fibers were optimized. The SEM micrographs of the prepared fibers have been displayed in Fig. 4.2a–d. As revealed through the micrographs, the appearance of the beads in the fibers was evident in fabricated nanofibers, which can be attributed to the effect of distance between the tip of the syringe needle and the drum collector. A decrease in the distance between the tip of the syringe needle and the drum collector and application of large electric field resulted in instability of the jet, leading to the formation of the beads [13].

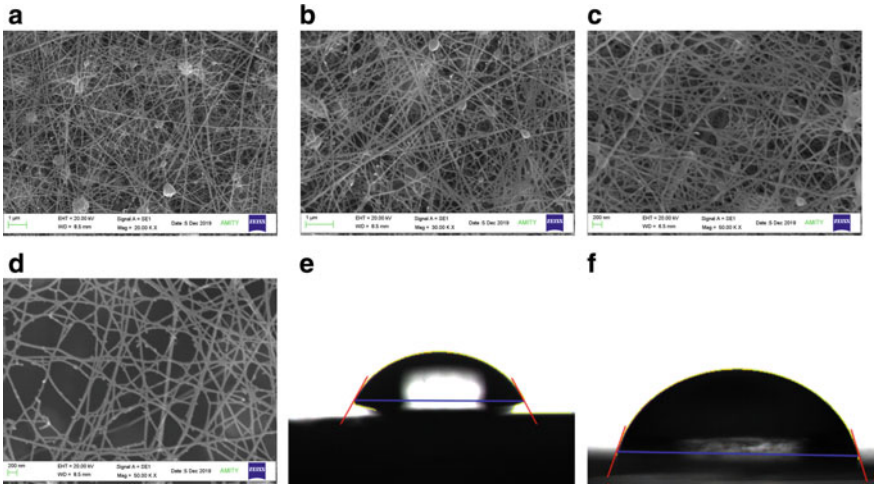

Fig. 4.2 **a**, **b**, **c**, and **d** SEM micrographs of CS/SA/PEO nanofibers; **e** and **f** contact angle of CS/SA/PEO and CS/SA/PEO-CFX respectively

4.3.2 Contact Angle

Contact angle measurements were carried out to study the surface properties of the prepared CS/SA/PEO and CS/SA/PEO-CFX nanofibers. As shown in Fig. 4.2e, f, the CS/SA/PEO exhibited a contact angle of about 60.45° and that of CS/SA/PEO-CFX was 72.6° (Fig. 4.2e, f). The loaded fibers showed increased hydrophobicity with respect to unloaded fibers.

4.3.3 FTIR Analysis

The FTIR spectra of CS/SA/PEO and CS/SA/PEO-CFX fibers have been displayed in Fig. 4.3. In the FTIR spectrum of chitosan, the observed peaks at 1653 cm^{-1} and 1595 cm^{-1} were attributed to the vibration and stretching of primary amine and secondary amine groups respectively. The peak of 1485–1380 cm^{-1} corresponds to asymmetric C–H bending of CH_2 group and that of 1035 cm^{-1} to bridge O-stretching of glucosamine residue [14]. For the FTIR spectrum of alginate in Fig. 4.3, peak at 1416 cm^{-1} may be attributed to the symmetric and asymmetric stretching of the carboxylate group. The bands at 1320, 1090 and 950 cm^{-1} were related to the stretching frequency of the C–O bond. Also, the peaks at 1130 cm^{-1} and 1020 cm^{-1} were credited to the C–C and C–O–C stretching respectively [15]. The peak near 1609 cm^{-1} was due to the shift in position of carboxylic peak near 1621 cm^{-1} and amine peak near 1653 cm^{-1}. The shift in the peak position was attributed to the

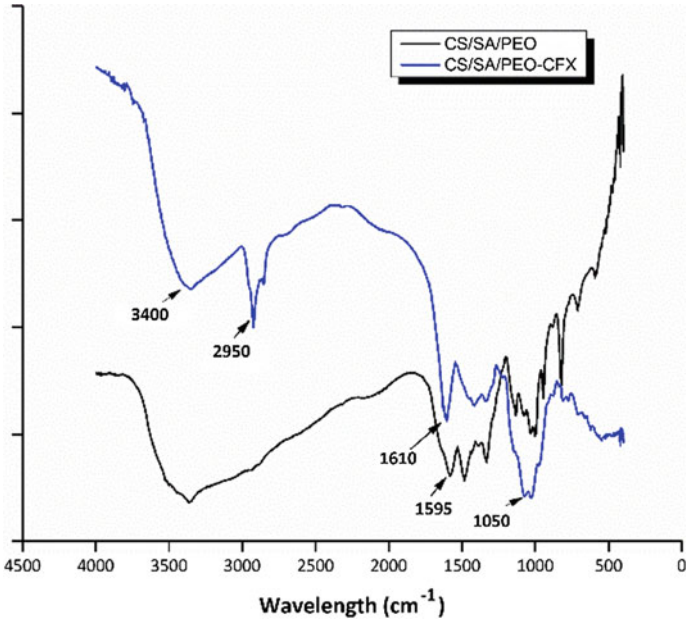

Fig. 4.3 FTIR spectra of CS/SA/PEO and CS/SA/PEO-CFX fibers

reaction between carboxylic group of alginate with the amine group of chitosan to form an anionic complex [16].

The major differences in the FTIR spectra of CS/SA/PEO and CS/SA/PEO-CFX in Fig. 4.3 was the presence of one prominent peak found at 3400 cm^{-1} which can be assigned to the OH-stretching vibration (intermolecular hydrogen bonding). Another band at 2950 cm^{-1} was attributed to the stretching of alkenes and aromatic C–H (mainly aromatic enes) of the Ciprofloxacin loaded fibers. Furthermore, a strong absorption peak at 1050 cm^{-1} corresponded to C–F group of the CFX moiety [17].

4.3.4 Antimicrobial Studies

Antimicrobial potential of CS/SA/PEO and CS/SA/PEO-CFX against *E. coli* was studied by well diffusion assay and evaluated by measuring diameter (cm) for Zone of Inhibition (Fig. 4.4). Zones of Inhibition (ZI) were indicated by the clear zones, showing no bacterial (*E. coli*) growth. The larger diameter of the ZI indicated the higher antimicrobial activity. CS/SA/PEO fibers showed some anti-microbial activity against *E. coli* as evident from the ZI (1 cm diameter) as shown in Fig. 4.4b. This owes to the fact that chitosan and sodium alginate have been reported to possess an innate anti-microbial property against various species of bacteria and at the same time lower toxicity toward mammalian cells [18, 19]. The drug loaded CS/SA/PEO-CFX

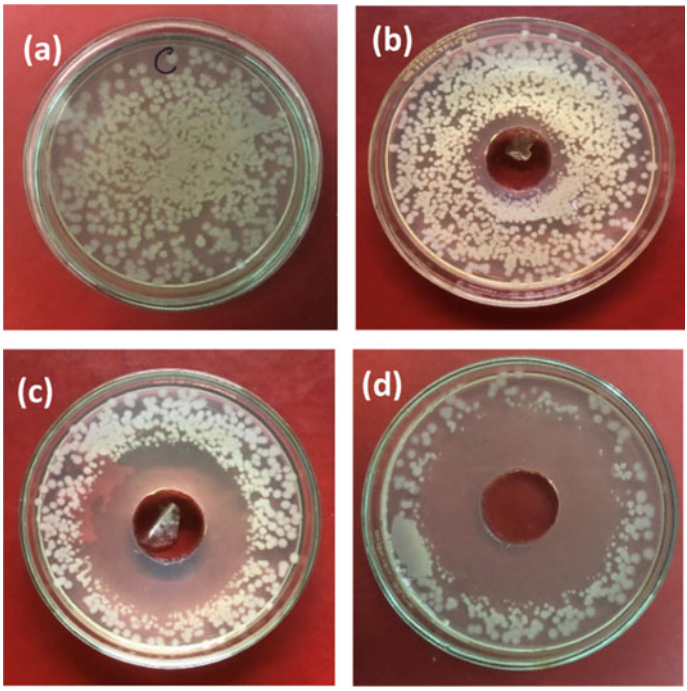

Fig. 4.4 Antimicrobial Test of Ch/Al/PEO and Ch/Al/PEO-CFX against *E. coli* bacterial strain. **a** Control, **b**, **c** and **d** Ch/Al/PEO, Ch/Al/PEO-CFX nanofibers and ciprofloxacin respectively

fibers rendered a significantly higher antimicrobial activity (ZI = 3 cm, Fig. 4.4c) against *E. coli* with respect to unloaded fibers, though the zone of inhibition was a little smaller in comparison to the CFX alone (4.5 cm, Fig. 4.4d). This increase in antimicrobial activity may be attributed to the anti-microbial effect of the drug (CFX) and polymers (CS/SA/PEO) used for the preparation of the fibers. Although the antimicrobial activity measured vis ZI test shows higher activity for standard CFX than CS/SA/PEO-CFX, the difference is due to the fact that CFX shows more drug induced toxicity while as the CFX loaded fibers (CS/SA/PEO-CFX) release the drug in a controlled and sustained way over a longer period of time. Moreover, chitosan fibers and scaffolds have widely been used to prepare systems for the controlled release of the drugs and the above properties makes our system a viable choice for being used as wound dressing material.

4.4 Conclusion

Electrospun nanofibers were successfully prepared by the mixture of chitosan (polymeric cation) and alginate (polymeric anion) to form an ionic complex, owing to the

ionic crosslinking between the polymeric chains. The morphology of the nanofibers was confirmed using SEM. Antibacterial testing of CS/SA/PEO fibres against *E. coli* demonstrated their antibacterial effect (in terms of inhibition of bacterial growth) with initial use, and the drug loaded CS/SA/PEO-CFX fibers showed their anti-microbial ability by controlled release of the drug, ciprofloxacin (data unpublished). These results demonstrated successfully fabricated (CS/SA/PEO and CS/SA/PEO-CFX) fiber sheets by electrospinning technique that showed a very potent antimicrobial activity. Hence, the drug loaded CS/SA/PEO fiber sheets can be used as potential antibiotic wound dressing materials for the controlled release of the antimicrobial drug.

Acknowledgements The author is thankful to the Amity University (UP, India) for providing required facilities.

References

1. C.J. Knill, J.F. Kennedy, J. Mistry, M. Miraftab, G. Smart, M.R. Groocock, H.J. Williams, Carbohydr. Polym. **55**, 65–76 (2004)
2. R.B. Trinca, C.B. Westin, J.A.F. da Silva, ÂM. Moraes, Eur. Polym. J. **88**, 161–170 (2017)
3. H. Jiang, Y. Hu, Y. Li, P. Zhao, K. Zhu, W. Chen, J. Control. Release **108**, 237–243 (2005)
4. S. Nisar, A.H. Pandit, L.F. Wang, S. Rattan, RSC Adv. **10**, 14694–14704 (2020)
5. N. Mati-Baouche, P.H. Elchinger, H. De Baynast, G. Pierre, C. Delattre, P. Michaud, Eur. Polym. J. **60**, 198–212 (2014)
6. M.N.V.R. Kumar, R.A.A. Muzzarelli, C. Muzzarelli, H. Sashiwa, A.J. Domb, Chem. Rev. **104**, 6017 (2004)
7. F.F. Bartone, E.D. Adickes, J. Urol. **140**, 1134 (1988)
8. H. Ueno, T. Mori, T. Fujinaga, Adv. Drug Deliver. Rev. **52**, 105 (2001)
9. X. Meng, F. Tian, J. Yang, C.N. He, N. Xing, F. Li, J. Mat. Sci. Mater. Med. **21**, 1751–1759 (2010)
10. S.I. Jeong, M.D. Krebs, C.A. Bonino, J.E. Samorezov, S.A. Khan, E. Alsberg, Tissue Eng. Part A **17**, 1–2 (2010)
11. S.J. Lee, J.J. Yoo, G.J. Lim, A. Atala, J. Stitzel, J. Biomed. Mater. Res., Part A **83**, 999–1008 (2007)
12. N. Bhardwaj, S.C. Kundu, Electrospinning: a fascinating fiber fabrication technique. Biotechnol. Adv. **28**, 325–347 (2010)
13. X. Zong, K. Kim, D. Fang, S. Ran, B.S. Hsiao, B. Chu, Polymer **43**, 4403–4412 (2002)
14. J. Singh, P.K. Dutta, J. Dutta, A.J. Hunt, D.J. Macquarrie, J.H. Clark, Carbohydr. Polym. **76**, 188–195 (2008)
15. A. Abruzzo, F. Bigucci, T. Cerchiara, B. Saladini, M.C. Gallucci, F. Cruciani et al., Carbohydr. Polym. **91**, 651–658 (2013)
16. M. George, E.T. Abraham, J. Control. Release **114**, 1–14 (2006)
17. S. Sahoo, C. Chakraborti, S. Mishra, J. Adv. Pharm. Tech. Res. **2**, 195 (2011)
18. M. Kong, X.G. Chen, K. Xing, H.J. Park, Int. J. Food Microbiol. **144**, 51–63 (2010)
19. I. Liakos, L. Rizzello, D.J. Scurr, P.P. Pompa, I.S. Bayer, A. Athanassiou, Int. J. Pharm. **463**, 137–145 (2013)

Chapter 5
Preparation and Optoelectronic Properties of Iridium (III) Complexes Based on 1,3,4-Oxadiazole and β-diketones

Anil Kumar, Amit Kumar, Abhishek Verma, D. P. Singh, Harish Mudila, Deepak Kumar, and Ritu Srivastava

Abstract Preparation and characterizations of iridium (III) complexes namely {2-(4-biphenylyl)-5-(4-tertbutylphenyl)-[1,3,4]-oxadiazolato-N4,C_2}$_2$ Ir(theonyltrifluoacetone) [(PBD)$_2$Ir(tta)] and {2-(4-biphenylyl)-5-(4-tertbutylphenyl)-[1,3,4]-oxadiazolato-N4,C_2}$_2$ Ir(2,2,6,6-tetramethyl-3,5-heptanedione)[(PBD)$_2$Ir(tmd)] having two cyclometalated ligands (CˆN) and a bidentate diketone ligand (X) denoted as [CˆN)$_2$Ir(X)] where X is a β-diketone with trifluoromethyl, theonyl or t-butyl groups, are detailed. Fourier transform infrared (FTIR) spectroscopy with CHN analysis structurally confirms the formation of these complexes. These metal complexes proved good thermal stability in air up to 300 °C. The UV–Visible spectra of these complexes revealed λ_{max} at 362 and 370 nm for [(PBD)$_2$Ir(tta)] and [(PBD)$_2$Ir(tmd)], respectively. The photoluminescence spectra of the complexes showed maximum emission at 549 and 559 nm, respectively. The electroluminescent properties of these complexes have also been studied through fabricating multilayer devices with the structure ITO/α-NPD(30 nm)/(PBD)$_2$Ir(tta) doped CBP(35 nm)/BCP(6 nm)/Alq$_3$(28 nm)/LiF(1 nm)/Al and

A. Kumar (✉) · H. Mudila · D. Kumar
Department of Chemistry, Lovely Professional University, Phagwara 144411, India
e-mail: rsanil.nit@gmail.com

A. Kumar (✉)
School of Engineering and Technology, Central University of Haryana, Jant-Pali, Mahendergarh, Haryana 123031, India
e-mail: kumaramit@cuh.ac.in

A. Verma
Advanced Research and Studies (Materials and Devices), Amity Institute, Amity University, Noida, Uttar Pradesh 201303, India

D. P. Singh
School of Physics and Materials Science, Thapar Institute of Engineering & Technology, Patiala 147004, India

R. Srivastava
Center for Organic Electronics, OLED Lab, Physics of Energy Harvesting Division, National Physical Laboratory, New Delhi 110012, India

V. K. Jain et al. (eds.), *Recent Trends in Materials and Devices*, Springer Proceedings in Physics 256, https://doi.org/10.1007/978-981-15-8625-5_5

ITO/α-NPD(30 nm)/$(PBD)_2$Ir(tmd) doped CBP(35 nm)/BCP(6 nm)/ Alq_3(28 nm)/LiF(1 nm)/Al. The electroluminescent spectra showed maximum emission at 555 and 563 nm, respectively.

5.1 Introduction

Since the last decade, much attention has been paid towards the phosphorescent materials for their potential application as highly efficient electroluminescent (EL) emitter in organic light-emitting diodes (OLEDs) [1–5]. Both singlet and triplet excitons can be harvested for light emission, which improves the electroluminescence (EL) performance of organic light-emitting diode (OLEDs) based on phosphorescent materials [6, 7]. Among various metal complexes, iridium complexes are the most effective as they show intense phosphorescence at room temperature and behave as a very promising phosphor material for OLEDs [8–10]. The spin–orbit coupling in heavy metals like iridium causes intersystem crossing and increases the singlet–triplet transition probability. The cyclometalated ligand tends to be associated with the main ligand-centered transition. The ancillary ligand is associated with the metal-to-ligand charge transfer (MLCT) transition and plays a more passive role in determining the nature of the excited state [11]. Some heteroleptic iridium (III) complexes based on fluorinated 1,3,4-oxadiazole were reported, and they could tune to blue by dithiolate ancillary ligands [11–13]. 1,3,4-Oxadiazole derivatives are one of the most widely studied classes of electron-injection/hole-blocking materials due to their electron deficiency, high photoluminescence quantum yield, good thermal, and chemical stabilities. It has been shown earlier that 2-(4-biphenyl)-5-(4-tertbutylphenyl)-[1,3,4]-oxadiazole (PBD) function very well as an excellent electron- transport material (ETM) in multilayer OLEDs [14, 15].

In present paper, the iridium based complexes called (2-(4 -biphenylyl)-5-(4-tert butylphenyl)-[1,3,4]-oxadiazole)$_2$Ir(Thenoyltrifluoroacetylacetone)[$(PBD)_2$Ir(tta)] and Ir(2-(4-biphenylyl)-5-(4-tert butylphenyl)-[1,3,4]-oxadiazole)$_2$ Ir(2,2,6,6-tetramethyl -3,5-heptanedione) [$(PBD)_2$Ir(tmd)] have been synthesized and characterized. These complexes have two cyclometalated ligands (CˆN) and a bidentate diketone ligand (X) represented as [CˆN)$_2$Ir(X)] where X is a β-diketone with trifloromethyl, theonyl or t-butyl groups. The electroluminescent properties of these complexes have been studied by fabricating multilayer devices structure ITO/α-NPD(30 nm)/8% $(PBD)_2$Ir(tta) doped CBP(35 nm)/BCP(6 nm)/Alq_3(28 nm)/LiF(1 nm)/Al and ITO/α-NPD(30 nm)/ 8% $(PBD)_2$Ir(tmd) doped CBP(35 nm) /BCP(6 nm)/ Alq_3(28 nm) /LiF(1 nm)/Al.

5.2 Experimental Work

5.2.1 Materials

In order to prepare electroluminescent Iridium complexes, the chemicals such as iridium trichloride hydrate, 2-(4-biphenylyl)-5-(4-tertbutylphenyl)-[1,3,4]-oxadiazole (PBD), thenoyl trifluoro acetyl acetone and 2,2,6,6-tetramethyl-3,5-heptanedione were purchased from Sigma Aldrich. All the solvents were used as received.

5.2.2 Preparation of Binuclear Iridium (III) Complex

Tetrakis{2-(4-biphenylyl)-5-(4-tertbutylphenyl)-[1,3,4]-oxadiazolato-N4,C_2}(μ-dichloro) diiridium [$(PBD)_2Ir(\mu\text{-}Cl)_2Ir(PBD)_2$].

0.153 mmol of Iridium trichloride hydrate and 2.5 equivalent of 2-(4-biphenylyl)-5-(4-tertbutylphenyl)-[1,3,4]-oxadiazole (PBD) were added in 40 ml solution of 2-ethoxyethanol and water (v/v = 3:1). Afterward the above mixture was refluxed for 24 h and cooled to room temperature. The resulting precipitate was collected by filtration and washed with ethanol, water and hexane, and pumped dry to give crude chloro-bridge dimer complex as shown in Fig. 5.1.

5.2.3 Preparation of $(PBD)_2Ir(tta)$

The $(PBD)_2Ir(tta)$ complex was synthesized by adding the above-prepared dimer in a mixture of Na_2CO_3 and theonyltrifluoroacetone in 2-ethoxyethanol (40 ml). The mixture was refluxed for 24 h; after that solution was poured into water. The brown precipitate was filtered through vacuum filtration method followed by washed with water, hexane, and finally with ether (Fig. 5.1).

$(PBD)_2Ir(tta)$: CHN (calculated: C% 60.04, H% 4.14, N% 5.00; found: C% 59.68, H% 4.17, N% 4.87), FTIR(KBr): cm^{-1}, 1006 (C–F); 680 (C-S); 1314 (C–N); 1300, 1251 (C–O); 2955 (C–H); 1067 (C–C); 1610 (C=N); 1583, 1553 (C=C); 1125,1039 (C–O–C) [15].

5.2.4 Preparation of $(PBD)_2Ir(tmd)$

The $(PBD)_2Ir(tmd)$ complex was also prepared like $(PBD)_2Ir(tta)$ by adding the dimer in a mixture of Na_2CO_3, 2,2,6,6-tetramethyl-3,5-heptanedione in 2-ethoxyethanol

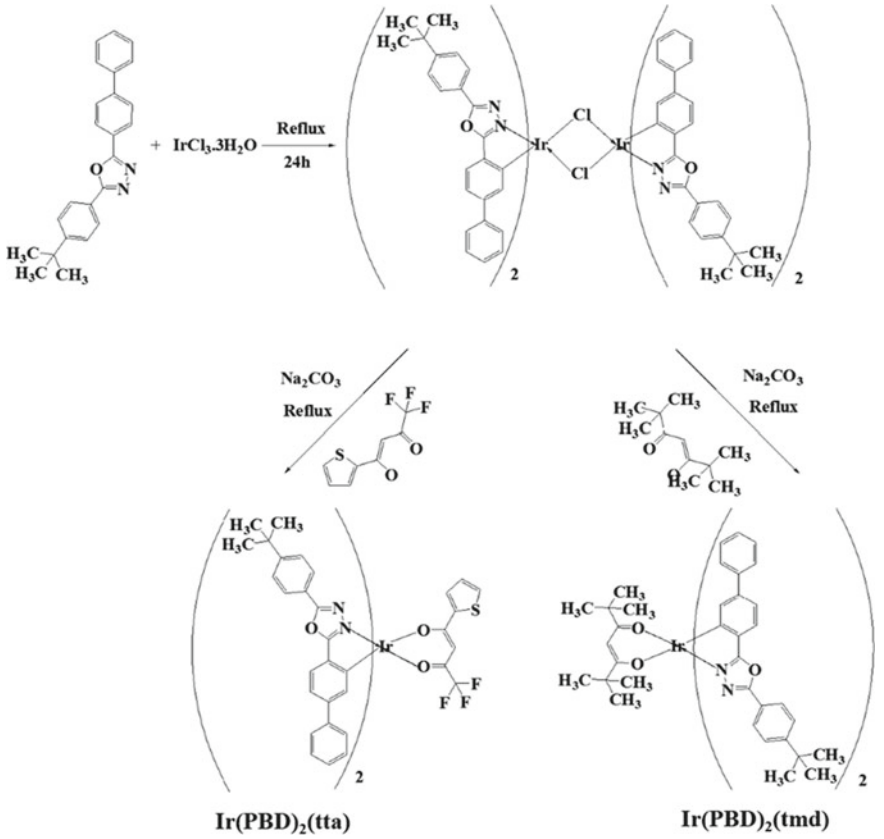

Fig. 5.1 Synthesis of Ir(III) complexes

(40 ml). After refluxing for 24 h, the solution was poured into water. The brown precipitate was filtered out and washed with water, hexane, and ether (Fig. 5.1).

Ir(PBD)$_2$(tmd): CHN (calculated: C% 65.47, H% 5.69, N% 5.18; found: C% 65.82, H% 4.04, N% 4.49), FTIR (KBr): cm^{-1}, 1316 (C–N); 1301, 1252 (C–O); 2956 (C–H); 1068 (C–C); 1611 (C=N); 1584, 1554 (C=C); 1126, 1040 (C–O–C) [15].

5.3 Characterizations

The bonding characteristics of all of the samples were recorded with Fourier transform infrared (FTIR) spectroscopy (Perkin-Elmer 2000 FTIR). The C, H, and N analyses of the complexes were done by an Elemental Analyzer PerkinElmer 2400

CHN. The absorption spectra of prepared complexes were done in CH_2Cl_2 solution by using ultraviolet–visible spectroscopies (Shimadzu 2401 PC). The Photoluminescence (PL) and electroluminescence (EL) spectra of prepared complexes were recorded using a spectrofluorometer (Fluorolog Jobin Yvon-Horiba, model-3–11) and with a high-resolution spectrometer (Ocean Optics HR-2000CG UV-NIR), respectively. The current–voltage–luminescence (I–V–L) measurements were carried out with a luminance meter (LMT l-1009) interfaced with a Keithley 2400 programmable voltage–current digital source meter.

5.3.1 OLED Device Fabrication and Characterizations

The OLED devices were fabricated by thermal evaporation deposition using Indium–tin oxide (ITO) coated glass substrate having sheet resistance 20Ω/□ (used as anode). Zinc dust and HCl were used for patterning the ITO followed by cleaning with deionized water, acetone, trichloroethylene, and isopropyl alcohol sequentially (for 20 min using an ultrasonic bath and dried in a vacuum oven). The emitting layer and hole transport layer were deposited on the ITO coated substrate with a deposition rate of 0.1 Å/s and under a high vacuum, i.e. 1×10^{-6} torr. The thickness of the layer in devices is as: 300 Å for *N*,*N*-diphenyl-*N*,*N*-bis(1-naphthyl)-1,1-biphenyl-4,4-diamine (α-NPD) (hole transporting layer), 350 Å of the complex doped (8%) (4,4′-biscarbazolylbiphenyl) CBP (emitting layer), 60 Å for 2,9-dimethyl 4,7-diphenyl-1, 10-phenanthroline (BCP) (hole and exciton blocking layer), 280 Å of aluminum tris-8-hydroxyquinoline (Alq_3) (electron transport layer). In the device, cathode is composed of 10 Å lithium fluoride and 1000 Å aluminum were sequentially deposited onto the substrate to complete the device structure.

5.4 Results and Discussion

5.4.1 Ultraviolet–Visible and Photoluminescence Spectroscopy

Ultraviolet–visible and photoluminescence spectra of $(PBD)_2Ir(tta)$ and $(PBD)_2Ir(tmd)$ complexes were recorded in with the solution of dichloromethane (CH_2Cl_2) at room temperature as depicted in Fig. 5.2a, b. The absorption spectra showed intense absorption at 362 and 370 nm, which corresponds to spin allowed $\pi-\pi^*$ transitions from the cyclometalated ligand. However, the broad absorptions at 433 and 441 nm indicate the spin allowed metal-to-ligand charge transfer (^{1}MLCT) transition. In spectra, the range from 441–500 nm is associated with both ^{3}MLCT and $^3\pi-\pi^*$ transition. The extended tail toward lower energy attribute to the ^{3}MLCT transitions that gained intensity by the ^{1}MLCT transition through the spin-orbital

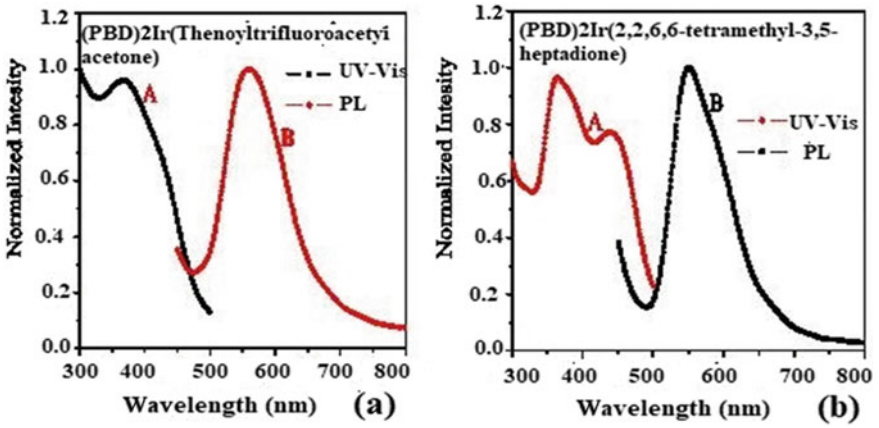

Fig. 5.2 **a** curve A (Exc): excitation spectrum of $(PBD)_2Ir(tta)$, Curve B (PL): emission spectrum of $(PBD)_2Ir(tta)$; **b** curve A (Exc): excitation spectrum of $(PBD)_2Ir(tmd)$, curve B (PL): emission spectrum of $(PBD)_2Ir(tmd)$ in CH_2Cl_2

coupling of iridium(III). The curve A and B in Fig. 5.2 shows the UV–Vis and PL spectra of $(PBD)_2Ir(tta)$ and $(PBD)_2Ir(tmd)$ respectively. The emission spectra of these complexes observed at 549 and 559 nm, which corresponds to orange-yellow light [16]. Hong et al. [17] reported that the band which detect from MLCT states are mostly broad while $^3(\pi-\pi^*)$ states usually gave highly structured emissions. It has been noted that trifluoro, In $(PBD)_2Ir(tta)$ complex is an electron-withdrawing group that displayed the emission wavelength blue shift than the corresponding complex that has electron-donating moiety [18]. The optical properties of $(PBD)_2Ir(tta)$ and $(PBD)_2Ir(tmd)$ complexes proved that these could be used as an emissive layer for the fabrication of orange-yellow light-emitting diodes [19].

5.4.2 Electroluminescent Characterization

The electroluminescent properties of these metal complexes were studied by fabricating the multilayer organic light-emitting devices using the prepared complexes as emissive layer materials. The schematic diagram of the device structure, along with the thickness of the layers is shown in Fig. 5.3.

Device 1: ITO/α-NPD (300 Å)/8% $(PBD)_2Ir(tta)$ doped CBP (350 Å)/BCP (60 Å)/Alq_3 (280 Å)/LiF (10 Å)/Al (1000 Å).

Device 2: ITO/α-NPD (300 Å)/8% $(PBD)_2Ir(tmd)$ doped CBP (350 Å)/BCP (60 Å)/Alq_3 (280 Å)/LiF (10 Å)/Al (1000 Å).

Figures 5.4 and 5.5 depict the current–voltage characteristics for device 1 and device 2 in the forward-biased. The inset of Figs. 5.4 and 5.5 shows the electroluminescence spectra of $(PBD)_2Ir(tta)$ and $(PBD)_2Ir(tmd)$ complexes at different

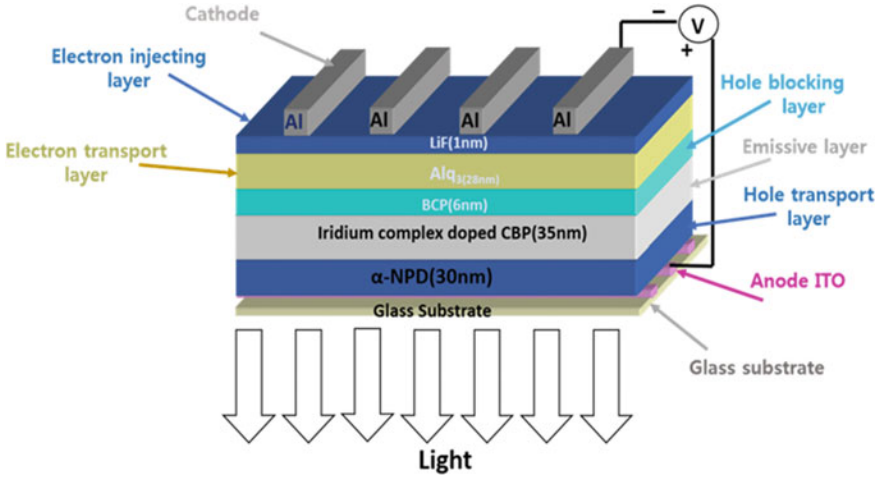

Fig. 5.3 General device structure of the fabricated devies

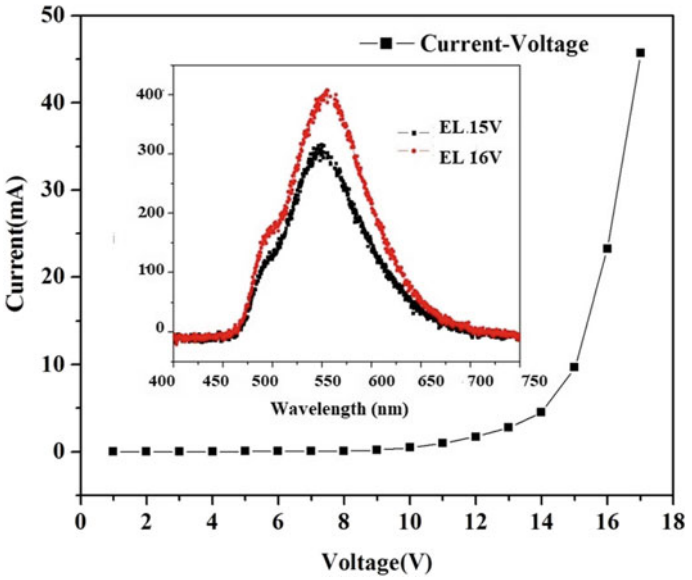

Fig. 5.4 I–V characteristics of device 1, inset shows the electroluminescent spectrum of complex $(PBD)_2Ir(tta)$

voltages. It is clear from the figures that complex $(PBD)_2Ir(tta)$ and $(PBD)_2Ir(tmd)$ emit at 555 nm and 563 nm, respectively. Furthermore, no emission from CBP or Alq_3 was observed, and it indicates a complete energy transfer from the host exciton to the Ir-dopants. Meanwhile, there is no exciton decay in the Alq_3 layer due to the

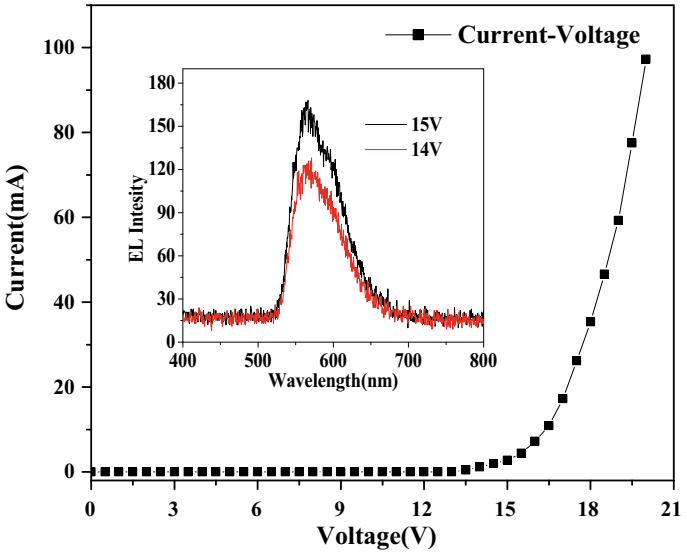

Fig. 5.5 I–V characteristics of device 2, inset shows the electroluminescent spectrum of complex $(PBD)_2Ir(tmd)$

hole blocking action of the BCP layer. Hence Alq_3 and BCP do not contribute to the EL spectrum but act as electron transport and a hole blocking layer correspondingly.

5.5 Conclusions

The present complexes synthesized using PBD, tta and tmd are highly stable in air and can be deposited by thermal evaporation technique during device fabrication. The devices show stable electroluminescence with different voltages. The electroluminescent characteristics of these metal complexes indicate that these materials can be used as emitting materials for OLED applications. The present study provides a convenient way to tune the emission color by changing the secondary ligand.

Acknowledgements The author Anil Kumar acknowledges the director of NPL for providing the opportunity to work in the lab.

References

1. Y. Feng, T. Lu, D. Liu, W. Jiang, Y. Sun, Org. Electron. **67**, 136 (2019)
2. C. Bizzarri, E. Spuling, D.M. Knoll, D. Volz, S. Brase, Coord. Chem. Rev. **373**, 49 (2018)
3. G. Zhang, H. Guo, Y. Chuai, D. Zou, Mater. Lett. **59**, 3002 (2005)

4. M.A. Baldo, M.E. Thompson, S.R. Forrest, Nature **403**, 750 (2000)
5. M.A. Baldo, D.F. O' Brien, Y. You, A. Shoustikov, M.E. Thompson, S.R. Forrest, Nature **395**, 151 (1998)
6. A. Kumar, V. Kumar, K. Awasthi, Polym.-Plast. Technol. Eng. **57**, 70 (2017)
7. A. Kumar, L.K. Jangir, Y. Kumari, M. Kumar, V. Kumar, K. Awasthi, J. Appl. Polym. Sci. **133**, 44091 (2016)
8. S. Lamansky, P. Djarovich, D. Murphy, F.A. Razzaq, R. Kwong, I. Tsyba, M. Bortz, B. Mui, R. Bau, M.E. Thompson, Inorg. Chem. **26**, 1704 (2001)
9. W.S. Huang, J.T. Lin, C.H. Chien, Y.T. Tao, S.S. Sun, Y.S. Wen, Chem. Mater. **16**, 2480 (2004)
10. L. Chen, C. Yang, M. Li, J. Qin, J. Gao, H. You, D. Ma, Cryst. Growth Des. **7**, 39 (2007)
11. J. Li, P.I. Djurovich, B.D. Alleyne, M. Yousufuddin, N.N. Ho, J.C. Thomas, J.C. Peters, R. Bau, M.E. Thompson, Inorg. Chem. **44**, 1713 (2005)
12. T. Yu, F. Yang, X. Chen, W. Su, Y. Zhao, H. Zhang, J. Li, New J. Chem. **41**, 2046 (2017)
13. Y.X. Hu, X. Xia, W.Z. He, Z.J. Tang, Y.L. Lv, X. Li, D.Y. Zhang, Org. Electron. **66**, 126 (2019)
14. A. Kumar, R. Srivastava, M.N. Kamalasanan, I. Singh, Indian J. Chem. **51A**, 937 (2012)
15. A. Kumar, R. Srivastava, P.S. Kadyan, M.N. Kamalasanan, I. Singh, J. Coord. Chem. **65**, 453 (2012)
16. K. Dedeian, P.I. Djurovich, F.O. Garces, G. Carlson, R.J. Watts, Inorg. Chem. **30**, 1685 (1991)
17. H.W. Hong, T.M. Chen, Mater. Chem. Phys. **101**, 170 (2007)
18. Y. Jia, S. Wu, Y. Zhang. S. Fan, X. Zhao, H. Liu, X. Dong, S. Wang, X. Li, Org. Electron. **69**, 289 (2019)
19. M. Colella, P. Pander, A.P. Monkman, Org. Electron. **62**, 168 (2018)

Chapter 6
Fabrication of Reduced Graphene Oxide Conductive Thin Films Using Doctor Blade Technique

Omita Nanda, Jampana Gayathri, A. M. Biradar, and Kanchan Saxena

Abstract Graphene based conductive films have gathered attention due to their potential applications in sensors, electrodes, supercapacitors, etc. Thin films of graphene oxide were fabricated on glass substrate by doctor blade technique. Substrates coated with graphene oxide were chemically treated with hydrazine hydrate to obtain thin films of reduced graphene oxide. Both graphene oxide and reduced graphene oxide were analyzed by X-ray diffraction technique to confirm their composition. The sheet resistance was found to be 600 and 1 kΩ/sq in case of ~50 μm thin films of graphene oxide and reduced graphene oxide respectively. The surface morphology of the films was analyzed by scanning electron microscopy (SEM).

6.1 Introduction

Graphene is a two dimensional material with sp^2-bonded carbon atoms densely packed in a honeycomb crystal lattice. Graphene and its derivatives have been extensively explored for various applications in sensors [1], electrodes [2], supercapacitors [3], etc. due to its high electron mobility [4], excellent mechanical and optical properties [5, 6].

Various methods have been reported in literature for synthesis of graphene oxide (GO) such as micro-mechanical exfoliation [7], chemical vapor deposition [8], epitaxial growth [9], etc. but chemical oxidation continues to be the most popular method due to its simplicity, scalability and economic feasibility. GO is obtained by the exfoliation of graphite oxide. Further, by removing the oxygen-containing

O. Nanda · J. Gayathri · K. Saxena (✉)
Amity Institute of Renewable and Alternative Energy and Amity Institute of Advanced Research and Studies (Materials and Devices), Amity University, Sector 125, Noida, Uttar Pradesh 201303, India
e-mail: ksaxena@amity.edu

A. M. Biradar
CSIR—National Physical Laboratory, Dr. K. S. Krishnan Road, New Delhi 110012, India

V. K. Jain et al. (eds.), *Recent Trends in Materials and Devices*, Springer Proceedings in Physics 256, https://doi.org/10.1007/978-981-15-8625-5_6

groups from GO, it can be reduced to graphene-like sheets. These sheets are known as reduced graphene oxide (rGO).

In the present work, GO was synthesized and thin films of GO were prepared by doctor blade method. The GO films were further reduced to rGO films and were characterized by scanning electron microscopy (SEM) and X-Ray diffraction (XRD) technique.

6.2 Experimental Details

Graphene oxide was prepared by modified Hummer's method [10]. The obtained graphene oxide was further rinsed with DI water to remove metal ions. The resultant GO was dispersed in DI water to obtain a colloidal solution. This GO was further reduced to rGO by treating it with hydrazine hydrate. Glass substrates were used for sample preparation. The substrates were cleaned with soap solution and sonicated in DI water, followed by boiling in isopropyl alcohol. Substrates were then dried in oven. 30 wt% of GO was dispersed in DI water. The GO solution was coated on glass substrates using doctor blade technique. The samples were dried in oven at 80 ˚C for three hours. These GO samples were further treated with hydrazine hydrate vapors which resulted in thin films of rGO.

The morphologies of the films were studied using Carl Zeiss EVO18 scanning electron microscope. The compositions of the samples were investigated by XRD technique (Rigaku Ultima IV). The Sheet resistance of the thin films was measured using four-point probe setup (Nvis 6105).

6.3 Results and Discussions

Color change during reduction process is the preliminary indication of formation of rGO from GO. On treatment of GO with hydrazine hydrate the color of the GO solution was found to change from brown to black which confirmed the formation of graphene. As shown in Fig. 6.1, the brown color of GO changes to black when the reduction of Go takes place.

GO has strong hydrophilic nature due to presence of oxygenated groups which allows its easy dispersion in water. Whereas the reduction to rGO results in the aggregation of GO which leads to removal of hydrophilic group and makes it hydrophobic in nature. This aggregation creates hindrance in forming dispersion of rGO and hence fabrication of stable thin films is complicated. Therefore, thin films of GO were first coated by doctor blade technique and then reduced to rGO by treatment with hydrazine hydrate vapors.

The sheet resistance of thin films of GO was found to be 600 kΩ/sq while the electrical conductivity of the films was enhanced when reduced to rGO by removing almost all the oxygen-containing groups. It was found that the sheet resistance

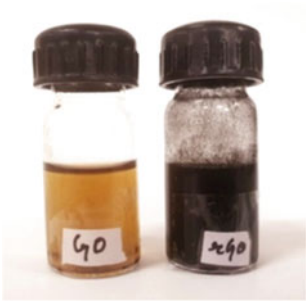

Fig. 6.1 Photograph of suspension of GO and rGO

decreased to 1 kΩ/sq in rGO. In the present study the concentration of GO was 30 wt% which resulted in the uniform films of GO of about 50 μm. The resistance of the film will depend on the film thickness as well as the GO concentration in the solution. Detail studies on the effect of varying the GO concentration and the thickness of the film on the sheet resistance is being carried out and will be reported elsewhere.

The surface of thin films of GO and rGO was analyzed by scanning electron microscopy. Figure 6.2a, b show the SEM images of thin films of GO and rGO. The exfoliation of graphite flakes leads to graphene oxide (GO). As shown in Fig. 6.2a the thin films of graphene oxide have multilayered sheets. Figure 6.2b shows the SEM images of reduced graphene oxide oriented as randomly crumpled layers.

Crystal structure of thin film of GO and rGO was examined using X-ray diffraction technique (Fig. 6.3) with Cu Kα radiation of wavelength of 1.54 Å. The spectra in Fig. 6.3 show two peaks corresponding to GO and rGO. A strong peak at $2\theta = 10.5°$ was observed for graphene oxide, which corresponds to interlayer spacing (*d* spacing) of 0.84 nm, which is similar to as reported previously [11]. This peak disappears in the rGO spectrum due to the removal of functional groups. A broad peak appeared at $2\theta = 24.7°$ for rGO. This peak corresponds to interlayer spacing

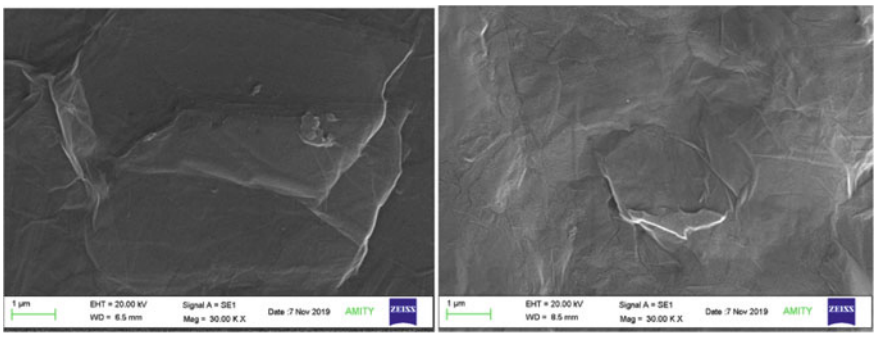

(a) (b)

Fig. 6.2 SEM microcrographs of thin films of GO (**a**) and rGO (**b**)

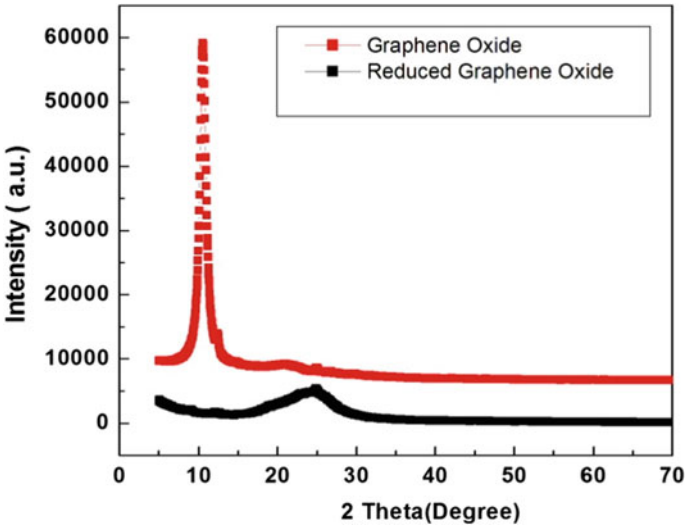

Fig. 6.3 XRD pattern of Graphene oxide and reduced graphene oxide

of 0.36 nm. The decrease in the d spacing from 0.84 nm (for GO) to 0.64 nm (for rGO) indicates the reduction and removal of oxygen containing functional groups. The broadening of peak and decrease in the peak intensity of rGO takes place due to the turbo static arrangement of stacked rGO sheets [12]. Further applications of Raman spectroscopy in characterizing the properties of graphene is being carried out and will be reported in our future work.

6.4 Conclusions

Graphene oxide was synthesized from graphite flakes and then reduced to rGO. The further reduction of GO to rGO lead to agglomeration of rGO in solution. Due to this it was difficult to prepare thin films from rGO suspension. Therefore thin films of GO were first prepared by doctor blade technique and which were later treated with hydrazine hydrate vapors to obtain rGO films. The XRD analysis also confirmed that the GO films were successfully reduced to rGO films. It was observed that the sheet resistance of the films decreases from 600 to 1 kΩ/sq when the reduction of GO takes place. To achieve good conducting graphene films using this technique detail studies are being carried out by varying the GO concentration and the thickness of the film.

References

1. L. Fan, Y. Hua, X. Wang, L. Zhang, F. Li, D. Han, Z. Li, Q. Zhang, Z. Wanga, L. Niu Fluorescence resonance energy transfer quenching at the surface of graphene quantum dots for ultra sensitive detection of TNT. Talanta **101**, 192 (2012)
2. E. Kymakis, E. Stratakis, M.M. Stylianakis, E. Koudoumas, C. Fotakis, Spin coated graphene films as the transparent electrode in organic photovoltaic devices. Thin Solid Films **520**, 128 (2011)
3. M.F. El-Kady, Y. Shao, R.B. Kaner, Graphene for batteries, supercapacitors and beyond. Nat. Rev. Mater. **1**, 16033 (2016)
4. K.I. Bolotin, K.J. Sikes, Z. Jiang, M. Klima, G. Fudenberg, J. Hone, P. Kim, H.L. Stormer, Ultrahigh electron mobility in suspended grapheme. Solid State Commun. **146**, 351 (2008)
5. Y. Liu, B. Xie, Z. Zhang, Q. Zheng, Z. Xu, Mechanical properties of graphene papers. J. Mech. Phys. Solids **60**, 591 (2012)
6. Z.Z. Zhang, K. Chang, F.M. Peeters, Tuning of energy levels and optical properties of graphene quantum dots. Phys. Rev. B **77**, 235411 (2008)
7. K.S. Novoselov, A.K. Geim, S.V. Morozov, D. Jiang, Y. Zhang, S.V. Dubonos, I.V. Grigorieva, A.A. Firsov, Electric field effect in atomically thin carbon films. Science **306**, 666 (2004)
8. X.Z. Yu, C.G. Hwang, C.M. Jozwiak, A. Köhl, A.K. Schmid, A. Lanzara, New synthesis method for the growth of epitaxial graphene. J. Electron Spectrosc. **184**, 100 (2011)
9. X. Chen, L. Zhang, S. Chen, Large area CVD growth of graphene. Synth Met. **2010**, 95 (2015)
10. F.T. Thema, M.J. Moloto, E.D. Dikio, N.N. Nyangiwe, L. Kotsedi, M. Maaza, M. Khenfouch, Synthesis and characterization of graphene thin films by chemical reduction of exfoliated and intercalated graphite oxide. J. Chem. **2013**, 1 (2012)
11. H. Liu, T. Kuila, N.H. Kim, B.C. Ku, J.H. Lee, In situ synthesis of the reduced graphene oxide–polyethyleneimine composite and its gas barrier properties. J. Mater. Chem. A **1**, 3739 (2013)
12. S. Dubin, S. Gilje, K. Wang, V.C. Tung, K. Cha, A. S. Hall, J. Farrar, R. Varshneya, Y. Yang, R.B. Kaner, A one-step, solvothermal reduction method for producing reduced graphene oxide dispersions in organic solvents. ACS Nano **4**, 3845 (2010)

Chapter 7
Design and Optimization of Solar Photovoltaic Power Plant in Case of Agrivoltaics

Mohd. Adil Faizi, Vyas Maharshi Sandipkumar, Abhishek Verma, Suman, and V. K. Jain

Abstract Agrivoltaics is the dual use of farming land, by combining solar PV electricity generation and crop growing, simultaneously. Nowadays, farmers are mostly facing the problems due to heavy rains, floods, hailstorms, drought, etc., by which all their efforts and investments go in vain, and farmers faces the extreme difficult conditions. Therefore, concept of Agrivoltaics came to maximize the use of the agricultural land by combining solar energy harvesting and crop growing. With this system, farmers can earn extra money by selling generated PV electricity along with crop, without affecting their crop's yield. In addition, they can utilize some part of generated electricity for their house, as they generally live nearby their farmland and can improve their livelihood. The most important factor here is the effect of the shadow of solar panel on the growth of the crops. Hence, this paper presents the most important findings of the effect of shadow under the dynamic conditions, as the shadow moves with the motion of the sun. To study the effect of the shadow, the height of solar panels on the agricultural land, is a crucial factor and optimization of the same is important. The optimum height of the solar panels on agricultural land is required to have minimum effect of its shadow on the crops, to provide farmers with flexibility in moving their vehicles easily for farming and it should not increase the effective cost of the solar power plant. A simulation and analysis was carried out at 4 different heights of solar panels, 4, 8, 12 and 16 ft. These heights were individually analysed with two different parameters, change in Shadow Area (SA) of the panel per hour and shadow Displacement Length (SDL) per hour. The movement of shadow was traced from morning 6.00 AM to evening 7.00 PM, at every 1 h of time interval. Through simulation studies, it was observed that as with the increase in height of the solar panel, the rate of shadow displacement increases on the land. However, the percent change in average Shadow Displacement Length Rate (SDLR) from 4 to 8, 8 to 12 and 12 to 16 ft (6.00 AM to 7.00 PM) was found to be ~75%,

Mohd. A. Faizi · V. M. Sandipkumar · A. Verma (✉) · Suman · V. K. Jain
Amity Institute of Renewable and Alternative Energy, Amity University, Noida, Uttar Pradesh 201303, India
e-mail: averma5@amity.edu

A. Verma · Suman · V. K. Jain
Amity Institute for Advanced Research and Studies (Materials and Devices), Amity University, Noida, Uttar Pradesh 201303, India

V. K. Jain et al. (eds.), *Recent Trends in Materials and Devices*, Springer Proceedings in Physics 256, https://doi.org/10.1007/978-981-15-8625-5_7

~55% and ~39%, respectively. Further extension of solar panel's height above 16 ft, SDLR kept dropping and didn't show any significant benefits neither in Shadow Area nor in Shadow Displacement rate. Therefore, on the basis of analysis it may be concluded that the optimum height of solar panels should be kept around 15 ft, which will project minimum shadow on crops with high SDL rate, allow farmers to do faming conveniently with their vehicle and keep the financial burden at the lower side.

7.1 Introduction

The utilization of the agricultural land can be enhanced by combining the crop harvesting along with solar photovoltaics power generation. The concept made as a secondary resource to the farmers for earning an extra income other than crop cultivation, without affecting the crop's yield. This term coined as Agrivoltaics System (AVS). In countries, like India, were non-uniform natural climatic conditions occurs in different regions of country, such as floods, droughts, hail storm, insufficient water supply, etc. Such challenges were faces by the farmers throughout the year, due to which, farmers are either unable to rebuild their land, or unable to regain financial losses, or shattered from their livestock or go under deep depression or even suicide. To overcoming such fatal conditions for specifically small marginal farmers, this Agrivoltaics model is best suited [1–3].

In India, most of the areas where solar PV plants have been installed are either on the non-fertile land or on the rooftop. In Agrivoltaic system, concept is different, utilization of the fertile land to its maximum by generating electricity and to grow crops to gather. To apply this model, it is important to make detailed study about the effect of the shadow on the growth of the crops. It is also important requires to do the simulations and optimization of the design of solar panels to minimize the shadow effect on the growth of the crop and to generate the maximum electric power [4, 5].

The Agrivoltaics concept is recently coined, therefore detailed information is not available, as not much studies have been done, such as, its effect of different crops, optimized solar power plant on agricultural land, etc. [6]. To minimize the effect of the shadow on crops, the design of the panels, w.r.t. height and distance between poles, are the crucial factor. There are no such factors and parameters, like height, shadow area and shadow displacement rate came in to the existence to minimize the shadow effect on the crop and no such research have been carried out on the basis of models and structures.

To analyze and optimize the solar power plant's design for AVS and their shadow effects on agricultural land, herein, the simulation studies were conducted to optimize the height of solar photovoltaic panels on the agricultural land, under dynamic condition, so that crops can be grown without any reduction in its yield, on the same field of land. It's a crucial factor, as its contribution affects percentage of generated shadows on the crop, therefore, it is required to have minimum effect of shadow on the crops.

7.2 Simulation and Analysis Details

As discussed, here in this paper, the study was carried out to analyze the effect of shadow on the agricultural land through simulation-based model. To analyze, simulations were performed using 'Google Sketchup Pro 2018, Version 18.0.16975', software. This simulation software is a computer programmed 3D modelling tool for design and structural purpose, which can be used for any field areas, such as architectural, civil-construction, mechanical design and more. The Google Sketchup is an easy and versatile tool to design, rebuild and construct specific end-to-end task [7]. In this model, analysis of projected solar panel's shadow was performed on the basis of varying solar panel's height 4, 8, 12 and 16 ft above the ground surface. In order to carry out simulations, two basic parameters were considered, (i) change in Shadow Area (SA) per hour, and (ii) Shadow Displacement Length (SDL) per hour; here these two points are required to observe the effect of solar panel's shadow on Agrivoltaics land, under dynamic conditions.

For analyzing the shadow effect through simulation, a particular season was chosen, i.e. peak month of summer (June) with the IST time zone (i.e., GMT + 05:30). Further, the orientation of solar panels was kept towards south facing with mounting angle of 28° (considering Delhi-NCR, India), as a standard, throughout the complete simulation analysis. For each height 4, 8, 12 and 16 ft, the movement of projected shadow was considered from morning 6.00 AM to evening 7.00 PM. Here, 6.00 AM shadow is set as a reference shadow for measuring shadow displacement per hour from its center point, as shown in Fig. 7.1. While area of shadow was calculated by normal geometrical shapes formed by projected shadow on ground, shown in Fig. 7.1. As time is shifted with an hour, the shadow displaced from its original location, along with the change in its shape and size from previous one. The path of the shadow is followed by the movement of the Sun.

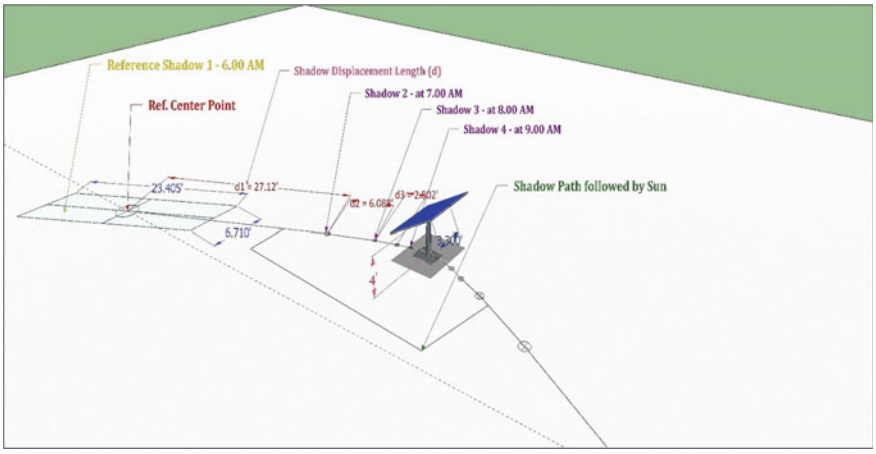

Fig. 7.1 Simulation and analysis details of solar panel at 4 ft height

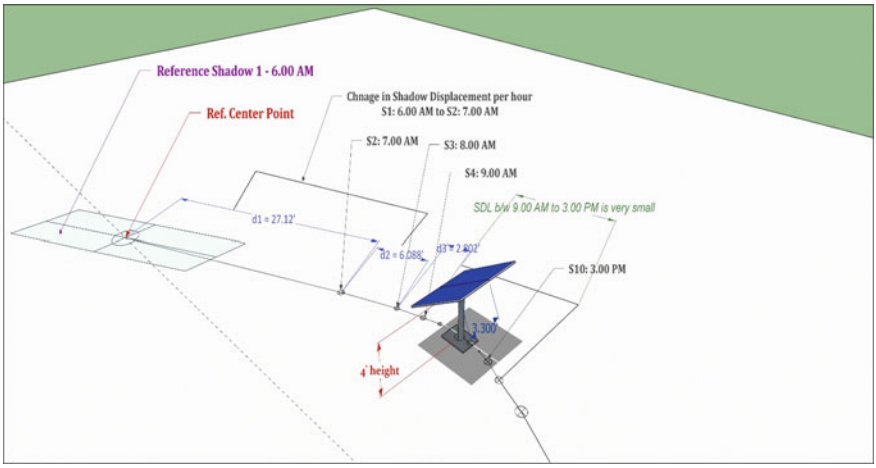

Fig. 7.2 Change in shadow displacement length per hour for 4 ft high solar panel

Considering different case, w.r.t., particular solar panel's height.

7.2.1 Case 1: Solar Panel at 4 ft High

In case 1, analysis was performed at 4 ft of height where shadow area and displacement length were measured in feet. To have a better understanding, as shown in Fig. 7.2, few initial shadows are marked as shadow1 (for 6.00 AM), shadow2, shadow3, …. till shadow14 (for 7.00 PM) along with time as per hour. Similarly, displacement of shadow is also marked, as shown in Fig. 7.2, d1, d2, d3,…. till d14, which is measured as displacement length of a moving shadow. At 4 ft of height, shadow displacement length (d) between two shadows is initially reduced rapidly from 6.00 to 9.00 AM, while gradually thereafter from 9.00 AM to 1.00 PM. Further, when time shifted nearly ahead from midday, i.e., approx. 1.00 to 7.00 PM, the displacement length is starts increasing, rapidly. Distance between two shadow is not much noticeable during peak hours and this length depends upon the height of the panel.

7.3 Case 2: Solar Panel at 8 ft High

In case 2, similar analysis was performed at 8 ft of height. In Fig. 7.3, the moving shadow is marked as shadow1, shadow2, … Shadow14 along with time as per hour. Here, shadow1 is considered as reference for examine the further displacement of shadow. Under the dynamic condition, as projected shadow of solar panel moves,

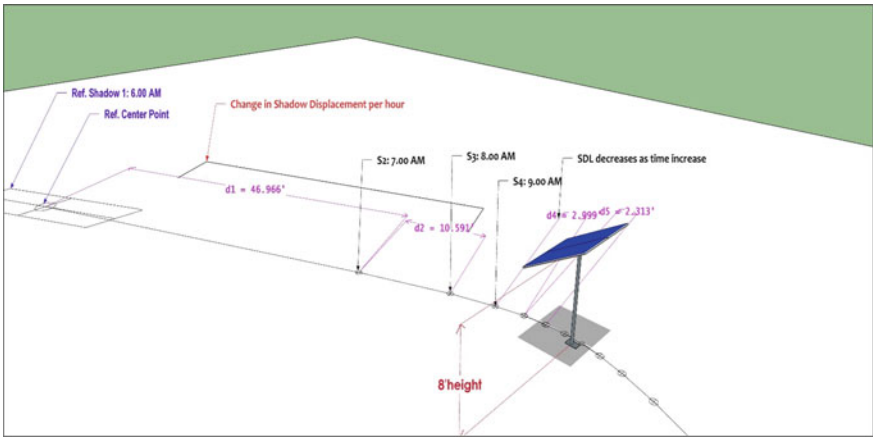

Fig. 7.3 Change in shadow displacement (d) with change in height of solar panel to 8 ft

the area of shadow and displacement length changes, accordingly. Due to change in height from 4 to 8 ft, the variation in shadow displacement is slightly increased with increase in height. It is also observed that when height increased from 4 to 8 ft the shadow falls quite away from the fixed solar panel, and the small changes might affect the shadow area and displacement length too.

7.4 Case 3: Solar Panel at 12 ft High

In case 3, analysis was performed at 12 ft high solar panel, where shadow area and displacement length have comparatively larger variation. In Fig. 7.4, solar panel's shadows are again marked as shadow1, shadow2…. till Shadow14 along with time as per hour. Where Shadow1 considered as reference for displacement of shadow, as d1, first SDL. Due to further increase in height from 8 to 12 ft, the variation in displacement is slightly increased. It is observed that at 12 ft of height, the distance between two shadows is relatively more, per hour, as compared to that of 4 and 8 ft high solar panels. The effect of height shows no overlapping of shadow fall on previous shadow, when time shifted from 9.00 AM to 2.00 PM, because with increase in panel's height, the gap between two consecutive projected shadows at an hour's difference, is increased more, as compared with that of lower height panels.

7.5 Case 4: Solar Panel at 16 ft High

In case 4, further analysis was performed at 16 ft of height, where shadow area and displacement length are more affected. In Fig. 7.5, solar panel's shadows are similarly

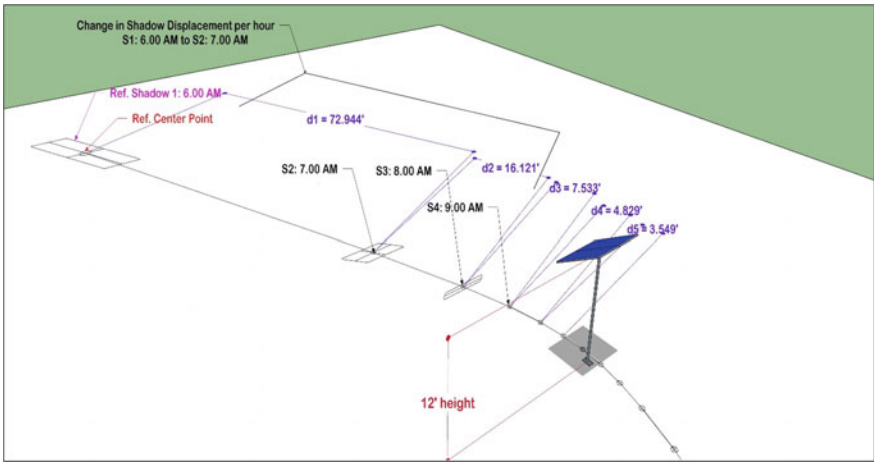

Fig. 7.4 Change in displacement (*d*) w.r.t time per hour for 12 ft high solar panel

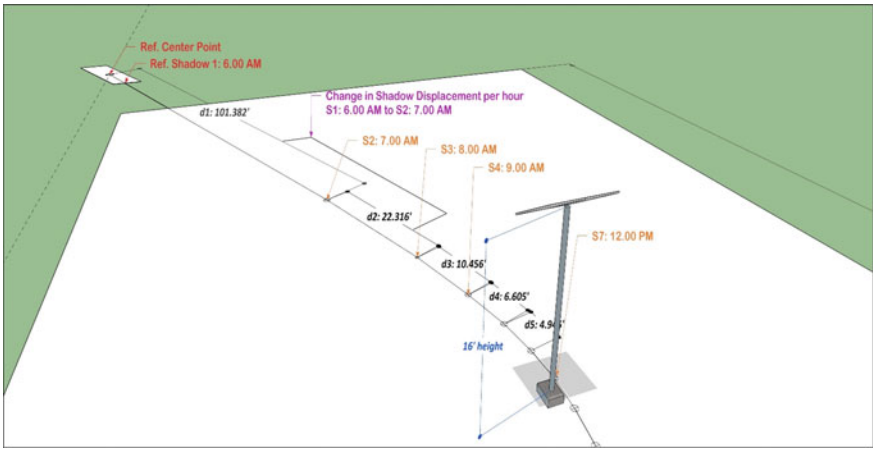

Fig. 7.5 Change in shadow displacement length per hour for 16 ft high solar panel

marked as shadow1, shadow2, … shadow14 along with time as per hour. Here too, shadow1 considered as reference for displacement of shadow, as d1, first SDL**.** Due to increase in height up to 16 ft, the variation in displacement of shadow is more and the distance between two consecutive projected shadows is also significant.

7.6 Result and Discussion

As discussed, simulation analysis was carried out at 4 different heights of solar panels, 4, 8, 12 and 16 ft, as solar panel's height is one of the important parameters to understand the effect of shadow on agricultural land. The solar panels with different heights are individually analysed with two essential parameters, Shadow Area (SA) of a solar panel and Shadow Displacement Length (SDL) per hour or Shadow Displacement Length Rate (SDLR), under dynamic conditions. The movement of shadow tracked from morning 6.00 AM to evening 7.00 PM, at every 1 h of time interval. When shadow moved from 6.00 AM to 7.00 AM shadow changes its shape and size with a certain displacement from its origin point. Therefore, to obtain SA and SDLR from 6.00 AM to 7.00 PM, shadow formed at 6.00 AM marked as a reference shadow or a reference centre, to measure SDL between two consecutive projected shadows, w.r.t., time.

The SDL analysis is summarized in Fig. 7.6 and is self-explanatory. It is well observed that as we increase the height of the solar panel, the rate of projected shadow displacement increases on the land. At initial and later hours, say from 6.00 AM till 9.00 AM and from 5.00 PM onward, the shadow displacement rate is quite high, however, it gradually reduces from 9.00 AM till 1.00 PM. Further from around 1.00 PM onward, the SDLR again starts increasing gradually, and then rapidly in later hours. Inset of Fig. 7.6 shows the variation in SDLR near noon time, for better understand.

For analysing the effect of solar panel's height on its shadow movement, further percent change in average shadow displacement length rate is calculated w.r.t. to the particular panel's height and is shown in Fig. 7.7. As observed for 6.00 AM–7.00 PM, the percentage change in average SDLR, while increasing the solar panel's height from 4 to 8 ft is around 75%, which is further reduced to around 55% for

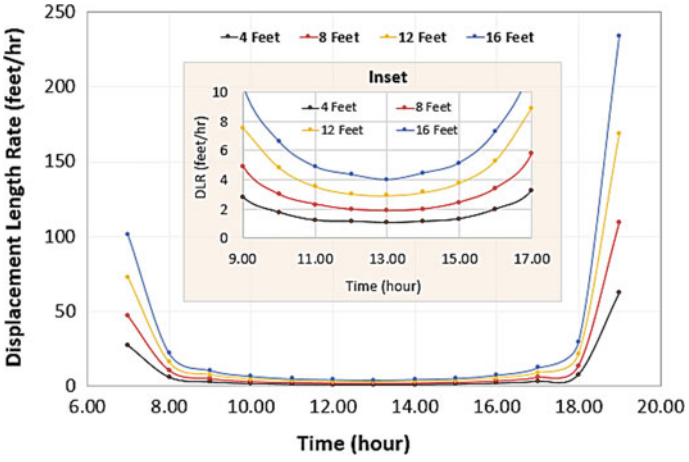

Fig. 7.6 Shadow displacement length w.r.t. time and height of the solar panel

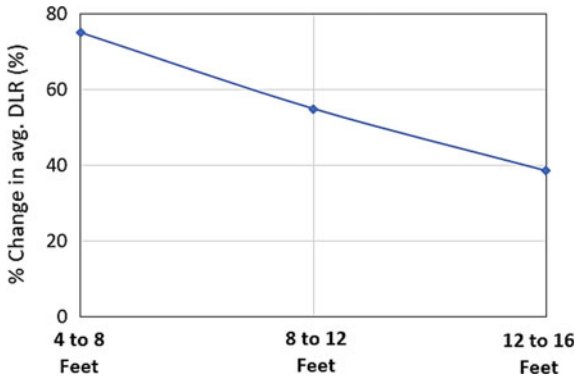

Fig. 7.7 Variation in percentage change in average SDLR w.r.t. change in height of solar panels

increasing the height of the panel from 8 to 12 ft, and yet further reduced to around 39% for increasing height from 12 to 16 ft. Therefore, through this investigation, it is absolutely clear that while increasing the height of the solar panels, their shadow displacement rate will definitely increase, however, the percentage of increase in this shadow displacement rate keeps on dropping and will doesn't show significant benefits, for further extension of panel's height.

The change in shadow area is also analysed per hour for each solar panel's height, as shown in Fig. 7.8. As seen from Fig. 7.8, the area of formed shadow on land varies throughout the day, such as it is very large only in early morning and evening time, however, at day time it is more or less equal to the solar panel's actual size (i.e., 20.5 sq. ft) and shows very gradual increase in its size, till early evening. Further, the variation in the size of shadow area throughout day for different solar panel's height is also analysed and summarized in Fig. 7.8. It has been observed that there is no as

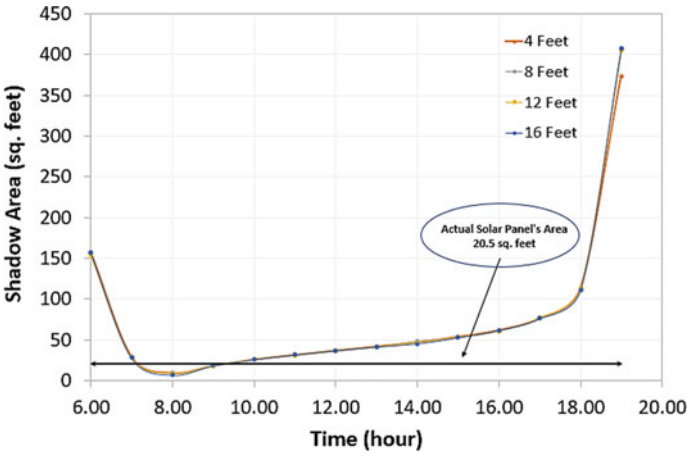

Fig. 7.8 Change in shadow area with four different heights

such variation in shadow area by just increasing the height of solar panels from 4 to 16 ft.

Moreover, in Fig. 7.9, the movement of the shadow w.r.t. the field, of respective height of solar panels are shown. Figure 7.9 clearly illustrate the comparative shadow's movement rate increases as per increase in height of solar panels. At 16 ft of height, the movement of the shadow formed on agricultural land is faster than that of any other height, also shown in Fig. 7.10.

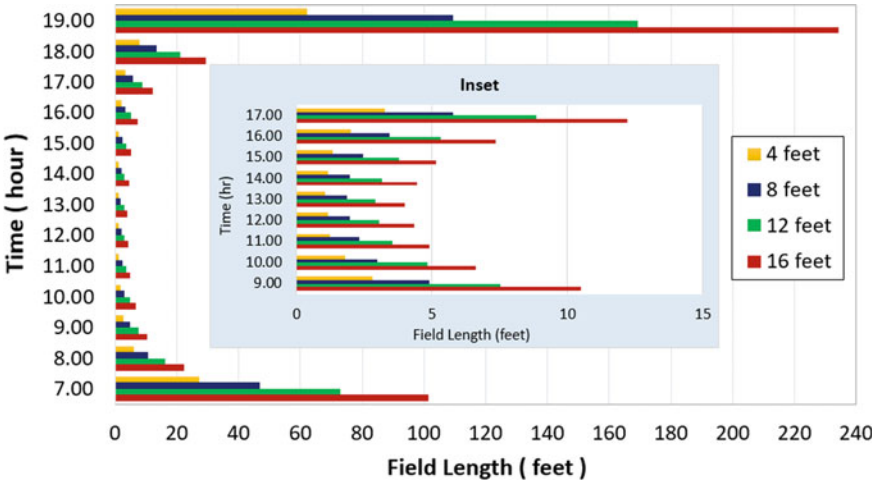

Fig. 7.9 Shadow movement variation due to time and height w.r.t. field length

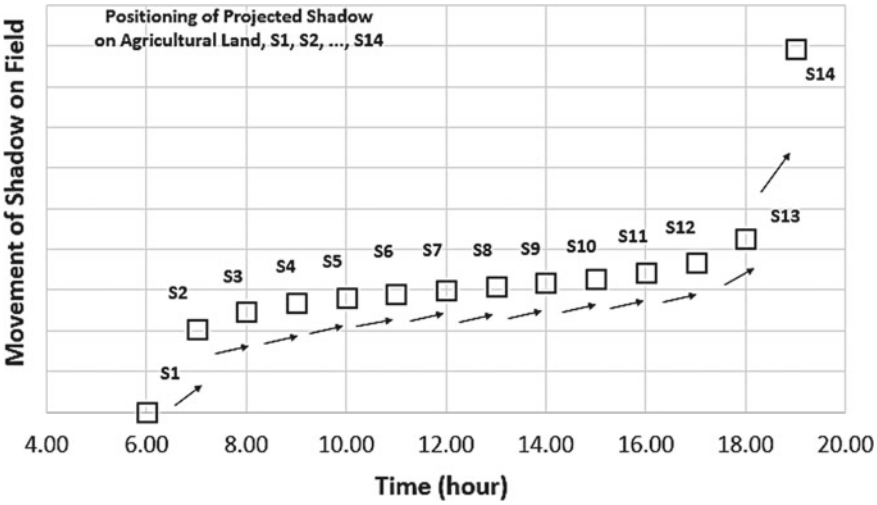

Fig. 7.10 Movement of shadow on field for 16 ft high solar panel

Therefore, the complete analysis shows that the optimum height of solar panels on agricultural land should be kept around 15 ft, which will project as minimum shadow on the crops with high SDL rate and farmers can conveniently do farming with their vehicles, while keeping financial burden at the lower side.

7.7 Conclusion

The concept of Agrivoltaics is to increase the income of the farmers, apart from their regular earning from crops. Adopting AVS can maximize the use of the agricultural land by combining solar energy harvesting and crop growing, which also support to enhance the livelihood of the farmers in remote areas, such as utilizing part of electricity for their household appliances, drinking water, as well as solar pumps, etc. To maximize the use of this model, simulation analysis was performed under dynamic conditions to minimize the shadowing effects on fertile land by optimizing the various parameters of the solar power plant. Through simulation, it is observed that the solar panel's height is a crucial factor for analyzing shadow effect in Agrivoltaics System. It is found that with increase in the height of the solar panel, the rate of shadow displacement rate increases on the land. However, there is no as such variation is found in size of shadow area projected on the land at any particular time, by just increasing the height of solar panels from 4 to 16 ft. Moreover, the percentage change in the average SDLR throughout the day while moving from 4 to 8 ft is around 75%, which is reduced to around 55% for increasing the height of the panel from 8 to 12 ft, and further reduced to around 39% for increasing height from 12 to 16 ft. Therefore, it has been analyzed that the optimum height of solar panels on agricultural land should be kept around 15 ft, which will project minimum shadow on the crops with high SDL rate, and farmers can easily perform farming with their vehicles, while keeping financial burden at the lower side.

Acknowledgements The authors are thankful to Dr. Ashok K. Chauhan, Founder President, Amity University, Noida for his continuous guidance and encouragement. The authors also gratefully acknowledge the financial support from the Department of Science and Technology (DST), Govt. of India, Project No. DST/TM/CERI/2K15/370(G).

References

1. W. Contributors, Agrivoltaic, in *Wikipedia, The Free Encyclopedia.* https://en.wikipedia.org/w/index.php?title=Agrivoltaic&oldid=961570874. Accessed Jul. 10, 2020
2. K. Vyas, Solar farming with agricultural land. Acta Sci. Agric. **3**(10), 23–25 (2019). https://doi.org/10.31080/asag.2019.03.0640
3. T. Harinarayana, K.S.V. Vasavi, Solar energy generation using agriculture cultivated lands. Smart Grid Renew. Energy **05**(02), 31–42 (2014). https://doi.org/10.4236/sgre.2014.52004

4. National Statistic Office Malta, Electricity Generation: 2008–2017 (Malta), no. Oct. pp. 1–5 (2018) [Online]. Available: https://twitter.com/NSOMALTA/
5. H. Dinesh, J.M. Pearce, The potential of agrivoltaic systems. Renew. Sustain. Energy Rev. **54**, 299–308 (2016). https://doi.org/10.1016/j.rser.2015.10.024
6. J.K. Chacko, K.J. Thomas, Analysis of different solar panel arrangements using PVSYST. Int. J. Eng. Res. **V4**(04), 510–513 (2015). https://doi.org/10.17577/ijertv4is040614.
7. Trimble, SketchUP, Aug. 2000. www.sketchup.com

Chapter 8
Synthesis and Characterisation of a Nanoalloy for Thermal Applications

Heena Yadav, Subhra Das, and Sudip Majumder

Abstract Metal oxide nano particles are potentially useful for heat transfer applications because of their chemical and physical properties. In this present study an attempt has been made to synthesize Fe_2O_3–Al_2O_3–CuO nano-composites by Co-precipitation method. The chemical, physical and thermal properties of the synthesized nano-particles were examined by Scanning Electron Microscopy, Energy Dispersive X-Ray Analyser, Fourier transform infrared spectroscopy and Thermo gravimetric Analyser. The properties of nano-alloy were studied along with those of the constituent nano-particles to estimate potential benefits of using this nano-composite for heat transfer applications. Energy Dispersive X-Ray analysis of metallic nano-alloy annealed at 500 °C revealed the presence of copper (Cu), aluminium (Al), iron (Fe), oxide(O) elements in metallic nano-alloy and data indicated that nano-particles were nearly stoichiometric. The molecules of metallic nano-alloy were found to be spiral in shape with size distribution of 200 nm. FTIR also confirms the presence of aluminium oxide, copper oxide and iron oxide in synthesized nano-alloy sample. Thermal analysis of the nano-alloy shows that there is significant increase in heat transfer characteristic of nano-fluid made of water with 0.4 wt% nano-alloy. It was observed that heat transfer characteristics increased with increase in concentration of nano-alloy in base fluid.

8.1 Introduction

The advancement in fabrication technology has made it possible to synthesize materials on micro and nanometer scale which exhibits novel properties. Nano-materials are those materials that posses at least one dimension less than 100 nm [1]. Nano-structured materials are synthesized on atomic or molecular scale to produce either

H. Yadav · S. Majumder
Amity School of Applied Sciences, Gurgaon, India

S. Das (✉)
Solar Engineering Department, Amity School of Engineering & Technology, Amity University Haryana, Gurgaon, India
e-mail: sdas@ggn.amity.edu

V. K. Jain et al. (eds.), *Recent Trends in Materials and Devices*, Springer Proceedings in Physics 256, https://doi.org/10.1007/978-981-15-8625-5_8

new or enhanced physical properties which are not exhibited by conventional bulk solids. Metal oxide nano-particles (NPs) are potentially useful for heat transfer applications showing promising results in enhancing thermal properties of heat transfer fluid when suspended with NPs.

A number of synthetic techniques can be used to prepare nano-materials with well-defined size and morphology. These techniques can be classified into two broad categories, namely, physical and chemical techniques. The physical techniques commonly used are namely laser ablation technique, inert gas condensation technique, high energy ball milling method, electro-deposition method and chemical vapor deposition technique [2]. Nano particles of various oxides can be synthesized by confining chemical reaction, nucleation and growth process. Various synthesis methods such as hydrothermal method, Sol–gel method [3], electro-spinning method, co-precipitation method [4–6] and sonochemical method [2] are used for synthesis of nano-materials.

A variety of nano-particles have been reported in literature [7]. There are two main types of oxides of iron: magnetite Fe_3O_4 and maghemite Fe_2O_3 [8]. Apart from above mentioned techniques, hydrolysis method is found by researchers to be suitable for synthesizing Fe_2O_3 nano-particles [9]. These are of great interest due to their paramagnetic properties and are used in various applications such as catalytic materials, adsorbents, pigments, flocculants, coatings, gas sensors and ion exchangers. Magnetite and maghemite are thermodynamically less stable than hematite [10]. Despite this, it has been found that stability increases for smaller nano-crystals of maghemite, because its surface energy is lower than that of hematite.

Cupric oxide (CuO) nano-particles can be prepared using copper sulphate 5-hydrate as a precursor and NaOH as a stabilizing agent by aqueous precipitation method [11]. This method is suitable for large scale production of CuO-NPs which can be utilized for removal of methylene blue dye. Vinyl-ester resin polymeric nano-composites were fabricated using cupric oxide (CuO) nano-particles and those functionalized with a bi-functional coupling agent methacryloxypropyltrimethoxysilane [12]. The nano-composite showed increased thermo-stability compared to unmodified nano-particle filled counterparts.

Thermal analysis of nano materials deals with action of heat on physical properties of materials. Mass, enthalpy, heat capacity, co-efficient of thermal expansion and thermal conductivity are some properties studied using thermal analysis. Thermo gravimetric analysis (TGA) is commonly used thermal analysis technique which record the change in weight of a sample as a function of either temperature or time. On the other hand, Differential Scanning Calorimetry (DSC) is a thermal analysis technique used for quantitative measurement of enthalpy changes. Thermal analysis of nano-fluids reveals that nano-fluids possess unique features with regard to their thermal performances [13]. The properties of nano-fluids are different from properties of conventional heat transfer fluids. The nano-particles have large total surface area which when added to base fluid results in increasing thermal conductivity of nano-fluid. Many research findings revealed that traditional thermo fluids in the presence of nano-particles exhibit better thermo physical properties. The experimental studies on nano-fluids confirm that fluids containing nano-particles are expected to give more

thermal conductivity and lower specific heats over conventional fluids. Researchers have reported that thermal conductivity of nano-fluids decreases with decreasing particle size [7]. Nano-fluids engineered in Argonne National Laboratory and tested by a group of researchers [13] revealed that nano-particles of Al_2O_3, Fe_2O_3 and CuO materials exhibited excellent dispersion quality and increased thermal conductivity when suspended in heat transfer fluids like water, oils and glycols mixtures. Brownian motion of the particles, large surface area and collisions between nano-particles in base fluids are supposed to be responsible factors for enhanced thermal conductivity of nano-fluids [14]. Higher vol% of hybrid nano-fluids increases interactions of nano-particles in base fluid which results information of more numbers of nano-particle chains. This results in enhancement of thermal conductivity in hybrid nano-fluid at high volume concentrations.

Qiang et al. [15] investigated convective heat transfer and flow characteristics of nano-fluid in a tube. It was observed that convective heat transfer coefficient increased about 60% for nano-fluid with 2.0 vol% Cu nano-particles in base fluid. Normally particles of millimeter or micro meter dimension when suspended in fluids will cause erosion of pipe materials, clogging of flow passages and sedimentation due to gravity. The present day modern technology facilitates to produce process and characterize materials having average crystalline size below 100 nm. Vayssieres [16] for the first time quantitatively modelled and demonstrated micro-emulsions phenomenon for transition metal oxide nano-particles in order to study thermodynamic stability of nano-particles in aqueous solution.

In this paper, an attempt has been made to synthesize nano-composite of copper, aluminium and iron oxides with the hope of enhancement of thermal stability and heat transfer characteristics of the resulting nano-alloy.

8.2 Materials and Methods

Synthesis of CuO NPs: CuO NPs are synthesized by co-precipitation method using copper sulphate (hydrated) as precursor and sodium hydroxide as reducing agent. In brief 0.2 M $CuSO_4 \cdot 5H_2O$ and 200 ml of distilled water were mixed in a round bottom flask. Glacial acetic acid is added to the mixture and heated to boil keeping it on a magnetic stirrer. Then 30 ml of 6 M NaOH was poured into the flask. The colour of solution turns from blue to black and suspension were formed simultaneously. The process was carried out for 2.5 h. The mixture was cooled to room temperature and centrifuged. Then wet CuO precipitates were filtered and purified using distilled water and absolute ethanol several times. NPs were dried in oven and transferred in a crucible which is placed in a muffle furnace for few hours at a temperature of 100 °C.

Synthesis of Iron Oxide: 100 ml of deionized distilled water is taken in round bottom flask which is maintained at 90 °C. Then 5 g of $FeSO_4 \cdot 7H_2O$ is added to it with continuous stirring. Standardized 100 ml ammonia solution loaded with ammonium hydroxide is added at a rate of 0.007 mol/s followed by stirring for one second.

200 ml mixture is obtained at the end of this process. Once the mixture has reached to precipitation state, it is allowed to cool and settle and setting of the precipitate in the bottom of the flask is observed. After precipitation, the supernatant liquid was first decanted using Whatman qualitative filter paper having pore size 20–25 μ without disturbing the precipitate. The filtrate was taken in centrifuge tube at 5000 rpm. The supernatant liquid was allowed to pass through filter paper followed by transfer of precipitate finally. Purification of precipitate is done by ethanol solution in water and then dried at 100 °C for 1 h in hot air oven and then annealed at high temperature in muffle furnace. In this methodology for the synthesis of hematite nanoparticles, no other impurities were obtained as side product(s).

Synthesis of Al_2O_3NPs: 4 g of $Al_2(SO_4)_3 \cdot 18HO$ and 5 g of polyethylene glycol is dissolved in 100 ml distilled water. An amount of ammonia (25%) was added into the above solution, giving rise to milky precipitates (pH = 9). The reaction mixture is stirred for 1 h at room temperature and placed in a crucible. It is heated at 300 °C for 6 h. The reaction mixture is gradually cooled to room temperature. The resulting precipitate is filtered and washed three to four times using double distilled water and ethanol to remove polyethylene glycol and other impurities. The synthesized $Al2O_3$ powder is dried at 100 °C for 1 h and was calcinated at 400 °C for 2 h.

Synthesis of Nanoalloy: Mixed metal oxides NPs is synthesised by co-precipitation method by mixing Al_2O_3, Fe_2O_3 and CuO NPs in a fixed ratio of 4:4:3. Mixed sample is transferred in a round bottom flask and 60 ml distilled water is added to it with continuous stirring for 1 h. Then filtered it using Whatmann paper and dried it well. Dried sample is transferred in a crucible and calcination at 500 °C for 3 h in muffle furnace. After 3 h, sample removed and kept at room temperature for 1 h. The sample is then parafilm coated and deep-freezed at −20 °C for 1 h. After this process, sample is kept at room temperature for some time and calcinated again for 3 h at 500 °C to get mixed metal oxides NPs.

8.3 Characterisation of Nano Particles and Nanoalloy

8.3.1 Scanning Electron Microscopy (SEM)

Microstructure morphology of nano-particles were studied under scanning electron microscope tool Zeiss (MA EVO-18 Special Edition) at Amity Institute of Advanced Research and Studies.

The molecules of copper oxide nano particles were found to be spherical in shape with size distribution of 66.6 nm as shown in Fig. 8.1. Some nanotubes have also formed, which is due to lower calcination temperature.

The molecules of iron oxide nano-particles were found to be spherical in shape with size distribution of 42.3 nm using scanning electron microscope tool JEOL MAKE (UK) MODEL-JSM6360 as shown in Fig. 8.2.

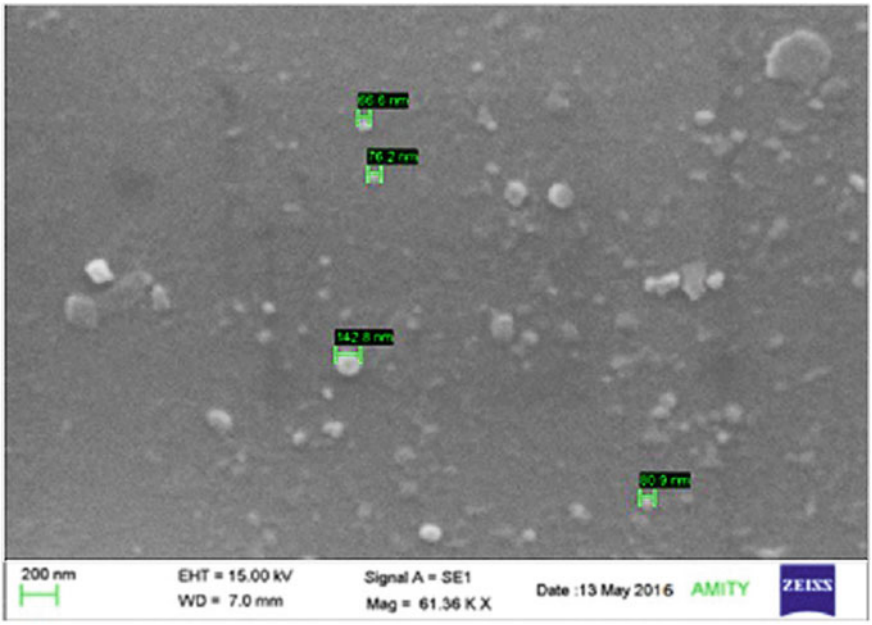

Fig. 8.1 SEM image for copper oxide NPs

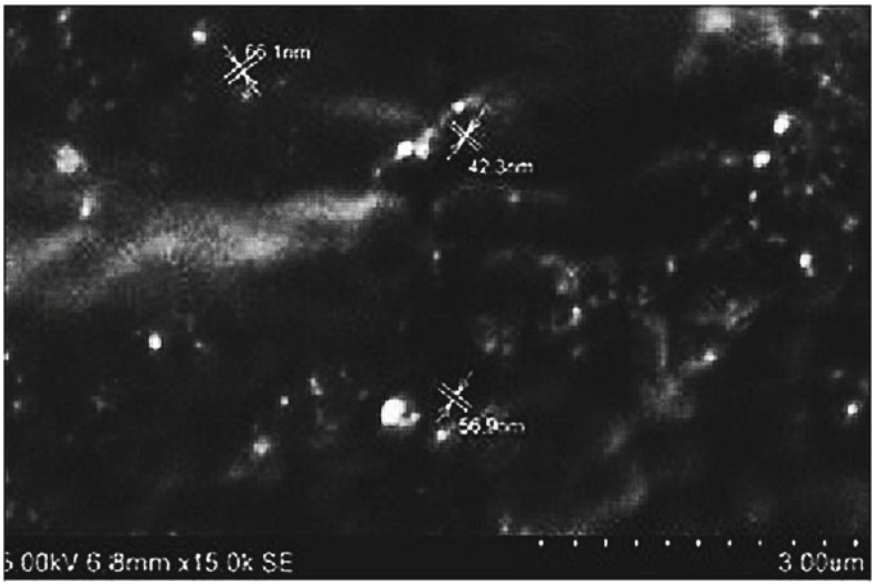

Fig. 8.2 SEM image for iron oxide NPs

The molecules of aluminium oxide nano particles were found to be spherical in shape with the size distribution of 26.67 nm using scanning electron microscope tool JEOL MAKE (UK) MODEL-JSM6360 as shown in Fig. 8.3.

The molecules of metallic nano alloy Fe_2O_3–Al_2O_3–CuO were found to be spiral in shape with the size distribution of 200 nm using scanning electron microscope tool Zeiss (MA EVO-18 Special Edition) as shown in Fig. 8.4.

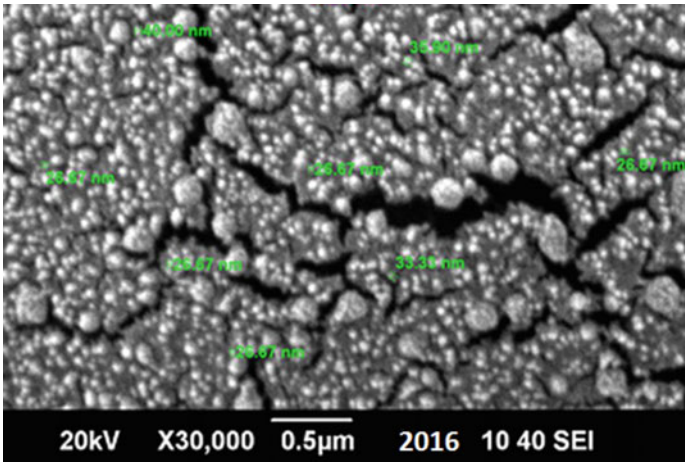

Fig. 8.3 SEM image for aluminium oxide NPs

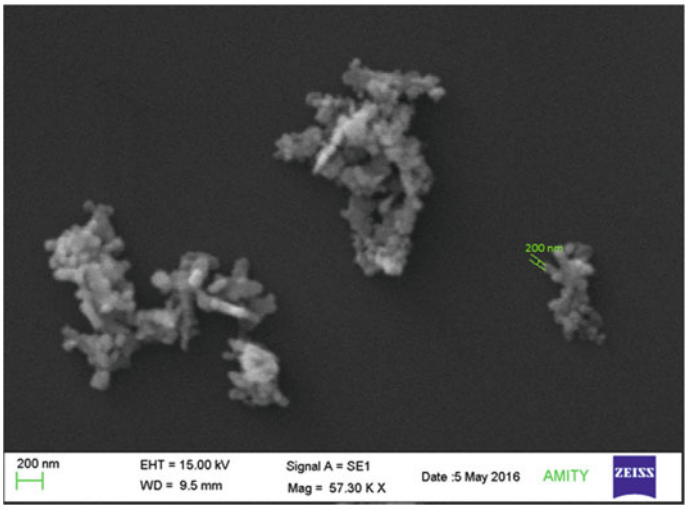

Fig. 8.4 SEM image for Fe_2O_3–Al_2O_3–CuO nano alloy

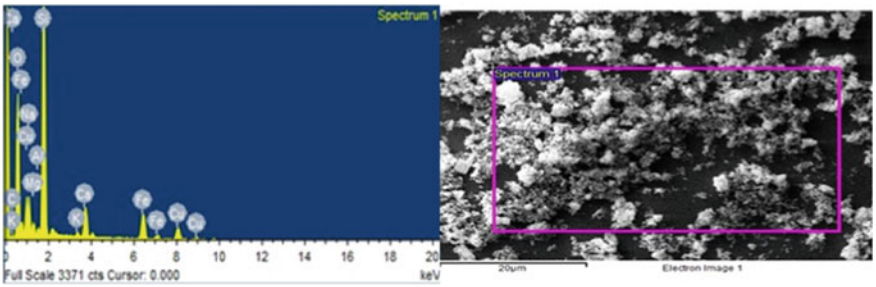

Fig. 8.5 EDX image for Fe_2O_3–Al_2O_3–CuO nano alloy

8.3.2 Energy Dispersive X-Ray Analyser

Energy-dispersive X-ray spectroscopy (EDX), is an analytical technique used for the elemental analysis or chemical characterization of a sample.

Figure 8.5 shows the EDX analysis of Fe_2O_3–Al_2O_3–CuO nano alloy annealed at 500 °C. Results revealed the presence of copper (Cu), aluminium (Al), iron (Fe), oxide (O) elements in metallic nanoalloy and the data indicated that nano particles were nearly stoichiometric. Weight percent of copper (Cu), aluminium (Al), iron (Fe), oxide(O) were calculated using EDX analysis as Cu: 7.43%, Fe: 8.27%, Al: 0.49% and O: 44.47%, respectively. The reaction for synthesis was carried out in $CaCl_2$-Tris buffer, therefore there is a presence of Ca_2^+ ions in the EDX analysis. Traces of Ca might be present but it is not the main composition of the alloy. There were no other elemental impurities in the EDX spectra. The EDX result showed presence of all constituent elements in nano alloy and thus confirms formation of nano alloy of copper, iron and alumina.

8.3.3 Fourier Transform Infrared Spectroscopy (FTIR)

FTIR is a method for measuring all the infrared frequencies simultaneously, rather than individually. Fourier Transformation FT-IR spectrum is measured by the tool IR-Prestige-21 make Japan Shimatzu.

Figure 8.6 shows the FT-IR spectra of oxide product CuO nanoparticles. Peaks are obtained at 3579.6, 3384, 1089.5, 871.9, 597 and 481.6 cm^{-1}. First two peaks obtained in above spectra are for organic compound (glacial acetic acid) which was used in small amount during synthesis. Last three peaks represent CuO stretching frequency.

Figure 8.7 shows the FT-IR spectra of Iron Oxide NPs. Peaks are obtained at 3399.42, 1626.24, 1400.65, 633.91 and 559.10 cm^{-1}. First peak obtained in above spectra are for organic compound (liquor ammonia), which was used in small amount

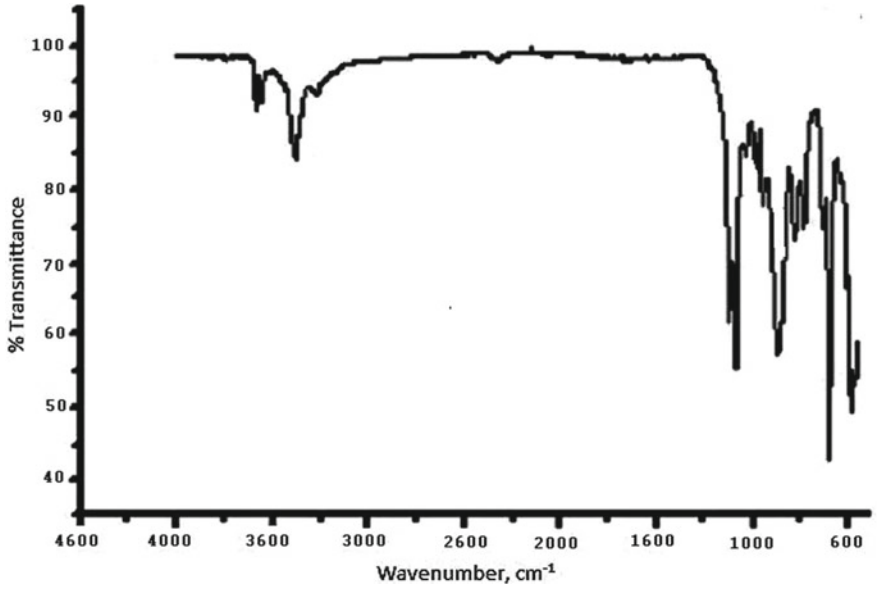

Fig. 8.6 FTIR spectra of copper oxide NPs

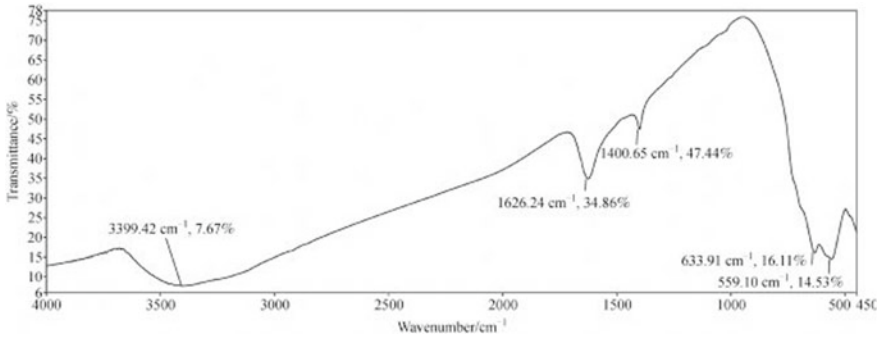

Fig. 8.7 FTIR spectra of iron oxide NPs

during synthesis. Next peak shows the presence of alkene. Last three peaks show presence of iron oxide in it.

Figure 8.8 shows the FT-IR spectra of Aluminium oxide NPs. Peaks are obtained at 3500.42, 1626.24, 859.10 and 660.210 cm^{-1}. First peak obtained in above spectra are for organic compound (polyethylene glycol) which was used in small amount during synthesis. Next peak shows presence of amide group and last two peaks show presence of aluminium oxide in it.

Figure 8.9 shows FT-IR spectra of Fe_2O_3–Al_2O_3–CuO nano-alloy. Peaks are obtained at 3584.75, 3488, 2346.98, 1637.08, 1540.38, 1122.86, 990, 886.23, 552.90

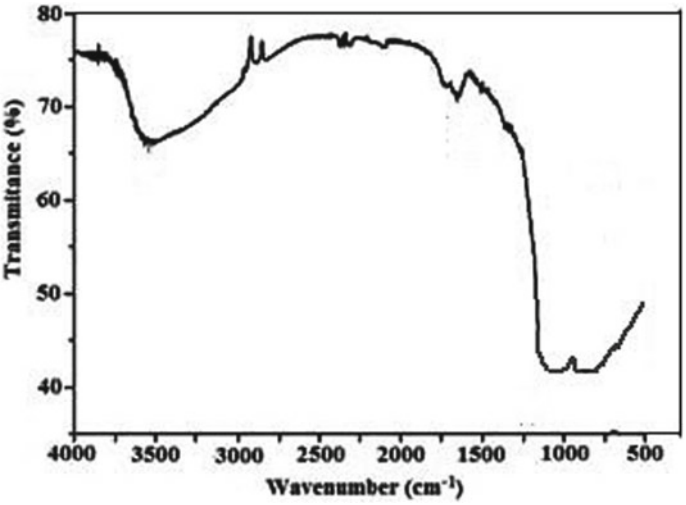

Fig. 8.8 FTIR spectra of aluminium oxide NPs

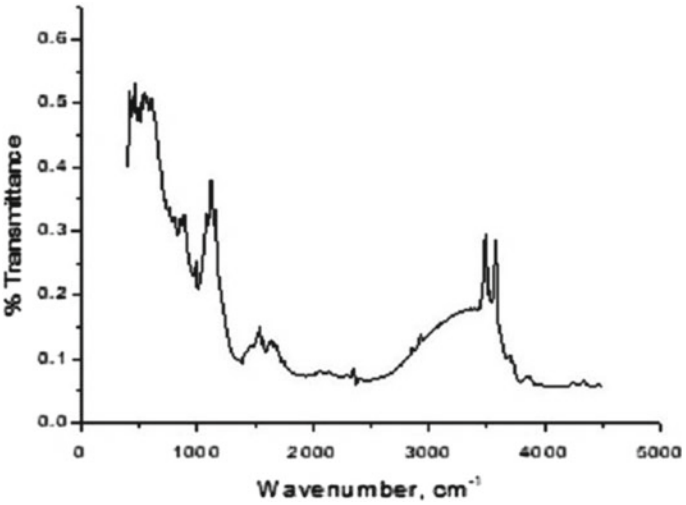

Fig. 8.9 FTIR spectra of Fe_2O_3–Al_2O_3–CuO nanoalloy

and 455.06 cm^{-1}. First two peaks obtained in above spectra are for organic compound (liquor ammonia) which was used in small amount during synthesis. Next peak shows presence of carbon dioxide. Fourth peak shows presence of amide group and seventh peak shows the presence of ethylene. Last three peaks show presence of aluminium oxide, copper oxide and iron oxide.

8.3.4 Thermal Analysis

8.3.4.1 Thermo Gravimetric Analysis (TGA)

TGA of CuO NPs

In TGA of CuO NPs, variation of temperature is taken from 25 to 1000 °C as shown in Fig. 8.10 wherein weight loss from 25 to 450 °C is 10%, weight loss from 500 to 700 °C is 14% and from 700 to 950 °C is 10%. The first weight loss is due to surface absorbed water and second weight loss from 500 to 700 °C is due to volatilization and combustion of glacial acetic acid, third weight loss is due to decomposition of prepared sample. Further parallel line shows stability of copper oxide nano particles. There is no associated signal further which confirms crystallization and phase transition events of copper oxide nano particles.

TGA of Iron Oxide NPs

In TGA of Iron oxide NPs, variation of temperature is taken from 35 to 1000 °C as shown in Fig. 8.11, wherein weight loss from 35 to 300 °C is 15%, weight loss from 400 to 800 °C is 1% and from 800 to 1009 °C is 1%. The first weight loss is due to surface absorbed water, second weight loss is due to volatilization and combustion of liquid ammonia and finally due to decomposition of prepared sample. Further parallel line shows high stability of iron oxide nano particles. There is no associated signal confirming crystallization and phase transition events of iron oxide nano particles.

TGA of Aluminium Oxide NPs

In TGA of Aluminium oxide NPs variation of temperature is considered from 25 to 1000 °C as shown in Fig. 8.12. Weight loss from 25 to 300 °C is 23%, weight loss from 300 to 600 °C is 12% and from 600 to 1000 °C is 2%. The first weight loss is due to surface absorbed water, second weight loss from 500 to 700 °C is due to volatilization

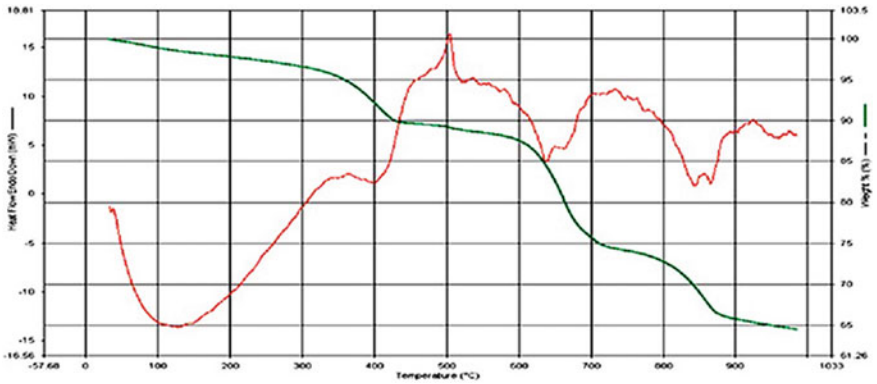

Fig. 8.10 TGA of copper oxide NPs

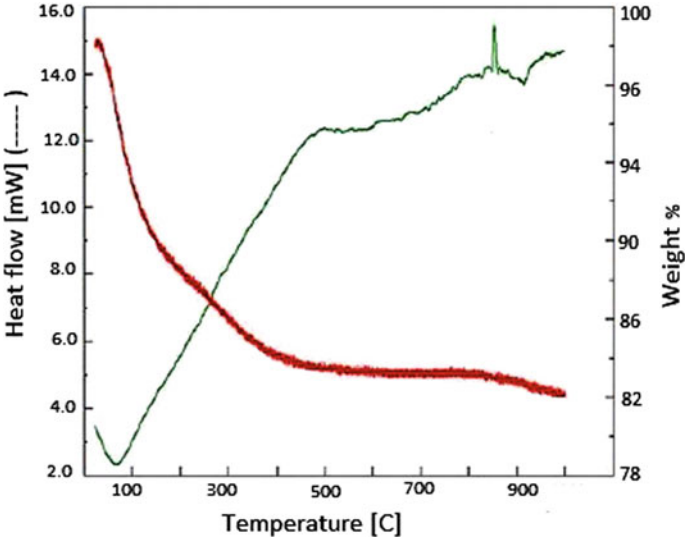

Fig. 8.11 TGA curve of iron oxide NPs

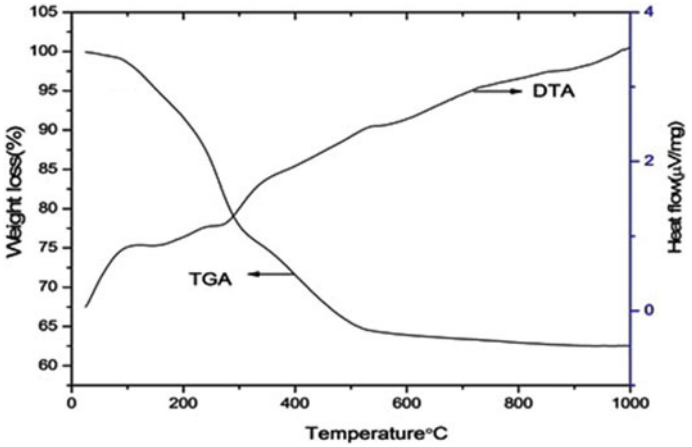

Fig. 8.12 TGA curve of aluminum oxide NPs

and combustion of poly ethylene glycol and finally due to decomposition of prepared sample. Further parallel line shows stability of aluminium oxide nano particles.

TGA of Fe_2O_3–Al_2O_3–CuO Nanoalloy

In TGA of Fe_2O_3–Al_2O_3–CuO nanoalloy, variation of temperature is considered from 25 to 1000 °C as shown in Fig. 8.13. The weight loss from 25 to 450 °C is 7.5%, weight loss from 500 to 700 °C is 12% and from 700 to 950 °C is 12%. The first weight loss is due to surface absorbed water; weight loss from 500 to

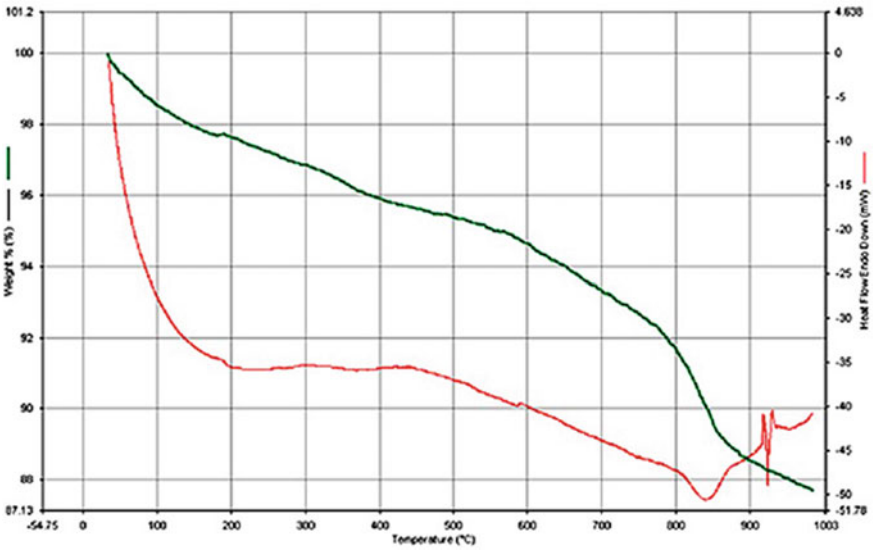

Fig. 8.13 TGA curve of Fe_2O_3–Al_2O_3–CuO nanoalloy

700 °C is due to volatilization and combustion of glacial acetic acid and polyethylene glycol and finally due to decomposition of prepared sample. There is no associated signal further which confirms crystallization and phase transition events of metallic nanoalloy particles.

8.3.4.2 Thermal Conductivity

Thermal properties of the constituent metal oxides were studied and are tabulated in Table 8.1.

In order to measure thermal conductivity of nanofluids, a prototype of thermal conductivity meter was designed and fabricated based on cylindrical cell method [17]. The equipment (shown in Fig. 8.14) consists of two coaxial cylinders made of steel. The outer surface of the equipment is covered with a layer of rock wool and wood dust to reduce heat loss from outer surface. The assembly is placed inside a thermocol box. Inner cylinder is filled with Test fluid and outer cylinder is filled with cooling water. Test fluid is heated using an electrical heater. It is assumed that heat

Table 8.1 Thermal property of metal oxides

Properties	CuO	Iron oxide	Alumina
Melting point, °C	1201	1590	2072
Boiling point, °C	2000	2623	2977
Thermal conductivity, W/mK	20	7.9	30

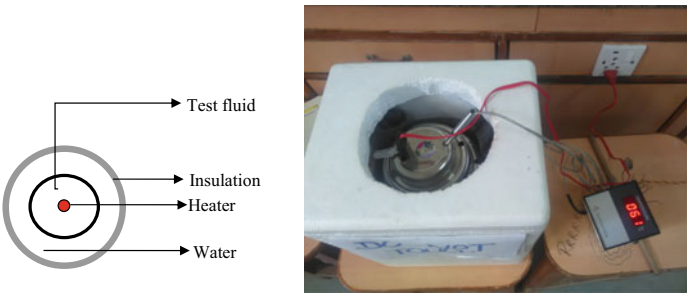

Fig. 8.14 Prototype of thermal conductivity meter

flows in outward radial direction through the test liquid, filled in annular gap, to the cooling water. Two calibrated Fe–Constantan thermocouples are used to measure outer and inner surface temperature of inner cylinder (T_i and T_o respectively). The thermocouples are positioned in the middle of test section and connected to a digital display. Temperatures T_i and T_o, voltage and current of the heater were measured during the test period for different temperature of test fluid.

Using Fourier's equation in cylindrical coordinates, thermal conductivity of nanofluid is calculated by the following equation [17]:

$$k = \frac{\ln\left(\frac{r_2}{r_1}\right)}{2\pi L\left[\left(\frac{\Delta T}{\dot{Q}_e}\right) - \ln\left(\frac{r_3}{r_2}\right)/2\pi L k_c\right]} \tag{1}$$

where $\dot{Q}_e$ is heat input [W] which is calculated by multiplying current and voltage of the heater, $\Delta T = T_\mathrm{i} - T_\mathrm{o}$ is temperature difference between outer and inner surface temperature of the inner cylinder, k_c is thermal conductivity of stainless steel [W/mK], L is length of cylinders [m], r_1 is outer radius of the inner cylinder containing heater [m], and r_2, r_3 are inner and outer radius of the outer cylinder respectively [m].

In order to check the accuracy of measuring instrument, thermal conductivity of water was first computed experimentally using the fabricated instrument. An absolute percentage error of 2.1% has observed between experimentally obtained and actual thermal conductivity of water as shown in Fig. 8.15. Difference in experimental and actual conductivity maybe due to various reasons like heat flow may occur along radial direction and as well as along the length of the cylinder which may be because of temperature gradient in test fluid as well as in cooling water; secondly there may be heat losses occurring from top where holes were made to insert thermocouples and heater and finally due to human error in measuring temperature and radius of cylinders.

Nano-fluid was prepared with various concentrations (0.1–0.4 wt%) of Fe_2O_3–Al_2O_3–CuO nano-alloy in the base fluid (water). Experiment was conducted using the

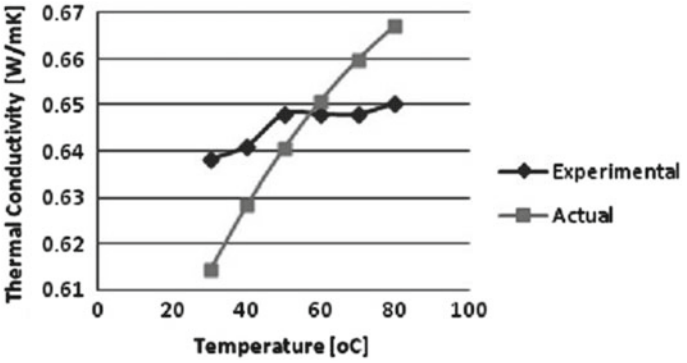

Fig. 8.15 Thermal conductivity of water

fabricated instrument by taking nano-fluid as test fluid to calculate thermal conductivity of nano-fluid at different temperatures say 30, 40 and 80 °C. First nano-fluid was heated to raise its temperature to desired temperature and is maintained at the same temperature during experimental period by occasional heating. The change in temperature of nano-fluid during heating was recorded at an interval of 2 min. Once nano-fluid attains desired temperature, outer cylinder was filled with cold water and then inner and outer surface temperature of inner cylinder was measured and recorded. In order to calculate thermal conductivity of nano-fluid at different temperatures, the experiment was repeated for different temperature of the nano-fluid. Similar set of experiments were performed for each concentration of Fe_2O_3–Al_2O_3–CuO nano-alloy in water.

For each concentration of nano-alloy in water, six sets of experiments were performed. It was observed that after a few sets of experimentation, nano-particles got deposited on inner wall of the cylinder containing test fluid which could not be removed completely by manual scraping. This led to unusual temperature patterns in nano-fluids; making it impossible to evaluate thermal conductivity of the test fluid.

However, it was observed that temperature of nano-fluid increased rapidly on heating and took less time to reach desired temperature compared to water without nano-alloy as shown in Fig. 8.16. Rate of change of temperature (dT/dt) of nano-fluid increased with increase in concentration of nano-alloy in water. It was observed that there was no considerable increase in dT/dt for concentration of 0.1 wt% NPs; dT/dt increased by 8.3% for concentration of 0.2 wt% NPs in water whereas it increased by 62% for concentration of 0.4 wt% NPs in water. Thus, it can be concluded that addition of nano-alloy in water enhances heat transfer characteristic of water.

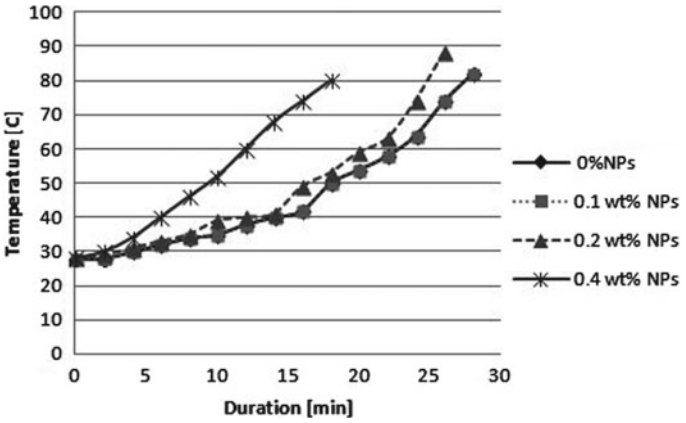

Fig. 8.16 Change in temperature of nano fluids with different concentration of nano-alloy with respect to time

8.4 Conclusions

CuO, Al_2O_3, Fe_2O_3 and Fe_2O_3–Al_2O_3–CuO NPs were synthesised by co-precipitation method because of its simple methodology which does not require usage of expensive equipments. The molecules of metallic nano-alloy were found to be spiral in shape with size distribution of 200 nm. FTIR confirms the presence of liquor ammonia, carbon dioxide, ethylene and metal oxides of aluminium, copper and iron in the nano-alloy. Although aluminium oxide and iron oxide NPs were found to be stable at temperature ranging from 700–1000 °C, significant weight loss is observed for CuO and Fe_2O_3–Al_2O_3–CuO NPs over the entire temperature range 25–1000 °C. The nano-alloy thus synthesised was not stable at higher temperature.

However, significant increase in heat transfer characteristic has been observed by adding nano-alloy to the base fluid (water) which increased with the increase in concentration of NPs. Thus, it can be concluded that Fe_2O_3–Al_2O_3–CuO nano-alloy when added to water increases its thermal conductivity.

Acknowledgements The authors acknowledge the support provided by Amity Institute of Advanced Research and Studies, Jadavpur University and Jawaharlal Nehru University instrumental facility for conducting sample characterization.

References

1. K.K. Chattopadhyay, A.N. Banerjee, Introduction to Nanoscience and Nanotechnology. PHI Learnings Pvt Ltd. Chap 1, pp 1–5 (2009)
2. A. Mahapatra, Fabrication and characterization of novel iron oxide/alumina nanomaterials for environmental applications. PhD Thesis, NIT Rourkela, Odisha, India (2013)

3. K. Nithya, P. Yuvasree, N. Neelakandeswari, N. Rajasekaran, K. Uthayarani, M. Chitra, S. Sathiesh Kumar, Preparation and characterization of copper oxide nanoparticles. Int. J. Chem. Tech. Res. **6**(3), 2220–2222 (2014)
4. N. Bader, A.A. Benkhayal, B. Zimmermann, Co precipitation as a sample preparation technique for trace element analysis: an overview. Int. J. Chem. Sci. **12**(2), 519–525 (2014)
5. M.S. Pudovkin, P.V. Zelenikhin, V. Shtyreva, O.A. Morozov, D.A. Koryakovtseva, V.V. Pavlov, Y.N. Osin, V.G. Evtugyn, A.A. Akhmadeev, A.S. Nizamutdinov, V.V. Semashko, Coprecipitation method of synthesis, characterization, and cytotoxicity of Pr3+: LaF3 (CPr = 3, 7, 12, 20, 30%) nanoparticles. Hindawi. J. Nanotechnol. **2018**, 9 (2018)
6. H. Wang, X. Xu, J. Zhang, C. Li, A cost-effective co-precipitation method for synthesizing indium tin oxide nanoparticles without chlorine contamination. J. Mater. Sci. Tech. **26**(11), 1037–1040 (2010)
7. M. Fernández-Garcia, J.A. Rodriguez, Metal oxide nanoparticles inorganic and bioinorganic perspectives nanomaterials (2007)
8. B.W. Ahn, T.J. Kang, Preparation and characterization of magnetic nanofibers with iron oxide nanoparticles and poly (ethylene terephthalate). J. Appl. Polym. Sci. **125**, 1567–1575 (2012)
9. M. Waseem, S. Munsif, U. Rashid, Imad-ud-Din, Physical properties of a-Fe_2O_3 nanoparticles fabricated by modified hydrolysis technique. Appl. Nanosci. (2013)
10. A. Barrañón (ed) (2009) Study of the properties of iron oxide nanostructures (Chap. 17). In: Research in nanotechnology developments. Nova Science Publishers
11. G. Mustafa, H. Tahir, M. Sultan, N. Akhtar, Synthesis and characterization of cupric oxide (CuO) nanoparticles and their application for the removal of dyes. Afr. J. Biotech. **12**(47), 6650–6660 (2013)
12. Z. Guo, X. Liang, T. Pereira, R. Scaffaro, H.T. Hahn, CuO nanoparticle filled vinyl-ester resin nanocomposites: fabrication, characterization and property analysis. Compos. Sci. Tech. **67**, 2036–2044 (2007)
13. S.U.S. Choi, J.A. Eastman, Enhancing thermal conductivity of fluids with nanoparticles. In: ASME International Mechanical Engineering Congress and Exposition, San Francisco, CA, 12–17 Nov 1995
14. S. Senthilraja, K. Vijayakumar, R. Gangadevi, A comparative study on thermal conductivity of Al_2O_3/water, CuO/Water and Al_2O_3–CuO/water nanofluids. Digest J. Nanomater. Biostruct. **10**(4), 1449–1458 (2015)
15. L. Qiang, X. Yimin, Convective heat transfer and flow characteristics of Cu-water nanofluid. Sci. China **45**(4), 408–416 (2002)
16. L. Vayssieres, On the thermodynamic stability of metal oxide nanoparticles in aqueous solutions. Int. J. Nanotechnol. **2**(4), 411–439 (2005)
17. G. Paul, M. Chopkar, I. Manna, P.K. Das, Techniques for measuring the thermal conductivity of nanofluids: a review. Renew. Sustain. Energy Rev. **14**, 1913–1924 (2010)

Chapter 9
Liquid Crystal-Based Biosensor to Detect Plant Pathogen

Ariba Parveen and Jai Prakash

Abstract This work demonstrates the specific sensing of plant-pathogen by using a nematic liquid crystal (NLC) material. Nowadays, plant-pathogen is the main component for lowering crop production, hence its detection is a major concern in food safety and quality purposes. The recent developments of liquid crystal (LC) materials have been remarkable in the application of advanced LC biosensors. The director alignment is so sensitive at the interface hence the binding event is amplified in the presence of this LC material which can be easily observed through dielectric and electro-optical spectroscopy. Here, we design a LC-based biosensor for the detection of biological hazards in food and agricultural sectors which directly affect the lifestyle of a human being. Plant infections are caused by different pathogenic microorganisms such as fungi, bacteria, viruses and nematodes. Nematodes are the plant-parasitic roundworms, microscopic, free-living in soil or water and create severe infection in plants and animals. This work illustrates the role of LC for sensing Root-knot nematodes (*Meloidogyne* species) affected disease in cowpea (*Vigna unguiculata*) plant and the sensing occurs due to realignment in LC material. This analysis was done through electro-optical measurements and dielectric spectroscopic techniques. Thus, there are several applications of LCs which offer an easy way to fabricate portable biosensors apart from their display applications. This type of sensor provides the fastest response and increases the sensitivity for advancement in diagnostics of various severe diseases.

9.1 Introduction

Most biological phenomena occur near room temperature and fluctuate near or far from the equilibrium. The soft matter physics tries to relate this gap between equilibrium and out-of-equilibrium physics through certain principles. The example of this soft matter includes liquid crystal (LC) materials which exhibit properties associated with both crystalline solids as well as isotropic liquids [1]. The LCs are the most

A. Parveen · J. Prakash (✉)
Department of Physics, Aligarh Muslim University, Aligarh 202002, India
e-mail: jpsphysics@gmail.com

V. K. Jain et al. (eds.), *Recent Trends in Materials and Devices*, Springer Proceedings in Physics 256, https://doi.org/10.1007/978-981-15-8625-5_9

remarkable and widely used materials due to high sensitivity of their alignment from the late nineteenth century after their discovery by Friedrich Richard Reinitzer and Otto Lehmann. A wide array of sensing application has been done by nematic LC (NLC) because of having long-range orientational order and their easily visualized response by interaction of external stimuli [2–5]. Abbott and co-workers in 1998 put their efforts in this area and design a LC based biosensor for detecting biomolecules [6].

Recently, scientists are concerned about early diagnose the rapid infectious diseases in plants [7–10] Different pathogens such as viruses, bacteria, nematodes serve as infectious agents and damage the crops or reduce its production [11, 12]. Nematodes are the plant-parasitic roundworms, free-living in soil or water and create severe diseases in plants as well as in animals. One of the most common pathogens of the nematode family is the root-knot nematodes (*Meloidogyne* species) which directly attack the roots of the plants [13]. These nematodes persuade gall swellings in diameter on plant roots and damage a wide variety of plants such as tomato, cucumber, watermelon etc. The morphology and physiology of the host plants are changed by such an organism [14]. Several *Meloidogyne* species have a wide host range on which it attacks and the process of plants to parasitism depends on the type of plants and cultivar.

In the present study, the plant-parasitic (root-knot) nematodes influence the host cowpea (*Vigna unguiculata*) plant. In the presence of these nematodes, the host plant resistance against the later remains not much effective. The host plant began to start destroying, particular rashes appear on the leaves and its growth is affected. Here, we present the preliminary results of a new biosensor to sense such plant-pathogen using NLC (biocompatible) material. The sensing mechanism has been verified through dielectric and electro-optical techniques. This type of sensor provides a faster response and increases the sensitivity for advancement in diagnostics.

9.2 Materials and Methods

For the experiments, the NLC namely ZLI-1565 was purchased from Sigma-Aldrich, U.S.A. and the sample cells (5 μm thick and 10 × 10 mm^2 effective area) were purchased from (Instec, Inc., USA). The cowpea (KSP-145) seeds were used for the host plant and the isolation of root-knot nematodes was done from brinjal roots in the area near Aligarh district during autumn (October 2019). The optical textures were recorded using 5 MP CCD digital camera attached to a Polarizing optical microscope (POM) (BX53-P, Olympus, Japan) and dielectric measurements were carried out with LCR meter (E4980A, Keysight, USA).

We have prepared two pots for the experiment and sowed the cowpea seeds after autoclaving the soil. When the proper germination is done, we incorporated 1000 nematodes in one pot and one fresh plant was taken as reference. After incorporating the nematodes on the host plant roots, it began to start damaging the plant. After

30 days, when the nematode-plant interactions were visually observed, we have taken the sample from both the pots.

The first sample was prepared with ZLI+ extract (fresh plant) and the second mixture was made by ZLI+ extract (nematode affected plant). All the process has been done at room temperature (i.e. 27 °C). The two mixtures and pure ZLI were filled separately in three sample cells of the same thickness through capillary action. The optical measurements for all the three samples have been done trough POM and the textural micrographs were recorded textural by the computer attached through a software. The dielectric parameters (i.e. dielectric permittivity, dielectric loss factor and dielectric loss) were measured in the frequency range of 20 Hz–2 MHz at a low oscillating voltage of 1 V.

9.3 Results and Discussion

Figure 9.1 illustrates the optical textures of different samples. The molecules of pure ZLI are visible under the crossed polarizer of the microscope (Fig. 9.1a). The presence of the molecules in the mixture of ZLI+ extract (fresh plant) cell is also confirmed through the texture observed under POM (Fig. 9.1b). The pattern/molecular structure

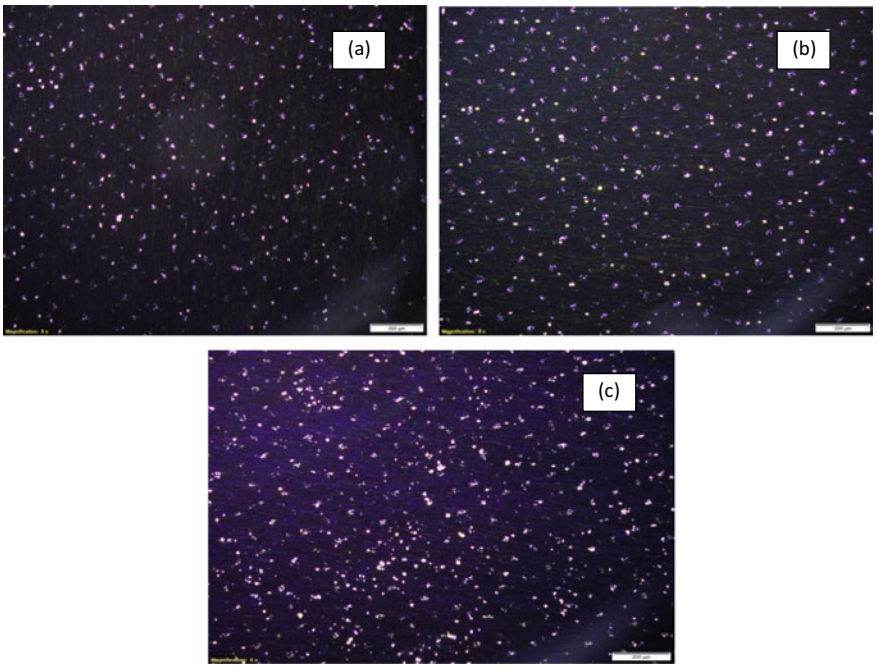

Fig. 9.1 Optical illustrations of molecules present in **a** pure ZLI, **b** ZLI + fresh plant and **c** ZLI + nematode affected plant; at room temperature

of the cell filled with ZLI + extract (nematode affected plant) has given in Fig. 9.1c. It has been clearly observed the molecules of the plants from the extract are present in the sample cells as all the three textures are not identical. In case of pure ZLI, the gaps between the molecules are very large which started reducing in ZLI + extract (fresh plant) and in case of ZLI + extract (nematode affected plant) we observed a disrupt texture showing the presence of molecules of infectious plant.

Following optical observations, the biosensor response is measured through dielectric measurements. Figure 9.2 shows the dielectric variation observed in the three sample cells at a very low oscillating voltage of 1 V and in a wide frequency range of 20 Hz–2 MHz. As reflected from Fig. 9.2a, the values of permittivity for pure ZLI and ZLI + extract (fresh plant) are almost same (i.e. ~4) but there is a sharp increase in its value (~62) as when we observed for ZLI + extract (infectious plant). Figure 9.2b shows the dielectric loss factor in which two small peaks are observed in case of both pure ZLI and ZLI + extract (fresh plant) but when we have calculated

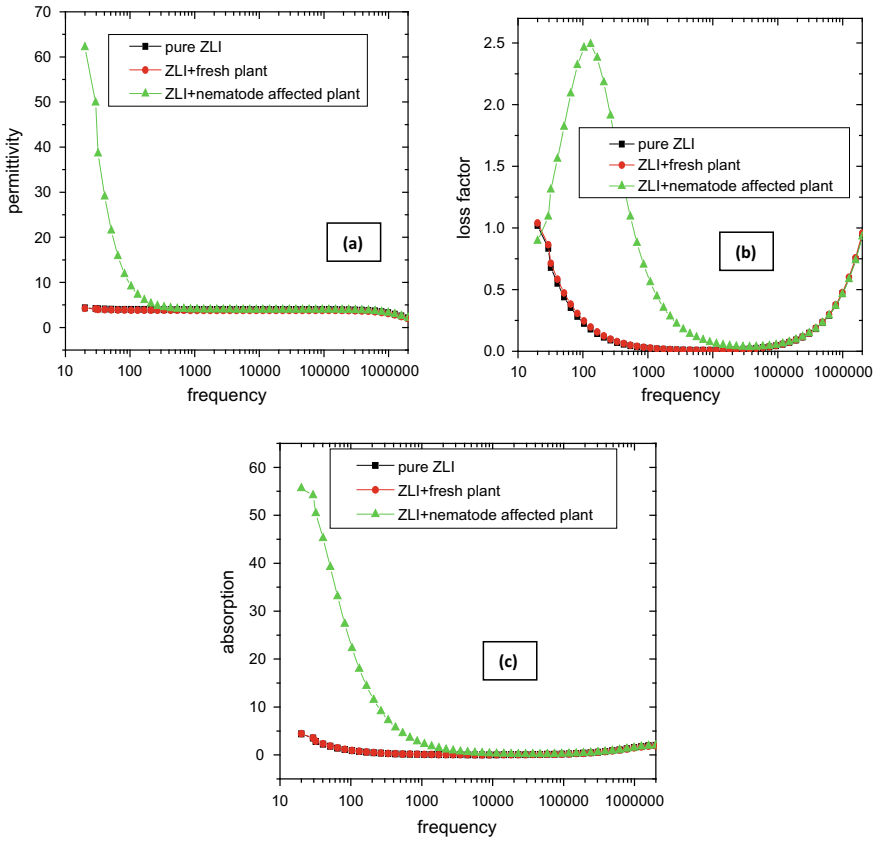

Fig. 9.2 Frequency dependence of **a** dielectric permittivity, **b** dielectric loss factor, **c** dielectric absorption for pure ZLI, ZLI with fresh plant and ZLI with nematode affected plant

the loss factor of the infectious sample, a higher peak is detected. The dielectric loss which indicates the energy dissipation in dielectric material is shown in Fig. 9.2c.

It is clearly observed that in case of ZLI + extract (fresh plant), the value of dielectric parameters (such as dielectric permittivity, dielectric loss factor and absorption) are same as pure ZLI while in case of the infected plant, there is a drastic change in the value of dielectric parameters. This is due to impurity ions produced in the chemical process involved in the infectious plant.

9.4 Conclusions

In conclusion, we demonstrate a NLC based biosensor to detect plant-pathogen in cowpea plant. The present work is based on the comparative measurement of affected plant concerning the fresh. This LC-based sensor is realized through the impurities created in the infectious plant induce some perturbation in the alignment of the LC. The limit of the detection of LC sensor has been studied experimentally through optical images under POM and dielectric measurements. This proposed method can be extended to sense other pathogens caused by different bacteria, fungi etc. and offer to design portable and label-free biosensors. This type of LC-based biosensor helps in the area of health care, food safety and quality purposes. LC-based biosensors are of low cost and will likely contribute to the identification of several new diseases and metabolites in plants and animals.

Acknowledgements Author (A. P.) is thankful to Atirah Tauseef for providing the extract of plants. One of the authors (J. P.) is grateful to the Department of Science and Technology (DST) for supporting this work under the Science and Engineering Research Board (SERB) funded EMR project (Project code: EMR/2016/006142).

References

1. P.J. Collings, *Liquid Crystals: Nature's Delicate Phase of Matter* (Princeton University Press, Princeton, 2002)
2. S. Chandrasekhar (Cambridge University Press, Cambridge, 1992). https://doi.org/10.1017/CBO9780511622496
3. M. Tyagi, A. Chandran, T. Joshi, J. Prakash, V.V. Agrawal, A.M. Biradar, Self assembled monolayer based liquid crystal biosensor for free cholesterol detection. Appl. Phys. Lett. **104**, 154104 (2014). https://doi.org/10.1063/1.4871704
4. P. Popov, E.K. Mann, A. Jákli, Thermotropic liquid crystal films for biosensors and beyond. J. Mater. Chem. B. **5**(26), 5061–5078 (2017). https://doi.org/10.1039/c7tb00809k
5. D. Needleman, Z. Dogic, Active matter at the interface between materials science and cell biology. Nature Rev. Mater. **2**, 17048 (2017). https://doi.org/10.1038/natrevmats.2017.48
6. V.K. Gupta, J.J. Skaife, T.B. Dubrovsky, N.L. Abbott, Optical amplification of ligand-receptor binding using liquid crystals. Science **279**(5359), 2077–2080 (1998). https://doi.org/10.1126/science.279.5359.2077

7. M. Khan, A.R. Khan, J.-H. Shin, S.-Y. Park, A liquid-crystal-based DNA biosensor for pathogen detection. Scientific Reports **6**, 22676 (2016). https://doi.org/10.1038/srep22676
8. G. Papadakis, N. Skandalis, A. Dimopoulou, P. Glynos, E. Gizeli, Bacteria murmur: application of an acoustic biosensor for plant pathogen detection. PLoS ONE **10**(7), 1–11 (2015). https://doi.org/10.1371/journal.pone.0132773
9. J. Beyond, Mater. Chem. B **5**, 5061–5078 (2017). https://doi.org/10.1039/C7TB00809K
10. E. Sentürk, S. Aktop, P. Sanlibaba, B.U. Tezel, Biosensors: a novel approach to detect food-borne pathogens. Appl. Microbiol. Open Access **4**, 1–8 (2018). https://doi.org/10.4172/2471-9315.1000151
11. M. Khater, A. Escosura-Muniz, A. de la Merkoci, Biosensors for plant pathogen detection. Biosens. Bioelectron. **93**: 72–86 (2017). https://doi.org/10.1016/j.bios.2016.09.091
12. Y. Fang, R.P. Ramasamy, Current and prospective methods for plant disease detection. Biosensors **4**, 537–561 (2015). https://doi.org/10.3390/bios5030537
13. W. Ye, R.T. Robbins, T. Kirkpatrick, Molecular characterization of root-knot nematodes (Meloidogyne spp.) from Arkansas, USA. Sci. Rep. **9**, 1 (2019). https://doi.org/10.1038/s41598-019-52118-4.
14. V.M. Williamson, C.A. Gleason, Plant–nematode interactions. Curr. Opin. Plant Biol. **6**(4), 327–333 (2003). https://doi.org/10.1016/s1369-5266(03)00059-1

Chapter 10
Synthesis and Characterization of GaO(OH)–FeO(OH) Nanorod Composite Prepared via Hydrothermal Method

Kavita Sharma, Isha Katyal, Alok Kumar Srivastava, V. Raghavendra Reddy, and Ajay Gupta

Abstract Nanorods of GaO(OH)–FeO(OH) composites are synthesized using green hydrothermal synthesis route. The prepared oxyhydroxide nanorods were characterized using X ray diffraction, Scanning Electron Microscopy, and low temperature (5 K) high magnetic field (5 T) Mossbauer spectroscopy. It is observed that hydrothermal synthesis route yields phase pure nanorods with crystallite size in nano-regime. Morphology is homogenous and non-agglomerating. From Mossbauer analysis, different iron sites with +3 oxidation state and high magnetic anisotropy are evident.

10.1 Introduction

Ceramic based nanomaterials such as metal oxide thin films and nanoparticles with ultrahigh surface area, low cost, and unique properties finds extensive application in gas sensors, electrochemical sensors, rechargeable electrodes, wide band gap semiconductors etc. [1]. In the past decades, researchers are focusing on miniaturization of these oxide materials owing to potential incorporation of multiple functions into a miniaturized device added with other functional merits [2]. However conventional nanoparticulate structures such as thin/thick films are usually unstable and tend to aggregate at higher temperature. The aggregation of active materials results in reduction of the accessible surface area for participating reactions, which in turn decrease their activities [3]. In this context, 1D structures could provide various benefits from

K. Sharma (✉) · I. Katyal · A. Gupta
Amity Center for Spintronic Materials, Amity University UP, Sector 125, Noida 201313, India
e-mail: ksharma4@amity.edu

A. K. Srivastava
Defence Materials and Stores Research and Development Establishment, Kanpur 208013, India

V. Raghavendra Reddy
UGC-DAE Consortium for Scientific Research, University Campus, Khandwa Road, Indore 452001, India

V. K. Jain et al. (eds.), *Recent Trends in Materials and Devices*, Springer Proceedings in Physics 256, https://doi.org/10.1007/978-981-15-8625-5_10

application point of view, which is well highlighted in literature for example Gallium oxide (Ga_2O_3) nanostructures have been realized as potential candidate for several applications such as catalysts, gas sensors, solar cells due to their wide band gap energy and good luminescence properties [4]. Similarly, iron oxide based nanostructures find extensive applications in water purification, biomedical applications such as MRI, lithium ion batteries, visible light photo catalytic activity etc. [4].

Nanostructure of these oxides can easily be obtained from the calcination of their respective nanostructured oxyhydroxides. These oxyhydroxides can be synthesized using various ways depicted in literature viz. sol–gel, hydrothermal synthesis, thermal evaporation, microwave assisted methods etc. [5]. However, large emphasis is given on green chemical processes that lead to minimization of generation waste. In this context, hydrothermal or hydro-solvothermal synthesis is the best choice owing to its uniqueness of obtaining crystalline substance from high temperature aqueous solutions at high vapor pressure. Due to the special advantage of highly controlled diffusivity of the reactants in a strong solvent media in the closed system, this technique is strongly preferred for the synthesis of nanostructured compounds [6]. Moreover this technique helps in processing monodispersed and highly homogeneous nanoparticles, and emerges as one of the most attractive techniques for processing nano composite materials. By controlling reaction parameters viz. concentration, reaction temperature, reaction time, etc., one can obtain different kinds of nanoarray structures for example nanorod, nano-wall, nanowire, ultrathin nanosheet, etc. of various metals oxides, metal hydroxide, mixed metals oxide, etc.) [7].

In the present work, we demonstrate the synthesis of GaO(OH)–FeO(OH) composite nanorods via hydrothermal synthesis. Since the atomic radii of Ga and Fe are close thus making a composite is expected to enhance the functional properties of individual oxide materials [8]. To the best of our knowledge this is the first report on synthesis of these composites using hydrothermal reaction route. The prepared composite samples are characterized by scanning electron microscopy (SEM), and x-ray diffraction (XRD) for morphological information and phase identification respectively. Low temperature (5 K) high magnetic field (5 T) Mossbauer spectroscopy measurements are also performed on the composite for magnetic investigations in the composites.

10.2 Experimental Details

Nanorods of GaO(OH)–FeO(OH) composite were synthesized using hydrothermal process. The details are as follows: 20 ml of deionized water was taken to which 5 ml of ethanol was added and stirred with magnetic stirrer. Subsequently 198.80 mg of $FeCl_2$ (purity 99.99%), 360 mg of urea, 255 mg of Gallium nitrate hydrate (purity 99.99%) and 106 mg of ammonium chloride were added. All the reagents used were of AR grade. The prepared solutions were directly transferred to a Teflon lined autoclave and maintained at 150 °C for 6 h. XRD measurement was done using Bruker D8 Advance diffractometer with Cu Kα radiation. Scanning Electron Microscope (SEM)

images were taken with a Supra 40 VP, Carl Zeiss, equipped with an energy dispersive X-ray micro analyzer (OXFORD EDAX). The ^{57}Fe Mossbauer measurements were carried out in transmission mode with a ^{57}Co (Rh) radioactive source in constant acceleration mode using a standard PC-based Mossbauer spectrometer equipped with a WissEl velocity drive. Velocity calibration of the spectrometer was carried out with a natural iron absorber at room temperature. For the low temperature high magnetic field measurements, the sample was placed inside a Janis superconducting magnet and an external field was applied parallel to the γ-ray (i.e., longitudinal geometry).

10.3 Results and Discussions

10.3.1 X Ray Diffraction (XRD)

The XRD patterns of as prepared composite is shown in Fig. 10.1. All the diffraction peaks of composite correspond to standard XRD pattern of FeO(OH) (JCPDS No. 81–0464) [9] and GaO(OH) (JCPDS No. 73–1028) [10].

Diffraction peaks are indexed to their respective Miller indices. It is observed that that these miller indices belong to space group Fddd with orthorhombic lattice structure of GaO(OH) and to space group Pbnm with orthorhombic lattice structure of FeO(OH). Sharp peaks are not present in XRD pattern of composite instead broad beaks are there indicating as prepared samples are having crystallite size in nanoregion. Crystallite size calculated using below Debye Scherrer formula

$$t = 0.9\lambda/\beta \ \cos\theta \tag{1}$$

where t is the mean size of ordered crystallite domain, β is the line broadening at half the maximum intensity (FWHM) of most intense reflection, θ is the Bragg angle of that reflection [11]. The calculated mean crystallite size comes out to be about 26 nm. Thus, from the XRD data one can conclude that the final product consists of composite of iron oxyhydroxide and gallium oxyhydroxide with no signature of any other phase. From EDAX measurements (not shown here) also Fe and Ga were found to be in equiatomic ration in the composite which is consistent with XRD results.

10.3.2 Scanning Electron Microscopy:

Morphology of the composite is a crucial factor that decides its performance therefore we have observed the morphology of prepared composite using SEM measurements. Figure 10.2 shows the SEM image of as prepared sample.

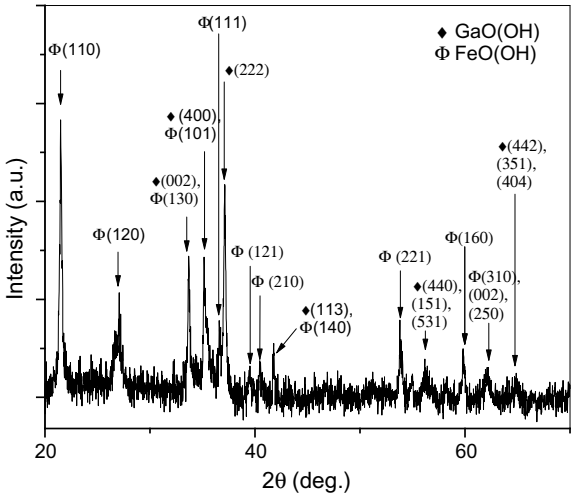

Fig. 10.1 Indexed XRD pattern of as prepared GaO(OH)–FeO(OH) composite. The peak corresponding to GaO(OH) are marked as "♦" while to FeO(OH) are marked as "ϕ"

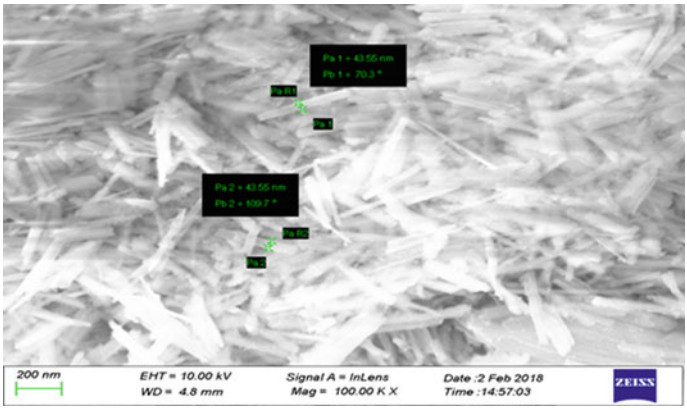

Fig. 10.2 SEM image of as prepared GaO(OH)–FeO(OH) composite

Recorded SEM image clearly show that morphology of the composite is homogeneous, with rod likes structures. The typical rod diameter is in the range of 43 nm and length in the range of 400 nm. This is to be noted that nanorods are non-agglomerating in nature and instead are well separated from each other which is desirable for their applications. Some of these nanorods are randomly oriented, while other are nanorods are sidewise parallel aligned with each other. Thus one can elucidate that hydrothermal synthesis leads in uniform rod like nanostructure of the prepared composite sample.

10.3.3 Low Temperature High Magnetic Field (LTHM) Mossbauer Spectroscopy

Figure 10.3a–c shows the Mossbauer spectra (MS) of composite recorded at 300 K, 5 K and 5 K, 5 T external magnetic field applied parallel to the γ-rays, i.e. longitudinal geometry. Using Mossbauer spectroscopy one can observe the true magnetic nature of the sample without perturbing the sample with any magnetic field which can be understood from following results. The observed paramagnetic doublet spectrum at

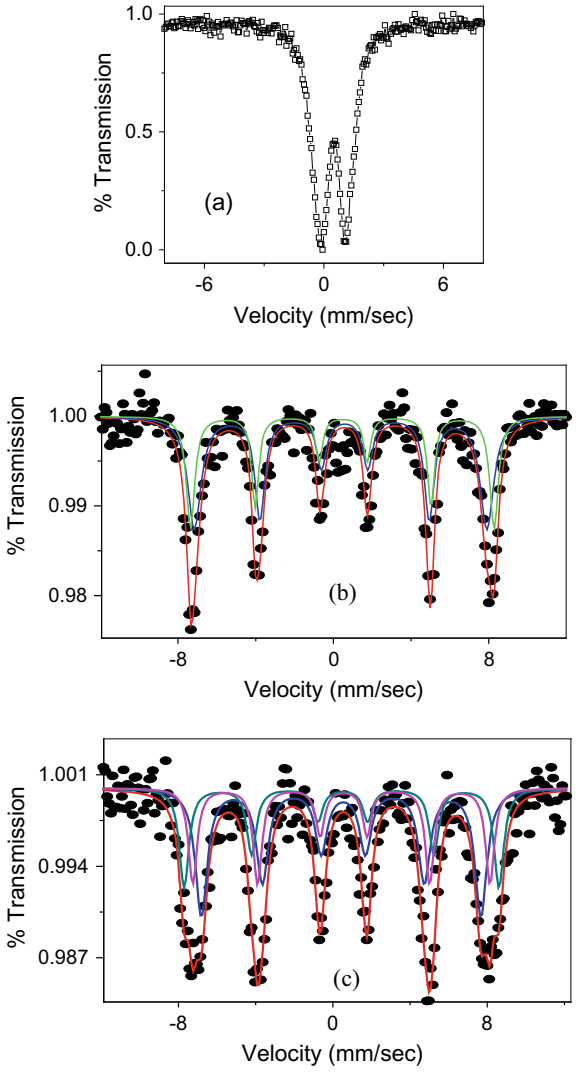

Fig. 10.3 Fitted Mossbauer spectra of GaO(OH)–FeO(OH) composite recorded at **a** room temperature, **b** 5 K, **c** 5 K, 5 T

Table 10.1 Hyperfine parameters with respect to natural iron obtained from the 5 T ^{57}Fe Mossbauer data. Isomer shift(mm/sec), Hyperfine field B_{hf}(Tesla), A_{23} area ratio of second and third lines in a sextet

Site	Fe1	Fe2	Fe3
Isomer shift	0.48 ± 0.01	0.48 ± 0.02	0.50 ± 0.02
B_{hf}	45.0 ± 0.20	50.0 ± 0.16	47.0 ± 0.25
A_{23}	1.5 ± 0.10	2	2

300 K corresponds to nonmagnetic nature of the composite. On cooling the composite down to 5 K a broad six line spectrum is observed that corresponds to magnetic nature of the sample. This is due to the fact that antiferromagnetic to paramagnetic transition in FeO(OH) lies below room temperature thus at 5 K internal magnetic hyperfine field (B_{hf}) is present which cause spitting of nuclear energy level and hence sextet is observed which is convolution of six line spectra corresponding to different sites of iron. This hyperfine field is not present at room temperature due to nonmagnetic nature of the sample and hence two-line spectrum is observed due to quadruple splitting [12].

On applying magnetic field of 5 T it is observed that the spectral lines broaden further. This is due to the fact that the composite has antiferromagnetic nature where spin of two sub lattices align antiparallel to each other. With the application of external magnetic field total internal field increases for the sub lattice which is parallel to the applied field and decreases for the sub-lattice which lies antiparallel to the applied field. The resultant spectra are the convolution of both the sites hence there is broadening in the spectra. Spectra have been fitted using NORMAS SITE program. The best fit to the data is obtained with 3 sextets with different hyperfine parameters that can be attributed to different sites of iron in iron oxy hydroxide. Fitting parameters are summarized in Table 10.1. From the obtained values of isomer shift, it can be elucidated that Fe is in +3 oxidation state in all three sites. Further, it may be noted that the intensity of the second and fifth lines (which correspond to $m = 0$ transition lines) is not zero in the high field which can be seen from no zero values of A_{23} in Table 10.1. This is due to the high magnetic anisotropy of the sample. The disappearance of the $m = 0$ lines depends on the anisotropy of the material and for systems with high anisotropy the disappearance requires very high fields [12] while low anisotropic systems are reported to be saturated at 1 T and hence these lines disappear at these applied fields. Presence of these lines up to high magnetic field of 5 T indicates high anisotropy in the composite which is consistent with the antiferromagnetic nature of the sample.

10.4 Conclusions

The hydrothermal synthesis and characterization of nanorods of GaO(OH)–FeO(OH) composite is reported. Nanostructure and phase purity of the composite is analyzed

from XRD data. Exclusive presence of GaO(OH)–FeO(OH) composite phase is also confirmed from X-ray diffraction analysis. Non agglomerating nanorods of uniform morphology with diameter of about 43 nm are observed from SEM measurements. Detailed low temperature high magnetic field Mossbauer measurements were performed. Mossbauer data revealed presence of three iron sites with +3 oxidation states and hyperfine field of 45, 50 and 47 T respectively and high magnetic anisotropy in the composite.

Acknowledgements KS, DST INSPIRE faculty thanks DST, New Delhi for financial assistance in the form of INSPIRE faculty award (DST/INSPIRE/04/2013/000772). The work was partly supported by CRS project No. CSR-IC/CRS-159.2015-16/16.

References

1. B. Zhang, P. Xian-Gao, Metal Oxide Chem. Sensors Rev. **6**, 55 (2019)
2. A.M. Soehartono et al. Miniaturized fluidic devices and their biophotonic applications. In: A.P. Ho, D. Kim, M. Somekh (eds) Handbook of Photonics for Biomedical Engineering (Springer, Dordrecht, 2016).
3. S.J. Pearton, J. Yang, P.H. Cary, F. Ren, J. Kim, M.J. Tadjer, M.A. Mastro, Appl. Phys. Rev. **5**, 011301 (2018); I. Angelov, S. Wiedmer, M. Evstatiev, K. Friedrich, G. Mennig Compos Part A, **38**(5), 1431–1438 (2007).
4. M. Mohapatra, S. Anand, Int. J. Eng. Sci. Techn. **2**, 127–146 (2010)
5. Yu. Quan, D. Fang, X. Zhang, S. Liu, K. Huang, Mater. Chem. Phys. **121**, 142–146 (2010)
6. M. Shandilya, R. Rai, J. Singh, Review: hydrothermal technology for smart materials. Adv. Appl. Ceram. (2016). https://doi.org/10.1080/17436753.2016.1157131
7. Q. Yang, Z. Lu, J. Liun, X. Lei, Z. Chang, L. Luo, X. Sun, Prog. Natur. Sci. Mater. Int. **23**, 351–366 (2013)
8. H. Ishizaki, N. Kijimaa, M. Yoshinaga, J. Akimoto, Key Eng. Mater. **566**, 119–122 (2013)
9. P. Viste, J. Galy, A. Potier, C.R. Seances, Acad. Sci. Ser. C, **277**, 159 (1953)
10. J.L.Hazemann, J.F. Berar, A. Manceau, Mater. Sci. Forum **79**, 821 (1991)
11. B.Ingham, M.F.Toney, Metallic films for electronic, optical and magnetic applications, structure, processing and properties, pp 3–38 (2014)
12. K. Sharma, V. Raghavendra Reddy, D. Kothari, A. Gupta, A. Banerjee, V.G. Sathe, J. Phys. Condens. Matter, **22**, 146005 (2010)

Chapter 11
Modelling and Analysis of Heat Waves for Excessive Heat Factor (EHF) Over Some Tropical Regions of India

Adarsh Kumar

Abstract Main key aspects of climate change are extreme climate and some unexpected, unpredictable or severe weather phenomenon which includes metrological parameters such as wind, cloud, rain, dust storms. Due to all these aspects, increase in temperature leads to severe effects of heat wave as it defines killer in diverse part of the world also known as silent disaster. Heat wave occurs when a system of high atmospheric pressure moves into an area, where air from upper level of our atmosphere is pulled towards the ground in such a high pressure system. At ground, it becomes compressed and increases in temperature. In this process, the temperature reaches at least 40 °C for plains and at least 30 °C for hilly regions. Sometimes increase in humidity also adds to this discomfort. So, whenever the maximum temperature in a day remains 40 °C or more and minimum temperature is 5° or more above the normal day temperature, then it may be defined as hot day. There are some estimated statistics of heat waves which includes excessive heat factor (EHF) and the 90th percentile. Heat wave lasts for several days and has large effects over globally and regionally due to their impacts on various sectors including health, agriculture, ecosystem and national economy. As in India day to day oscillation of pre-monsoon and daily maximum and minimum temperature have been studied, so this shows the result of past two decades that the frequency of hot days and nights shows increasing trends while cold days and night also shows decreasing trends. The main objective is to examine the heat wave behavior over the land surface region and conditions.

11.1 Introduction

The type, frequency and intensity of extreme events are expected to change as the Earth's climate changes, and such changes could occur even with relatively small mean climate changes [1]. As extreme weather events were expected to occur more frequently and become more intense, the socioeconomic costs of events are likely to

A. Kumar (✉)
Department of Physics, Amity Institute of Applied Sciences, Amity University, Noida 201313, UP, India
e-mail: akumar25@amity.edu

V. K. Jain et al. (eds.), *Recent Trends in Materials and Devices*, Springer Proceedings in Physics 256, https://doi.org/10.1007/978-981-15-8625-5_11

increase as well [2]. Heat waves (HWs) are one of the hazardous extreme temperature events [3, 4]. Extremes of heat waves have broad and far-reaching impacts, such as significant loss of life, health issues, and increased economic costs in transportation, agricultural production, energy and infrastructure [5–8].

In India, the HWs occur during the summer season months, March to June (MAMJ), mainly over north, northwest, central and the eastern coastal regions [9, 10]. HWs over India were known to be linked with the climate mode such as El-Niño-Southern Oscillation or ENSO [11, 12]. In the recent years, there is a noticeable increase in the frequency, persistency and spatial coverage of the HW days [13]. Studies indicate that HWs over India are associated with the anomalous sub-tropical persistent high with anti-cyclonic flow, depleted soil moisture over Indian land and with the SST anomalies over the tropical Indian and central Pacific Oceans [14, 15]. HWs can occur over the north-central India, which were associated with anomalous blocking over the North Atlantic Ocean [16] and also over the coastal eastern India [17]. Recent studies suggested that, HWs in India will become more frequent and populations are especially vulnerable to these extreme temperatures [18–21]. The frequency of concurrent day and night-time HWs in India has increased significantly in large part of western and southern parts during the post-1984 period [22]. Although there were many studies on the mechanisms and future projections of HWs, but very few studies have focused on the prediction of such events [23]. Considering the impacts of such events across various sectors of the society, including health, vegetation as well as agriculture and others, there is a need to develop new strategy for the real time monitoring and prediction of such silent disastrous events over Indian region [24, 25]. In the present work, heat wave analysis has been made utilizing excessive heat factor (EHF) containing maximum temperature data for the Indian territory for over 17 years covering 2000–2016.

11.2 Observations, Data and Methodology

Daily surface maximum temperature data for different stations of India were obtained from the National Data Centre (NDC), and Indian Meteorological Department (IMD), New Delhi for the time period of 2000–2016. The data provided by the NDC undergoes a series of robust quality control methods before archival [9], that includes manual checking of data manuscripts at designated data keying centers in IMD, and ensures the removal of doubtful values at the initial stages of processing. In addition, NDC subjects the data to further quality assessment/quality control measures to eliminate any spurious values [11–13]. Further information about the data collection and quality control of the station level data is available elsewhere [7]. As per IMD, there are four official seasons in India, namely winter (December, January and February), summer (March, April, and May), monsoon (June, July, August, and September), and post-monsoon (October, November). Each station was checked for missing data and other data discrepancies. Initial quality checks of the station level data revealed several stations with incomplete data [20]. The station distribution for each season

was checked for clustering, by applying the widely-used statistics nearest neighbor statistics [13]. It is calculated as the ratio between the observed mean distance among the stations and the expected mean distance for a random distribution. The resulting statistics showed a significantly dispersed pattern with less than a 1% likelihood of a random chance for each of the seasons [15]. Every daily maximum temperature inconsistency was inferred dependent on the day by day climatology [17]. The heat wave occasions are recognized utilizing the maximum temperature oddities fulfilling the criteria set by the IMD [7]. The spatial dissemination of the maximum temperature irregularities is checked for all the times of the occasion in order to fulfill the criteria of HW [13].

11.3 Results and Discussion

For computing the spatial conveyance of heat waves over India, day by day maximum temperature inconsistencies over every network point are standardized by their standard deviation [7]. A heat wave occasion is set to have happened at a network point if the standardized maximum temperature abnormalities are more noteworthy than one standard deviation for at least 6 days [18]. The Analysis of Grid and system of display graphs (Grads) is an intelligent work area instrument that is utilized for simple access, control, and perception of earth science information. Graduates have two information models for taking care of gridded and station information. Graduates bolsters numerous information document designs, including double (stream or successive), GRIB (rendition 1 and 2), Net CDF, HDF (form 4 and 5), and BUFR (for station information). Graduates have been executed worldwide on an assortment of usually utilized working frameworks and are openly disseminated over the Internet. The four customary measurements (longitude, scope, vertical level, and time) in addition to a discretionary fifth measurement for lattices that is commonly actualized however intended to be utilized for gatherings. Graduates grasp matrices that are normal, non-directly separated, Gaussian, or of variable goals. Information from various informational collections might be graphically overlaid, with right spatial and time enlistment. A good arrangement of inherent capacities is given, yet we can likewise include our own capacities as outside schedules which is written in any programming language. line and reference diagrams, dissipate plots, smoothed forms, concealed shapes, streamlines, wind vectors, network boxes, concealed lattice boxes, and station model plots. Illustrations might be yield in PostScript or picture groups. Graduates give geophysical natural defaults, yet we have the choice to control all parts of illustrations yield. Graduates have a programmable interface (scripting language) that takes into account complex investigation and show applications. Use contents to show catches and drop menus just as illustrations and after that make a move dependent on our point-and-snaps. Graduates can be kept running in clump mode, and the scripting language encourages utilizing Grads to do long medium-term cluster occupations.

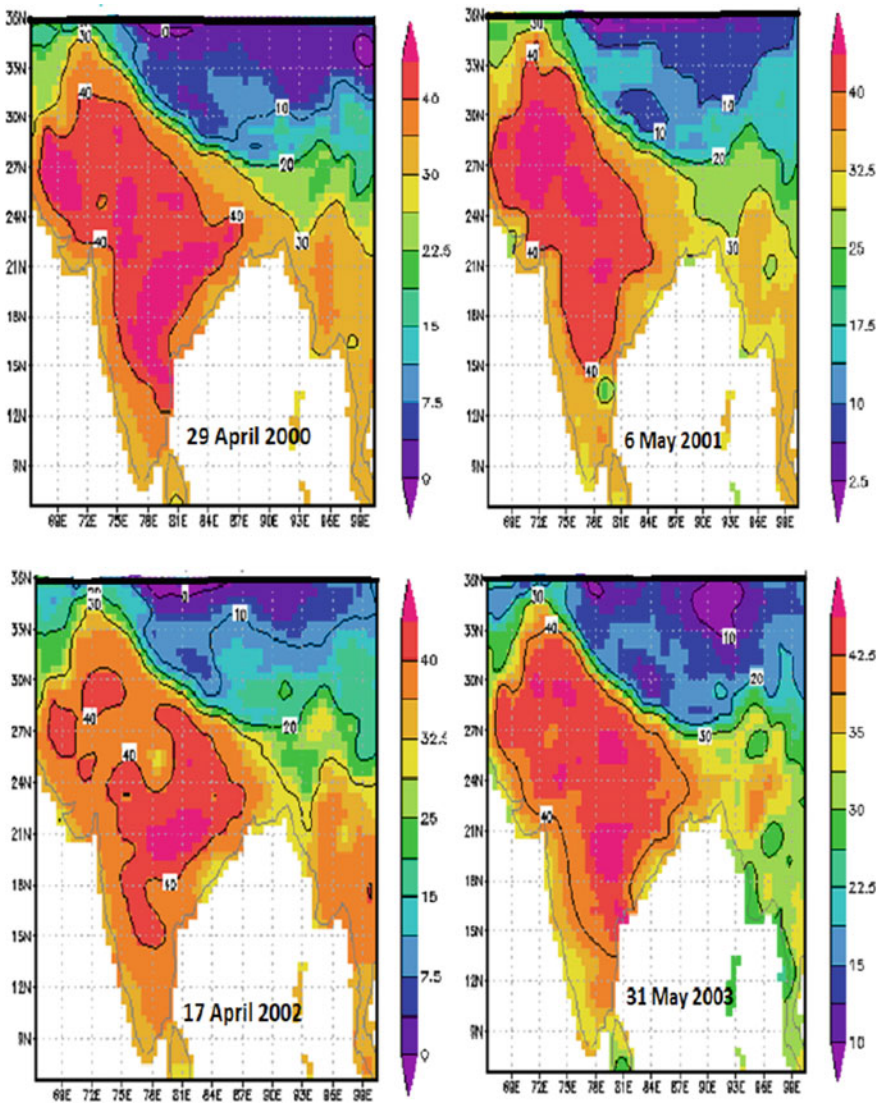

Fig. 11.1 Heat wave (HW) analysis over Indian region from 2000 to 2003. The side bar shows the maximum temperature due to heat wave in degree celsius for different colours used in Indian maps

In the present work, trends of the heat wave in India was analyzed using maximum temperature data over India from 2000 to 2016 (Figs. 11.1, 11.2, 11.3 and 11.4). The heat wave trend estimation was made using GRADS and FORTRAN. The maximum temperature over India was made available from IMD (Indian meteorological department), and NOAA (National Oceanic and Atmospheric Administration). The GRADS software was used for the detection of the heat wave and to

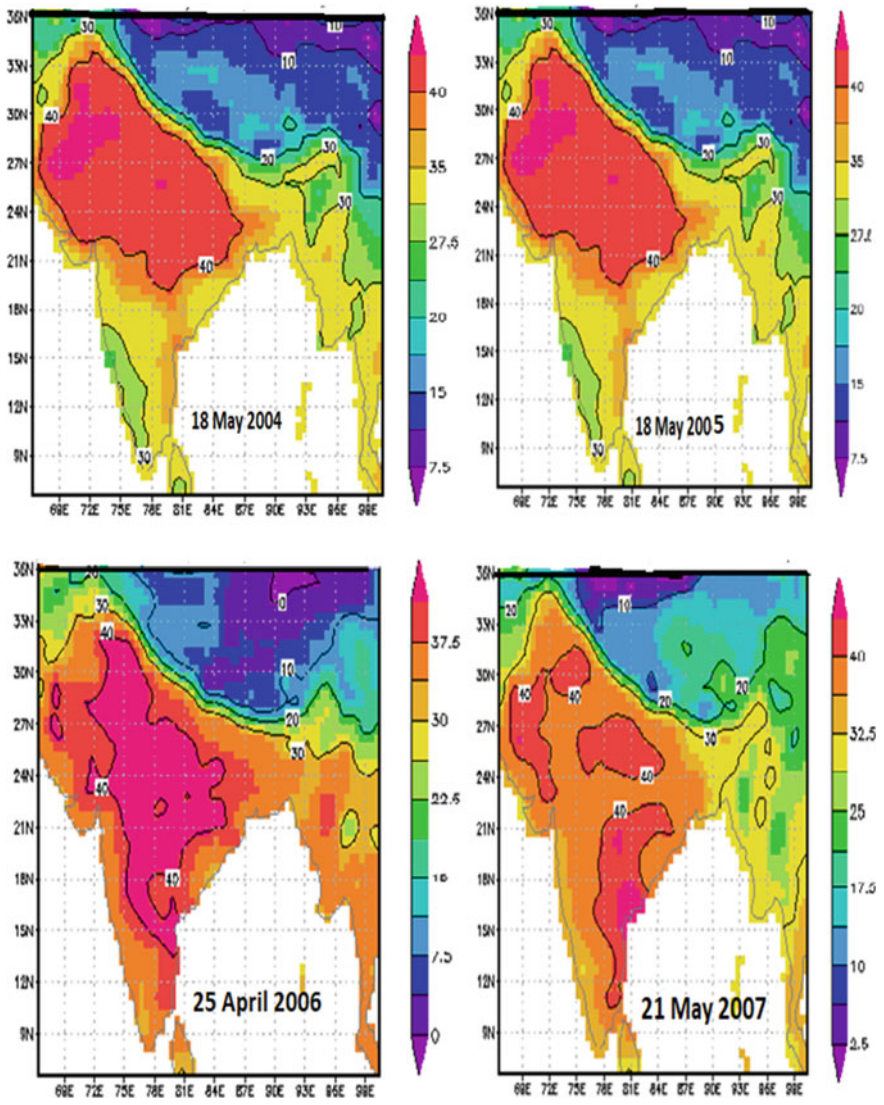

Fig. 11.2 Heat wave (HW) analysis over Indian region from 2004 to 2007. The description of side bars are same as that of Fig. 11.1

know whether the heat wave present in the area or not. The heat wave index was also calculated by the mean relative humidity and mean temperature on the daily basis in 3–5 meteorological stations in India during the time span of 1981–2005. The patterns for heat wave evaluated from heat wave index is based on the least square relapse investigation at each station level, And the result shows that the heat wave trends are increasing on the daily basis. It was found that the longest heat wave

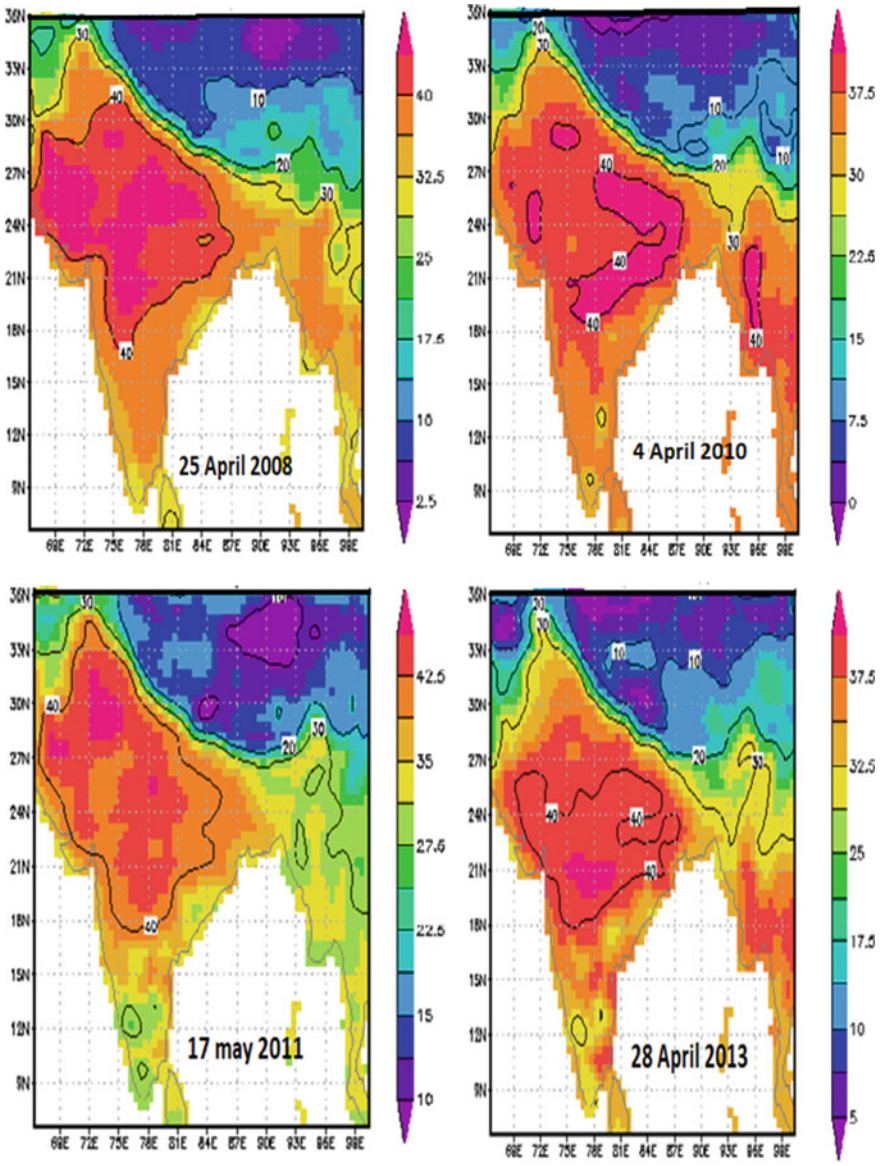

Fig. 11.3 Heat wave analysis over Indian region from 2008 to 2013

occurred in Dholpur on 28th May in 1998 and in Rajasthan (Phalodi) on 23 May in 2016 which was observed as 50 °C. In hilly regions, the temperature was found to be above then 40 °C. Although, the maximum heat wave index was also found to occur in some places. On the global basis, we observe that the highest heat wave index occurred in England during the above study period. the extreme caution was

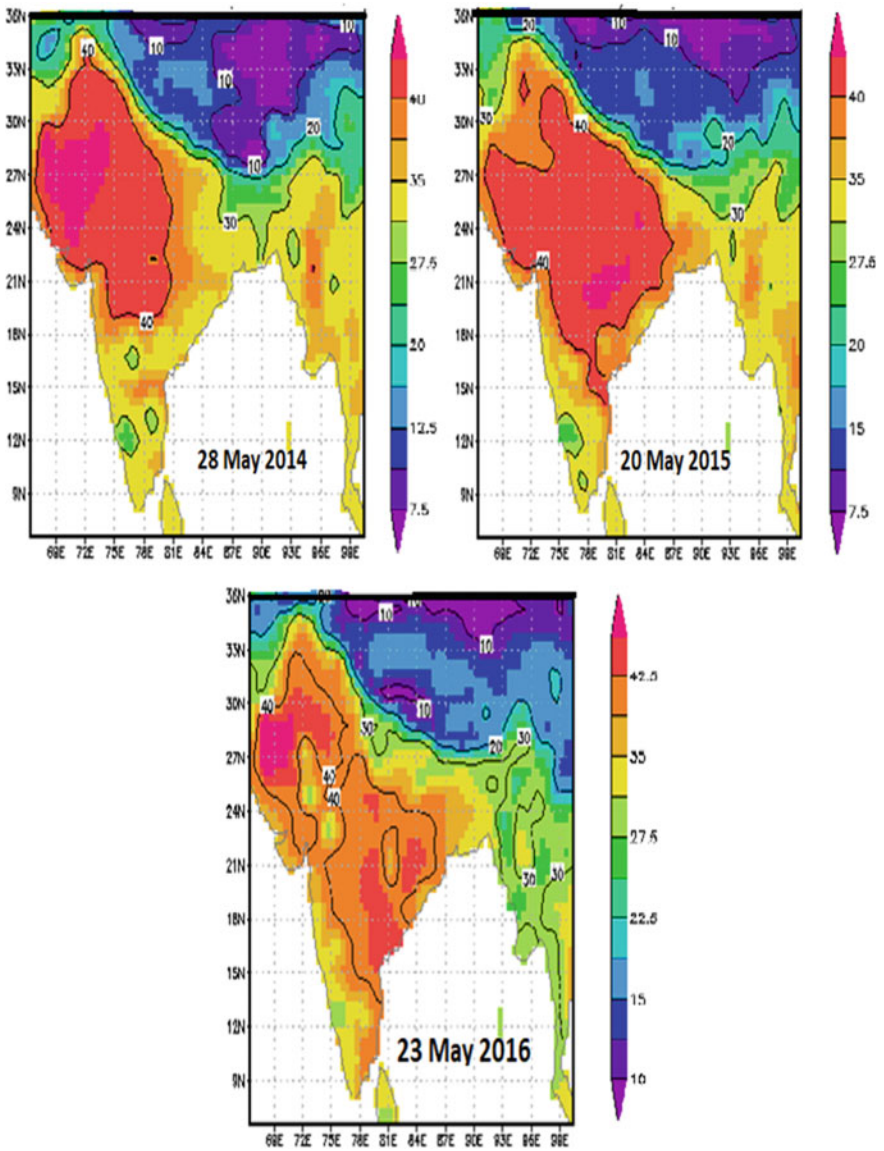

Fig. 11.4 Description of this figure is same as that of earlier figures except that heat wave analysis was made over Indian region from 2014, 2015 and 2016

observed the monsoon during south (May–July), and in east the heat wave having the safety condition, the part of world is possibly weak to moderate the occurrence of El Nino most of the time [8].

11.4 Conclusions

In this paper, the average maximum temperature of around 17-year data, and interpolation of some 0.5-degree data was done for finding the average maximum temperature over India. We have also calculated the 90th percentile of IMD HW data from 2000–2016 after completion of the interpolated data. Then the 90th percentile data was subtracted to find out the heat wave. It was found that some leap years does not exceed 40 °C on an average and some years were recorded as the hottest year such as 2001. One may note that over some hilly areas, the maximum temperature recorded exceed 30 °C. Therefore, the natural climate changes have been added to change the instances of remarkable atmosphere over the globe, from longer and sizzling heat waves to heavier storms. This evidence suggests that phenomenal atmosphere may be affected impressively more than predicted.

Acknowledgements The corresponding author is thankful to Indian Meteorological Department (IMD) for providing the maximum temperature data over different zones of India. Special thanks are due to National Oceanic and Atmospheric administration (NOAA) for utilizing their temperature data over India to complete the present work. The authors are also thankful to Director, National Atmospheric Research Laboratory (NARL), Gadanki, Andhra Pradesh (India) for providing necessary computational facilities.

References

1. S.K. Dash, A. Mamgin, Changes in the frequency of different categories of temperature extremes in India. J. Clim. Appl. Meteorol. **50**, 1842–1858 (2011)
2. H.H. Dholakia, D. Bhadra, A. Garg, Short term association between ambient air pollution and mortality and modification by temperature in five Indian cities. Atmos. Environ. **99**, 168–174 (2014)
3. A.P. Dimri, Comparison of regional and seasonal changes and trends in daily surface temperature extremes over India and its subregions. Theor. Appl. Climatol. 1–22 (2018).
4. M.G. Donat, L.V. Alexander, H. Yang, I. Durre, R. Vose, R.J.H. Dunn, K.M. Willett, E. Aguilar, M. Brunet, J. Caesar, B. Hewitson, Updated analyses of temperature and precipitation extreme indices since the beginning of the twentieth century: the HadEX2 dataset. J. Geophys. Res. Atmos. **118**, 2098–2118 (2013)
5. A.A. Faris, Y.S. Reddy, Estimation of urban heat island using Landsat ETM+ imagery at Chennai city—a case study. Int. J. Earth Sci. Eng. **3**(3), 332–340 (2010)
6. H.J. Fowler, D.R. Archer, Conflicting signals of climate change in the upper indus basin. J. Clim. **19**, 4276–4293 (2006)
7. A.K. Jaswal, N.M. Narkhede, S. Rachel, Atmospheric data collection, processing and database management in India Meteorological Department. Proc. Ind. Natl. Sci. Acad. **80**, 697–704 (2014)

8. Y.J. Kaufman, D. Tanré, O. Boucher, A satellite view of aerosols in the climate system. Nature, **419**, 215–223 (2002)
9. D.R. Kothawale, K.R. Kumar, One the recent changes in surface temperature trends over India. Geophys. Res. Lett. **32**, L18714 (2005)
10. A. Kumar, Spatio-temporal synoptic variability of aerosol optical depth and cloud properties over the Central North region of India through MODIS collection V satellite sensors. Ind. J. Phys. (Springer, 1.78), **90**(6), 613–625 (2016). ISSN: 0973–1458.
11. A. Kumar, Aerosols-cloud properties in dynamic atmosphere over Kedarnath sub-himalayan region of India: a long term study from MODIS satellite. Nat. Environ. Pollut. Technol. **14**(3), 493–500 (2015)
12. A. Kumar, Atmospheric electrical conductivity measurements during Monsoon period at a semi-urban Tropical Station of Northern India. Emerging Issues in Ecology and Environmental Science, Springer Briefs in Environmental Science book series, Springer, Cham, 1–9, 2019 (ISBN 978–3–319–99398–0)
13. A. Kumar, D. Saxena, R. Yadav, J. Rai, Measurement of atmospheric aerosols during monsoon period at Roorkee. Atmospher. Sci. Lett. **12**(4), 345–350
14. A. Kumar, Fast melting rate of Himalayan glaciers since 2000 posing threat to water deficiency in the Indian Himalayan region. Astron. Geophys. **60**(4), 4.12, August 2019
15. A. Kumar, Satellite derived spatio-temporal characteristics of aerosol optical depths and cloud parameters over tropical Indian region. J. Indian Geophys. Union **22**(6), 649–658 (2018)
16. N. Kumar, A.K. Jaswal, M. Mohapatra, P.A. Kore, Spatial and temporal variation in daily temperature indices in summer and winter seasons over India (1969–2012). Theor. Appl. Climatol. **129**, 1227–1239 (2017)
17. M. Lei, D. Niyogi, C. Kishtawal, R.A. Pielke Sr., A. Beltrán-Przekurat, T.E. Nobis, S.S. Vaidya, Effect of explicit urban land surface representation on the simulation of the 26 July 2005 heavy rain event over Mumbai, India. Atmos. Chem. Phys. **8**(20), 5975–5995 (2008)
18. A. Mathew, S. Sreekumar, S. Khandelwal, N. Kaul, R. Kumar, Prediction of surface temperatures for the assessment of urban heat island effect over Ahmedabad city using linear time series model. Energy Build. **128**, 605–616 (2016)
19. R.K. Pachauri, L.A. Meyer (eds.), Climate change 2014: synthesis report. Contribution of Working Groups I, II and III to the Fifth Assessment Report of the Intergovernmental Panel on Climate Change (Cambridge University Press, London, 2014)
20. I. Pal, A. Al-Tabbaa, Long-term changes and variability of monthly extreme temperatures in India. Theor. Appl. Climatol. **1–2**, 45–56 (2010)
21. S.M. Pingale, D. Khare, M.K. Jat, J. Adamowski, Spatial and temporal trends of mean and extreme rainfall and temperature for the 33 urban centers of the arid and semi-arid state of Rajasthan, India. Atmos. Res. **138**, 73–90 (2014)
22. N. Ramankutty, J. Foley, Estimating historical changes in global land cover: croplands from 1700 to 1992. Glob. Biogeochem. Cycles **13**, 997–1027 (1999)
23. S. Sen Roy, R.B. Singh, Role of local level relative humidity on the development of urban heat Island across the Delhi Metropolitan Region. Urban Development Challenges, Risks and Resilience in Asian Mega Cities (pp 99–118, Springer, Tokyo, 2015).
24. D. Saxena, R. Yadav, A. Kumar, J. Rai, Measurement of atmospheric aerosols during monsoon and winter period at Roorkee (India). Indian J. Radio Space Phys. **39**, 208–217 (August 2010)
25. S.I. Seneviratne, M.G. Donat, B. Mueller, L.V. Alexander, No pause in the increase of hot temperature extremes. Nat. Clim. Change **4**, 161–163 (2014)

Chapter 12
Thermodynamic Characteristics of Liquid Crystal-Nanocomposites

Ch. Kartikeshwar Patro, Aakarti Garg, Rohit Verma, Ravindra Dhar, and Roman Dabrowski

Abstract Nanomaterials dispersed liquid crystals have introduced a new era for the liquid crystal (LC) based display devices and other technologies. Carbon nanotubes (CNTs) due to their exceptional mechanical strength, high thermal and electrical conductivity have become significant for various applications in nanotechnology. Furthermore, in many research works, it has been established that liquid crystalline materials act as captivating host for the dispersion of CNTs which leads to spontaneous ordering of CNTs with high degree of alignment. Also, it has been investigated that the dispersion of CNTs to LCs influence and enhance the properties (electro-optical and dielectric properties) of liquid crystalline materials. In the present work, change in the thermodynamic characteristics of 6CHBT due to the dispersion of carboxylic group (–COOH) functionalized multi walled carbon nanotubes (a-MWCNTs) have been studied. Transition temperature, transition enthalpies and transition entropies have been determined for pure as well as a-MWCNTs dispersed 6CHBT samples.

12.1 Introduction

Among all the nanomaterials dispersed into liquid crystals (LCs), CNTs have allured a great research interest in order to enhance the characteristics of LC materials due to their exceptional electronic and mechanical properties. The added functionalities of liquid crystal nanocomposites are achieved by combining the self-organization property of liquid crystals with the characteristics of nanotubes. The composites of

Ch. K. Patro · A. Garg · R. Verma (✉)
Department of Applied Physics, Amity Institute of Applied Sciences, Amity University Uttar Pradesh, Noida 201313, India
e-mail: rverma85@amity.edu

R. Dhar
Centre of Material Sciences, Institute of Interdisciplinary Studies, University of Allahabad, Allahabad 211002, India

R. Dabrowski
Institute of Applied Sciences and Chemistry, Military University of Technology, Warsaw, Poland

V. K. Jain et al. (eds.), *Recent Trends in Materials and Devices*, Springer Proceedings in Physics 256, https://doi.org/10.1007/978-981-15-8625-5_12

LCs and CNTs are extensively studied across the globe [1–6, 9, 10]. Garcia et al. have reported the electrical response of LC cells doped with multi walled CNTs (MWCNTs) [1]. They have shown the dominant resistor behavior at mid frequencies. They also revealed that the magnitude of impedance of the MWCNTs dispersed LC cells decrease with the applied voltage [1]. Yadav et al. have described the method of aligning CNTs, process of dispersion of CNTs in LCs and the effect of CNTs on various properties of LCs [2]. They have investigated that hysteresis width decreases with the dispersion of CNTs in nematic liquid crystal. They also reported improvement of display parameters such as threshold voltage and response time [2]. Paul et al. have reported the change in relative dielectric permittivity, decrease in transition temperature and transition enthalpy along with the electro-optical properties such as threshold voltage of pure 6CHBT as well as $BaTiO_3$ dispersed 6CHBT [3]. We have also observed change in electro-optical and dielectric properties of 5CB due to the dispersion of single walled CNTs (SWCNTs). It has been observed that dielectric anisotropy, isotropic to nematic transition temperature, threshold and switching voltages decrease with the increase in the concentration of SWCNTs [4]. In the present work, we have dispersed 0.04 wt.% carboxylic group (–COOH) functionalized multi walled carbon nanotubes (a-MWCNTs) in a room temperature nematic liquid crystal 4-(trans-4′-n-hexylcyclohexyl) isothiocyanatobenzoate (6CHBT) and carried out the thermodynamic studies.

12.2 Experimental Details

The liquid crystalline sample 6CHBT has been obtained from Prof. R. Dabrowski, Institute of Applied Science and Chemistry, Military University of Technology, Poland.

Liquid crystal nanocomposites (LC-a-MWCNTs) were prepared by adding 0.04 wt.% of a-MWCNTs in 6CHBT. 6CHBT and a-MWCNTs have been dissolved in chloroform ($CHCl_3$). The liquid crystal nanocomposites were then ultrasonicated for about 60 min so as to reduce the bundling tendencies of MWCNTs and to obtain the uniform dispersion. The solution is then kept overnight for slow evaporation of the solvent and finally the desired dispersion is obtained. Differential scanning calorimeter (DSC) has been used for the thermodynamic study of the material. In order to stabilize the thermodynamic parameters, 5 cycles of DSC were allowed to run at the scan rate of 5.0 °C/min in the temperature range of −20 to 50 °C. The phase transition temperatures and enthalpy of transitions were measured for heating and cooling cycles at different scan rates ranging between 2.5 and 15.0 °C/min. Phase transition temperatures were determined to an accuracy of 0.1 °C, whereas transition enthalpies (ΔH) were determined to an accuracy better than 2% for fully grown peaks. However, for very weak peaks, uncertainties were large. Further details about experiments can be find in some of our earlier publications [7, 8].

12.3 Results and Discussions

The thermodynamic characterization of the pure as well as dispersed samples have been carried out by differential scanning calorimetry. Transition temperatures, transition enthalpies and transition entropies of pure and a-MWCNTs dispersed 6CHBT have been determined. The measured values of transition temperatures (°C), transition enthalpies (Cal/mol) and entropies (Cal/mol K) of various transitions for dispersed and pristine 6CHBT samples are collected in Table 12.1. The values of transition temperature and transition enthalpies mentioned in the table have been obtained from the DSC thermograms and the values of transition entropies have been determined through the second law of thermodynamics ($\Delta H = T \cdot \Delta S$). Figures 12.2 and 12.3 show the variation of transition temperature (°C) of various transitions with scan rates (°C/min) for the pure and dispersed 6CHBT respectively. From the plots of Figs. 12.2 and 12.3 true transition temperatures at the hypothetical scan rate of 0 °C/min have been determined.

It can be observed from the table that for the endothermic cycle, the transition temperatures for Cr–N and N–I transitions for the dispersed sample decrease as

Table 12.1 Transition temperatures (in °C) acquired at the scan rate of 10 °C/min, average transition enthalpies (ΔH in Cal/mol), average transition entropies (ΔS in Cal/mol-K) of the pure 6CHBT and a-MWCNTs dispersed 6CHBT

Transitions	Transition temperatures in °C	Average ΔH in Cal/mol	Aaverage ΔS in Cal/mol K
Pure 6CHBT			
Cr–N	16.9	14,329.2	49.4
N–I	44.1	355.2	1.1
I–N	40.2	645.9	2.1
N–Cr	−5.5	10,819.6	40.4
6CHBT + a-MWCNTs			
Cr–N	14.7	16,159.7	56.1
N–I	43.2	445.0	1.4
I–N	41.3	656.8	2.1
N–Cr	−6.0	7468.4	28.0

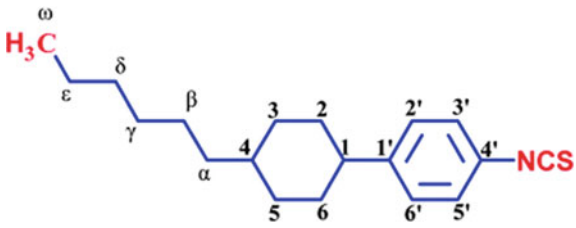

Fig. 12.1 Molecular structure of 6CHBT

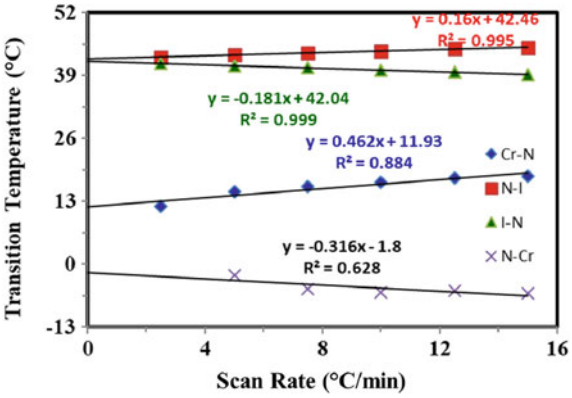

Fig. 12.2 Variation of transition temperature (°C) with the scan rate (°C/min) of pure 6CHBT

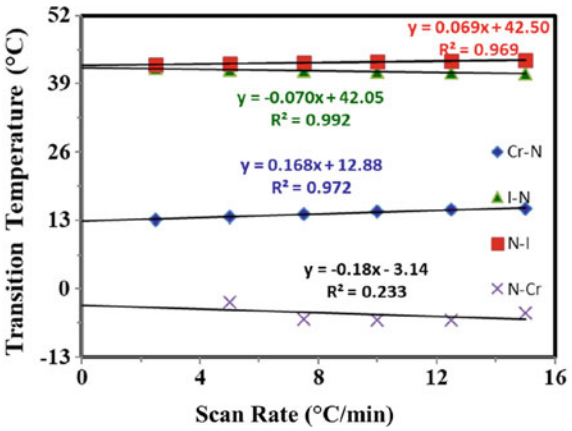

Fig. 12.3 Variation of transition temperature (°C) with the scan rate (°C/min) of 6CHBT + –COOH functionalized MWCNT

compared to those of the pristine sample. For exothermic cycle, transition temperature for the I–N transition increases and transition temperature for N–Cr transition decreases as compared to those of the pristine sample.

From the table given above, it can be observed that the values of transition enthalpies increase for heating cycle. For cooling cycle, it increases for I–N transition and decreases for N–Cr transition and same behavior is observed for the transition entropies. The increase in transition temperature and transition enthalpies signifies that the a-MWCNTs are better aligned with the LCs in the exothermic cycles. CNTs are known to align along the director of LCs due to the π–π stacking/interaction between the phenyl rings of LCs and CNTs [9, 10]. Therefore, we can conclude that the increase in the enthalpies of transitions are due to the stabilization of the nematic phase in the exothermic cycle. However, the presence of iron impurities used as catalyst during the synthesis of a-MWCNTs may also have some contribution in the rise of transition enthalpies. The decrease in transition enthalpy for the N–Cr transition is due to incomplete crystallization of the sample.

12.4 Conclusions

The phase transition temperatures of the dispersed sample are decreased for the endothermic cycle and are increased for the exothermic cycle as compared to those of the virgin sample. The transition enthalpies of the dispersed sample are increased as compared to those of the pure sample. The increase in transition temperature and transition enthalpies for the exothermic cycle reveals that the CNTs are better aligned with LCs in the cooling cycle. The increase in transition enthalpies is attributed to the $\pi-\pi$ interaction between the LC and CNT molecules. The transition entropies of the dispersed sample are increased as compared to those of the pure sample.

References

1. A.G. Garcia, R. Vergaz, J.F. Algorri, X. Quintana, J.M. Oton, Beilstein J. Nanotech. **6**, 396–403 (2015)
2. S.P. Yadav, S. Singh, Prog. Mat. Sci. **80**, 38–76 (2016)
3. S.N. Paul, R. Dhar, R. Verma, S. Sharma, R. Dabrowski, Mol. Cryst. Liq. Cryst. **545**, 105–111 (2011)
4. R. Verma, M. Mishra, R. Dhar, R. Dabrowski, J. Mol. Liq. **221**, 190–196 (2016)
5. P. Malik, A. Chaudhary, R. Mehra, K.K. Raina, J. Mol. Liq. **165**, 7–11 (2012)
6. S. Tripathi, J. Prakash, A. Chandran, T. Joshi, A. Kumar, A. Dhar, A.M. Biradar, Liq. Cryst. **40**, 1255–1262 (2013)
7. R. Verma, R. Dhar, V.K. Agrawal, M.C. Rath, S.K. Sarkar, V.K. Wadhawan, R. Dabrowski, Liq. Cryst. **36**, 1003–1014 (2009)
8. R. Verma, M. Mishra, R. Dhar, R. Dabrowski, Liq. Cryst. **44**(3), 544–556 (2017)
9. J.P.F. Lagerwall, G. Scalia, J. Mater. Chem. **18**(25), 2890 (2008)
10. R. Basu, G.S. Iannacchione, Phys. Rev. E **81**, 051705 (2010)

Chapter 13
Production of Superposition of Coherent States Using Kerr Non Linearity

Shivani A. Kumar, H. Prakash, N. Chandra, and R. Prakash

Abstract The coherent states are often called as Glauber coherent states and were named after the American Scientist Glauber who was first to realize the extraordinary usefulness of these coherent states for explanation and analysis of many optical phenomena. These states were first introduced by Sudarshan also and are now been extensively studied and applied to quantum-optical problems. The most explicit form of these states are expressed as, $|\alpha\rangle = \sum_{n=0}^{\infty} e^{-\frac{1}{2}|\alpha|^2} \frac{\alpha^n}{\sqrt{n!}} |n\rangle$ where, the Fock states $|n\rangle$ is the eigen state of the number operator $N = a^{\dagger}a$, i.e., $N|n\rangle = n|n\rangle$ and $\alpha = \alpha_r + i\alpha_i$ is a complex number. These Glauber coherent states are the eigen states of annihilation operator and are well known. They play a very important role in many applications of quantum information processing including quantum teleportation. But it has been a long dream for physicists to generate these superposed coherent states in the most general desired form $|\psi\rangle = N\left(\cos\frac{\theta}{2}|\alpha\rangle \pm \sin\frac{\theta}{2} e^{i\varphi}|-\alpha\rangle\right)$ where, N is the normalization factor. In this paper, we propose a scheme to generate any such general superposition of coherent states $|\alpha\rangle$ and $|-\alpha\rangle$ using Kerr effect, two beams in coherent states, a single photon beam and optical devices like polarization beam splitter and mirrors. In the output, if a single photon is detected in a polarization state defined by angle θ and φ, the desired superposition of coherent states $|\alpha\rangle$ and $|-\alpha\rangle$ results. If the photon is detected in an orthogonal polarization state (the state in which the electric field strength at a given point in space is normal to the direction of propagation), a superposition state different from the desired one results.

13.1 Introduction

The coherent states, often called as Glauber states [1–3] after the American Scientist who was first to realize their extraordinary usefulness for the description of optical

S. A. Kumar (✉)
Amity Institute of Applied Sciences, Amity University, Noida, India
e-mail: sakumar@amity.edu

H. Prakash · N. Chandra · R. Prakash
Department of Physics, University of Allahabad, Allahabad, India

V. K. Jain et al. (eds.), *Recent Trends in Materials and Devices*, Springer Proceedings in Physics 256, https://doi.org/10.1007/978-981-15-8625-5_13

phenomena. These states were introduced by Sudarshan [4] also and are now been extensively studied and applied to quantum-optical problems. The explicit form of these states are expressed as,

$$|\alpha\rangle = \sum_{n=0}^{\infty} \mathrm{e}^{-\frac{1}{2}|\alpha|^2} \frac{\alpha^n}{\sqrt{n!}} |n\rangle \tag{1.1}$$

where, the Fock states [5] $|n\rangle$ is the eigen state of the number operator $N = a^{\dagger}a$, i.e.

$$N|n\rangle = n|n\rangle \tag{1.2}$$

and $\alpha = \alpha_r + i\alpha_i$ is a complex number. These state are the eigen states of annihilation operator and are well known. Their coordinate representation is the minimum-uncertainty packet of harmonic oscillators [6]. Although these states are non-orthogonal, they do form a complete set of states, i.e., they obey a completeness relation and hence form a good set of basis states. The overcompleteness of coherent states allows the expansion of many important field operators as a single integral over projectors on these states.

It has been a dream for many physicists to generate superposition of coherent states $|\pm\alpha\rangle$ which are out of phase with each other by a phase difference of 180°

$$|\psi\rangle_{\pm} = N_{\pm}(|\alpha\rangle + |-\alpha\rangle) \tag{1.3}$$

where $N_{\pm}$ is the normalization factor. But it has now been shown [7–10] that a coherent state propagating through an optical Kerr medium may evolve into a superposition of a set of coherent states differing in phases by multiple of some constant. This superposition of macroscopically distinguishable quantum states is popularly known as Schroedinger cat states [9, 11]. In practice, the superposition states can be generated in various non-linear process [7, 8, 12–19], back action evading measurements [20–22], Jaynes-Cummings Model [23–27], quantum non-demolition measurements [28], and resonant cavity [29–33].

Several other possibilities also exist to generate the non-classical state of electromagnetic field with the help of superposition of two or more states [34–50]. One of the earlier methods for generating these superposition states was proposed by Yurke and Stoler who proposed to generate a coherent superposition of the form

$$|\psi\rangle = \frac{1}{\sqrt{2}}\left[|\alpha\rangle + \mathrm{e}^{\mathrm{i}\pi/2}|-\alpha\rangle\right], \tag{1.4}$$

using a Kerr nonlinearity.

A scheme of back action evading coupling to correlate the signal and readout modes was proposed by Song et al. [21]. The calculations done by the authors show that a superposition of quantum states is generated in the signal mode as evidence by interference fringes in a homodyne measurement of the quadrature component

orthogonal to the axis of maximum separation between the superposed states. Yurke et al. [28] interchanged the parametric amplifier and the back action evader in their calculations and showed that both devices generated the same Schroedinger cat wave function provided a suitable choice of gain parameter is made.

In 1993, Tara et al. [51] showed production of Schrodinger macroscopic quantum superposition states in a Kerr medium. They also proposed a scheme for production of superposition of squeezed coherent states. Gerry [31] proposed a method for generation of Schrodinger cat states and entangled coherent states [41, 51] in the motion of a trapped ion by a dispersive interaction. They showed that these entangled coherent states may be generated that are a particular form of Schrodinger-cat state showing strong correlations between the modes.

In 1999, Gerry [52] proposed a method to generate Schroedinger cat states for optical fields. Their method involved two modes of the field interacting in a Kerr medium. In 2005, Kim and Paternostro [10] also proposed a scheme to generate a superposition of coherent states using small Kerr effect and a single photon or two entangled twin photons. However, the authors of [52] and [53] used cross Kerr nonlinearity whose evolution operator is given by $\hat{U}_{CK} = \exp(-\mathrm{i}\,\chi\,\hat{n}_a\hat{n}_b)$ which affects the phase of the system depending on the photon numbers of the two modes a and b ($\hat{n}_b$ is the photon number operator for mode b). If mode a is in a coherent state of its amplitude α and mode b is in single photon state, then by the action of cross Kerr nonlinearity,

$$\hat{U}_{CK}|\alpha\rangle_a|n\rangle_b = \left|\alpha \mathrm{e}^{\mathrm{i}\,n_b\chi\,t}\right\rangle_a|n\rangle_b \tag{1.5}$$

i.e. the Fock state $|n\rangle_b$ remains unaffected by the interaction but the coherent state $|\alpha\rangle_a$ picks up a phase shift directly proportional to the number of photons n_b in the $|\,n\,\rangle_b$ state.

These coherent states have several attractive non-classical properties. [7, 8, 10, 53, 54]. These states lead to squeezing [55, 56], normal second order squeezing, higher order squeezing [116, 122] and sub-poissonian statistics [55, 57]. These superposed coherent states also show maximum simultaneous squeezing, maximum antibunching, and maximum higher order squeezing, higher order sub poissonian statistics [57, 58].

In this chapter, we propose a scheme to generate any desired superposition of coherent states $|\alpha\rangle$ and $|-\alpha\rangle$ using simple Kerr effect and linear optical devices like polarization beam splitters and mirrors. We show that in the output, if a single photon is detected in a definite polarization state defined by angle θ and φ, the desired superposition of coherent states $|\alpha\rangle$ and $|-\alpha\rangle$ results. If the photon is detected in an orthogonal polarization state, a superposition different from the desired one results.

It may be noted that other authors who studied generation of superposition of coherent states $|\alpha\rangle$ and $|-\alpha\rangle$ have taken $|\in_H| = |\in_V|$ and have not considered the general case. Also, those who considered use of cross Kerr effect have not taken the Kerr effect into account. As is obvious, the cross Kerr effect is a dimension of the Kerr effect only.

13.2 Generation of Superposed Coherent State Using Kerr Non-linearity

Figure 13.1 depicts our scheme for generation of superposed coherent states. Each number, 1–15 represents a set of two modes having the same direction of propagation but one having a horizontal linear polarization and the other having a vertical linear polarization. We refer to the two modes for the number n by nH and nV.

The whole scheme is based mainly on two components, viz, Kerr-cells and polarizing beam splitters. The Kerr-cells have a non-linearity expressed by the Hamiltonian

$$H_I = gN^2 = g(N_H + N_V)^2. \tag{2.1}$$

This gives the time evolution operator

$$U_I = \mathrm{e}^{-\mathrm{i}H_I t} = \mathrm{e}^{-\mathrm{i}\chi N^2}, \quad \chi = gt \tag{2.2}$$

Constant χ represents the interaction time and is proportional to the third order non-linear susceptibility and the length of the Kerr-cell. If a light beam, initially in modes IH and IV passes through the Kerr-cell, and emerges in the modes FH and FH, the initial and final mode operators are related to each other by,

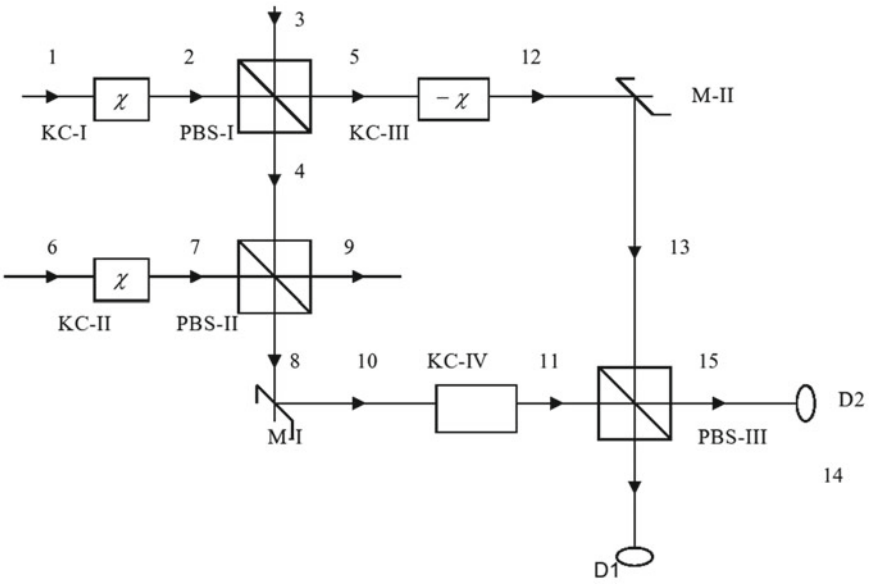

Fig. 13.1 Schematic diagram showing coherent superposition state generated by an entangled pair of photons

$$a_{IH,IV} = U^{\dagger} a_{FH,FV}\, U = \mathrm{e}^{\mathrm{i}\chi (N_{FH}+N_{FV})^2} a_{FH,FV} \mathrm{e}^{-\mathrm{i}\chi (N_{FH}+N_{FV})^2} \tag{2.3}$$

since, $N_{IH} = N_{FH}$ and $N_{IV} = N_{FV}$.

For the other element, the polarizing beam splitter connection between the four input modes and four output modes is obvious if we take into account the fact that the horizontal polarization is transmitted through the beam splitter but the vertical polarization is reflected.

Consider the input having a single photon in modes $3H$ and $3V$ and two coherent beams in the state $|\beta\rangle$ in modes $1H$ and $6V$ (see Fig. 13.1). The input state can be written as,

$$|\Psi\rangle_{1,3,6} = \exp[\beta a_{1H}^{\dagger} - \beta^* a_{1H}]\Big(\in_H a_{3H}^{\dagger} + \in_V a_{3V}^{\dagger}\Big) \exp[\beta a_{6V}^{\dagger} - \beta^* a_{6V}]|vac\rangle \tag{2.4}$$

Here, a and $a^{\dagger}$ are annihilation and creator operators for the modes denoted by the subscripts.

The effect of Kerr-cell KC-I on mode $1H$ would be given by,

$$a_{1H} = \mathrm{e}^{\mathrm{i}\chi N_{2H}^2} a_{2H} \mathrm{e}^{-\mathrm{i}\chi N_{2H}^2}. \tag{2.5}$$

Modes $2H$, $3H$ and $3V$ pass through the polarizing beam splitter PBS-I for which we have,

$$a_{2H} = a_{5H}, \quad a_{2V} = a_{4V}, \quad a_{3H} = a_{4H}, \quad a_{3V} = a_{5V} \tag{2.6}$$

Using (1.5) and (2.1), we can express the state of light written in earlier (1.4) in the form,

$$\begin{aligned} |\Psi\rangle_{5,4,6} = \mathrm{e}^{\mathrm{i}\chi N_{5H}^2} \exp\Big[\beta\, a_{5H}^{\dagger} - \beta^* a_{5H}\Big]\Big(\in_H a_{4H}^{\dagger} + \in_V a_{5V}^{\dagger}\Big) \\ \times \exp\Big[\beta a_{6V}^{\dagger} - \beta^* a_{6V}\Big] \mathrm{e}^{-\mathrm{i}\chi N_{5H}^2} |vac\rangle \end{aligned} \tag{2.7}$$

For light mode in $6V$ passing through the Kerr-cell KC-II, we can write

$$a_{6V} = \mathrm{e}^{\mathrm{i}\chi N_{7V}^2} a_7 \mathrm{e}^{-\mathrm{i}\chi N_{7V}^2} \tag{2.8}$$

Effect of Polarizing beam splitter PBS-II is given by,

$$a_{4H} = a_{8H}, \quad a_{4V} = a_{9V}, \quad a_{7H} = a_{9H}, \quad a_{7V} = a_{8V} \tag{2.9}$$

Also, if the mirror M-I gives

$$a_{8H} = a_{10H}, \quad a_{8V} = a_{10V}$$

(2.2) takes the form,

$$|\Psi\rangle_{5,10,9} = \mathrm{e}^{\mathrm{i}\chi\,(N_{5H}^2+N_{10V}^2)}\,\exp\Big[\beta a_{5H}^{\dagger} - \beta^{*} a_{5H}\Big]\Big(\in_H a_{10H}^{\dagger} + \in_V a_{5V}^{\dagger}\Big) \times \exp\Big[\beta a_{10V}^{\dagger} - \beta^{*} a_{10V}\Big]\mathrm{e}^{-\mathrm{i}\chi\,(N_{5H}^2+N_{10V}^2)}|vac\rangle \tag{2.10}$$

There are no photons in the modes $9H$ and $9V$ and it is therefore left out of consideration and the subscript 9 on $|\Psi\rangle$ is dropped.

Light beams in modes $5H$ and $5V$ and $10H$ and $10V$ are now passed through Kerr-cells KC-III and KC-IV, each of which has interaction time $-\chi$. This can be obtained by having a nonlinear material in the cells which has a different sign of the third order nonlinearity.

For these Kerr cells we have,

$$a_{5H,5V} = \mathrm{e}^{-\mathrm{i}\chi\,(N_{12H}+N_{12V})^2} a_{12H,12V}\,\mathrm{e}^{\mathrm{i}\chi\,(N_{12H}+N_{12V})^2} \tag{2.11}$$

and

$$a_{10H,10V} = \mathrm{e}^{-\mathrm{i}\chi\,(N_{11H}+N_{11V})^2} a_{11H,11V}\,\mathrm{e}^{\mathrm{i}\chi\,(N_{11H}+N_{11V})^2} \tag{2.12}$$

Mirror M-II gives,

$$a_{12H,V} = a_{13H,V} \tag{2.13}$$

The state of light then can be written as,

$$\begin{aligned}
|\Psi\rangle_{13,11} &= \exp\big[-\mathrm{i}\chi\{N_{13H}+N_{13V}\}^2 + \{N_{11H}+N_{11V}\}^2\big]\mathrm{e}^{\mathrm{i}\chi\,(N_{13H}^2+N_{13V}^2)} \\
&\exp\Big[\beta a_{13H}^{\dagger} - \beta^{*} a_{13H}\Big]\Big(\in_H a_{11H}^{\dagger} + \in_V a_{13V}^{\dagger}\Big)\exp\Big[\beta a_{11V}^{\dagger} - \beta^{*} a_{11V}\Big] \\
&\mathrm{e}^{-\mathrm{i}\chi\,(N_{13H}^2+N_{13V}^2)}\exp\big[\mathrm{i}\chi\{N_{13H}+N_{13V}\}^2 + \{N_{11H}+N_{11V}\}^2\big]|vac\rangle \\
&= \exp\big[-i\chi\big(N_{13V}^2 + 2N_{13H}N_{13V} + N_{111H}^2 + 2N_{11H}N_{11V}\big)\big] \\
&\quad\times \exp\Big[\beta a_{13H}^{\dagger} - \beta^{*} a_{13H}\Big]\Big(\in_H a_{11H}^{\dagger} + \in_V a_{13V}^{\dagger}\Big)\exp\Big[\beta a_{11V}^{\dagger} - \beta^{*} a_{11V}\Big]|vac\rangle
\end{aligned} \tag{2.14}$$

For terms with $\in_H$, $N_{11H} = 1$ but $N_{13V} = 0$ and for terms with $\in_V$, $N_{11H} = 0$ but $N_{13V} = 1$. Hence, we can write (2.14) in the form

$$\begin{aligned}
|\Psi\rangle_{13,11} = \mathrm{e}^{-i\chi}\Big\{&\in_H a_{11H}^{\dagger}\exp\Big[\beta a_{13H}^{\dagger} - \beta^{*} a_{13H}\Big]\mathrm{e}^{-2\mathrm{i}\chi N_{11V}}\exp[\beta a_{11V}^{\dagger} - \beta^{*} a_{11V} \\
&\times \mathrm{e}^{2\mathrm{i}\chi N_{11V}} + \in_V a_{13V}^{\dagger}\mathrm{e}^{-2i\chi N_{13H}}\exp\Big[\beta a_{13H}^{\dagger} - \beta^{*} a_{13H}\Big]\mathrm{e}^{2\mathrm{i}\chi N_{13H}} \\
&\times \exp\Big[\beta a_{11V}^{\dagger} - \beta^{*} a_{11V}\Big]\Big\}|vac\rangle
\end{aligned} \tag{2.15}$$

$$= \mathrm{e}^{-\mathrm{i}\chi}\Big\{\in_H a_{11H}^{\dagger}\ \exp\Big[\beta a_{13H}^{\dagger} - \beta^* a_{13H}\Big]\exp\Big[\beta a_{11V}^{\dagger} - \beta^* a_{11V}\Big]$$
$$+ \in_V\ a_{13V}^{\dagger}\exp\Big[\beta a_{13H}^{\dagger} - \beta^* a_{13H}\Big]\exp\Big[\beta a_{11V}^{\dagger} - \beta^* a_{11V}\Big]\Big\}|vac\rangle \tag{2.16}$$

$$= \mathrm{e}^{-\mathrm{i}\chi}\Big[\in_H a_{11H}^{\dagger}|\beta\rangle_{13H}|\beta'\rangle_{11V} + \in_V a_{13V}^{\dagger}|\beta'\rangle_{13H}|\beta\rangle_{11V}\Big] \tag{2.17}$$

where

$$|\beta'\rangle = |\beta \mathrm{e}^{-2\mathrm{i}\chi}\rangle. \tag{2.18}$$

The polarizing beam splitter PBS-IV gives

$$a_{11H} = a_{15H}, \quad a_{11V} = a_{14V}, \quad a_{13H} = a_{14H}, \quad a_{13V} = a_{15V} \tag{2.19}$$

and therefore light is in the state

$$|\Psi\rangle_{14,15} = \mathrm{e}^{-\mathrm{i}\chi}\Big[\in_H a_{15H}^{\dagger}|\beta, \beta'\rangle_{14H,14V} + \in_V a_{15V}^{\dagger}|\beta', \beta\rangle_{14H,14V}\Big] \tag{2.20}$$

If we consider linear polarizations in directions dividing the horizontal and vertical directions and denote these modes by + and −, defined by,

$$a_H = \frac{1}{\sqrt{2}}(a_+ + a_-),\ a_V = \frac{1}{\sqrt{2}}(a_+ - a_-), \tag{2.21}$$

we have,

$$|\beta,\ \beta'\rangle_{13H,13V} = \left|\frac{1}{\sqrt{2}}(\beta + \beta'),\ \frac{1}{\sqrt{2}}(\beta - \beta')\right\rangle_{13+,13-} \tag{2.22}$$

and a similar relation for $|\beta', \beta\rangle$.

Since $\beta' = \beta \mathrm{e}^{-2\mathrm{i}\chi}$,

$$\frac{1}{\sqrt{2}}(\beta + \beta') = \sqrt{2}\beta \mathrm{e}^{-\mathrm{i}\chi}\cos\chi$$
$$\frac{1}{\sqrt{2}}(\beta - \beta') = \sqrt{2}i\beta \mathrm{e}^{-\mathrm{i}\chi}\sin\chi, \tag{2.23}$$

If we write

$$\alpha \equiv \sqrt{2}i\beta\, \mathrm{e}^{-i\chi}\sin\chi$$
$$\alpha_0 \equiv \sqrt{2}\beta\, \mathrm{e}^{-i\chi}\cos\chi = -i\alpha\cot\chi, \tag{2.24}$$

(2.16) takes the form,

$$|\Psi\rangle_{14,15} = \frac{1}{\sqrt{2}} e^{-i\chi}\Big[\in_H a^{\dagger}_{15H}|\alpha\rangle_{14-} + \in_V a^{\dagger}_{15V}|-\alpha\rangle_{14-}\Big]|\alpha_0\rangle_{14+} \tag{2.25}$$

If we now define modes 15± using (2.19), we get,

$$\begin{aligned}|\Psi\rangle_{14,15} = \frac{1}{\sqrt{2}} e^{i\chi}\Big[a^{\dagger}_{15+}\big(\in_H |\alpha\rangle_{14+} + \in_V |-\alpha\rangle_{14-}\big) \\ + a^{\dagger}_{15-}\big(\in_H |\alpha\rangle_{14+} - \in_V |-\alpha\rangle_{14-}\big)\Big]|\alpha_0\rangle_{14+}\end{aligned} \tag{2.26}$$

This makes it clear that if a photon is detected in mode 15+, radiation in mode 14+ will be in the superposed coherent state,

$$\in_H |\alpha\rangle_{14+} + \in_V |-\alpha\rangle_{14-}, \tag{2.27}$$

while if a photon is detected in 15−, the state

$$\in_H |\alpha\rangle_{14+} - \in_V |-\alpha\rangle_{14-} \tag{2.28}$$

will be generated.

If we write $\in_H/\in_V = \tan\left(\frac{1}{2}\theta\right) e^{i\delta}, 0 \le \theta \le \pi,\ 0 \le \delta \le 2\pi$,

The probabilities of detection of a single photon in the modes 15± are

$$\frac{1}{2}\Big[1 + 2\mathrm{Re}\left(\in^*_H \in_V\right) e^{-2|\alpha|^2}\Big] = \frac{1}{2}\Big[1 \pm \sin\theta \cos\delta\ e^{-2|\alpha|^2}\Big]. \tag{2.29}$$

If $|\alpha|^2$ is appreciable, the probabilities are close to 1/2 and hence it may be expected that the desired superposition state should be produced within two attempts. It may also be noted, that for $0 < \delta < \pi$ if the probability of success in any one attempt is >1/2.

13.3 Conclusion

It may be mentioned that one could have chosen $\chi = \pi/2$ and $\beta = \frac{\alpha}{\sqrt{2}}$, necessitating the least possible value of $|\beta|$ for a given $|\alpha|$. The advantage of having a larger value of $|\beta|$ (note that $\beta = -i\alpha e^{i\chi}/\sqrt{2}\sin\chi$ or $|\beta| = |\alpha|/\sqrt{2}\ \sin\chi$) and a smaller value of χ is that only a smaller interaction time and therefore a smaller length of the Kerr-cell is required. In this case, however, the energy going in the mode 14+ is wasted in the signal in the state $|-i\alpha\cot\chi\rangle$.

Thus, one has to make a compromise between requirements of (i) larger length of Kerr-cell and (ii) wastage of the energy in the orthogonal mode 14+. It may be

noted that the states $|\alpha\rangle_+|0\rangle_-$ and $|-\alpha\rangle_-|0\rangle_-$ can also be written as $\left|\frac{\alpha}{\sqrt{2}}, \frac{\alpha}{\sqrt{2}}\right\rangle_{H,V}$ and $\left|-\frac{\alpha}{\sqrt{2}}, -\frac{\alpha}{\sqrt{2}}\right\rangle_{H,V}$, respectively. Hence, the states $\in_H |\alpha\rangle_+ + \in_V |-\alpha\rangle_+$ is same as the state $\in_H |\gamma, \gamma\rangle_{H,V} + \in_V |-\gamma, -\gamma\rangle_{H,V}$. Note that such states are entangled in the modes H and V and have been used extensively in literatures.

Acknowledgements Shivani A. Kumar would like to thank Amity University, Noida, Uttar Pradesh for its support in every way wherever required.

References

1. R.J. Glauber, Phys. Rev. **130**, 2529 (1963)
2. R.J. Glauber, Phys. Rev. **131**, 2766 (1963)
3. R.J. Glauber, In quantum optics and electronics. In: C. De Witt, A. Blandin, Cohen Tanaudiji C Gordon and Breach, New York (1965)
4. E.C.G. Sudarshan, Phys. Rev. Lett. **10**, 277 (1963)
5. V. Fock, Z. Phys. **49**, 339 (1928)
6. E. Schrodinger, Phys. Rev. **14**, 644 (1927)
7. B. Yurke, D. Stoler, Phy. Rev. Lett. **57**, 13 (1986)
8. G.J. Milburn, C.A. Holmes, Phys. Rev. Lett. **56**, 2237 (1986)
9. E. Schrodinger, Die gegenwartige Situation in der Quantenmechanik. *Naturewissenschaften* 23:807, 823, 844. An English translation of this can be found in Quantum Theory of Measurement, edited by J. Wheeler and W. H. Zurek (Princeton: Princeton University Press, 1983) (1935)
10. M.S. Kim, Paternostro M *arXiv quant-Ph*/0510057 v1
11. C.C. Gerry, Phys. Rev. A **55**, 2479 (1996)
12. C.M. Savage, W.A. Cheng, Opt. Comm. **70**, 439 (1989); N. Qureshi, H. Schmidt, A.R. Hawkins, Appl. Phys. Lett. **85**, 431 (2004); N. Qureshi, S.Q. Wang, M.A. Lowther, A.R. Hawkins, S. Kwon, A. Liddle, J. Bokor, Schmidt H. Nano Lett. **5**, 1413
13. P. Tombesi, A. Mecozzi, J. Opt. Soc. Am. B **4**, 1700 (1987); P.R. Cantwell, U.J. Gibson, D.A. Allwood, H.A.M. Macleod, J. Appl. Phys. **100**, 093910 (2006)
14. T. Ogawa, M. Uede, N. Imoto, Phys. Rev. A **43**, 6458 (1991)
15. J.J. Slosser, P. Meystre, E.M. Wright, Opt. Lett. **15**, 233 (1990)
16. J. Banacloche, Phys. Rev. A **44**, 5913 (1991)
17. J.J. Slosser, P. Meystre, Phys. Rev. A **41**, 3867 (1990)
18. P. Meystre, J.J. Slosser, M. Wilkens, Phys. Rev. A **43**, 4959 (1991)
19. M. Wilkens, P. Meystre, Phys. Rev. A **43**, 3832 (1991)
20. A. La Porta, R.E. Slusher, B. Yurke, Phys. Rev. Lett. **62**, 28 (1989)
21. S. Song, C.M. Caves, B. Yurke, Phys. Rev. A **41**, 5261 (1990)
22. B. Yurke, J. Opt. Soc. Am. B. **2**, 732 (1986)
23. E.T. Jaynes, E.W. Cummings, Proc. IEEE **51**, 89 (1963)
24. S.J.D. Phoenix, P.L. Knight, Ann. Phys. (New York) **186**, 381 (1988)
25. S.J.D. Phoenix, P.L. Knight, J. Opt. Soc. Am. B **7**, 116 (1990)
26. J. Gea-Banacloche, Phys. Rev. Lett. **65**, 3385 (1990)
27. S.J.D. Phoenix, P.L. Knight, Phys. Rev. Lett. **66**, 2833 (1991)
28. B. Yurke, W. Schleich, D.F. Walls, Phys. Rev. A **42**, 1703 (1990)
29. J. Eiselt, H. Risken, Opt. Comm. **72**, 351 (1989)
30. V. Buzek, H. Moya-Cessa, P.L. Knight, S.J.D. Phornix, Phys. Rev. A **45**, 8190 (1992)
31. A. Auffeves, Phys. Rev. Lett. **91**, 230405 (2003)

32. M.S. Kim, G.S. Agarwal, J. Mod. Opt. **46**, 2111 (1999)
33. P.K. Pathak, G.S. Agarwal, Phys. Rev. A **71**, 043823 (2005)
34. N. Chandra, H. Prakash, Ind. J. Pure Appl. Phys. **9**, 688 (1971)
35. N. Chandra, H. Prakash, Indian J. Pure Appl. Phys. **2**, 767 (1971)
36. N. Chandra, H. Prakash, Lett Nuovo Cim **4**, 1196 (1970)
37. N. Chandra, H. Prakash, Phys. Rev. Lett. **22**, 1068 (1969)
38. D. Stoler, B.E.A. Saleh, M.C. Teich, Opt. Acta **32**, 345 (1985)
39. Y. Xia, G. Guo, Phys. Lett. A **136**, 281 (1989)
40. D.T. Pegg, S.M. Barnett, J. Mod. Opt. **46**, 1657 (1999)
41. B.C. Sanders, Phys. Rev. A **39**, 4284 (1989)
42. P.L. Knight, V. Buzek, Opt. Comm. **81**, 331 (1991)
43. C.L. Chai, Phys. Rev. A **46**, 7187 (1992)
44. B.C. Sanders, Phys. Rev. A **45**, 6811 (1992)
45. C.T. Lee, Phys. Rev. A **52**, 3374 (1995)
46. R. Ragi, B. Baseia, V.S. Bagnato, Int. J. Mod. Phys. B **12**, 1495 (1998)
47. K. Nemoto, B.C. Sanders, J. Phys. A **34**, 2051 (2000)
48. W. Schleich, M. Pernigo, F.L. Kein, Phys. Rev. A **44**, 2172 (1991)
49. V.V. Dodonov, S.Y. Kalmykov, V.I. Man'ko Phys. Lett. A **199**, 123 (1995)
50. K. Tara, G.S. Agarwal, S. Chaturvedi, Phy. Rev. A **47**, 5024 (1993)
51. H. Jeong, M.S. Kim, J. Lee, Phys. Rev. A **64**, 052308 (2001)
52. Christopher C. Gerry, Phy. Rev. A **59**, 4095 (1999)
53. M. Hillery, Phys. Rev. A **36**, 3796 (1987)
54. A. Mecozzi, P. Tombesi, Phys. Rev. Lett. **58**, 1055 (1987)
55. H. Prakash, N. Chandra, Phys. Rev. A **9**, 2167 (1974)
56. D.F. Walls, Nature **306**, 141 (1983)
57. R. Loudon, P.L. Knight, J. Mod. Opt. **34**, 709 (1987)
58. V.V. Dodonov, J. Opt. B **4**, R1 (2002)

Chapter 14
Nanoparticles of Statins Synthesized from Mushroom Using Two Different Solvents and Evaluating Their Cytotoxic Potential Using HepG2 Cell Lines

Akansha Mehra, Sonal Chauhan, Rajiv Narang, V. K. Jain, and Suman Nagpal

Abstract Statins, a class of drugs commercially available to treat atherosclerosis and various cardiovascular diseases that come under the same umbrella but these drugs have various side-effects, like low bioavailability and less solubility in human body, associated with them. Earlier, we synthesized herbal nano-statins from mushroom as an alternative solution to combat this problem. The present work demonstrates synthesis and characterization of nanoparticles of statins in two different solvents namely, acetonitrile (ACN) and dimethyl sulfoxide (DMSO). The cytotoxicity of the synthesized nanoparticles of statins was evaluated using HepG2 cell lines, MTT assay was performed and the results showed that nanoparticles of statins synthesized in DMSO showed significant reduction in cell viability of cancerous cells even at lower doses (50–60 μL) without any significant effect on normal cells. Thus, nanoparticles of statins synthesized in DMSO were proven to be effective to treat cancerous cells, whereas nanoparticles of statins synthesized in acetonitrile were comparatively less effective with only 30–35% cell death even at higher doses (100 μL). Also, it is found to be toxic for normal cells, hampering its overall potential to act as anti-atherosclerotic. This study provides us a platform to further evaluate nano-statins synthesized in DMSO for their anti-atherosclerotic and anti-inflammatory potential by evaluating their efficacy in endothelial cells.

A. Mehra · V. K. Jain · S. Nagpal (✉)
Amity Institute of Advanced Research and Studies (Materials & Devices), Amity University, Noida, UP 201303, India
e-mail: snagpal@amity.edu

S. Chauhan
Amity Institute of Applied Sciences, Amity University, Noida, UP 201303, India

R. Narang
Department of Cardiology, All India Institute of Medical Sciences (AIIMS), New Delhi, India

V. K. Jain et al. (eds.), *Recent Trends in Materials and Devices*, Springer Proceedings in Physics 256, https://doi.org/10.1007/978-981-15-8625-5_14

14.1 Introduction

Cardiovascular diseases (CVDs) are found to be the leading cause of mortality these days [1]. Atherosclerosis is found to be one of the main reasons behind it. To treat this problem, many drugs are available in the market but among them, statins, a class of lipid lowering drugs, acts as a competitive inhibitor of the enzyme, 3-hydroxy-3methyl-glutaryl enzyme in the process of converting HMG CoA to mevalonate in cholesterol are best in all [2, 3]. They act by blocking the active site of the first enzyme and key rate-limiting enzyme in the mevalonate pathway, HMG-CoA reductase. It blocks the conversion of HMG-CoA to mevalonic acid and supports an increased clearance of LDL-cholesterol from the bloodstream [4]. Though statins are beneficial for the cardiovascular health, however, long-term abidance to statin therapy is not the best possible choice recommended [5]. Statins therapy is associated with higher dose side effects and also, they exhibit poor solubility in water and low bioavailability in human body [6]. To combat this problem, herbal medicines are also one of the solutions to this problem. There are many herbs like mushroom, drumstick, pomegranate and their parts which have medicinal properties and are used to treat cardiovascular diseases [7, 8]. But due to processing difficulties, they were not considered for the development of innovative formulations.

Nano drugs can combat the drawbacks enhancing solubility, dissolution and bioavailability and hence, making the drug more effective [9].

We have already synthesized and characterized nanoparticles of statins isolated from mushroom in acetonitrile [10]. In the present work, we have synthesized nanoparticles of statins in DMSO. The characterization of synthesized nanoparticles and the comparison of cytotoxicity in two solvents has also been evaluated using HepG2 cell lines to check their effectiveness in treating CVDs.

14.2 Materials and Methods

14.2.1 Chemicals and Reagents

Dimethyl sulfoxide (DMSO) and acetonitrile (ACN) were purchased from Fisher Scientific. Lovastatin (PHR1285) standard from Sigma Aldrich and HPLC grade water from Qualikems. Fetal bovine serum, antibiotic mix, Dulbecco's Modified Eagle Medium (DMEM), MTT (3-(4,5-dimethylthiazol-2-yl)-2,5-diphenyltetrazolium bromide were procured from HiMedia.

14.2.2 Plant Material and Cell Lines

Sky Mushrooms, Nagpur, Maharashtra, India, a mushroom dealing company provided us Pleurotus sajor-caju (Psc1 strain) species of oyster mushroom.

HepG2 cell lines were procured from National Centre for Cell Sciences, Pune. The anti-proliferative activity of the nano formulation was then evaluated in cancerous cell lines.

14.2.3 Synthesis of Herbal Nanoparticles of Statins

Nanoparticles of statins have been synthesized from oyster mushroom in two solvents namely, acetonitrile and DMSO separately, using the method of Akansha et al. [10] with slight modifications.

Mushrooms were thoroughly cleaned, air dried and grinded to fine powdered form. Nanoparticles of statins were synthesized in combined mixture of ACN and water (1:1 v/v) (Nano-statins A (NS-A)) by dissolving mushroom powder (50 mg/mL). Suspension was kept on magnetic stirrer for 2–3 h and was centrifuged at 12,000 g for 2 min at 30 °C. The supernatant was filtered and filtrate was added in HPLC grade water with continue stirring on magnetic stirrer for 1 h at 30–40 °C. The colorless solution changed to pale yellow.

Similar protocol was repeated to prepare nanoparticles of statins in DMSO only combined mixture of DMSO and water (1:1 v/v) was used in place of ACN and water (1:1 v/v) (Nano-statins B (NS-B)) and rest of the protocol is same.

14.2.4 Characterization of Synthesized Herbal Nanoparticles of Statins

Characterization of synthesized NS-A and NS-B was done using UV-Visible Spectrophotometer, Dynamic Light Scattering (DLS), Scanning Electron Microscope (SEM), Fourier Transform Infrared Spectroscopy (FTIR) and High Permissible Liquid Chromatography (HPLC).

14.2.4.1 UV Visible Spectrophotometric Analysis

UV visible spectrophotometry, the primary method to get confirmation of synthesized nanoparticles by comparing their spectrum with the spectrum of standard by evaluating lambda max, was done.

14.2.4.2 Particle Size Analysis

Dynamic light scattering (DLS) analysis was performed to check for estimation of average particle size. When monochromatic light (laser) hits the moving particles in Brownian motion and the wavelength of incoming light is changed, Doppler shift is observed. DLS is used to determine the size of nanoparticles in colloidal suspensions in the range of nano and submicron [11].

14.2.4.3 Scanning Electron Microscope (SEM) Analysis

Size, shape and surface morphology of samples can easily be determined using this type of electron microscopy. NS-A and NS-B were mounted on two different sample holders and were subjected to coating with a conductive metal (e.g. gold) using a sputter coater. Then all samples were analyzed by scanning with a focused beam of electrons. The surface characteristics of samples were determined by electrons emitted from surface of the sample.

14.2.4.4 Fourier Transform Infrared Spectroscopy (FTIR) Analysis

Infrared spectroscopy offers a sensitive way to determine functional groups within a sample. Different functional group absorbs different particular frequency of IR radiation. Also, there is very less possibility that any two compounds have same spectrum. The near IR region (overtone region), mid IR region (vibration rotation region) and far IR region (rotation region) are various subdivisions of infrared region [12]. Interpretation of the various bands can be done according to the characteristic functional groups present in the compound. Spectra of NS-A and NS-B were scanned, and results were compared.

14.2.4.5 High Permissible Liquid Chromatographic (HPLC) Analysis

NS-A and NS-B were characterized using HPLC under optimized conditions i.e. C-18G (250 × 4.6 mm; 5 μm) column with a column temperature of 30 °C, λ 238 nm, isocratic pump with a pressure of 250–450 KgF and UV–DAD detection system. Flow rate was maintained at 1.5 mL/min. Acetonitrile and 0.1% phosphoric acid (65:35) synthesized in HPLC grade water was used as a mobile phase [13].

14.2.5 Evaluation of Cytotoxicity

The cytotoxic potential of NS-A and NS-B was determined using HepG2 cell lines and compared with that of normal control cells, the detailed process involves:

14.2.5.1 Maintenance of Cell Lines and Cell Seeding

The HepG2 cancerous cell lines was cultured in DMEM medium supplemented with 10% of fetal bovine serum and 1% antibiotic mix in T-25 flask and incubated at 37 °C with 5% CO_2 in a humidified atmosphere. The viability of cells was determined by staining cells with trypan blue and counting using hemocytometer under microscope. Cells were seeded keeping cell density of 20,000 cells/mL and from this cell suspension, 100 μL was pipetted into each well of a 96-well plate and incubated for 24 h in a 5% CO_2 incubator at 37 °C to carry out MTT assay of both NS-A and NS-B and also acetonitrile and DMSO were taken individually in separate wells as solvent control to check solvent toxicity.

14.2.5.2 Determination of Percent Cell Viability Using MTT Assay

The MTT (3-(4,5-dimethylthiazol-2-yl)-2,5-diphenyltetrazolium bromide) assay was conducted based on the method described by Badawi et al. with slight modifications [14] to carry out the comparative analysis of cytotoxicity of both NS-A and NS-B and their solvents (acetonitrile and DMSO) cells were observed in each wells and medium was removed. 100 μL of fresh medium was added in each well. Drug was also added in triplicates having concentration 25, 50, 75 and 100 μL. Plate was kept in incubator for overnight (37 °C, 5% CO_2). Then, 20 μL of MTT reagent (3-(4,5- dimethylthiazol-2-yl)-2,5-diphenyltetrazoliumbromide) was added to each well and left in incubator for 4 h. Subsequently, 50 μL of solubilizing agent was added to each well and reading was taken at wavelength of 570 nm using ELISA reader. The protocol was followed for both NS-A and NS-B, individually. The relative changes in percent viability of cells treated with various concentrations of the synthesized nanomaterial was calculated with respect to untreated control having 100% cell viability.

The cytotoxicity percentage was determined using the following formula:

$$\%\ \text{cytotoxicity} = (\text{optical density of sample}/\text{optical density of control}) \times 100 \quad (1)$$

14.3 Results and Discussion

Nanoparticles of statins synthesized in ACN and DMSO were synthesized and characterized. The cytotoxic effect of NS-A and NS-B on HepG2 cell lines was also evaluated.

14.3.1 Characterization Studies

Characterization studies of NS-A and NS-B was done and results were recorded.

14.3.1.1 UV Visible Spectrophotometric Analysis

The primary confirmation study was done using UV Visible spectrophotometer which revealed presence of statins in both NS-A and NS-B at 238 nm, the same the lambda max of reference drug, lovastatin was also obtained.

14.3.1.2 Particle Size Analysis

Nanoparticles of statins synthesized in ACN were found to have the average diameter of particles in the range 60–90 nm, which substantiated the synthesis of particles in nano scale.

Nanoparticles of statins synthesized in DMSO had average diameter of particles in the range 50–90 nm, revealing the further reduction in size by as compared to NS-A.

14.3.1.3 Scanning Electron Microscope (SEM) Analysis

SEM analysis was done to determine the size and surface structure of nanoparticles of statins synthesized in ACN and DMSO. NS-A were found to have particle size of about 73 and 63 nm (Fig. 14.1a), whereas, NS-B showed particle size of about 73, 82 and 58 nm (Fig. 14.1b).

Both NS-A and NS-B exhibited spherical morphology when they were subjected for SEM analysis.

14.3.1.4 Fourier Transform Infrared Spectroscopy (FTIR) Analysis

Both NS-A and NS-B, were scanned over a wavenumber range of 4000–500 cm^{-1} and spectrums were recorded.

The spectrum of nanoparticles of statins synthesized in acetonitrile exhibited intense absorption bands at 2258 cm^{-1} (C triple bond N), 1636 cm^{-1} (C double bond C alkene), 1374 cm^{-1} (CH_3 bending) and 996 cm^{-1} (Alkenes mono substitution) as depicted in Fig. 14.2.

The spectrum of nanoparticles of statins synthesized in DMSO was also studied. It was observed that absorption band at wave number 1636 cm^{-1} (C double bond C alkene) and alkenes mono substitution at 996 cm^{-1}, (Fig. 14.2) was spotted [12].

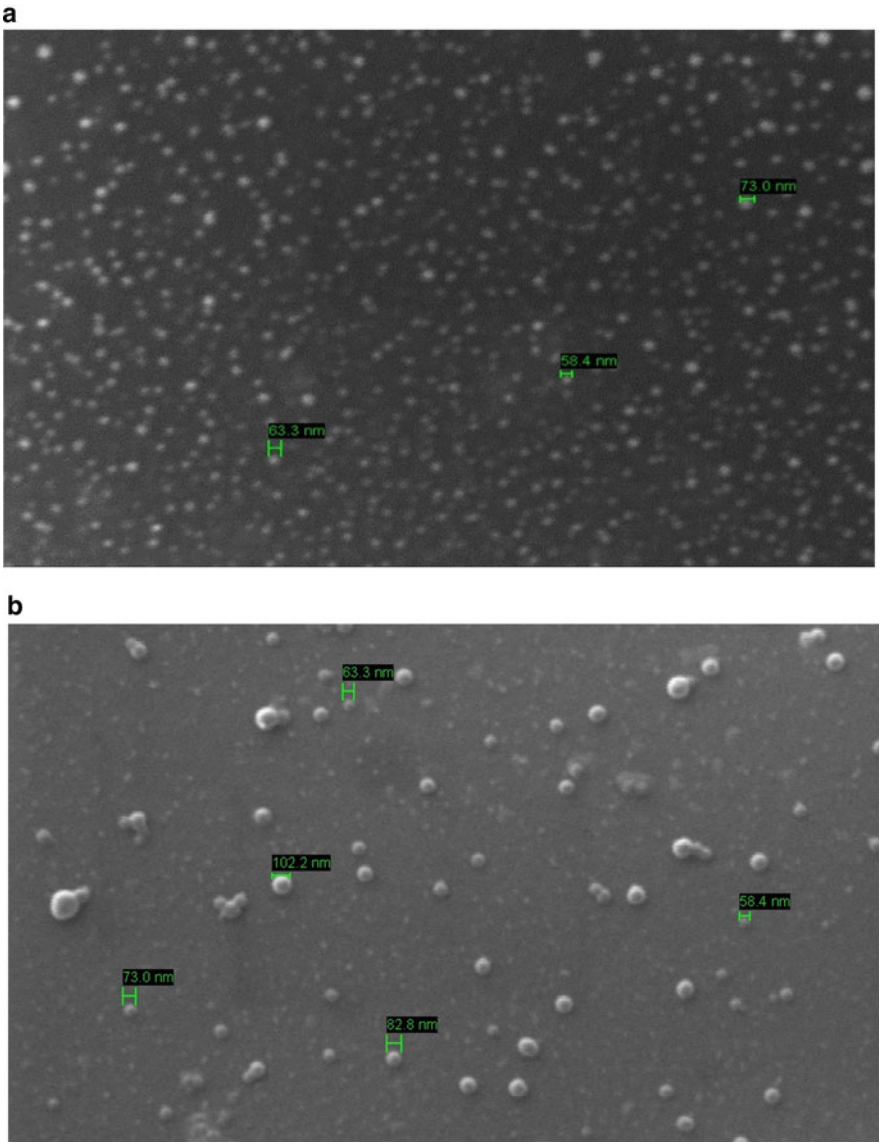

Fig. 14.1 **a** SEM image of nanoparticles of statins synthesized from herbal source, mushroom in acetonitrile. **b**. SEM image of nanoparticles of statins synthesized from herbal source, mushroom in DMSO

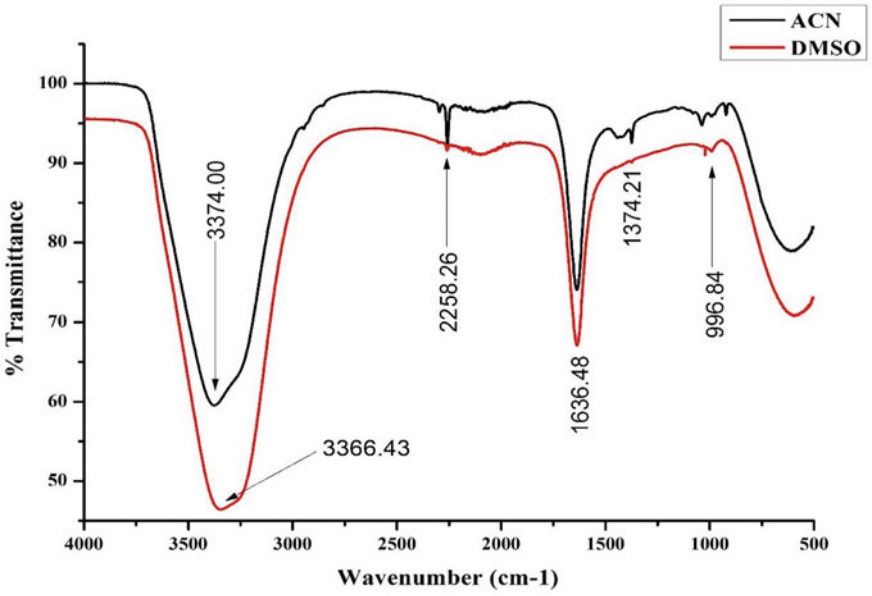

Fig. 14.2 Comparative FTIR spectrum of synthesized nanoparticles of statins from herbal source, mushroom in Acetonitrile and DMSO

The FTIR analysis depicted C double bond C alkene and alkenes mono substitution as a common part of their spectra, which indicated the matching of functional groups in both NS-A and NS-B.

14.3.1.5 High Permissible Liquid Chromatographic (HPLC) Analysis

NS-A and NS-B, were subjected to HPLC analysis and results were studied. Retention time (t_R) of statins in NS-A and NS-B was found to be 9 min and 9.22 min, respectively with a slight difference of ±0.22 min. The closeness of HPLC retention time in both NS-A and NS-B favoured the fact that nanoparticles of statins were eluted out in both the formulations utilizing different solvents.

14.3.1.6 Cytotoxicity Studies Using MTT Assay

The nanoparticles of statins synthesized from herbal source, mushroom, decreased cell viability of cancerous cells in a concentration dependent manner with respect to untreated control group in both the solvents (Fig. 14.3). At a lower concentration (20 μL) of nanoparticles of statins synthesized in acetonitrile, there was 5% reduction in cancerous cells, whereas DMSO induces cell death by 10% at the same volume indicating its anti-cancerous effect on cells even at such a lower dose. However,

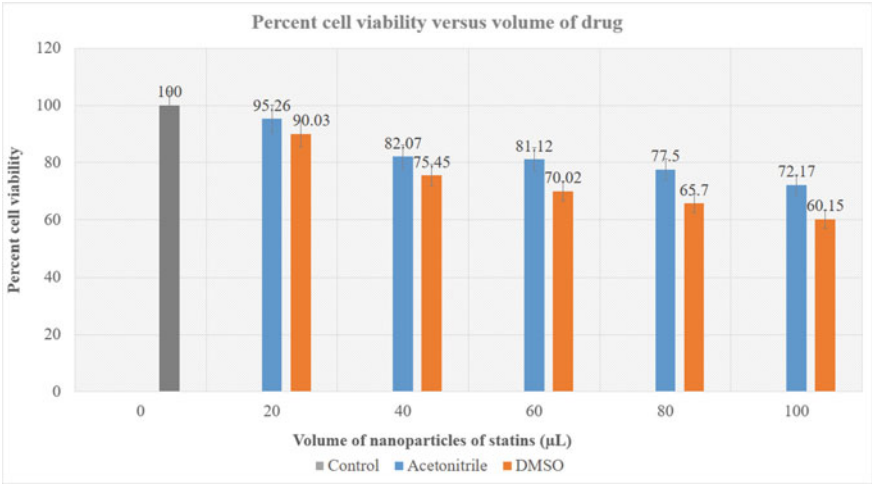

Fig. 14.3 Effect of nanoparticles of statins on percent cell viability in HepG2 cancerous cell lines

when the dose of NS-B was increased to 40 µL and 60 µL, the percent viability was significantly affected with the decrease by approximately 25% with respect to control cells. Cancerous cells treated with NS-A also showed reduction in cell viability (approx. 20%) but it was comparatively less than cancerous cells treated with NS-B at the same dose. On further addition of nanoparticles of statins synthesized in DMSO, the cell viability of cancerous cells got reduced from 100 (untreated cells) to 65.7% (80 µL) and to 60% (100 µL). NS-A were proved to have inhibiting effect for the growth of cancerous cells but they were not as effective as NS-B when the same dose was given to cancerous cells. This called for the fact that NS-B had better anti-cancerous, which can be attributed to the presence of an active ingredient, statins in the herbal extract of mushroom.

While in case of normal cells it was observed that NS-A affected the cell viability (92.12%) of normal cells even at lower dose of 20 µL (7.88% cell cytotoxicity) showing their toxic effect whereas, NS-B did not induce cell death of normal cells significantly even at the higher doses (only 8.84% cell cytotoxicity at 100 µL). The untreated control showed negligible mortality. At 20 µL, the cell death caused by NS-B (1.8%) was almost similar to untreated control (Fig. 14.4) while the solvent control of acetonitrile showed nearly 15 times higher cytotoxicity even at lower dose as reported earlier, in comparison the DMSO which is a safer and biocompatible solvent. Our results also showed that NS-B has better potential than NS-A as far as cytotoxicity issue of normal cells of the body is concerned keeping in mind the use of nanoparticles to treat CVDs. This study may provide us a better benchmark to evaluate anti-atherosclerotic effect of statins prepared in DMSO for its further potential application using specific cell lines, i.e. (endothelial cells) for CVDs.

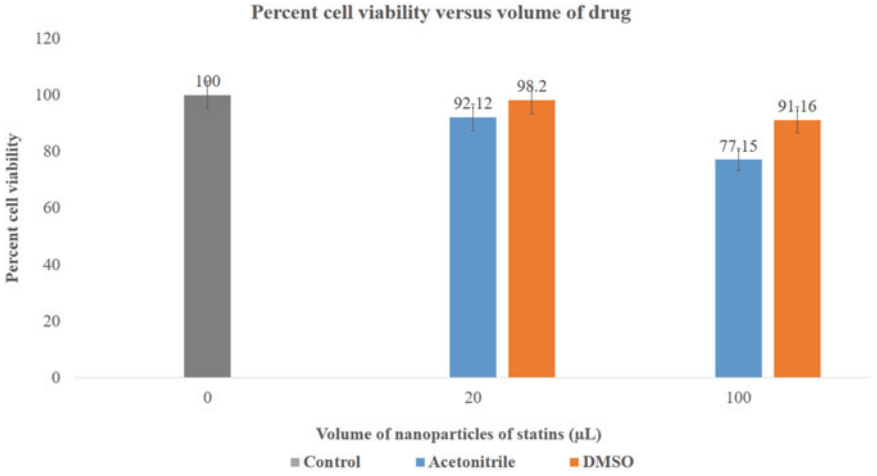

Fig. 14.4 Effect of nanoparticles of statins on percent cell viability in normal cell lines

14.4 Conclusion

The study demonstrates the comparison of method of synthesis and characterization of nanoparticles of statins from herbal source mushroom in two different solvents. The study also dealt with evaluation of cytotoxicity of herbal nanoparticles of statins synthesized in DMSO as well as in ACN using HepG2 cancerous cell lines. This study is the first step towards synthesis of nanoparticles of statins in two different solvents. Formulations of statins in its nano form not only overcome the poor solubility issue associated with it but also enhance its bioavailability even in lesser dose. The study helped us in determining the cytotoxic effect of solvent on cancerous cell lines by showing that DMSO is a better solvent as compared to acetonitrile as far as evaluation of cytotoxic potential of nanoparticles of statins with respect to cancerous cells is concerned. The findings in this study provide insight for further research to evaluate the dose and the capability of the synthesized nanoparticles of statins in both the solvents by subjecting nano formulations to other cell lines specific for the study of CVDs.

Acknowledgements This research was supported by Amity University, Noida, Uttar Pradesh. We would also like to show our gratitude to Dr. Ashok K. Chauhan, Founder President, Amity University for their continuous encouragement and support.

References

1. A. Boutayeb, The double burden of communicable and non-communicable diseases in developing countries. Trans. R. Soc. Trop. Med. Hyg. **100**(3), 191–199 (2006)
2. P. Kotyla, The role of 3-hydroxy-3-methylglutaryl coenzyme a reductase inhibitors (statins) in modern rheumatology. Therapeutic Adv. Musculoskeletal Disease **2**(5), 257–269 (2010)
3. C.M. Minder, M.J. Blaha, A. Horne, E.D. Michos, S. Kaul, R.S. Blumenthal, Evidence-based use of statins for primary prevention of cardiovascular disease. Am. J. Med. **125**(5), 440–446 (2012)
4. N.C. Ward, G.F. Watts, R.H. Eckel, Statin toxicity: mechanistic insights and clinical implications. Circ. Res. **124**(2), 328–350 (2019)
5. C.B. Newman, D. Preiss, J.A. Tobert, T.A. Jacobson, R.L. Page, L.B. Goldstein, C. Chin, L.R. Tannock, M. Miller, G. Raghuveer, Statin safety and associated adverse events: a scientific statement from the American Heart Association. Arterioscler. Thromb. Vasc. Biol. **39**(2), e38–e81 (2019)
6. B. Romana, M. Batger, C. Prestidge, G. Colombo, F. Sonvico, Expanding the therapeutic potential of statins by means of nanotechnology enabled drug delivery systems. Curr. Top. Medicinal Chem. **14**(9), 1182–1193 (2014)
7. A. Tachjian, V. Maria, A. Jahangir, Use of herbal products and potential interactions in patients with cardiovascular diseases. J. Am. Coll. Cardiol. **55**(6), 515–525 (2010)
8. A. Fugh-Berman, Herbs and dietary supplements in the prevention and treatment of cardiovascular disease. Preventive Cardiol. **3**(1), 24–32 (2000)
9. K. Chakraborty, A. Shivakumar, S. Ramachandran, Nano-technology in herbal medicines: a review. Int. J. Herbal Med. **4**(3), 21–27 (2016)
10. A. Mehra, R. Narang, V. Jain, S. Nagpal, Preparation and characterization of nano statins using oyster mushroom (Pleurotus sajor-caju): a new strategy to reduce toxicity and enhance efficacy for the treatment of cardiovascular disease. Euro. J. Integrative Med. **33**, 101014 (2020)
11. D.N. De Assis, V.C.F. Mosqueira, J.M.C. Vilela, M.S. Andrade, V.N. Cardoso, Release profiles and morphological characterization by atomic force microscopy and photon correlation spectroscopy of 99mTechnetium-fluconazole nanocapsules. Int. J. Pharm. **349**(1–2), 152–160 (2008)
12. R. Bhargava, I.W. Levin, Fourier transform infrared imaging: theory and practice. Anal. Chem. **73**(21), 5157–5167 (2001)
13. M. Piecha, M. Sarakha, P. Trebše, D. Kočar, Stability studies of cholesterol lowering statin drugs in aqueous samples using HPLC and LC–MS. Environ. Chem. Lett. **8**(2), 185–191 (2010)
14. N.M. Badawi, M.H. Teaima, K.M. El-Say, D.A. Attia, M.A. El-Nabarawi, M.M. Elmazar, Pomegranate extract-loaded solid lipid nanoparticles: design, optimization, and in vitro cytotoxicity study. Int. J. Nanomed. **13**, 1313 (2018)

Chapter 15
Thermal and Electrical Characteristics of Nematic Liquid Crystal and Gold Nanoparticle Composites

Ch. Kartikeshwar Patro, Aakarti Garg, Rohit Verma, Ravindra Dhar, and Roman Dabrowski

Abstract A small amount of gold nanoparticles (GNPs) of diameter 2 nm has been dispersed in a room temperature liquid crystalline material 4-(trans-4′-n-hexylcyclohexyl) isothiocyanatobenzoate (6CHBT). Both the virgin as well as dispersed samples have been characterized by differential scanning calorimetry and frequency domain dielectric spectroscopy. The phase sequence of both the samples is I–N–Cr. Thermodynamic studies of the pristine vis-a-vis dispersed samples demonstrate that dispersion of 0.05 wt.% GNPs in 6CHBT results in the increased thermal stability of the Nematic (N) phase of the sample. Dielectric measurements illustrate that the longitudinal component of the dielectric permittivity and hence the dielectric anisotropy of the dispersed sample are decreased as compared to those of the pure sample. The relaxation frequency of an observed relaxation mechanism for the homeotropically aligned molecules of the dispersed sample is increased as compared to those of the pristine sample.

15.1 Introduction

Due to the intense tunable absorption and scattering resonances triggered by the collective oscillations of the conduction band electrons (known as surface plasmons), metal nanoparticles have continued to attract the interest of various researchers [1]. Among the metal nanoparticles, gold nanoparticles (GNPs) have been the center of interest because of the fact that their surface plasmon resonances (SPR) lie in the

Ch. Kartikeshwar Patro · A. Garg · R. Verma (✉)
Department of Applied Physics, Amity Institute of Applied Sciences, Amity University Uttar Pradesh, Noida, 201313, India
e-mail: rverma85@amity.edu

R. Dhar
Centre of Material Sciences, Institute of Interdisciplinary Studies, University of Allahabad, Allahabad 211002, India

R. Dabrowski
Institute of Applied Sciences and Chemistry, Military University of Technology, 00-908 Warsaw, Poland

V. K. Jain et al. (eds.), *Recent Trends in Materials and Devices*, Springer Proceedings in Physics 256, https://doi.org/10.1007/978-981-15-8625-5_15

optical spectrum [1, 2]. The dispersion of nanoparticles (NP) in liquid crystals (LCs) is considered as a promising method for faster switching times [3], lower energy consumption [4] or brighter display colors [5]. Prakash et al. and Marino et al. have studied the non-volatile memory effects in the nematic phase of ferroelectric LCs doped with bare and polymer capped gold nanoparticles (GNPs) [6, 7]. Inam et al. have observed large changes in the electro-optical properties of a nematic LC (NLC) mixture, E7 due to inclusion of small concentration of GNPs [8]. Sharma et al. have studied the effect of GNPs on the memory of ferroelectric LC material and have reported that the memory is enhanced remarkably due to electric field induced charge transfer from LC molecules to the GNPs [9].

In the present work, we have dispersed gold nanoparticles (GNPs) of diameter 2 nm in a LC material 4-(trans-4′-n-hexylcyclohexyl) isothiocyanatobenzoate (6CHBT) and studied the thermodynamic and electrical properties of pure as well as dispersed 6CHBT.

15.2 Experimental Details

The liquid crystalline sample 6CHBT, used in this study was synthesized at the Institute of Applied Sciences and Chemistry, Military University of Technology, Warsaw, Poland. The GNPs obtained from Plasma Chem, GmbH, Berlin were used without any additional treatments. The desired LC composites were prepared by adding 0.05 wt.% of GNPs to 6CHBT. Chloroform ($CHCl_3$) was used to dissolve both 6CHBT and GNPs which was then ultrasonicated at a temperature 10 °C above the nematic to isotropic liquid (N-I) transition temperature for 300 min approximately. The dispersions of LC and GNPs in $CHCl_3$ were then heated to make the solvent evaporate slowly and hence giving out the required dispersed medium. Differential Scanning Calorimeter (DSC) has been used to characterize the pristine and dispersed samples. The thermodynamic study of the pristine and dispersed samples has been carried out on a DSC of NETZSCH model DSC-200-F3-Maia.

For the dielectric measurements, electrical cells in the form of parallel plate capacitor were prepared using ITO and gold coated glass plates as electrodes having sheet resistance less than 25 Ω/cm^2, using 10 μm and 40 μm thick mylar spacers. For keeping the electrodes separated by a distance equal to the thickness of the mylar spacers, the electrodes are clamped on a brass sample holder by using screws. We have not used any adhesives for this purpose because they have their own dielectric response. The active capacitance (C_L) was determined by using organic liquid of known dielectric permittivity (cyclohexane), into the cell. Capacitance (C) and conductance (G) of the cell filled with material were determined in the frequency range 1 Hz to 35 MHz using N4L's phase sensitive multi meter (model PSM-1735) coupled with impedance analysis interface (model IAI-1257). A measuring electric field of 0.5 V_{rms} has been applied across the material. Acquired values of C and G were used to determine the frequency dependent dielectric permittivity (ε') and dielectric loss (ε'') [10] as follows:

$$\varepsilon' = \left(\frac{C_m - C_a}{C_L}\right) + 1 \tag{15.1}$$

$$C_L = \left(\frac{C_l - C_a}{\varepsilon_l}\right) \tag{15.2}$$

$$\varepsilon'' = \left(\frac{G_m - G_a}{\omega C_L}\right) = \frac{\sigma}{\varepsilon_o \omega} \tag{15.3}$$

where C_m and G_m are the measured capacitance and conductance of the cell filled with material, C_a and G_a are the measured capacitance and conductance of the cell without any material i.e. with air, C_l is the measured capacitance with standard liquid (in this case cyclohexane) in the cell and ε_l is the dielectric permittivity of the standard liquid filled in the cell. C_L is the live or geometrical capacitance of the cell. Further details about the experiments can be found in our previous articles [11, 12].

15.3 Results and Discussions

The thermal studies of the pure and dispersed samples have been carried out by using DSC. Figure 15.1 displays the thermograms showing the variation of heat flow (mW) with temperature (°C) for the pure and dispersed samples. From the comparisons of the thermodynamic data of the pure and dispersed samples, it has been observed that in the heating cycle, the transition temperatures for Cr–N and N–I transitions of the dispersed sample are decreased as compared to those of the pure sample. While in the cooling cycle, the transition temperatures for I–N and N–Cr transitions of the dispersed sample are increased as compared to those of the pure sample. The increase of transition temperature for the exothermic cycle signifies the increased stability of the nematic phase and may be due to the increase in order parameter of the LCs because of the doping of GNPs.

From the comparisons of the thermograms of the pure and dispersed samples, it has been also observed that the transition processes are becoming fast due to dispersion of GNPs as evidenced from the width of the peaks of different transitions of the pure and dispersed samples as shown in Fig. 15.1.

Figure 15.2 show the variation of longitudinal (when the extraordinary axes of the LC molecules are parallel to the measuring electric field) and transverse components (when the extraordinary axes of the LC molecules are normal to the measuring electric field) of the dielectric permittivity with common reduced temperature. From the comparison of the dielectric data of the pure and dispersed samples, it has been observed that the longitudinal component of the dielectric permittivity in the nematic (N) phase of the dispersed sample is decreased as compared to that of the pure sample. The value of the transverse component of the dielectric permittivity in the N phase is almost unchanged due to the dispersion of GNPs. The decrease in the value of the longitudinal component of the dielectric permittivity may be associated with the

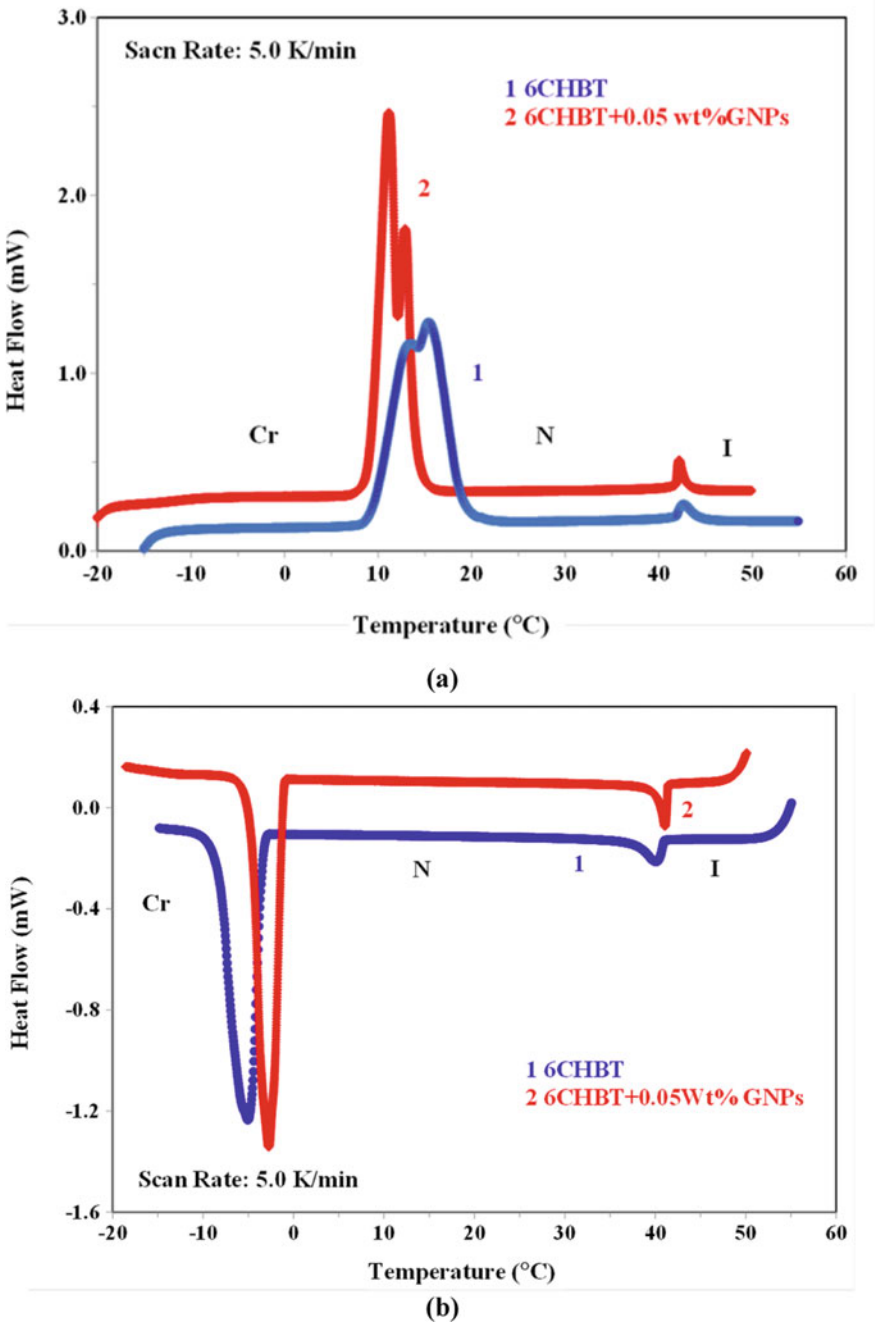

Fig. 15.1 DSC thermograms for the pristine and GNPs dispersed 6CHBT at the scan rate of 5.0 K/min for **a** Heating (endothermic) cycle, **b** Cooling (exothermic) cycle. Cr, N and I stand for crystal, nematic and isotropic liquid phase respectively

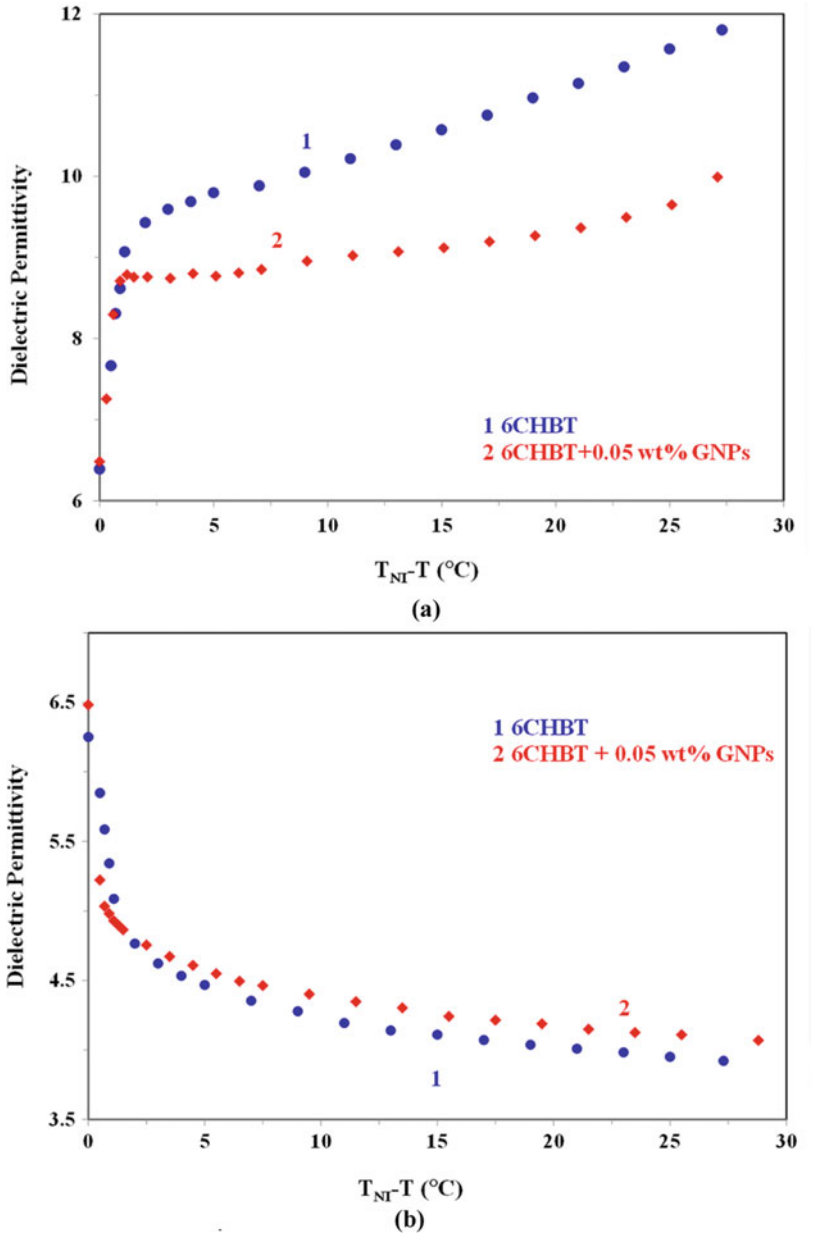

Fig. 15.2 **a** Variation of the longitudinal ($\varepsilon'_{\parallel}$) component of the dielectric permittivity of the pure and dispersed 6CHBT with common reduced temperature (T_{NI}-T (°C)). **b** Variation of the transverse ($\varepsilon'_{\perp}$) component of the dielectric permittivity of the pure and dispersed 6CHBT with common reduced temperature (T_{NI}-T (°C)). Circles (blue) and Rhombus (red) are representing the pure and dispersed data respectively

reduction in number density of LC molecules due to the dispersion of GNPs as from the Maier and Meier theory [13], $\varepsilon'_{\parallel}$ is directly proportional to number density of LC molecules. From the analysis of the dynamic dielectric data for the pure and dispersed samples, it has been observed that for both of the samples a relaxation mechanism corresponding to rotation of molecules about their short axes is observed in the low MHz frequency range. From the comparison of the relaxation frequencies of this relaxation mechanism, it has been observed that the relaxation frequency of this relaxation mechanism for the dispersed sample is increased as compared to those for the virgin sample. The increase in relaxation frequency due to the dispersion of GNPs can also be related with the reduction in number density of LC molecules. Due to reduction of number density, LC molecules will take less time to rotate about their short axes which consequently increase the relaxation frequency as relaxation frequency is reciprocal of relaxation time.

15.4 Conclusions

All the phase transition temperatures of the dispersed sample are decreased in the heating cycle and increased in the cooling cycle as compared to those of the virgin sample. The longitudinal component of the dielectric permittivity of the dispersed sample is decreased as compared to that of the pure sample. The reduction in the longitudinal component of the dielectric permittivity of the dispersed sample may be attributed to the decrease of number density of LC molecules due to the dispersion of GNPs. The relaxation frequency of an observed relaxation mechanism corresponding to the rotation of molecules about their short axes is increased as compared to those of the pure sample owing to the decrease of relaxation time.

References

1. H. Qi, T. Hegmann, Liq. Cryst. Tod. **20**, 102–114 (2011)
2. H.K. Bisoyi, S. Kumar, Chem. Soc. Rev. **40**, 306–319 (2011)
3. M.J. Cho, H.G. Park, H.C. Jeong, J.W. Lee, Y.H. Jung, D.H. Kim, J.H. Kim, J.W. Lee, D.S. Seo, Liq. Cryst. **41**, 761–767 (2014)
4. H. Yoshida, K. Kawamoto, H. Kubo, T. Tsuda, A. Fujii, S. Kuwabata, M. Ozaki, Adv. Mater. (Deerfield Beach, Fla.), **22**, 622–626 (2010)
5. K. Bourzac, Nature **493**, 283 (2013)
6. J. Prakash, A. Choudhary, A. Kumar, D.S. Mehta, A.M. Biradar, Appl. Phys. Lett. **93**, 11294 (2008)
7. L. Marino, S. Marino, D. Wang, E. Bruno, N. Scaramuzza, Soft Matter **10**, 3842 (2014)
8. M. Inam, G. Singh, A.M. Biradar, D.S. Mehta, AIP Adv. **1**, 042162 (2011). https://doi.org/10.1063/1.3668125
9. S.C. Sharma, R.A. Ramsey, Physica B **405**, 499 (2010)
10. M.B. Pandey, R. Dhar, V.K. Agrawal, R.P. Khare, R. Dabrowski, Phase Transitions **76**, 945–958 (2003)

11. M.C. Rath, S.K. Sarkar, V.K. Wadhawan, R. Verma, I.M.L. Das, R. Dabrowski, M. Tykarska, R. Dhar, Opto-Electron. Rev. **16**, 399 (2008)
12. R. Verma, R. Dhar, M.C. Rath, S.K. Sarkar, V.K. Wadhawan, R. Dabrowski, M.B. Tykarska, J. Disp. Tech. **6**(1), 8–13 (2010)
13. W. Maier, G. Meier, Z. Naturforsch. **16A**, 262–267 (1961)

Chapter 16
GPS Device Based Equatorial Plasma Bubbles (EPB) Analysis on Radio Wave Propagation Over Low Latitude

Adarsh Kumar

Abstract Radio wave propagation through space has been a topic of research for more than a century now. However, recent advancements in application of satellite navigation have generated renewed interest in this subject. Equatorial plasma bubble (EPB) is a unique phenomenon that occurs in equatorial and low latitude ionosphere during post sunset hours. Forecasting the hazardous effects of EPBs on trans-ionospheric electromagnetic signals is the current research problem. Global positioning system (GPS) signals, when pass through such irregularities, experience rapid fluctuations in phase and amplitude. The amplitude/phase fluctuations are called scintillations. Total delay of the signal due to ionospheric electron density can be represented as total electron content (TEC). The signal also exhibits steep changes in TEC during scintillations. Thus, the EPB manifest variations in scintillations and TEC in GPS signal. Using observation records from a dual frequency GPS Receiver 'GSV4004B' installed at Gadanki, both the parameters have been studied to find out the effect of EPBs on the signal.

16.1 Introduction

Ionosphere is the ionized component of Earth's upper atmosphere that can affect the radio wave propagation [1, 2, 26]. Solar radiation is the major cause production of ionization in ionosphere [3]. Ionosphere research has been going on to quantify several phenomena and related variability of the plasma involving several scales and dimensions [4, 5]. The ionosphere has been a topic of interest and hence lots of research is going on as it affects the electromagnetic waves (radio wave) and also a natural laboratory to study the physics of plasma [6]. Ionosphere exhibits electron density irregularities predominantly in E-region during day time and in F-region during night time that makes the ionosphere research more interesting [7, 8]. Equatorial ionosphere exhibits several interesting phenomena like equatorial electro

A. Kumar (✉)
Department of Physics, Amity Institute of Applied Sciences, Amity University Noida, Noida, UP 201313, India
e-mail: akumar25@amity.edu

V. K. Jain et al. (eds.), *Recent Trends in Materials and Devices*, Springer Proceedings in Physics 256, https://doi.org/10.1007/978-981-15-8625-5_16

jet (EEJ), equatorial ionization anomaly (EIA), equatorial plasma bubbles (EPB) etc. that occur in natural plasma owing to the special geometry of geomagnetic field [9]. Indian lies in the north of the geomagnetic equator which passes through Trivandrum [10]. Therefore, this special geometry of horizontal magnetic field gives rise to currents and electric field that modify the low latitude electrodynamics of the plasma density [11, 12].

Equatorial plasma bubbles (EPB) is a night time ionospheric phenomena. EPB causes irregularities in electron density throughout the equatorial and low latitude F region [13]. They affect the radio signal and also degrade the performance of GPS [14]. After sunset when rate of ionization production becomes less in E layer, recombination process takes place [15]. Thus just after sunset, the F-region electron density become suddenly larger than the E-region and valley region electron density. There is uplifting of F layer during post sunset by the pre reversal enhancement [16]. Random fluctuation in phase/amplitude of radio signal when it passes through ionosphere due to irregularities in electron densities is referred as ionospheric scintillation [17]. Ionospheric scintillations are caused by major phenomena of ionosphere known as equatorial plasma bubbles [18]. Majorly, scintillations occur due to electron density irregularities in the F-region. Rapid change in phase of signal called phase scintillation generally large near equatorial and higher latitudes, which results in variation in refractive index of ionospheric medium. On the other hand, fluctuation in amplitude of signal is called amplitude scintillation, which mostly occurs at lower latitudes [19]. Scintillation depends on various factors, operating frequency, local time, geographical location, solar cycle, season etc. [20, 21]. Amplitude Scintillation index S4 is given by following Sau et al. [21].

$$\text{Amplitude Scintillation index S4} = \sqrt{\frac{\langle I^2 \rangle - \langle I \rangle^2}{\langle I \rangle^2}}$$

where, I is the signal intensity, S4 > 0.6 said to be strong scintillation and less than this called as weak scintillation. To determine the scintillations, occurring in ionosphere total electron content (TEC) plays an important role [22], which is nothing but total number of electrons along a tube of one meter squared cross section along line of sight of satellite to receiver. Mathematically it can be defined as integration of electron density with location along path ds through ionosphere, hence TEC is path dependent.

$$\text{TEC} = \int n_e(s)\, \mathrm{d}s$$

where, n_e is electron density and ds is surface element. The unit of total electron content i.e. TECU can be defined as 1 TECU = 10^{16} electrons per meter square [23].

16.2 Observations and Methodology

The equatorial plasma bubbles occurring in equatorial and low latitude ionosphere produce major impact on radio wave propagation. Signals from navigation satellites like GPS and other satellites gets affected by scintillation and excess delay due to ionosphere. The variations in the electron density degrades the strength of received radio signal and this leads to positioning error.

Dual frequency GPS receiver has been used for the current study to measure total electron content along the path from GPS satellite to receiver called total electron content (TEC). Strong irregularities have been seen at equatorial regions due to the fact that near equator geomagnetic field lines become horizontal and gives rise to unique phenomena known as equatorial plasma bubbles. Irregularities in ionosphere majorly observed at night time with TEC and airglow depletion called bubbles.

This paper aims to study major phenomena of the equatorial ionosphere and observe the manifestation of EPBs using GPS. The present work of ionospheric phenomena (EPBs) is done with data analysis of 16 days of data and plots are made using MATLAB software. GPS data of 02 January 2014, 4–7 March 2014 and 20 March–30 March 2014 was utilized for the present work.

Scintillations and TEC are plotted using MATLAB Software. For the subplots, elevation angle is taken greater than 30° in order to reject multipath related noise in TEC and Scintillation plots. And also Slant TEC has been converted to Vertical TEC, vertical TEC is found better because it does not depend on elevation angle. Then, values of vertical TEC less than 0 has been ignored.

16.3 Results and Discussion

Radio signals are affected by ionosphere [20, 23]. GPS is the system that not only provides position and navigation all over globe at any time but also a good tool to study the ionospheric phenomena [24]. In present study we represent the fluctuations in phase/altitude (scintillations) of radio signal when passes through ionosphere and changes in total electron contents (TEC) as measured with GPS. TEC from GAGAN SBAS (55°E and 83°E) PRN 127,128 was also measured, since for estimation of TEC, measurements, only two frequencies are required. Elevation angle of GAGAN satellite for PRN 127 and 128 has been fixed as about 58° and 74° respectively. GAGAN SBAS (Satellite Based Augmentation System) has been chosen for the experimental TEC and S4 data because it is Geostationary GPS Satellites. In figures, the first panel of each plot represents vertical TEC for all GPS satellites whereas second panel shows scintillation index for all GPS satellites, third panel shows scintillation index for GAGAN SBAS PRN 127 and last fourth panel shows scintillation index for GAGAN SBAS PRN 128 versus IST (Hours).

Scintillations can be divided in three categories (i) minor (ii) moderate (iii) Strong respectively corresponding to S4 index <= 0.17, 0.17 < S4 < 0.3 and S4 >= 0.45.

We found that in almost all night of March 2014, scintillations occurred with varying category. The depletion structures in TEC corresponding to scintillation has also been simultaneously observed from GPS. However, the GAGAN satellite shows mismatch between GPS-TEC depletions and GAGAN Scintillation occurrences. This can happen so because the line of sight between GAGAN satellites and the GPS receiver at Gadanki may not be crossing the EPBs at the same time [27]. As given above, the GAGAN satellite is geostationary and therefore, when the EPBs move across this stationary line of sight, scintillations are observed. Thus the EPBs manifest as TEC depletions and Scintillation in GPS signal simultaneously but with different values when seen from GAGAN satellites. This manifestation is important from point of view of forecasting the occurrence and strength of EPBs and scintillations using GPS data along with GAGAN satellite based augmentation system (SBAS). Thus, the observation presented in the paper show the manifestation of EPBs in GPS and GAGAN satellite signals [27].

It is clear from Fig. 16.1 that on 02 January 2014, S4 index was found to be similar in GPS as well as in GAGAN PRN 127 and 128 derived observations. It is observed that there is no scintillation found on day 02 Jan 2014. However, VTEC was found to be increased between 05:00 h to 20:00 h IST. Major fluctuations in S4 index in GPS observations as well as in GAGAN 127 and 128 observations were found between 20:00 h to 02:00 h IST (Fig. 16.2) on 04 March 2014. However, GPS derived TEC was found to be increased from 05:00 h, becoming steady between 10:00 h to 20:00 h and then further decreasing continuously till 05:00 h is reached (Fig. 16.2). It is clear from first panel of Fig. 16.3 that S4 index remains well below 0.1 throughout the

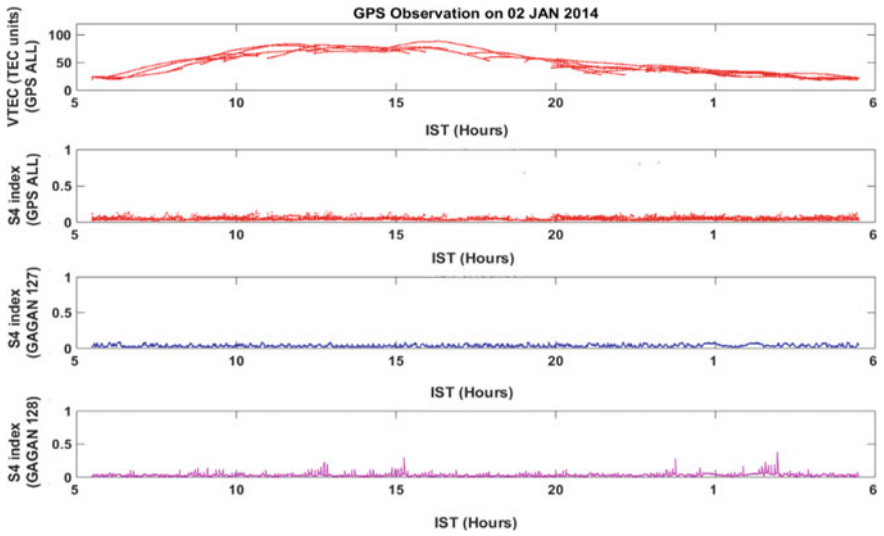

Fig. 16.1 GPS Observations on 02 JAN 2014 in IST (hours), First panel represents VTEC for all GPS Satellites versus IST (hours). Second panel shows S4 index for all GPS Satellites, whereas third and fourth panels display S4 index for GAGAN PRN 127 and 128 respectively

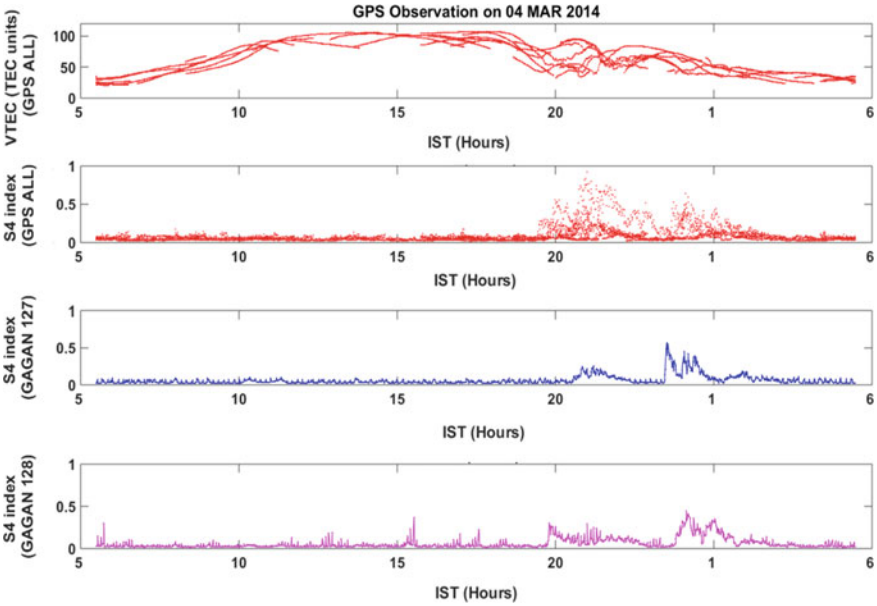

Fig. 16.2 GPS Observation on 04 MARCH 2014, Descriptions of all the panels are same as that of Fig. 16.1

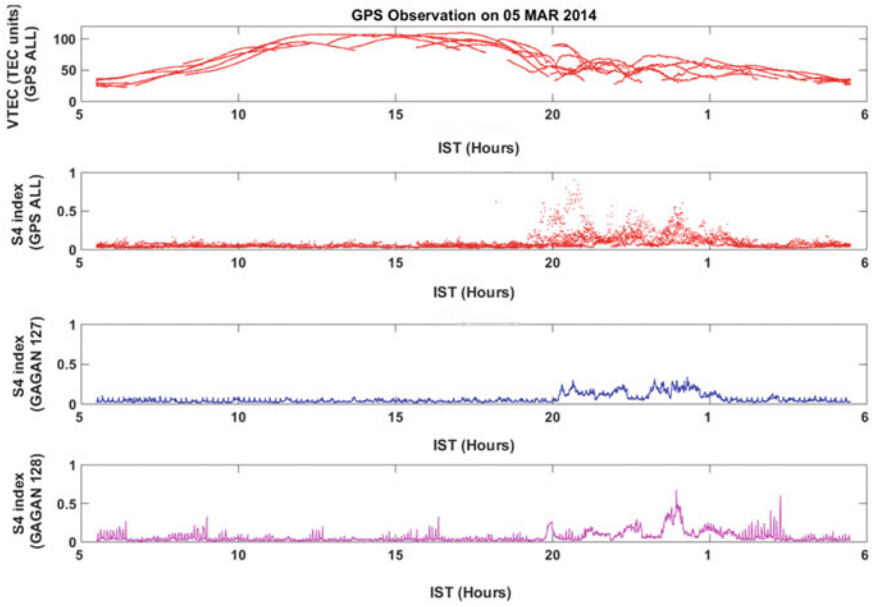

Fig. 16.3 GPS Observation on 05 March 2014

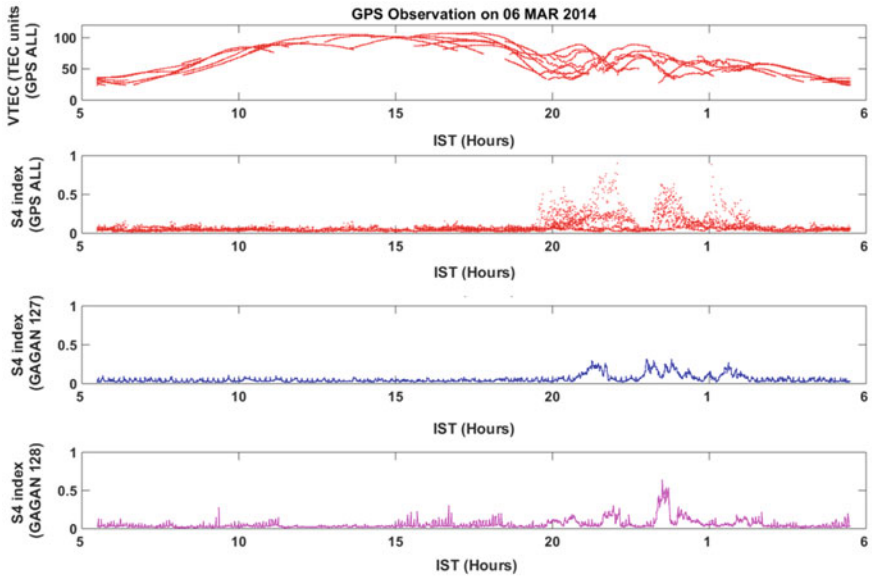

Fig. 16.4 GPS Observation on 06 March 2014

day. This day marks a "No Scintillation" day and hence manifest that there were no EPBs between 75° and 82°E longitude on that night [25].

On 05–07 March 2014, almost similar observations were found as that of 04 March 2014 (Figs. 16.3, 16.4 and 16.5). It is clear from Fig. 16.6 that GPS derived S4 index was found to be prominent as compared to the GAGAN derived S4 results. Figure 16.7 shows that GAGAN SBAS derived S4 data observations were varying with GPS S4 index between 20:00 h to 03: Hours IST, showing the night time effects. Figure 16.8 displays the similar results on 22 March 2014 as that of 21 March 2014. Figure 16.9 shows depletions in GPS derived VTEC on 23 March 2014 between 20:00 h to 01:00 h, which clearly shows the EPB effects. On 24 March 2014, clear variations were found in S4 index for GPS as well as GAGAN derived observations between 20:00 h to 02:00 h IST (Fig. 16.10). Figure 16.11 displays the similar results on 25 March 2014 as that of 24 March 2014 (Fig. 16.10). It is clear from Fig. 16.12 that depletions in GPS derived VTEC were found on 26 March 2014 with enhancing S4 index of GPS as well as GAGAN SBAS observations. Figure 16.13 exhibits marked enhancements in S4 index along with decrease in VTEC between 20:00 h to 01:00 h IST on 27 March 2014, which further establishes the phenomenon of EPB. On March 28-30, 2014 (Figs. 16.14, 16.15 and 16.16), GPS and GAGAN derived observations were found to be similar as that of 27 March 2014. One important feature of all the observations was that marked variations in S4 index occur between 20:00 h and 02:00 h IST in the night time, however, the VTEC was found to have its maximum development during day time noon hours. This is an important result as ionization sources due to solar radiation are maximum during noon hours, whereas

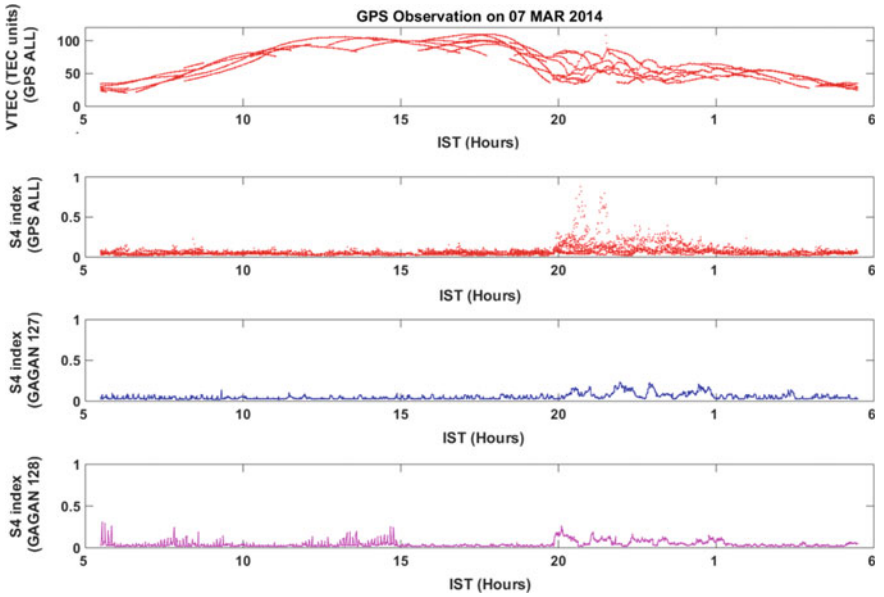

Fig. 16.5 GPS Observation on 07 March 2014

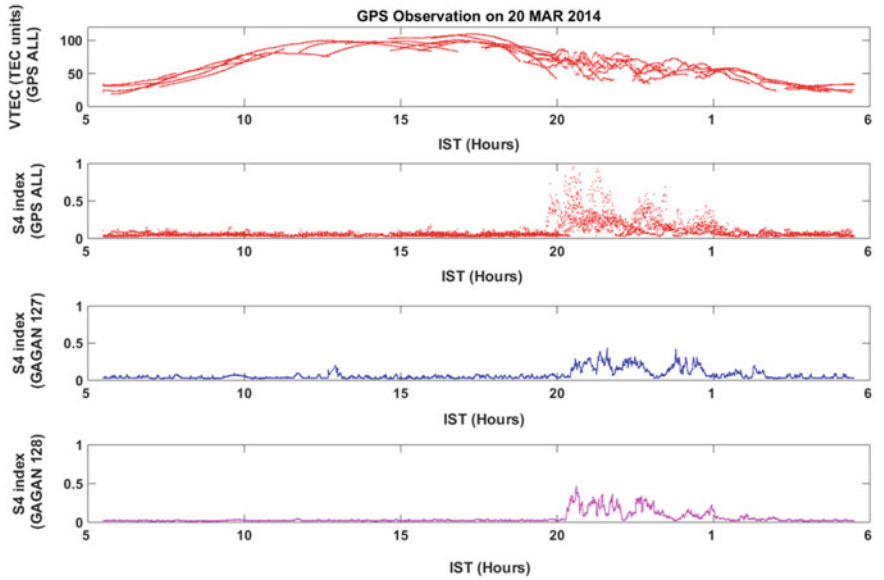

Fig. 16.6 GPS Observation on 20 March 2014

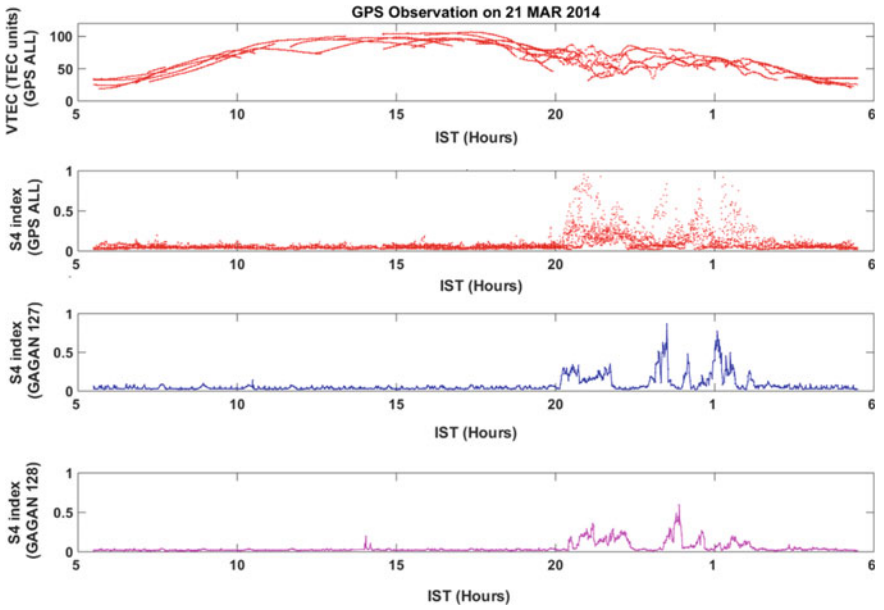

Fig. 16.7 GPS Observation on 21 March 2014

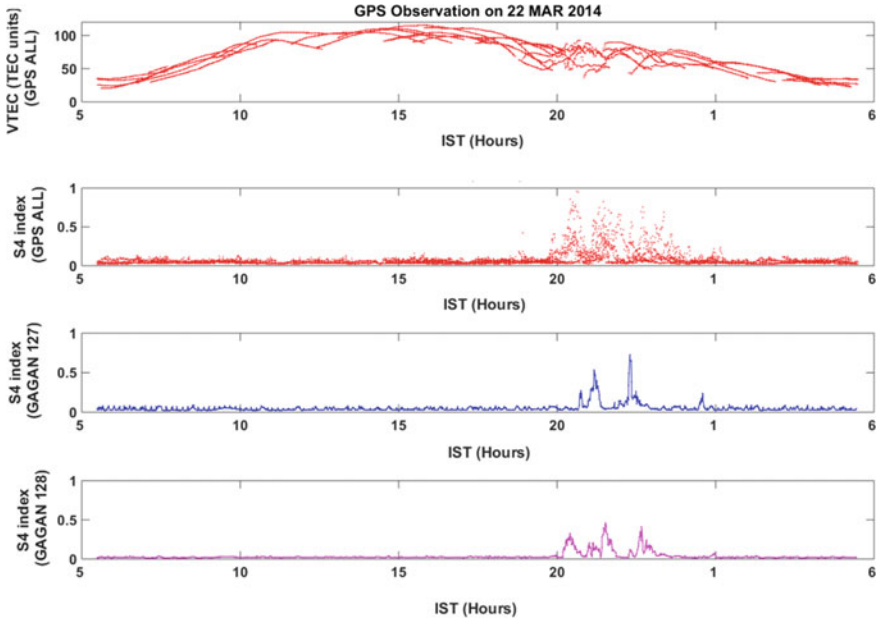

Fig. 16.8 GPS Observation on 22 March 2014

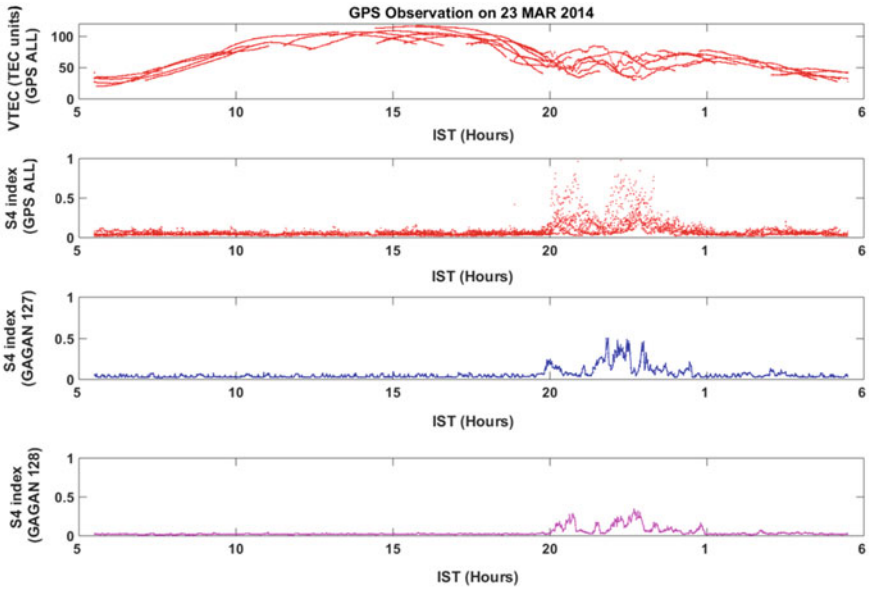

Fig. 16.9 GPS Observation on 23 March 2014

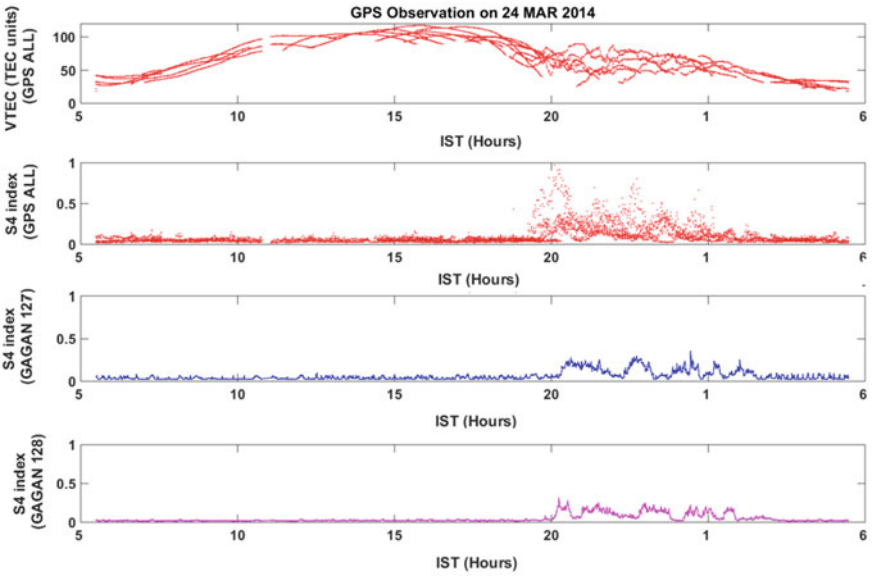

Fig. 16.10 GPS Observation on 24 March 2014

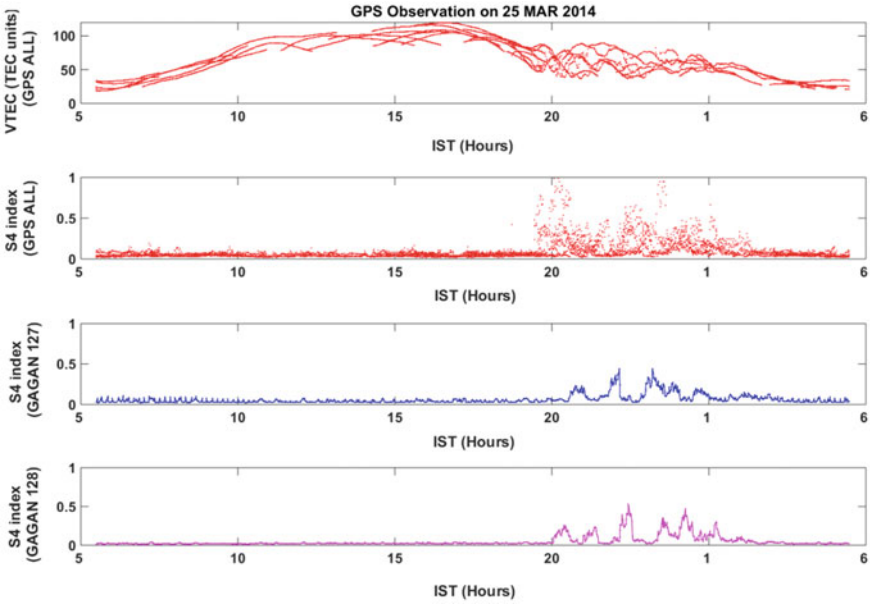

Fig. 16.11 GPS Observation on 25 March 2014

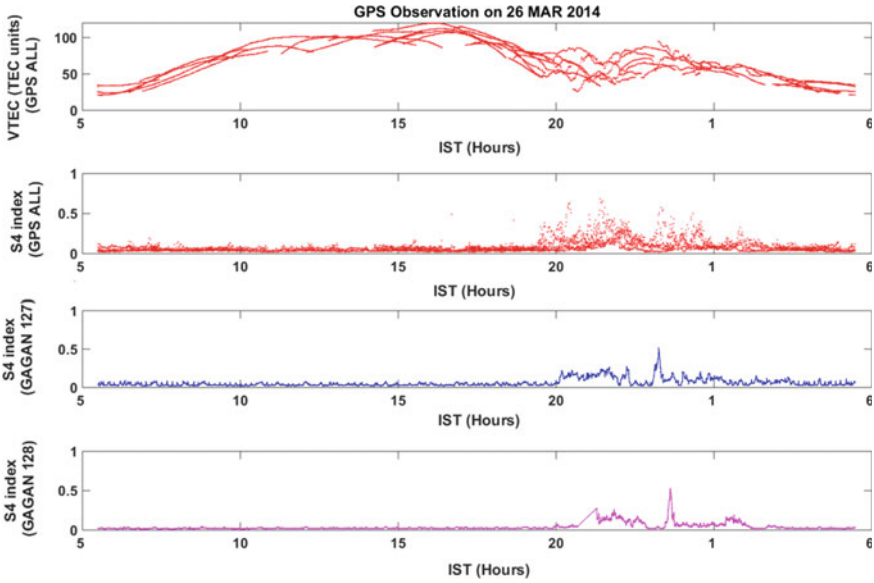

Fig. 16.12 GPS Observation on 26 March 2014

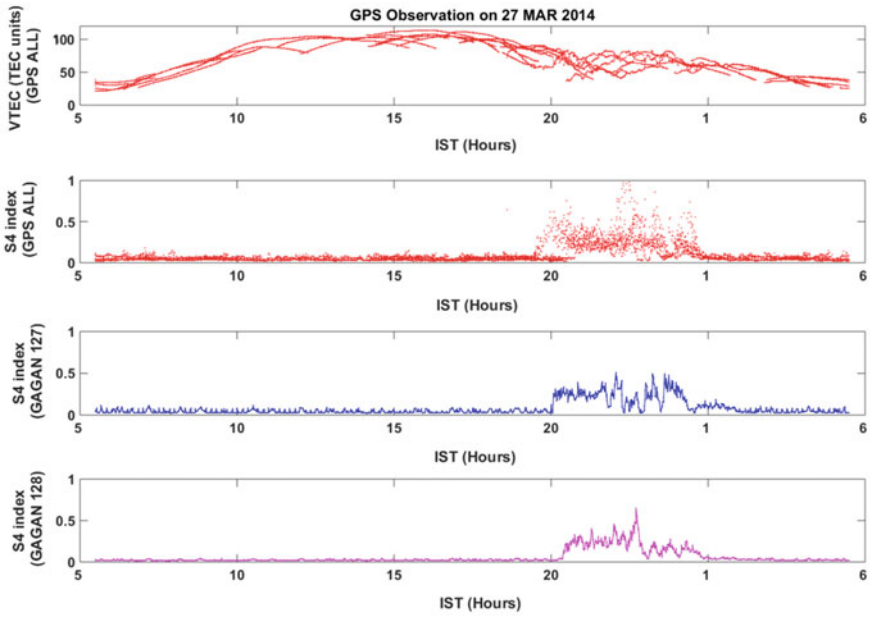

Fig. 16.13 GPS Observation on 27 March 2014

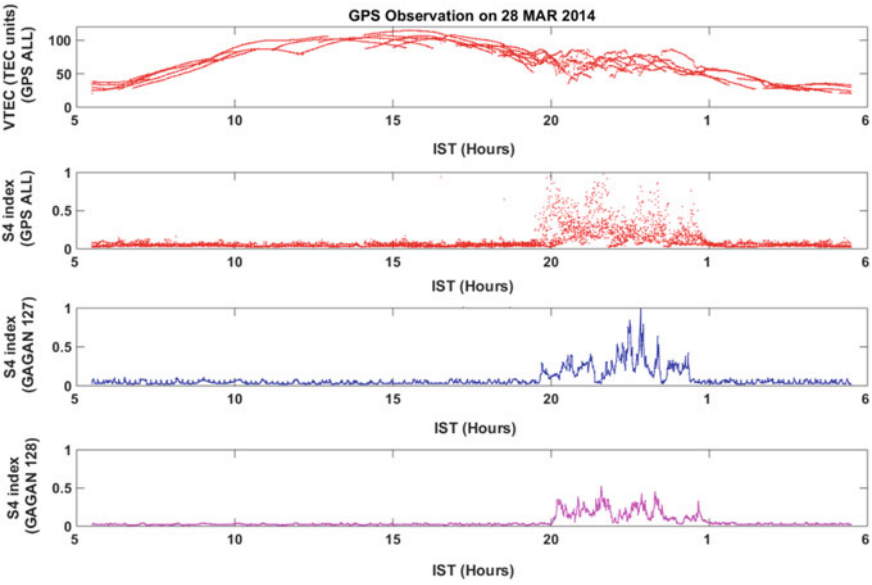

Fig. 16.14 GPS Observation on 28 March 2014

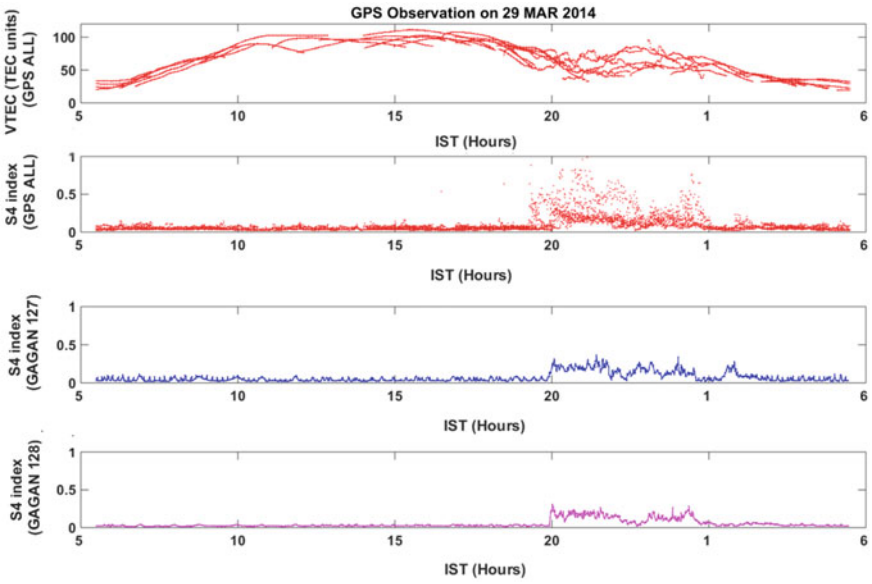

Fig. 16.15 GPS Observation on 29 March 2014

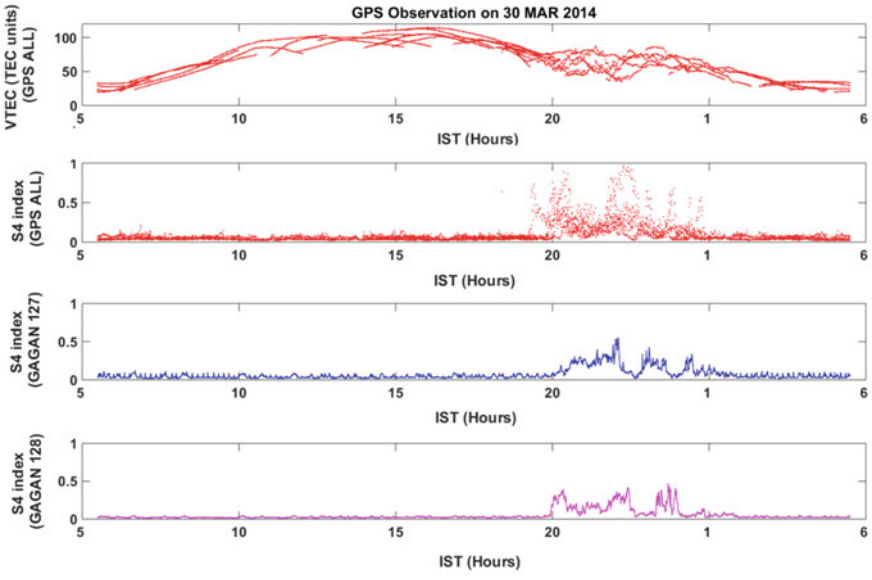

Fig. 16.16 GPS Observation on 30 March 2014

ionized sources are minimized during night hours [26]. Such effect was clearly found in our results obtained at low latitude region of Indian ionosphere.

16.4 Conclusions

Present work highlights detailed aspects of equatorial ionospheric phenomena and provide its manifestation using GPS. In GPS signal this manifestation is found to occur in TEC depletions as well as Scintillations. Scintillation index (S4) data at L1 band frequency 1575.42 MHz and GPS TEC data were used for the present work.

Main conclusions are as follows:

(1) When there is no scintillation or TEC depletions in GPS observations, it can be found that there was no event of EPB on that night in that region.
(2) Strong scintillations are found during night time after 19.5 IST on most of the night of March 2014. Scintillations are highly correlated with TEC depletions when seen from GPS.
(3) When seen from GAGAN satellites, the scintillations from 127 and 128 PRN show mismatch with GPS observed TEC depletions. This has been explained with geometry of line of sight of the GAGAN satellites versus GPS satellite for a given time.

Acknowledgements The corresponding author is thankful to Director, National Atmospheric Research Laboratory (NARL), Gadanki, Andhra Pradesh (India) for providing necessary experimental facilities for GPS measurements. Fruitful discussions with his colleague scientists to prepare and improve the manuscript are highly grateful and acknowledged.

References

1. S.J. Adebiyi, O.O. Odeyemi, I.A. Adimula, O.A. Oladipo, S.O. Ikubanni, B.O. Adebesin, B.W. Joshua, GPS derived TEC and foF2 variability at an equatorial station and the performance of IRI-model. J. Adv. Space Res. **54**(4):565–575 (2014)
2. S. Arunpold, N. Tripathi, R. Chowdhary, V.R. Chowdhary, D.K. Raju, Comparison of GPS-TEC measurements with IRI-2007 and IRI-2012 modeled TEC at an equatorial latitude station, Bangkok, Thailand. J. Atmos. Sol. Terr. Phys. **117**, 88–94 (2014)
3. P.K. Bhuyan, R. Hazarika, GPS TEC near the crest of the EIA at 95E during the ascending half of solar cycle 24 and comparison with IRI simulations. Adv. Space Res. **52**(7), 1247–1260 (2013)
4. D. Bilitza, D. Altadill, Y. Zhang, C. Mertens, V. Truhlik, P. Richards, L.A. McKinnell, B. Reinisch, The International Reference Ionosphere 2012–a model of international collaboration. J. Space Weather Space Clim. **4**(A07), 1–12 (2014)
5. A.A. Chernyshov, D.V. Chugunin, M.M. Mogilevsky, A.A. Petrukovich, Studies of the ionosphere using radiophysical methods on ultra-small spacecrafts. Acta Astronaut. **167**, 455–459 (2020)

6. N. Dashora, R. Pandey, Observation in equatorial anomaly region of total electron content enhancements and depletion. Ann. Geophys. (EGU) **23**, 2449–2456 (2005)
7. J. Feltens, M. Angling, N. Jackson-Booth, N. Jakowski, M. Hoque, M. Hernández-Pajares, Á. Aragón, Á. María, R. Orús-Pérez, Comparative testing of four ionospheric models driven with GPS measurements. Radio Sci. **46**(6), RS0D12 (2011)
8. R. Jin, S. Jin, G. Feng, M_DCB: Matlab code for estimating GNSS satellite and receiver differential code biases. GPS Solut. **16**(4), 541–548 (2012)
9. R. Kakoty, S. Bora, P.K. Bhuyan, Spatial asymmetry in topside ion density and vertical E × B plasma drift velocity within 75°E–95°E. Adv. in Space Res. **63**(3), 1176–1191 (2019)
10. S.P. Karia, N.C. Patel, K.N. Pathak, Comparison of GPS based TEC measurements with the IRI-2012 Model for the period of low to moderate solar activity (2009–2012) at the crest of equatorial anomaly in Indian region. Adv. Space Res. **55**(8), 1965–1975 (2015)
11. H.B. Lee, G. Jee, Y.H. Kim, J.S. Shim, Characteristics of global plasmaspheric TEC in comparison with the ionosphere simultaneously observed by Jason-1 satellite. J. Geophys. Res. **118**(2), 935–946 (2013)
12. S.K. Leong, T.A. Musa, K. Omar, M.D. Subari, N.B. Pathy, M.F. Asilam, Assessment of ionosphere models at Banting: Performance of IRI- 2007, IRI-2012 and Ne-Quick 2 models during the ascending phase of Solar Cycle 24. J. Adv. Space Res. **55**(8), 1928–1940 (2015)
13. Z. Li, Y. Yuan, N. Wang, M. Hernandez-Pajares, X. Huo, SHPTS: towards a new method for generating precise global ionospheric TEC map based on spherical harmonic and generalized trigonometric series functions. J. Geodesy **89**(4), 331–345 (2015)
14. C.H. Lin, J.Y. Liu, H.F. Tsai, C.Z. Cheng, Variations of the equatorial ionization anomaly peaks in the west pacific region during the April 6 and July 15, 2000 geomagnetic storms. Earth Planets Space **59**(5), 401–405 (2007)
15. K. Liu, G. Li, B. Ning, Possible evidence for small-scale wave seeding of equatorial plasma bubbles. Adv. Space Res. **63**(11), 3612–3620 (2019)
16. W. Luo, Z. Liu, M. Li, A preliminary evaluation of the performance of multiple ionospheric models in low- and mid-latitude regions of China in 2010–2011. GPS Solut. **18**(2), 297–308 (2014)
17. O.A. Maltseva, N.S. Mozhaeva, O.S. Poltavsky, G.A. Zhbankov, Use of TEC global maps and the IRI model to study ionospheric response to geomagnetic disturbances. Adv. Space Res. **49**(6), 1076–1087 (2012)
18. D. Okoh, L. McKinnell, P. Cilliers, P. Okeke, Using GPS-TEC data to calibrate VTEC computed with the IRI model over Nigeria. Adv. Space Res. **52**(10), 1791–1797 (2013)
19. S.K. Panda, S.S. Gedam, G. Rajaram, Study of Ionospheric TEC from GPS observations and comparisons with IRI and SPIM model predictions in the low latitude anomaly Indian sub continental region. J. Adv. Space Res. **55**(8), 1948–1964 (2015)
20. A.B. Rabiu, A.O. Adewale, R.B. Abdulrahim, E.O. Oyeyemi, TEC derived from some GPS stations in Nigeria and comparison with the IRI and Ne Quick models. J. Adv. Space Res. **53**(9), 1290–1303 (2014)
21. S. Sau, V.L. Narayanan, Gurubaran S., K. Emperumal, Study of wave signatures observed in thermospheric airglow imaging over the dip equatorial region. Adv. Space Res. **62**(7), 1762–1774 (2018)
22. L.A. Scidá, R.G. Ezquer, M.A. Cabrera, M. Mosert, C. Brunini, D. Buresova, On the IRI 2007 performance as a TEC predictor for the South American sector. J. Atmos. Sol. Terr. Phys. **81–82**, 50–58 (2012)
23. A.K. Sharma, O.B. Gurav, G.A. Chavan, H.P. Gaikwad, R.N. Ghodpage, P.T. Patil, Variation in occurrence of equatorial plasma bubbles (EPBs) using All Sky Imager from low latitude station Kolhapur (16.8 °N, 74.2 °E, 10.6° dip. Lat.). Adv. Space Res. **60**(11), 2452–2463 (2017)
24. V.K.D. Srinivasu, N. Dashora, D.S.V.V.D. Prasad, N. Niranjan, S. Gopi Krishna, On the occurrence and strength of multi-frequency multi-GNSS Ionospheric Scintillations in Indian sector during declining phase of solar cycle 24. Adv. Space Res. **61**(7), 1761–1775 (2018)
25. Y. Xiang, Y. Yuan, Z. Li, N. Wang, Analysis and validation of different global ionospheric maps (GIMs) over China. J. Adv. Space Res. **55**(1), 199–210 (2015)

26. A.E. Yeboah, I. Paulino, A.F. Medeiros, R.A. Buriti, C.M. Wrasse, Seasonal variation of plasma bubbles during solar cycle 23–24 over the Brazilian equatorial region. Adv. Space Res. **64**(7), 1365–1374 (2019)
27. I.E. Zakharenkova, IuV Cherniak, A. Krankowski, I.I. Shagimuratov, Vertical TEC representation by IRI 2012 and IRI Plas models for European mid latitudes. J. Adv. Space Res. **55**(8), 2070–2076 (2015)

Chapter 17
Magneto Tunable Defect Modes in One-Dimensional Photonic Crystal Based on Magnetic Fluid Film

Sanjeev K. Srivastava

Abstract In the present communication we theoretically investigate and study the properties of defect modes in one dimensional defective photonic crystal (PC) based on magnetic fluid film (MFF). The magnetic fluid film (MFF) is a type of stable colloidal suspensions of magnetic nanoparticles. When the MFF is subjected to an external applied magnetic field, the nanoparticles form a chain along certain direction of magnetic field and its refractive index changes; this property of MFF can be used to tune the defect modes (transmission peaks) in PC. In this study, first, we take a PC structure composed of alternate layers of TiO_2 and SiO_2 and MFF (water based $MnFe_2O_4$ nanoparticles) as a defect layer having different porosity. In second case we take, two symmetric PC structure composed of alternate layers of MFF with different porosity and the effect of magnetic field on the surface mode (acts as a defect mode) has been studied. In order to calculate transmission spectra, we use transfer matrix method (TMM). Investigation of transmission curves show that tunability of defect modes (transmission peaks) are greatly influenced by magnetic field factor as well as the porosity of magnetic fluid film. This type of PC structure can be used to design the optical devices such as magnetic field sensors, tunable optical grating, optical switches, tunable narrow transmission filter, wavelength division multiplexer etc.

17.1 Introduction

Photonic crystals (PCs) are a novel class of optical materials with periodic variation in dielectric constant and the period equal to optical wavelength. During the past few decades great deal of attention has been focused on theoretical and experimental research on photonic crystals. PCs have ability to control and manipulate the propagation of optical wave due to which they possess many potential applications in modern photonics [1–8]. Photonic crystals have most fundamental property of the existence of photonic band gaps (PBGs) also called as forbidden bands or stop

S. K. Srivastava (✉)
Department of Physics, Amity Institute of Applied Sciences, Amity University Uttar Pradesh, Noida 201301, India
e-mail: sanjeev17th@yahoo.co.in

V. K. Jain et al. (eds.), *Recent Trends in Materials and Devices*, Springer Proceedings in Physics 256, https://doi.org/10.1007/978-981-15-8625-5_17

bands. The frequencies or wavelengths of optical waves which fall within PBG are prohibited to propagate through the PCs. One can produce transmission mode or tunneling mode within the forbidden region by introducing the defect into conventional one-dimensional PC. The defect inside the photonic crystal can be done by changing the thickness of the layer, inserting another material into the structure or by removing a layer from normal PC structure [9–11]. The frequency (or wavelength) of transmission mode (or defect mode) can be tuned by two ways. The first one is based on changing the concentrations or ingredients of constituents' materials of Photonic crystals and second one is based on controlling the refractive indices of the materials. Refractive index of the defect layer can be controlled by changing the operating temperature, by applying an external electric and/or magnetic field or by optical illuminations and leads to various photonic devices [12–19]. The optoelectronic devices whose properties can be manipulated by varying the refractive index are much applicable because of the tunability and flexibility of the devices.

In this paper, we present the theoretical investigation and study of defect modes in one-dimensional defective photonic crystal based on the magnetic fluid film (MFF). Magnetic fluids have attracted much attention of researcher because, their refractive indices are altered by the magnetic field and also, they have versatile structural patterns under applied magnetic fields. The magnetic fluid film (MFF) also called as a colloidal ferrofluid or magnetic liquid is a type of stable colloidal suspensions of magnetic nanoparticles. When the MFF is subjected to an external applied magnetic field, the nanoparticles form a chains or column structure along the dominate direction of magnetic field and its refractive index changes [20–26]. Due to this property, MFF may be the suitable candidate materials for realizing the tunable PCs.

In this study first we take a PC structure composed of alternate layers of TiO_2 and SiO_2 and MFF as a defect layer having different porosity. In second case we take, symmetric PC structure composed of alternate layers of same MFF with different porosity and has studied the effect of magnetic field on the surface mode (acts as a defect mode). In symmetric PC structure one obtains the transmission mode or tunneling mode within the forbidden frequency region without inserting any defect in the structure.

17.2 Theoretical Model and Formulations

The schematic diagram of proposed one- dimensional PC is shown in the Fig. 17.1a, b. In Fig. 17.1a A and B represents the low (SiO_2) and high (TiO_2) refractive index materials having refractive indices n_1, n_2 and thicknesses h_1 and h_2 respectively; D represents the defect layer in the form of magnetic fluid film (MFF) with refractive index n_D and thickness h_D. In Fig. 17.1b both A and B represents the MFF with different porosity.

Since the dielectric constant (refractive index) of magnetic fluids ε_{mff} varies with external magnetic field, it is given by [27].

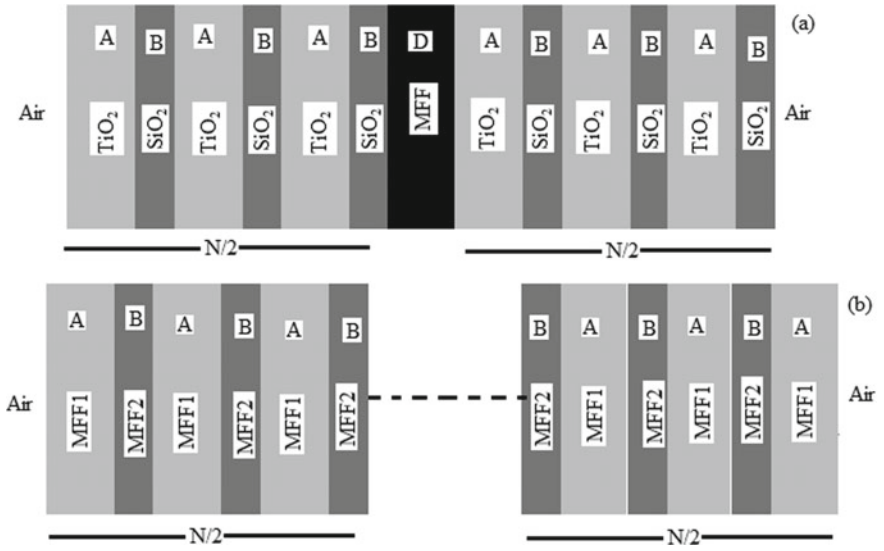

Fig. 17.1 **a**, **b** Schematic diagram of proposed one-dimensional Photonic crystal Structure

$$\frac{\varepsilon_{mff} - \varepsilon_k}{\alpha\varepsilon_{mff} + (3-\alpha)\varepsilon_k} = P\frac{\varepsilon_p - \varepsilon_k}{\varepsilon_p + 2\varepsilon_k} \tag{17.1}$$

Here, ε_k and ε_p represents the dielectric constant of the carrier liquid and magnetic nanoparticles.

In this case we use water as carrier liquid ($\varepsilon_k = 1.77$) and $MnFe_2O_4$ ($\varepsilon_p = 13.9876$) as magnetic nanoparticles, respectively. P is the volume fraction of magnetic nanoparticles and α is a function of magnetic field H and represents the factor of magnetic field H that lies in the range 0–1. The value of α tends to zero for large value of H while it tends to 1 for small value of H. Refractive index of magnetic film can be calculated by using (17.1).

For the calculation of transmission spectra we use transfer matrix method which is very effective technique to study the transmission properties of the finite PCs. The total characteristics matrix for the proposed defective PC can be represented as

$$\begin{aligned} M(h) &= (M_A M_B)^{N/2} M_D (M_A M_B)^{N/2} \\ &= \begin{bmatrix} M_{11} & M_{12} \\ M_{21} & M_{22} \end{bmatrix} \end{aligned} \tag{17.2}$$

where, M_A, M_B, and M_D are characteristic matrices of layers A, B, and D, respectively, N is the number of periodic layers and h represents thickness of unit cell.

The characteristic matrix M_j for the jth layer in the PC for transverse electric (TE), i.e. s-polarized and transverse matrix (TM) i.e. for p-polarized waves can be given as [28, 29]

$$M_j = \begin{bmatrix} \cos\delta_j & \frac{1}{iq_j}\sin\delta_j \\ -iq_j\sin\delta_j & \cos\delta_j \end{bmatrix} \tag{17.3}$$

where $\delta_j = \frac{2\pi\nu}{c} n_j h_j \cos\theta_j$, $(j = A, B, D)$ θ_j is the ray angle inside the layer j of refractive index n_j and ν is the frequency of light in the incidence medium. $q_j = \sqrt{\frac{\varepsilon_j}{\mu_j}}\cos\theta_j$, for the TE wave and $q_j = \sqrt{\frac{\mu_j}{\varepsilon_j}}\cos\theta_j$ for the TM wave and $\cos\theta_j = \sqrt{1 - \left(n_0^2\sin^2\theta_0/n_j^2\right)}$. n_0 is the refractive index of incident medium and θ_0 is the incident angle.

The transmission coefficient for TE (s-polarized) and TM (p-polarized) waves are given by [28]

$$t(s) = \frac{2q_0(s)}{(M_{11} + q_t(s)M_{12})q_0(s) + (M_{21} + q_t(s)M_{22})} \tag{17.4}$$

$$t(p) = \frac{2q_0(p)}{(M_{11} + q_t(s)M_{12})q_0(s) + (M_{21} + q_t(s)M_{22})} \tag{17.5}$$

where $M_{11,}\, M_{12}, M_{21}, M_{22}$ are the elements of the total characteristic matrix of the N period multilayer structures. The values of q_0 and q_t for TE(s) and TM (p) polarized waves are given as

$$q_0(s) = n_0\cos\theta_0; \quad q_t(s) = n_t\cos\theta_t \quad \text{and} \quad q_0(p) = \cos\theta_0/n_0 q_t(p) = \cos\theta_t/n_t$$

Here, n_t is the refractive index of the substrate and θ_t ray angle inside it. Finally, the transmittance of the proposed PC structure can be obtained by using the expression:

$$T(s, p) = \frac{q_t}{q_0}|t(s, p)|^2 \tag{17.6}$$

17.3 Results and Discussions

In this section, we numerically compute the transmission spectrum of the proposed defective PC by using the MATHCAD software.

The proposed structures have the form: (1) ir/$(AB)^{N/2}D(AB)^{N/2}$/air, and (2) air/$(AB)^{N/2}(BA)^{N/2}$/air at normal incidence angle. In the first case A and B represent SiO_2 and TiO_2 with refractive indices $n_1 = 1.46$ and $n_2 = 2.4$, respectively, while, D represents the $MnFe_2O_4$ magnetic fluid film as a defect layer of different porosity i.e. of different volume fraction, while in the second case A and B represent $MnFe_2O_4$ magnetic fluid film of different porosity. The thicknesses of the alternate layers are taken as quarter wave stack condition $n_1h_1 = n_2h_2 = \frac{\lambda_0}{4}$ where λ_0 (=600 nm) is

the central wavelength, whereas thickness of defective MFF layer is chosen as $h_D = (h_1 + h_2)/2$. In second case thickness of MFF layers are also taken as using the same condition but refractive indices correspond to the value at $\alpha = 0$. Figures 17.2, 17.3 and 17.4 show the transmission curves for $n_1 = 1.46$ (SiO_2), $n_2 = 2.4$ (TiO_2), $h_1 = 102.7$ nm, $h_2 = 62.5$ nm, and $N = 10$, respectively. The MFF layers are taken here having volume fraction $P = 0.05$, 0.25 and 0.75, respectively but of the same thickness (h_D) equal to 82.6 nm. From the analysis of these curves we find that as the value of α (magnetic field factor) increases the peak of transmission curves shift towards the higher wavelength for larger P values. This is due to the fact that for large porosity of or volume fraction P, the MFF layer shows higher values of the refractive index and the peaks are well separated. In Fig. 17.2 the first three peaks lie exactly at the wavelength while fourth peak is very slightly shifted. We can see that peaks of first three curves corresponding to $\alpha = 0, 0.3$ and 0.6 lie at 573 nm while for $\alpha = 1$, it is slightly shifted and lies at 573.2 nm. All the transmission peaks show nearly same intensity equal to 90.6%. But when the porosity (volume fraction) of MFF increases to $P = 0.25$ and 0.75, the transmission peaks get separated considerably though their intensity decreases with increasing value of α. For $P = 0.25$ wavelength of transmission modes (peaks) are found at 588.3 nm, 589.3 nm,

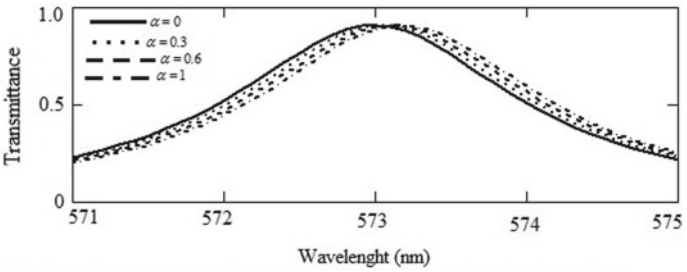

Fig. 17.2 This figure shows transmittance curves for 1D photonic crystal structure having alternate layers of SiO_2 and TiO_2 and MFF as defect layers at $\alpha = 0, 0.3, 0.6$ and 1 and $P = 0.05$

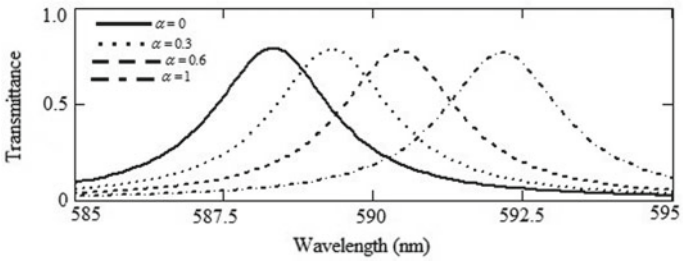

Fig. 17.3 This figure shows transmittance curves for 1D photonic crystal structure having alternate layers of SiO_2 and TiO_2 and MFF as defect layers at $\alpha = 0, 0.3, 0.6$ and 1 and $P = 0.25$

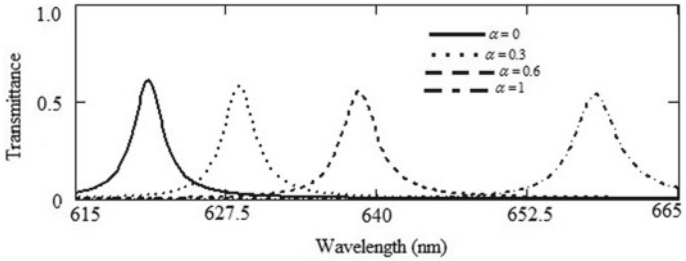

Fig. 17.4 This figure shows transmittance curves for 1D photonic crystal structure having alternate layers of SiO_2 and TiO_2 and MFF as defect layers at $\alpha = 0, 0.3, 0.6$ and 1 and $P = 0.75$

590.4 nm and 592.1 nm respectively for $\alpha = 0, 0.3, 0.6$ and 1 respectively, which can be seen from Fig. 17.3.

In this case intensity of transmission peaks are 79.2%, 78.5%, 77.7% and 76.5% respectively.

In Fig. 17.4 transmission curves are plotted for the MFF layer having $P = 0.75$. It can be observed that the transmission peaks (or modes) are very well separated and tunable in the wider range of wavelength.

The peaks lie at 621 nm, 628.5 nm, 638.5 nm and 658 nm, respectively, for $\alpha = 0, 0.3, 0.6$ and 1 respectively, but the intensity of peaks is very low and varies from 60.6% to 53.9%. From the above results we can conclude that water based $MnFe_2O_4$ magnetic film having low porosity P, effect of magnetic field factor (α) is almost negligible and there is no tunability in the defect modes. For intermediate value of P there is good tunability in the defect modes though intensity slightly decreases. But for MFF possessing large porosity the defect modes are tunable in comparatively wider range with decreased intensity.

Now we will discuss the effect of magnetic field factor (α) on the second type of PC structure air/$(AB)^{N/2}(BA)^{N/2}$/air. The proposed structure gives transmission mode without having a defect in the structure because of the presence of the symmetry in the structure. In The transmission curves for MFFs having volume fraction $P = 0.05$ and 0.25; 0.05 and 0.75; 0.25 and 0.75, respectively, are depicted in the Figs. 17.5, 17.6 and 17.7.

The thickness of the alternate MFFs layers are chosen as 107.3 nm and 91.3; 107.3 nm and 70.4 nm; 91.3 nm and 70.4 nm, respectively, and total number of layers $N = 10$. From all the transmission curves it is evident that transmission modes shift toward higher wavelength side when the magnetic field factor (α) increases. When the contrast between porosity of MFFs layers are small peaks are much closed to each other and the peaks are obtained at wavelength 600.2 nm, 603.7 nm, 607.4 nm and 613.4 nm, respectively.

In other words, we can say that tunability in transmission peaks lie in the narrower region as can be seen from Fig. 17.5. But for larger contrast in the porosity of the two MFFs layers tunability range of wavelengths increases widely. For $P = 0.05$ and 0.75, transmission modes are found at 614.4 nm, 636.2 nm, 666.9 nm and 735.9 nm

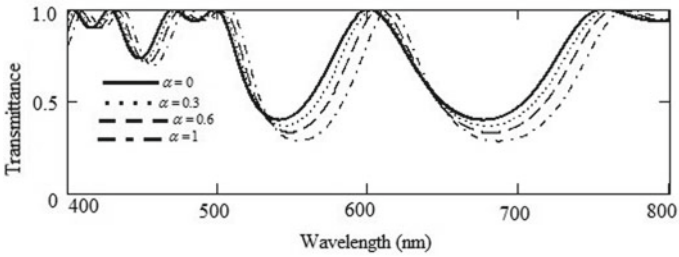

Fig. 17.5 This figure shows the transmittance curves for symmetric one-dimensional photonic crystal structure having alternate layers of MFFs at $P = 0.05$ and 0.25 respectively and $\alpha = 0, 0.3, 0.6, 1$

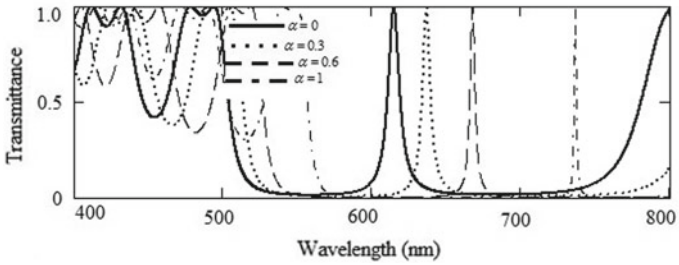

Fig. 17.6 This figure shows the transmittance curves for symmetric one-dimensional photonic crystal structure having alternate layers of MFFs at $P = 0.05$ and 0.75 respectively and $\alpha = 0, 0.3, 0.6, 1$

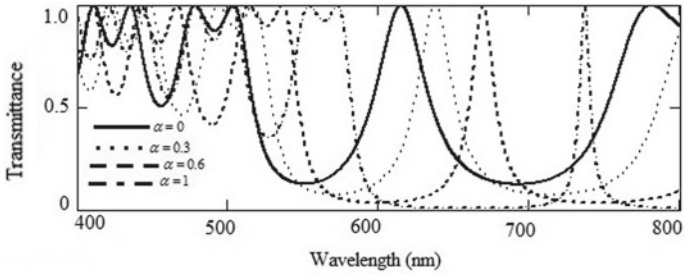

Fig. 17.7 This figure shows the transmittance curves for symmetric one-dimensional photonic crystal structure having alternate layers of MFFs at $P = 0.25$ and 0.75 respectively and $\alpha = 0, 0.3, 0.6, 1$

respectively, while for $P = 025$ and 0.75 these peaks are found at 614.4 nm, 637.5 nm, 668.8 nm and 736.3 nm respectively, for $\alpha = 0, 0.3, 0.6$ and 1.

In Figs. 17.5, 17.6 and 17.7 intensity of all the curves are same and equal to 100%. Further, the curves become sharper with increase in the contrast of porosity of two

layers. Hence the quality factor of PC structure increases by increasing the contrast in porosity of MFF as well as with increasing the magnetic field factor.

17.4 Conclusion

In conclusion, theoretical investigation and study of defect modes in one dimensional defective photonic crystal (PC) based on magnetic fluid film (MFF) have been discussed and presented. In these study two types of PC structures has been considered. In one type we have taken a PC structure composed of alternate layers of TiO_2 and SiO_2 and MFF (water based $MnFe_2O_4$ nanoparticles) as a defect layer having different porosity. In second case we have taken, two symmetric PC structure composed of alternate layers of MFF with different porosity and the effect of magnetic field on the surface mode (acts as a defect mode) has been studied. Transmission spectra have been calculated by employing the transfer matrix method (TMM). From the analysis of the transmittance spectra it has been observed that the effect of magnetic field factor (α) on the transmission modes is almost negligible and there is no tunability in the defect modes on the water based $MnFe_2O4$ magnetic film having low porosity P. But for intermediate value of P there is good tunability in the defect modes though intensity slightly decreases. But for MFF possessing large porosity the defect modes are tunable in comparatively wider range with decreased intensity. Further, for low contrast of porosity (in second type of structure) in MFFs films tunability in transmission peaks are narrower and it covers broad range for high contrast MFFs. Such types of PC structure can be used to design the optical devices such as magnetic field sensors, tunable optical grating, optical switches, tunable narrow transmission filter, wavelength division multiplexer etc.

Acknowledgements Author is also thankful to Amity Institute of Applied Sciences, Amity University Uttar Pradesh, Noida, India, for providing the necessary facilities for this work.

References

1. E. Yablonovitch, Inhibited spontaneous emission in solid state physics and electronics. Phys. Rev. Lett. **58**, 2059–2062 (1987)
2. S. John, Strong localization of photons in certain disordered dielectric super-lattices. Phys. Rev. Lett. **58**, 2486–2489 (1987)
3. S.M. Weiss, M. Haurylau, P.M. Fauchet, Tunable photonic bandgap structures for optical interconnects. Opt. Mater. **27**, 740–745 (2005)
4. Y. Fink, J.N. Winn, S. Fan, C. Chen, J. Michel, J.D. Joannopoulos, E.L. Thomas, A dielectric omnidirectional reflector. Science **282**, 1679–1682 (1998)
5. A. Mekis, J.C. Chen, I. Kurland, S. Fan, P.R. Villeneuve, J.D. Joannopoulos, High transmission through sharp bends in photonic crystal waveguides. Phys. Rev. Lett. **77**, 3787–1390 (1996)

6. D.N. Chigrin, A.V. Lavrinenko, D.A. Yarotsky, S.V. Gaponenko, Observation of total omnidirectional reflection from a one-dimensional dielectric lattice. Appl. Phys. A **68**, 25–28 (1999)
7. S.K. Srivastava, S.P. Ojha, Broadband optical reflector based on Si/SiO_2 one-dimensional graded photonic crystal structure. Mod Opt. **56**, 33–40 (2009)
8. S.K. Srivastava, A. Aghazamali, Analysis of reflectance properties in 1D photonic crystal containing metamaterial and high temperature superconductor. J. Supercond. Nov. Magn. **30**, 343–351 (2017)
9. H. Ren, C. Jiang, W. Hu, M. Gao, J. Wang, Photonic crystal channel drop filter with a wavelength selective reflection microcavity. Opt. Exp. **14**, 2446 (2006)
10. J. Zimmermann, M. Kamp, A. Forchel, R. März, Photonic crystal waveguide directional couplers as wavelength selective optical filters. Opt. Commun. **230**, 387 (2004)
11. A. Martinez, A. Griol, P. Sanchis, J. Marti, Mach Zender interferometer employing coupled resonator optical waveguide. Opt. Lett. **28**, 405 (2003)
12. S.K. Srivastava, M. Upadhyay, S.K. Awasthi, S.P. Ojha, Tunable reflection bands and defect modes in one-dimensional tilted photonic crystal structure. Opt. Phot. J. **3A**, 230–236 (2012)
13. B. Suthar, A. Bhargava, Temperature dependent tunable photonic channel filter. IEEE: Photon. Tech. Lett. **24**, 338–340 (2012)
14. H.C. Hung, C.J. Wu, S.J. Chang, Terahertz temperature dependent defect mode in a semiconductor dielectric photonic crystal. J. Appl. Phys. **110**, 093110-1–6 (2011)
15. V. Skoromets, H. Nmec, C. Kadlec, D. Fattakhova-Rohlfing, P. Kužel, Electric filed tunable defect mode in one-dimensional photonic crystal operating in the terahertz range. Appl. Phys. Lett. **102**, 241106-1-4 (2013)
16. S.K. Srivastava, Electrically controlled reflection band and tunable defect modes in one-dimensional photonic crystal by using potassium titanyl phosphate (KTP) crystal. J. Nano Electron. Optoelctron. **11**, 284–289 (2016)
17. H. Tian, J. Zi, One-dimensional tunable photonic crystals by means of external magnetic fields. Opt. Commum. **252**, 321–328 (2005)
18. D. MacPhail, M. Straub, GuM optical, tuning of three-dimensional photonic crystals fabricated by femtosecond direct writing. Appl. Phys. Lett. **87**, 091117-1–3 (2005)
19. S.K. Srivastava, Aghazamali, A Narrow transmission mode in one-dimensional symmetric defective photonic crystal containing metamaterial and high Tc superconductor. Opt. Appl **XLIX**, 37–50 (2019)
20. S.Y. Yang, H.E. Horng, C.Y. Hong, H.C. Yang, Structures, optical properties and potentially electrooptical applications of magnetic fluid films. Tamkang J. Sci. Eng. **5**, 85–93 (2002)
21. J. Chen, X. Chen, S. Pu, Z. Di, Y. Xia, Realization of optical limiting with a magnetic fluid film. Opt. Commun. **276**, 268–271 (2007)
22. R. Patel, R.V. Mehta, Experimental investigations on magnetically induced photonic band gap in ferrodispersions. Eur. Phys. J. Appl. Phys. **52**, 30702-1-6 (2010)
23. J. Li, Y.Q. Lin, X.D. Liu, B.C. Wen, T.Z. Zhang, Q.M. Zhang, H. Miao, The modulation of coupling in the relaxation behavior of light transmitted through binary ferrofluids. Opt. Commun. **283**, 1182–1187 (2010)
24. T.Z. Zhang, J. Li, H. Miao, Q.M. Zhang, J. Fu, B.C. Wen, Enhancement of the field modulation of light transmission through films of binary ferrofluids. Phys. Rev. E **82**, 021403 (2010)
25. R. Patel, Mechanism of chain formation in nanofluid based MR fluids. J. Magn. Magn. Mater. **323**, 1360–1363 (2011)
26. S. Pu, T. Geng, X. Chen, X. Zeng, M. Liu, Z. Di, Tuning the band gap of self-assembled superparamagnetic photonic crystals in colloidal magnetic fluids using external magnetic fields. J. Magn. Magn. Mater. **320**, 2345–2349 (2008)
27. C.Z. Fan, G. Wang, J.P. Huang, Magneto controllable photonic crystals based on colloidal ferrofluids. J. Appl. Phys. **103**, 094107 (2004)
28. P. Yeh, *Optical waves in layered media* (Wiley, New York, 1988)
29. M. Born, E. Wolf, *Principles of optics* (Cambridge University Press, Cambridge, 1998)

Chapter 18
Changes in the Thermodynamic Parameters of an Achiral Liquid Crystalline Material Due to Li Ion Beam Irradiation

Satendra Kumar, Rohit Verma, and Ravindra Dhar

Abstract Energetic ion beam radiations produced in accelerators have been widely used for the modifications of materials. Sometimes the properties of the irradiated materials are improved and in other cases the materials are deteriorated. The damages caused by irradiation are responsible for the changes in materialistic properties of the irradiated materials. The nature of these changes depends on the type of energy, ion and fluence (ions/cm^2) of irradiation. Therefore, it becomes important to study the effect of Li ion beam radiation on different properties of materials. In view of the above, Li ion beam irradiation-induced effects in the thermodynamic parameters of liquid crystalline material 4-n (heptyloxy) benzoic acid (HOBA) have been investigated in this study. The materials were irradiated in their crystalline phase (at room temperature) by Li ion beam of different fluences ranging from 10^{10} to 10^{13} ions/cm^2. The pure as well as the irradiated material has phase sequence of I–N–Cr. The pure and irradiated materials were explored using differential scanning calorimeter (DSC). The DSC studies of the pure and irradiated samples show that all the transition temperatures of the irradiated materials are reduced as compared to those of the pure material.

18.1 Introduction

In 1888, an Austrian Botanist F. Reinitzer was extracting cholesterol from carrots. During this experiment, he perceived the dual melting behavior of cholesterol [1]. He deliberated this with O. Lehmann which led to the identification of a new phase of matter, termed as the liquid crystal (LC) phase. Since the discovery, the research of LC material is matured and is undergoing a modern-day renaissance. Devices and

S. Kumar · R. Verma (✉)
Department of Applied Physics, Amity Institute of Applied Sciences, Amity University Uttar Pradesh, Noida 201313, India
e-mail: rverma85@amity.edu

R. Dhar
Centre of Material Sciences, Institute of Interdisciplinary Studies, University of Allahabad, Allahabad 211002, India

V. K. Jain et al. (eds.), *Recent Trends in Materials and Devices*, Springer Proceedings in Physics 256, https://doi.org/10.1007/978-981-15-8625-5_18

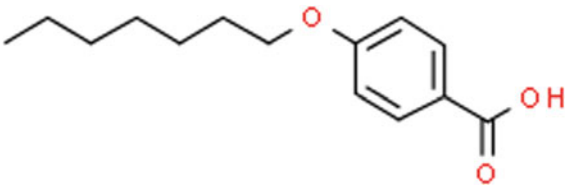

Fig. 18.1 Molecular structure of 4-n (heptyloxy) benzoic acid (HOBA)

configurations based on LC materials are being utilized for wide area displays, spectroscopy, imaging and microscopy, leading to new techniques for optically probing biological systems. Biosensors fabricated with LC materials can allow label free observations of biological phenomena. Liquid crystal polymers are being utilized in biomimicking colour producing structures, lenses and muscle-like actuators. The devices made with LC materials are often used in radiation prone areas such as space, nuclear reactors, war fields occasionally for long durations. When these devices are used in such an environment, the presence of various types of radiation often create malfunctioning of these devices. Hence, it is essential to study the behavior of the materials with which these devices are made up of under the exposure of various types and doses of radiations for ensuring their durability and development of future radiation hardened materials. Preliminary studies on the effect of radiations on LC materials suggest that different types and doses of radiation strongly affect several physical properties of these materials for instance phase transition temperatures, enthalpies and entropies of transitions are decreased, ac and dc conductivities are increased etc. [2–8, 11–14]. In the present work, we report the effect of Li ion beam irradiation (of fluences 10^{10}, 10^{11}, 10^{12}, 10^{13} ions/cm^2) in the phase transition temperatures of an achiral liquid crystalline material 4-n (heptyloxy) benzoic acid (HOBA). The molecular structure of HOBA is shown in Fig. 18.1.

18.2 Experimental Details

The liquid crystalline materials were irradiated by using Li ion beam from a 15UD pelletron beam setup at Inter University Accelerator Centre (IUAC), New Delhi. The irradiation has been carried out by the pelletron beam using 3 nA current at fluences (10^{10}, 10^{11}, 10^{12}, 10^{13} ions/cm^2) at room temperature when the material was in its crystalline phase. All irradiations were performed in a vacuum (of 10^6 Torr). The beam current was maintained below 3 pnA. In order to expose the target of area 1.5 cm × 1.5 cm, the beam was scanned in the *x*–*y* plane. The time of the beam bombardment for a particular fluence has been determined by the following formula

$$\text{Time} = \frac{\text{Fluence} \times \text{Area}}{6.25 \times 10^9 \times \text{current (pnA)}}$$

where pnA = nA/Charge State and it stands for particle nano ampere and area is area of beam scan. More details about the irradiation of the materials can be found in some previously published articles [8–10]. Pure and irradiated materials are characterized by Differential Scanning Calorimeter (DSC). The thermodynamic study of the pure and irradiated materials has been carried out on a DSC of NETZSCH model DSC-F3-200-MAIA. DSC is allowed to run initially for the first five cycles at the scan rate of 5.0 °C/min in the range 20–170 °C in order to stabilize the transition temperatures and enthalpies of transitions. Transition temperatures are determined with the accuracy of 0.1 °C whereas transition enthalpies are determined with the accuracy better than 2% for fully grown peaks. However, for very weak peaks, the uncertainties are large due to the uncertainties in the localization of start and end point of peaks. Further details about the experimental procedures can be found in some of our earlier publications [11, 12].

18.3 Results and Discussions

Thermodynamic study of the pure and irradiated materials is performed on DSC. For each of the samples, DSC was firstly run for five heating and cooling cycles in the range 20–170 °C for stabilizing the peak transition temperatures and enthalpy of transitions. The obtained transition temperatures of various transitions both for the pure and irradiated samples vary linearly with scan rate. The variation of the transition temperature (°C) of 10^{10} ions/cm^2 irradiated HOBA with scan rate (°C/min) is shown in Fig. 18.2. Figure 18.3 show the variation of phase transition temperatures (°C) with the irradiation fluence (ions/cm^2). From Fig. 18.3, it can be observed that

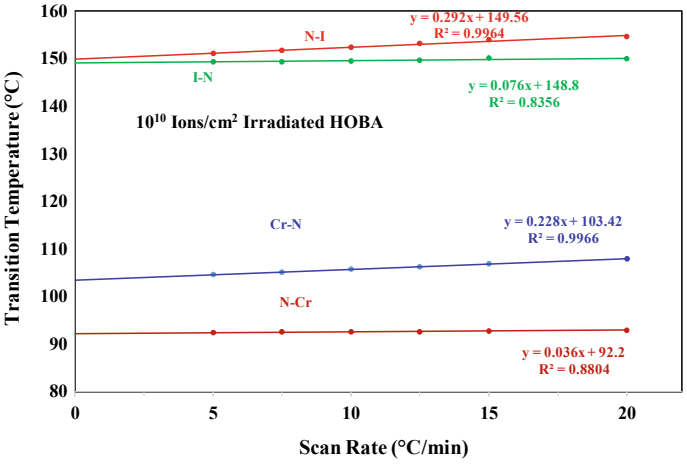

Fig. 18.2 Variation of the transition temperature (°C) of 10^{10} ions/cm^2 irradiated HOBA with scan rate (°C/min)

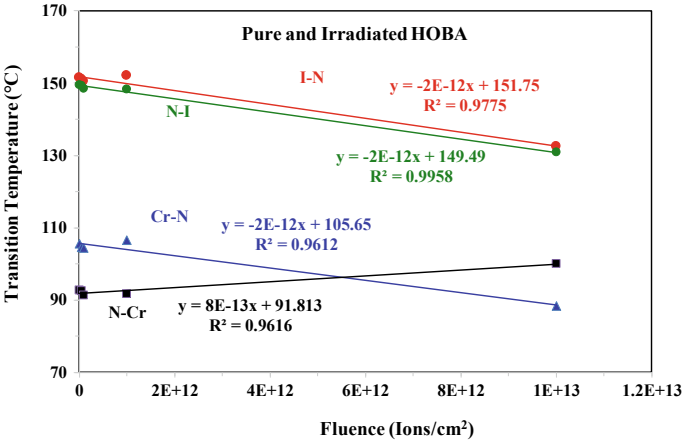

Fig. 18.3 Variation of the transition temperatures (°C) of pure and irradiated HOBA with irradiation fluence (ions/cm^2)

the transition temperatures of various phase transitions vary linearly with irradiation fluence. From the thermodynamic studies, we find that the phase transition temperatures of the irradiated samples are decreased as compared to those of the pure sample. Peaks of irradiated HOBA are becoming broader of all transition temperatures and decreasing their heights too as compared to those of pure material. Our thermodynamic data show that, in the heating cycle Cr–N and N–I transition temperatures are decreased by 25.3 and 18.4 °C respectively due to the Li ion beam irradiation of highest fluence 10^{13} ions/cm^2. However, in the cooling cycle, I–N, and N–Cr transitions are decreased by 18.8 °C and 14.2 °C respectively due to the Li ion beam irradiation of fluence 10^{13} ions/cm^2. Normally the mixing of any impurity in a mesogenic compound depresses the transition temperatures of the material [2–4]. Alfassi et al. have found that the color transition temperatures of cholesteryl esters are lowered due to γ-irradiation and that lowering in the transition temperature depends upon the absorbed dose of irradiation [3]. The decrease in the transition temperature of irradiated material is due to irradiation induced non-mesogenic impurities. We have acquired ultraviolet–visible (UV–Vis) spectra for the pure and irradiated materials. The UV–Vis spectra of the irradiated HOBA show an additional peak with that for the pure HOBA. This supplementary peak in the spectrum of the irradiated material advocates formation of some novel species due to irradiation. The proportion of such irradiation induced novel species increases linearly with the increase of irradiation fluence because of which the transition temperature varies linearly with irradiation fluence. Kłosowicz has also demonstrated that the temperature of phase transitions of cholesterol derivatives depends linearly on the exposure dose of γ radiation in a wide range of doses [13].

18.4 Conclusions

From the above results and discussion, we conclude that the transition temperatures of the irradiated material are decreased as compared to those of the pure material. Various transition temperature of the pure and irradiated compounds varies linearly with scan rates. It has been also observed that the different transition temperatures decrease linearly with the variation of irradiation fluence. Peaks of irradiated HOBA are becoming broader of all transition temperatures and decreasing their heights too as compared to those of pure material. The reduction in the transition temperatures of irradiated materials is attributed to irradiation induced non-mesogenic impurities which increase linearly with the irradiation fluence.

References

1. F. Reinitzer, Beiträge zur Kenntniss des Cholesterins. Monatshefte Chemie/Chem. Mon. **9**, 421–441 (1888)
2. S.L. Srivastava, R. Dhar, M.V. Kurik, Mol. Mat. **2**, 261 (1993)
3. Z.B. Alfassi, A.P. Kushelevsky, L. Feldman, Mol. Cryst. Liq. Cryst. **39**, 33 (1977)
4. S.J. Kłosowicz, Z.B. Alfassi, Mol. Cryst. Liq. Cryst. **239**(1), 181 (1994). https://doi.org/10.1080/10587259408047181
5. G.A. Kosinov, O.D. Lavrentovich, V.A. Linev, G.A. Puchkoskaya, S.Z. Shulga, A.A. Yakubov, Translated from Khimiya Vysokikh Energii **22**, 26 (1988)
6. R. Verma, R. Dhar, R. Dabrowski, M. Tykarska, V.K. Wadhawan, M.C. Rath, S.K. Sarkar, J. Phys. D Appl. Phys. **42**, 085503 (2009)
7. R. Verma, R. Dhar, R. Dabrowski, M. Tykarska, V.K. Wadhawan, M.C. Rath, S.K. Sarkar, Liq. Cryst. **36**, 1003 (2009)
8. S. Kumar, R. Verma, R. Dhar, A. Tripathi, Liq. Cryst. **46**, 356–366 (2019)
9. K. Hareesh, R.P. Joshi, B. Shateesh, K. Asokan, D. Kanjilal, D.J. Late, S.S. Dahiwale, V.N. Bhoraskar, S.K. Haram, S.D. Dhole, J. Phys. D: Appl. Phys. **48**, 365105 (8 pp) (2015)
10. T. Nandi, K. Haris, Hala, Gurjeet Singh, P. Kumar, R. Kumar, S.K. Saini, S.A. Khan, A. Jhingan, P. Verma, A. Tauheed, D. Mehta, H.G. Berry, Phys. Res. Lett. **110**, 163203 (2013)
11. S. Kumar, R. Verma, A. Dwivedi, R. Dhar, A. Tripathi, A.I.P. Conf, Proc. **1953**, 050014 (2018)
12. R. Dhar, R. Verma, V.K. Wadhawan, M.C. Rath, S.K. Sarkar, M. Tykarska, R. Dabrowski, Appl. Phys. Lett. **92**, 014108 (1–3) (2008)
13. S. Klosovicz, Rad. Phys. Chem. **43**, 243–248 (1994)
14. K. Hudson, B. Ellman, V. Gettwert et al., Appl. Phys. Lett. **87**, 152103 (2005)

Chapter 19
Thermal Analysis of Cu Doped Sodium Hexa-Titanate ($Na_2Ti_6O_{13}$)

Navshad Alam, Tahira Khatoon, Vishal Singh Chandel, and Rashmi

Abstract The present paper discusses the thermal analysis of pure and copper doped sodium hexa-titanate ($Na_2Ti_6O_{13}$) (NHT). These samples were synthesized by the conventional solid-state reaction method having 4, 8 and 12% doping. The XRD and FE-SEM of the pure and doped samples have been done for crystallographic and morphological characterization, which reveals the single-phase formation of samples and the particle size in the micrometer range and rod-shaped. Thermal analysis (DSC/TGA) of the samples has also been done for the phase transition study.

19.1 Introduction

Synthesis of nanostructures and their applications due to enhanced properties have inspiring researchers across the world to synthesize them with even more specific morphologies and improved properties. Titania or titanium dioxide is a commercially important material that has widelybeen studied for photocatalysis, gas sensing, solar cells and many more [1–4]. Titanium dioxide nanoparticles, nanorods, nanowires and nanotubes have been synthesized using various synthesis procedures [5–11], means physical and chemical conditions have good control over morphology and particle size etc. Besides titanium dioxide, alkali titanates are extensively studied

N. Alam · V. S. Chandel (✉)
Department of Applied Science, BNCET, Affiliated to Dr. A.P.J. Abdul, Kalam Technical University, Lucknow 226201, India
e-mail: chandel.integral@gmail.com

T. Khatoon
Department of Physics, Integral University, Lucknow 226026, India

V. S. Chandel
Department of APSH, Rajkiya Engineering College, Affiliated to Dr. A.P.J. Abdul, Kalam Technical University, Ambedkar Nagar, Lucknow 224122, India

Rashmi
Material Science Programme, IIT Kanpur, Kanpur, India

V. K. Jain et al. (eds.), *Recent Trends in Materials and Devices*, Springer Proceedings in Physics 256, https://doi.org/10.1007/978-981-15-8625-5_19

materials due to applications in fuel cells, photocatalysis, ion exchange, gas sensors etc. [12–16], they also have interesting biological applications [17–19]. Family of alkali titanates, generally represented as $A_2O.Ti_nO_2n$ (n may take values ranging from 1 to 8 and A can be any alkali metal like K, Na or Li), comprises of layers which have zigzag ribbons sharing terminal ends with identical ribbons and hence resulting in a tunnel-like structure (layered structure $n \leq 2$, tunnel structure $n > 2$) [20]. The content of alkali metal governs the morphology and other properties of resulting alkali titanate and thus different alkali titanates possess different physical and chemical properties. Nanostructures of sodium hexa-titanate have low thermal conductivity, higher infrared reflectance, excellent chemical stability and outstanding mechanical properties. These materials have extensively been used in harvesting energy, heat-insulating and frictional materials [21–23].

Sodium hexa-titanate has been synthesized using various techniques including solid-state reaction route, sol–gel method and hydrothermal synthesis [24–28]. Sauvet et al. reported synthesis and characterization (TGA-DTA) of sodium tri and hexa-titanates $Na_2Ti_3O_7$ and $Na_2Ti_6O_{13}$, Stengl et al. investigated synthesis, microstructure characterization, photocatalytic activity, thermal analysis of sodium titanate nanorods (DTA–TG of the sample coupled with mass spectroscopy, emanation thermal analysis), Cardoso et al. reported thermal characterization of lamellar titanates ($K_2Ti_4O_9$ and $Na_2Ti_3O_7$), Umek et al. reported the effect of the temperature on the morphology of one dimensional sodium titanate nanostructures (sodium titanate nano tubes and nano ribbons) and their thermal stability [29–32]. Dielectric, optical, photocatalytic and electronic properties of pure and doped alkali titanates (sodium, potassium) have also been done by our group [33–35]. The present paper examines the effect of doping a transition metal copper in pure sodium hexa-titanate by solid-state reaction route.

19.2 Materials and Methods

Anatase titanium dioxide (TiO_2) was purchased from Sigma Aldrich with purity 99.5%, while analytical reagent (AR) grade sodium carbonate (Na_2CO_3), as well as copper oxide (CuO) were purchased from Thomas Baker having purity greater than or equal to 99.5%.

For the synthesis of pure and copper doped sodium hexa-titanate, TiO_2, Na_2CO_3 and CuO were added in a proper molar ratio. Further this mixture was ground for 6 h in a ceramic mortar. After that mixtures (for pure and doped samples) were heat treated with a controlled heating rate of 5 °C/min and calcined at 900 °C for 12 h [36, 37].

$$Na_2CO_3 + 6TiO_2 \rightarrow Na_2Ti_6O_{13} + CO_2 \uparrow$$

$$Na_2CO_3 + (6 - x)\,TiO_2 + xCuO \rightarrow$$

$$Na_2Ti_{6-x}\,Cu_x\,O_{13} + CO_2 \uparrow \ (x = 0.04,\ 0.08 \text{ and } 0.12)$$

19.3 Characterizations

19.3.1 X-Ray Diffraction Analysis

The crystallographic information of a sample can be obtained by X-ray diffraction analysis. In the present investigation X-ray diffraction was studied in the range of 10°–70° with a scanning rate of 5°/min at room temperature with Cu-K_α radiation ($\lambda = 1.5406$ Å). The X-ray diffraction (XRD) patterns of pure and copper doped NHT showed monoclinic structure of sample, which was confirmed with $\alpha = \gamma = 90°$, and $\beta \neq 90°$. The single-phase formation of sample presented in Fig. 19.1. The d_{hkl} values were calculated using powder X-ray software by varying the cell parameters (hkl are miller indices and α, β and γ are inter-axial angles).

Using the equation given below lattice constants were calculated and are presented in Table 19.1.

$$\frac{1}{d^2} = \frac{h^2}{a^2 \sin^2 \beta} + \frac{k^2}{b^2} + \frac{l^2}{c^2 \sin^2 \beta} - \frac{2hl \cos \beta}{ac \sin^2 \beta}$$

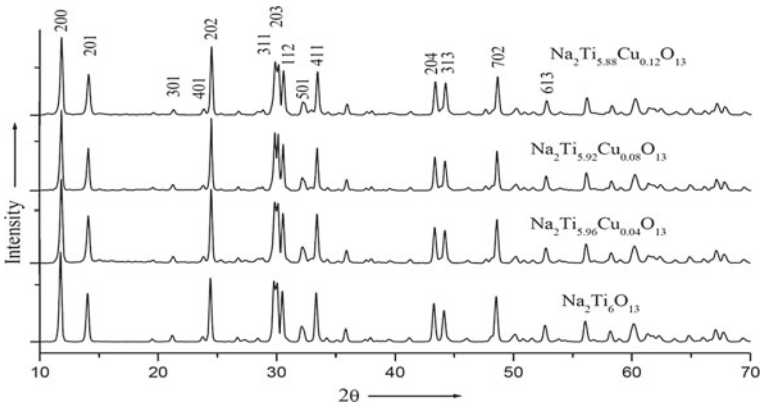

Fig. 19.1 XRD analysis of pure and Cu doped NHT

Table 19.1 Lattice parameters of pure and Cu doped NHT

S. No.	Samples name	Lattice parameter a (Å)	Lattice parameter b (Å)	Lattice Parameter c (Å)	*B* (°)	Unit cell volume V ($Å^3$)
1	$Na_2Ti_6O_{13}$	15.5999	3.8000	9.1600	99.1	543.001
2	$Na_2Ti_{5.96}Cu_{0.04}O_{13}$	15.596	3.7990	9.1550	98.9	542.426
3	$Na_2Ti_{5.92}Cu_{0.08}O_{13}$	15.5888	3.7990	9.1500	98.9	541.879
4	$Na_2Ti_{5.88}Cu_{0.12}O_{13}$	15.5500	3.8000	9.1100	98.7	538.31

19.3.2 Field Emission Electron Microscopy (FE-SEM) Analysis

The micron size topographic details of the synthesized samples can be visualized using Field Emission Electron Microscopy. Since sodium hexa-titanate and Cu doped sodium hexa-titanate are semiconductor in nature, therefore, all samples were coated with gold for 90 s. Furthermore, the morphologies of pure and Cu doped NHT have been observed using FE-SEM (Nova Nanosem 450) analysis, in secondary mode at 10 kV accelerating voltage and micrographs shown in Figs. 19.2, 19.3, 19.4 and 19.5 confirms that all samples have hexagonal rod-shaped structures.

The average length of pure sodium hexa-titanate is 1.20 μm. Since atomic radius of copper is smaller than titanium, hence on doping copper in NHT average length of the doped samples are slightly less than pure (average length of copper doped lies between 1.10 and 1.17 μm). Edge to edge diameter of pure and copper doped NHT lies between 0.1 and 0.2 μm.

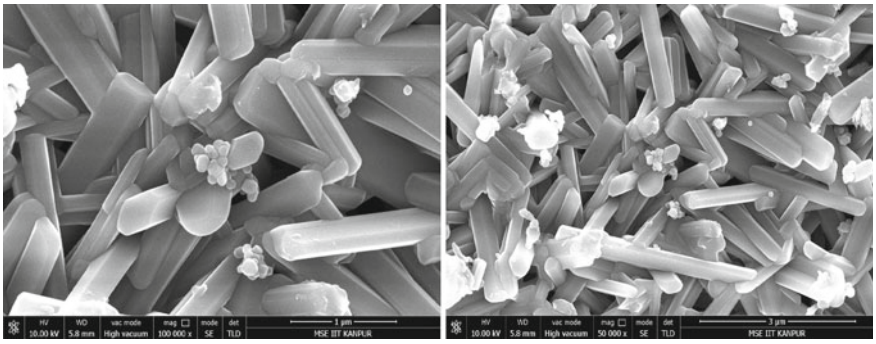

Fig. 19.2 FE-SEM image of pure NHT

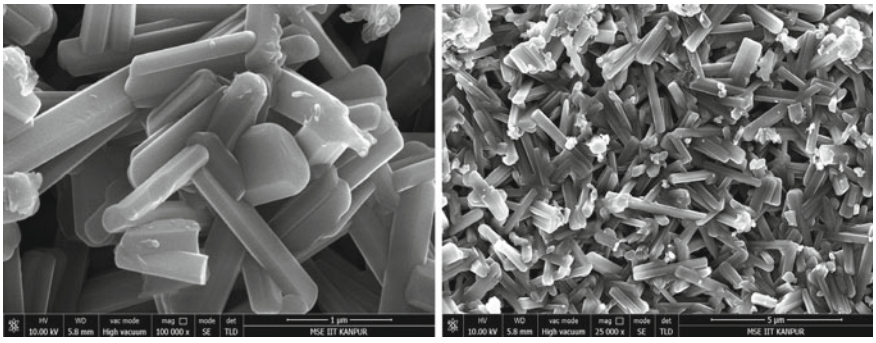

Fig. 19.3 FE-SEM image of Cu doped NHT at $x = 4\%$

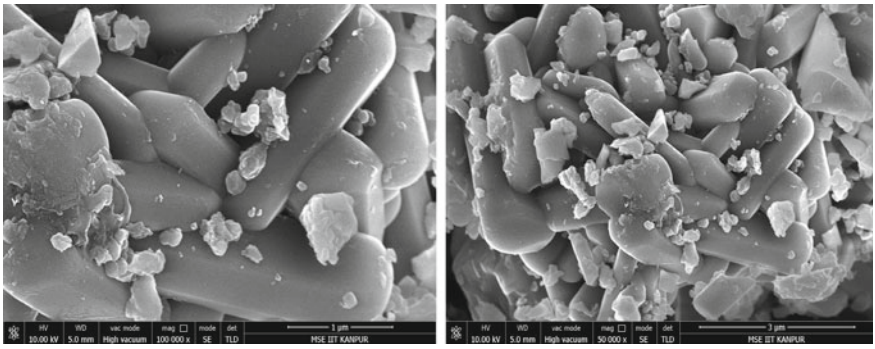

Fig. 19.4 FE-SEM image of Cu doped NHT at $x = 8\%$

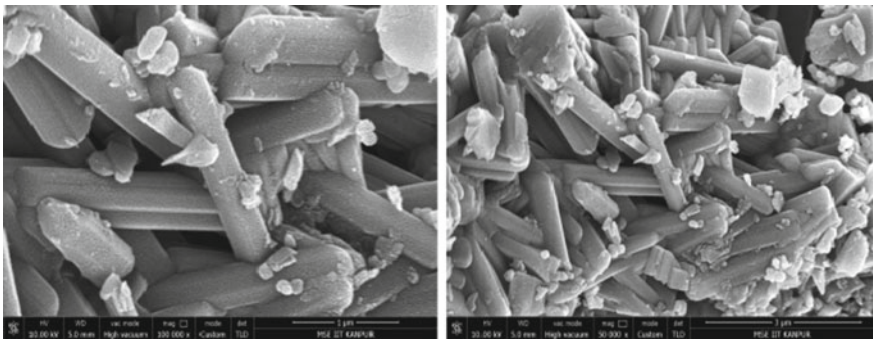

Fig. 19.5 FE-SEM image of Cu doped NHT at $x = 12\%$

19.3.3 Energy Dispersive Spectroscopy (EDS) Analysis

Using an attachment of EDS in FE-SEM, elemental study of the samples can also be performed. EDS analysis scan the surface of the smaller particle and analyzed the elements present in the samples and gives the prominent peak of the elements. In the present case EDS analysis confirms that Na, Ti, Cu and O are present. The prominent peaks of the elements are shown in Figs. 19.6, 19.7, 19.8 and 19.9.

19.3.4 Differential Scanning Calorimetry (DSC)

In order to study the thermal stability of pure and Cu doped NHT, differential scanning calorimetry (DSC) was performed in nitrogen atmosphere from room temperature to 900 °C, with heating and cooling rate of 10 °C/min. This analysis was done at MSE lab IIT Kanpur.

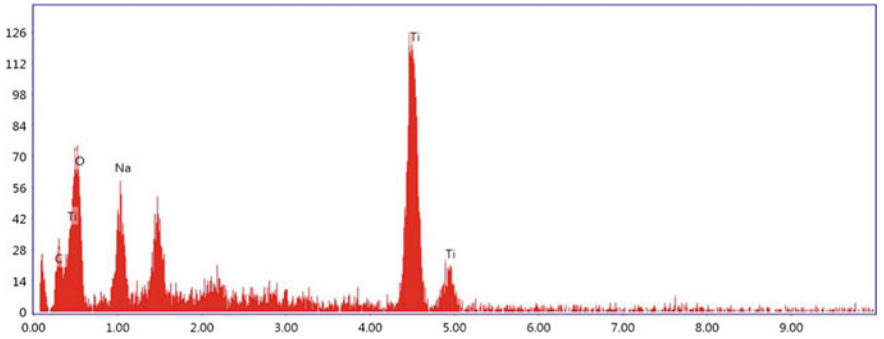

Fig. 19.6 EDS analysis of pure NHT

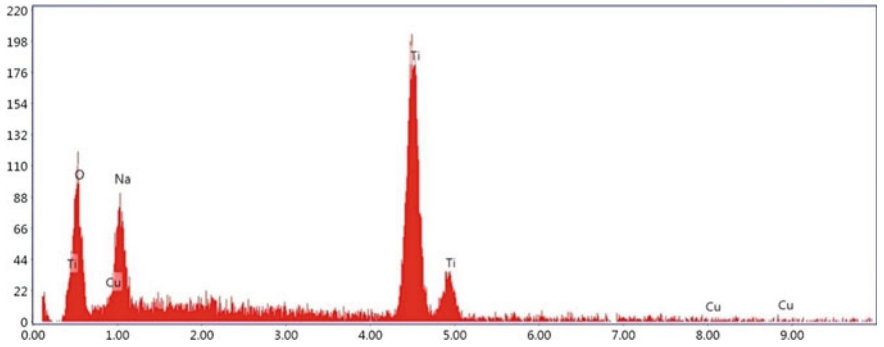

Fig. 19.7 EDS analysis of 4% Cu doped NHT

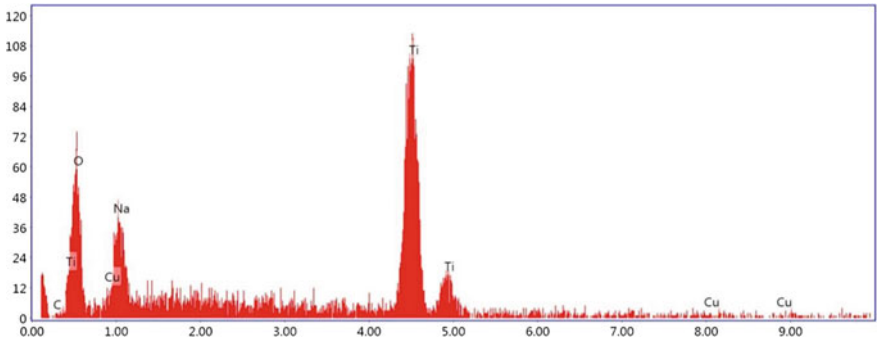

Fig. 19.8 EDS analysis of 8% Cu doped NHT

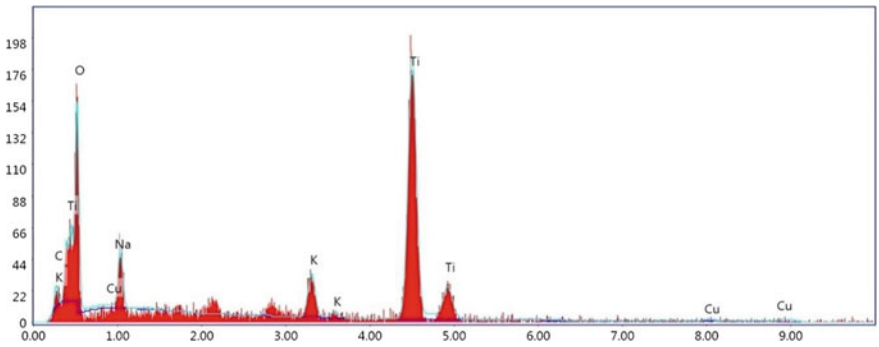

Fig. 19.9 EDS analysis of 12% Cu doped NHT

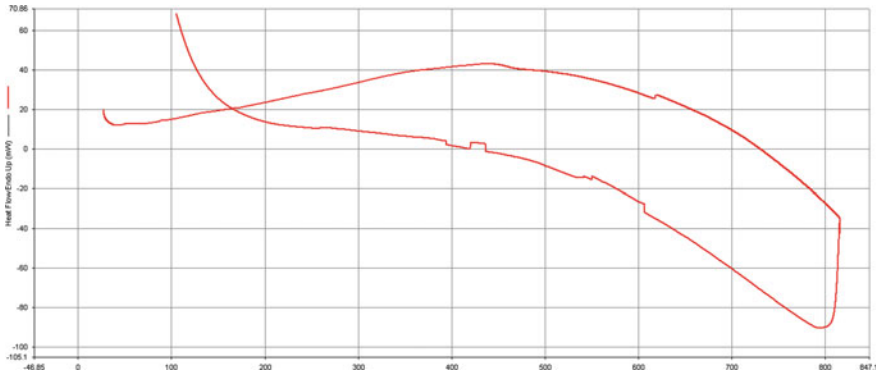

Fig. 19.10 DSC analysis of pure NHT

Figures 19.10, 19.11, 19.12 and 19.13 show a small peak nearly at 100 °C. The shrinkage process of pure and Cu doped NHT at 100 °C is observed because of the evaporation of water. Furthermore, it has been analyzed that no shrinkage process was obtained in pure and Cu doped NHT. Thermal analysis also confirms that no melting points were obtained between 0 to 900 °C.

19.4 Conclusions

$Na_2Ti_6O_{13}$ and its doped ($x = 0.04, 0.08, 0.12$ mol%) specimens were synthesized using solid state route. Lattice constants have been evaluated from XRD data at room temperature, revealed monoclinic phase formation. Unit cell volume decreases with increasing the doping percentage of Cu in sodium hexa-titanate. It has also been confirmed from FE-SEM analysis that particle size slightly decreases on increasing

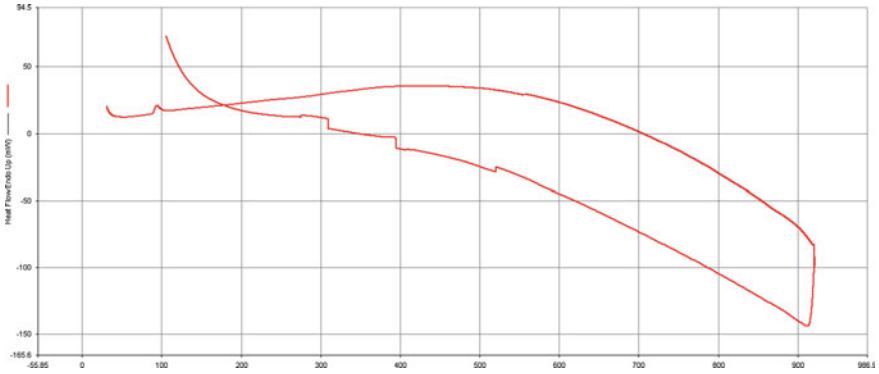

Fig. 19.11 DSC analysis 4% Cu doped NHT

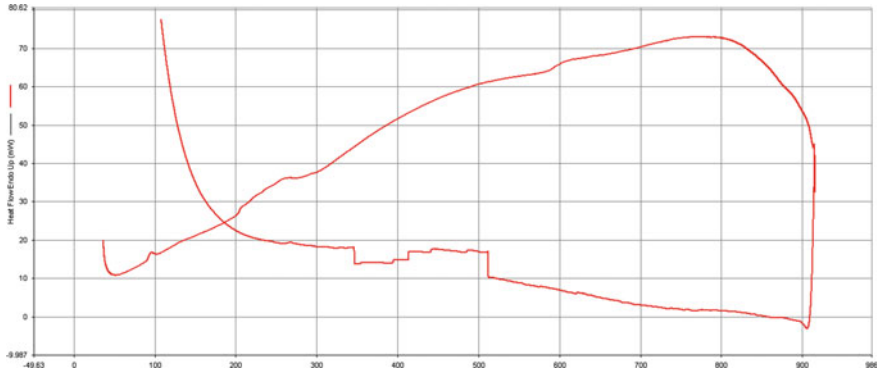

Fig. 19.12 DSC analysis 8% Cu doped NHT

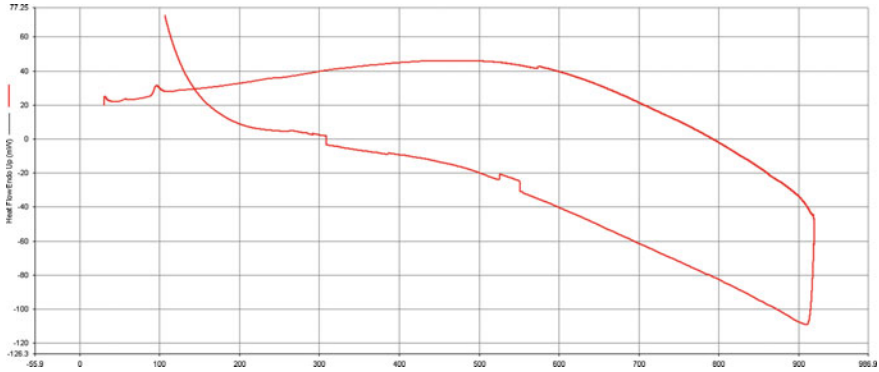

Fig. 19.13 DSC analysis 12% Cu doped NHT

the copper in pure NHT. Thermal analysis confirms no melting points as well as no exothermic peak in pure and copper doped Sodium Hexa-titanate.

Acknowledgements One of the author is thankful to TEQIP-III of REC Ambedkar Nagar for providing the financial assistant of the project. Authors are also thankful to Dr. Sri Siva Kumar, Associate Professor, Department of Chemical Engineering and Material Science Programme, IIT Kanpur, for providing the experimental facility.

References

1. U. Diebold, Surf. Sci. Rep. **48**, 53 (2003)
2. A.G. Evans, B.J. Dalgleish, Mater. Sci. Series. (Academic Press Inc., New York, NY) (1988)
3. A. Kudo, T. Sakata, J. Mater. Chem. **3**, 1081 (1993)
4. M. Shibata, A. Kudo, A. Tanaka, T. Onishi, Chem. Lett. **6**, 1017 (1987)
5. K. Madhusudan Reddy, S.V. Manorama, A. Ramachandra Reddy, Mater. Chem. Phys. **78**, 239 (2002)
6. J. Tang, F. Redl, Y. Zhu, T. Siegrist, L.E. Brus, M.L. Steigerwald, Nano Lett. **5**, 543 (2005)
7. Y. Lei, L.D. Zhang, G.W. Meng, G.H. Li, X.Y. Zhang, C.H. Liang, W. Chen, S.X. Wang, Appl. Phys. Lett. **78**, 1125 (2001)
8. G.H. Du, Q. Chen, R.C. Che, Z.Y. Yuan, L.M. Peng, Appl. Phys. Lett. **79**, 3702 (2001)
9. B.D. Yao, Y.F. Chan, X.Y. Zhang, W.F. Zhang, Z.Y. Yang, N. Wang, Appl. Phys. Lett. **82**, 281 (2003)
10. D. Maestre, A. Cremades, J. Piqueras, Nanotechnology **17**, 1584 (2006)
11. D. Maestre, A. Cremades, L. Gregoratti, J. Piqueras, J. Nanosci. Nanotechnol. **8**, 6533 (2008)
12. A. Hagfeldt, M. Gra¨tzel, Chem. Res. **95**, 49 (1995)
13. J. Ramı´rez-Salgado, E. Djurado, P. Fabry, J. Eur. Ceram. Soc. **24**, 2477 (2004)
14. M.W. Anderson, J. Klinowski, Inorg. Chem. **29**, 3260 (1990)
15. T. Kasuga, M. Hiramatsu, A. Hoson, T. Sekino, K. Niihara, Langmuir **14**, 3160 (1998)
16. T. Kasuga, M. Hiramatsu, A. Hoson, T. Sekino, K. Niihara, Adv. Mater. **11**, 1307 (1999)
17. G.H. Li, J.M. Hong, Mat. Res. Bull. **34**, 2349 (1999)
18. S. Anderson, A.D. Wadsley, Acta ChemicaScandinavica **15**, 663 (1961)
19. L. Suchow, J. Inorg. Nucl. Chem. **30**(1), 87 (1968)
20. K.L. Berry, V.D. Aftandilian, W.W. Gilbert, E.P. Meibohm, H.S. Young, J. Inorg. Nucl. Chem. **14**, 231 (1960)
21. B. Inés, H. Ingo, A.M. Frank, Euro. Ceram. Soc. **27**, 4553 (2007)
22. Kikkawa, M. Koizumi, Fine Ceramics. Else. Publ. Co., USA. 83 (1988)
23. M. Tournoux, R. Marchand, L. Brohan, Prog. Solid St. Chem. **17**, 33 (1986)
24. M.A. Siddiqui, V.S. Chandel, M. Sharique, A. Azam, Appl. Surf. Sci. **258**, 7354 (2012)
25. S.V. Vikram, D.M. Phase, V.S. Chandel, J. Alloy. Compd. **489**, 700 (2010)
26. M.A. Siddiqui, V.S. Chandel, M. Sharique, A. Azam, Mater. Sci. Poland **31**, 555 (2013)
27. S.V. Vikram, D. Maurya, V.S. Chandel, J. Alloys Compound. **478**, 398 (2009)
28. S.V. Vikram, D. Maurya, V.S. Chandel, J. Mater. Sci. Mater. Electron. **23**, 718 (2010)
29. A.L. Sauvet, S. Baliteau, C. Lopez, P. Fabry, J. Solid-State Chem. **177**, 4515 (2004)
30. S. Vaclav, B. Snejana, S. Jan, Eva Vecernı´kova, S. Lorant, K. Mariana, B. Vladimir, Appl. Catalysis B: Environ. **63**, 30 (2005)
31. V.A. Cardoso, L.M. Nunes, J.C.O. Santos, I.M.G. Santos, M.M. Conceição, J.R. Santos Jr., A. G. Souza, J. Therm. Anal. Calorimetry **79**, 365 (2005)
32. U. Polona, C.K. Romana, J. Bostjan, D. Robert, D.A. Dominko, J. Nanosci. Nanotechnol. **7**, 3508 (2007)
33. N. Alam, V.S. Chandel, A. Azam, J. Sci. Arts. **19**, 485 (2019)

34. R. Manohar, S. Manohar, V.S. Chandel, Mater. Sci. Appl. **2**, 838 (2011)
35. V.S. Chandel, M.A. Siddiqui M. Shariq, D. Kaur, Acta Phys. Polon. A **127**, 1675 (2015)
36. N. Alam, V.S. Chandel, T. Khatoon, S. Tripathi, A. Azam, M. Shariq, Tailoring of band gap in manganese doped sodium hexa-titanate, in *2018 International Conference on Computational and Characterization Techniques in Engineering & Sciences (CCTES)*, pp. 291–294
37. N. Alam, T. Khatoon, V.S. Chandel, A. Azam, Indian. J. Sci. Technol. **12**(21), 5 (2019)

Chapter 20
Nonlinear Optical Susceptibilities of a Piezoelectric Semiconductor Magneto-Plasma

Manjeet Singh, Jyoti Gahlawat, Anita Sangwan, Navneet Singh, and Mahender Singh

Abstract In this analytical investigation, using the fluid model for one-component plasma, we have obtained expressions of intensity independent/dependent second- and third-order optical susceptibilities in a piezoelectric magneto-active semiconductor. The cause of nonlinear interaction lies in parametric coupling of pump field with induced density and acoustic perturbations. Theoretical model has been developed under rotating-wave-approximation. Numerical estimations have been prepared for a typically chosen *n*-type doped InSb–CO_2 laser system. Efforts have been directed towards optimizing the doping level of semiconductor crystal, externally applied magnetic field and laser (pump) intensity to attain enhanced magnitude of nonlinear optical susceptibilities as well as alter of their sign. An enhancement in magnitude and alter of sign of nonlinear optical susceptibilities of a piezoelectric semiconductor with suitable choice of magnetic field and doping concentration, proves the selected medium as a potential candidate material for the manufacture of highly efficient optoelectronic devices.

20.1 Introduction

The investigation of nonlinear optical (NLO) susceptibilities of a material give us a valuable knowledge regarding its nonlinear properties and also play a crucial role in manufacturing the efficient NLO devices such as optical amplifiers/oscillators,

M. Singh (✉)
Department of Physics, Government College Matanhail, Jhajjar, Haryana 124106, India

J. Gahlawat
Department of Physics, Baba Mastnath University, Asthal Bohar, Rohtak, Haryana 124021, India

A. Sangwan · M. Singh
Department of Physics, Singhania University, Pacheri Bari, Jhunjhunu, Rajasthan 333515, India
e-mail: msgur_18@yahoo.com

N. Singh
Department of Physics, Rajiv Gandhi Government College for Women, Bhiwani, Haryana 127021, India

V. K. Jain et al. (eds.), *Recent Trends in Materials and Devices*, Springer Proceedings in Physics 256, https://doi.org/10.1007/978-981-15-8625-5_20

sensors, optical frequency converters [1, 2], and optical signal processing [3, 4]. Moreover, the alter of sign of NLO susceptibilities lead to interesting phenomena including amplification/attenuation, self focusing/defocusing etc. which have been utilized in the manufacture of optical amplifiers, optical limiters, optical switches etc. [5, 6].

The selection of a NLO medium as well as its operating wavelength are fundamental features in designing and manufacturing the NLO devices. Among various NLO media, semiconductor crystals put forward substantial flexibility in manufacturing the efficient NLO devices [7–9].

Until now, semiconductor resonant optical nonlinearities (SRONs), because of their large values, have been employed in improving the performance of NLO devices [10]. Nevertheless, the response time of such devices is very slower because their operation depend upon (i) excitation of charge carriers during real transition, (ii) building up of energy, and (iii) relaxation time of charge carriers. On the other hand, the semiconductor non-resonant optical nonlinearities (SNONs) are generally smaller than SRONs but the response time of based devices is much faster. This is because SNONs do not involve the creation and relaxation of charge carriers. Hence, SNONs based NLO phenomena have been successfully implemented in fast operating optical communication networks. Since the origin of nonlinear optics, an enhancement and monitoring of SNONs have been important topics of research to improve the performance and enhance the efficiency of NLO devices based on them. Available literature reveals that composition, doping, micro-structuring etc. have been generally utilized in enhancing SNONs and hence the efficiency and performance of dependent NLO devices [11, 12]. In addition, SNONs may be altered by the application of magnetic and/or electric fields applied from outside. This technique is being utilized in understanding the concept of various NLO phenomena such as magneto/electro-optic effects [13]. In the presence of an externally applied magnetic field, an improvement in terahertz emission from various III–V semiconductor crystals have been reported [14–16]. In addition, in the appearance of an external dc magnetic field, III–V semiconductor crystals support new modes and afford a number of channels for scattering, which have been utilized in opto-acoustic diagnostics [17].

It is well established fact that non-centrosymmetric crystals possess both as even ($\chi^{(2)}$, $\chi^{(4)}$, …) as well as odd ($\chi^{(3)}$, $\chi^{(5)}$, …) order optical nonlinearities. The second- and third-order ($\chi^{(2)}$, $\chi^{(3)}$) optical nonlinearities give rise the fundamental nonlinear phenomena and have been utilized in the manufacture of fundamental NLO devices viz., optical parametric amplifiers/oscillators, frequency converters, optical phase conjugate mirrors, optical switches etc. [18]. Hence, in order to improve the performance of these devices, it becomes important to enhance the magnitude of $\chi^{(2)}$ and $\chi^{(3)}$.

Motivated by intense interest in the optoelectronics, using the coupled-mode theory, here we have obtained expressions for $\chi^{(2)}$ and $\chi^{(3)}$ in a piezoelectric semiconductor magneto-plasma. Numerical analysis has been performed for *n*-InSb–CO_2 laser system to set up the validity of developed model. The outcomes signify that the magnitudes of $\chi^{(2)}$ as well as $\chi^{(3)}$ can be enhanced as well as their sign can be altered

by suitably choosing doping level, external dc magnetic field and pump intensity; and open up the opportunities of fabrication of fast NLO devices.

20.2 Theoretical Formulations

In this analysis, we use the popularly known hydrodynamic (fluid) model of one-component (viz., *n*-type) homogeneous semiconducting magneto-plasma, under the condition $k_a l \ll 1$, where k_a is the acoustic wave number and l being the electron-mean free path. In addition, it agrees to neglect the non-uniformity of pump field under electric-dipole approximation [19].

Let us consider an intense pump wave $\vec{E}_0 = \hat{x} E_0 \exp[i(k_0 x - \omega_0 t)]$ irradiating a piezoelectric semiconductor crystal placed in an externally applied static magnetic field $\vec{B} = \hat{z} B_0$. In a piezoelectric semiconductor NLO crystal, the time varying pump field sets up piezoelectric as well electrostrictive strain and as a result induces an acoustic wave. Let $u(x, t)$ be the deviation of a lattice point x from its equilibrium location so that one-dimensional strain along $+x$ axis is represented by $\partial u/\partial x$. The net force acting along $+x$ axis (i.e. the propagation direction of pump wave) per unit volume is given by.

$$F_e = \frac{\partial}{\partial x}\left(-\beta E_0 + \frac{\gamma}{2}|E_0|^2\right), \tag{20.1}$$

in which, β is the piezoelectric coefficient and γ represent the electrostrictive coefficient of chosen NLO crystal. The equation of motion for lattice vibrations of the crystal can be expressed as

$$\rho \frac{\partial^2 u}{\partial t^2} - C \frac{\partial^2 u}{\partial x^2} + 2\Gamma_a \frac{\partial u}{\partial t} = F_e, \tag{20.2}$$

where ρ is mass density, C is elastic stiffness constant and Γ is damping parameter (introduced phenomenologically) of the chosen NLO crystal. Let us consider that the acoustic wave induced in crystal is a plane wave traveling along the propagation direction of pump wave. The acoustic field can be represented as: $\vec{E}_a = \hat{x} E_a \exp[i(k_a x - \omega_a t)]$. The incident pump wave is scattered by acoustic field at Stokes shifted frequency (ω_s), which subsequently modulates the optical dielectric constant of semiconductor medium and thus causes an energy exchange between pump and scattered Stokes fields (differing in frequency by ω_a). The scattered Stokes field can be represented as: $\vec{E}_s = \hat{x} E_s \exp[i(k_s x - \omega_s t)]$.

Here, the pump wave is considered as an output of pulsed laser with pulse duration $\tau_0 > \Gamma_a^{-1}$ and frequency $\omega_0 \gg \omega_a$ in infrared regime. Under these assumptions, the laser-semiconductor interaction can be considered as a quasi (steady-state) process. In a laser—semiconductor magneto-plasma interaction process, the equation of charge carriers motion can be represented by the zeroth and first-order momentum transfer

equations given by

$$\frac{\partial \vec{v}_0}{\partial t} + \nu \vec{v}_0 = -\frac{e}{m}[\vec{E}_0 + (\vec{v}_0 \times \vec{B}_0)] \tag{20.3}$$

and

$$\frac{\partial \vec{v}_a}{\partial t} + \nu \vec{v}_1 + \vec{v}_0 \times (\nabla . \vec{v}_1) = -\frac{e}{m}[\vec{E}_1 + (\vec{v}_1 \times \vec{B}_0)], \tag{20.4}$$

respectively. Here, v_0 and v_1 represent the zeroth (i.e. equilibrium) and first-order (i.e. perturbed) oscillatory velocities of electron fluid, respectively. m is the effective mass of an electron in the semiconductor crystal and $-e$ is the electronic charge. ν is the electron–electron collision frequency. In presence of a strong pump wave, a strong effective Lorentz force $[\vec{E}_{0,1} + (\vec{v}_{0,1} \times \vec{B}_0)]$, act on electrons because of their very small effective mass.

The other needful equations of present analysis are:

$$\frac{\partial n_1}{\partial t} + v_1 \frac{\partial n_1}{\partial x} + n_1 \frac{\partial v_0}{\partial x} + n_0 \frac{\partial v_1}{\partial x} = 0 \tag{20.5}$$

$$\frac{\partial E_{sc}}{\partial x} = -\frac{1}{\varepsilon}\left(n_1 e + \beta \frac{\partial^2 u}{\partial x^2} - \gamma \frac{\partial^2 u^*}{\partial x^2} E_1\right). \tag{20.6}$$

Equation (20.5) is the well known equation of continuity, in which n_1 and n_0 represent the perturbed and un-perturbed electron densities, respectively. Equation (20.6) is Poisson's equation which represents the induced space charge electric field E_{sc} arising due to electron density perturbations, piezoelectric and electrostrictive strains. Here, ε $(=\varepsilon_0 \varepsilon_l)$ represent the dielectric function of semiconductor medium, with ε_0 and ε_l stand for permittivity of free space and static dielectric constant of semiconductor medium, respectively.

In the semiconductor medium, the optical nonlinearity arises because of nonlinear interaction of acoustic wave with electron-plasma wave under the influence of external magnetic field. In weak magnetic field ($\omega_c \tau \ll 1$, in which $\omega_c = (e/m)B_0$ is electron-cyclotron frequency and τ is carriers relaxation time), the electrons complete a small number of orbits prior to collision and as a consequence the magnetic field has very small effect of electrons orbit deflection. On the other hand, in sufficiently strong magnetic field ($\omega_c \tau \gg 1$), the electrons are able to complete a large number of orbits before their scattering and hence their mean-free path become comparable to cyclotron radius. Using linearized perturbation theory, the equation of carrier density fluctuations in a semiconductor magneto-plasma has been obtained from (20.1)–(20.6) as

$$\frac{\partial^2 n_1}{\partial t^2} + \nu_e \frac{\partial n_1}{\partial t} + \omega_p^2 \delta_1 n_1 + \frac{ik_a^3 \omega_p^2 \delta_1 E_a(\beta^2 + \beta\gamma E_0)}{\rho e \Omega_a^2} + \frac{iek_0 n_1 \omega_p^2 E_0}{m\delta_{pl}^2} - \frac{k_0 k_a^3 \omega_p^2 E_a E_0(\beta^2 + \beta\gamma E_0)}{\rho m \Omega_a^2 \delta_{pl}^2} - \delta_0 E_0 \frac{e}{m} \frac{\partial n_1}{\partial x} - i\frac{e}{m} k_0 n_1 \delta_0 E_0 = 0 \tag{20.7}$$

where $\nu_e = \nu + ik_0 v_0$, $\Omega_a^2 = \omega_a^2 - k_a^2 v_a^2 + 2i\Gamma_a \omega_a$, $\delta_{pl}^2 = \frac{(\delta_0^2+\omega_c^2)(\delta_1^2+\omega_c^2)}{\delta_0 \delta_1}$, $\delta_0 = 1 - \frac{\omega_c^2}{(\omega_c^2+\Delta_0^2)}$, $\delta_1 = 1 - \frac{\omega_c^2}{(\omega_c^2+\Delta_1^2)}$, $\Delta_0 = \nu - i\omega_0$, $\Delta_1 = \nu - i\omega_s + ik_s v_0$, and $\omega_p = \left(\frac{n_0 e^2}{m\varepsilon}\right)^{1/2}$(electron-plasma frequency).

The carrier density perturbation n_1 oscillate at induced acoustic wave frequency and scattered Stokes wave frequency components (i.e. ω_a and ω_s). It can be expressed as: $n_1 = n_{1s}(\omega_a) + n_{1f}$ (ω_s), where n_{1s} (low-frequency component) and n_{1f} (high-frequency component) are associated with acoustic wave frequency ω_a and electromagnetic wave frequencies $(\omega_0 \pm \omega_a)$, respectively. In the present analysis, the higher-order terms at frequencies $\omega_{s,q}(=\omega_0 \pm q\omega_a)$, for $q \geq 2$ being off-resonant have been neglected and only the first-order (with $q = 1$) scattered Stokes component has been considered.

Under rotating-wave-approximation, (20.7) give rise to following coupled equations for density perturbation components (n_{1s} and n_{1f}) as

$$\frac{\partial^2 n_{1s}}{\partial t^2} + \nu_e \frac{\partial n_{1s}}{\partial t} + \omega_p^2 \delta_1 n_{1s} - \frac{ik_a^3 \omega_p^2 \delta_1 E_a(\beta^2 + \beta\gamma E_0)}{\rho e \Omega_a^2} - i(e/m) k_a n_{1f}^* \delta_0 E_0 = 0 \tag{20.8a}$$

and

$$\frac{\partial^2 n_{1f}}{\partial t^2} + \nu_e \frac{\partial n_{1f}}{\partial t} + \omega_p^2 \delta_1 n_{1f} + \frac{iek_0 n_{1s}^* \omega_p^2 E_0}{m\delta_{pl}^2} - \frac{k_0 k_a^3 \omega_p^2 E_a^* E_0(\beta^2 + \beta\gamma E_0)}{\rho m \Omega_a^2 \delta_{pl}^2} - i(e/m) k_s n_{1s}^* \delta_0 E_0 = 0 \tag{20.8b}$$

Equations (20.8a) and (20.8b) reveal that n_{1s} and n_{1f} are coupled to one another by means of pump electric field E_0. On solving (20.8a) and (20.8b), expressions for n_{1s} and n_{1f} can be obtained as well as their values can be determined by putting the values of pump electric field and material parameters. We obtained an expression for n_{1s} as

$$n_{1s}^* = \frac{ik_a^3 \omega_p^2 (\beta^2 + \beta\gamma E_0) E_a^*}{\rho \delta_{pl}^2} \left(\frac{\delta_1^*}{e\Omega_a^2} - \frac{e\delta_0^* k_0 k_a |E_0|^2}{m^2 \Omega_a^2 \Omega_{pl}^2 \Omega_{pd}^2} \right), \tag{20.9}$$

where $\Omega_{pl}^2 = \omega_p^2\delta_1 - \omega_a^2 - i\nu_e\omega_a$ and $\Omega_{pd}^2 = \omega_p^2\delta_1 - \omega_s^2 - i\nu_e\omega_s$.

Let us now deal with theoretical formulations for nonlinear induced polarization (at ω_s), which arises because of nonlinear induced current density of semiconductor medium. The back-scattered Stokes component of effective nonlinear induced current density may be expressed as

$$J_e(\omega_s) = -(n_{1s}^* e v_0 + n_0 e v_1). \tag{20.10a}$$

The time integral of effective induced current density gives effective nonlinear induced polarization as.

$$P_e(\omega_s) = \int J_e(\omega_s)\,\mathrm{d}t. \tag{20.10b}$$

After further solving effective polarization is obtained as

$$P_e(\omega_s) = \frac{iek_a^3\omega_p^2\Delta_0(\beta^2+\beta\gamma E_0)E_0E_a^*}{\rho m\Omega_{pl}^2(\omega_c^2+\Delta_0^2)}\left(\frac{\delta_1^*}{\Omega_a^{2*}} - \frac{e^2k_0k_a\delta_0^*|E_0|^2}{m^2\Omega_a^2\Omega_{pd}^2\delta_{pl}^2}\right). \tag{20.11a}$$

The nonlinear polarization may be defined by well known equation as

$$\begin{aligned} P_e(\omega_s) = \varepsilon_0(([\chi^{(2)}(\omega_s)]_\beta + [\chi^{(2)}(\omega_s)]_{\beta,I}).E_0E_a^* \\ + ([\chi^{(3)}(\omega_s)]_{\beta,\gamma}. + [\chi^{(3)}(\omega_s)]_{\beta,\gamma,I}).E_a^*|E_0|^2), \end{aligned} \tag{20.11b}$$

where $[\chi^{(2)}(\omega_s)]_\beta$, $[\chi^{(2)}(\omega_s)]_{\beta,I}$, $[\chi^{(3)}(\omega_s)]_{\beta,\gamma}$ and $[\chi^{(3)}(\omega_s)]_{\beta,\gamma,I}$ represent the intensity independent second-order optical susceptibility, intensity dependent second-order optical susceptibility, intensity independent third-order optical susceptibility, and intensity dependent third-order optical susceptibility, respectively. Using (20.11a) and (20.11b), these are given as

$$[\chi^{(2)}(\omega_s)]_\beta = \frac{i(e/m)k_a^3\omega_p^2\delta_1^*\Delta_0\beta^2}{\rho\varepsilon_0\Omega_a^{2*}\Omega_{pl}^2(\omega_c^2+\Delta_0^2)} \tag{20.12a}$$

$$[\chi^{(2)}(\omega_s)]_{\beta,I} = \frac{2i(e/m)^3k_0k_a^4\omega_p^2\delta_0^*\Delta_0\beta^2I_0}{\rho\eta\varepsilon_0\Omega_a^2\Omega_{pl}^2\Omega_{pd}^2\delta_{pl}^2(\omega_c^2+\Delta_0^2)} \tag{20.12b}$$

$$[\chi^{(3)}(\omega_s)]_{\beta,\gamma} = \frac{i(e/m)k_a^3\omega_p^2\delta_1^*\Delta_0\beta\gamma}{\rho\varepsilon_0\Omega_a^{2*}\Omega_{pl}^2(\omega_c^2+\Delta_0^2)}, \tag{20.12c}$$

$$[\chi^{(3)}(\omega_s)]_{\beta,\gamma,I} = \frac{2i(e/m)^3k_0k_a^4\omega_p^2\delta_0^*\Delta_0\beta\gamma I_0}{\rho\eta\varepsilon_0\Omega_a^2\Omega_{pl}^2\Omega_{pd}^2\delta_{pl}^2(\omega_c^2+\Delta_0^2)} \tag{20.12d}$$

where $I = \frac{1}{2}\eta\varepsilon_0|E_0|^2$ represents the intensity of pump wave, in which η stands for background refractive of semiconductor medium.

In (20.12a–d), Ω_a^2 represents the dispersion of acoustic wave. Ω_{pl}^2 and Ω_{pd}^2 represent the plasma frequency modified by acoustic frequency and Stokes wave frequency, respectively. In the forthcoming section (20.12a–d) have been utilized for detailed analysis.

20.3 Results and Discussions

In order to make the numerical estimations well-matched with the requirements, let us consider *n*-type doped InSb sample (at liquid nitrogen temperature, i.e. 77 K) as a representative weakly-piezoelectric semiconductor crystal illuminated by CO_2 laser at 10.6 μm wavelength (corresponding frequency, $\omega_0 = 1.78 \times 10^{14}\ s^{-1}$) so as to fulfill the off-resonant laser excitation requirement. Here, it should be noted that at 77 K temperature, the leading scattering mechanism for energy and momentum transfer of electrons in piezoelectric semiconductors is because of acoustic phonons [20, 21]. The material parameters of the representative sample are:

$m = 0.014m_0$ (with $m_0 = 9.1 \times 10^{-31}$ kg), $\varepsilon_l = 15.8$, $\eta = 3.8$, $\beta = 0.054\ cm^{-2}$, $\gamma = 5 \times 10^{-10}$ SI units, $\rho = 5.8 \times 10^3\ kg\ m^{-3}$, $\omega_a = 2 \times 10^{11}\ s^{-1}$, $\omega_s = 1.77 \times 10^{14}\ s^{-1}$, $\Gamma_a = 2 \times 10^{10}\ s^{-1}$, $\nu = 3 \times 10^{11}\ s^{-1}$, $k_a = 5 \times 10^7\ m^{-1}$, $v_a = 4 \times 10^3\ ms^{-1}$.

Equations (20.12a–d) show that $[\chi^{(2)}(\omega_s)]_\beta$, $[\chi^{(2)}(\omega_s)]_{\beta,I}$, $[\chi^{(3)}(\omega_s)]_{\beta,\gamma}$ and $[\chi^{(3)}(\omega_s)]_{\beta,\gamma,I}$ are complex quantities. The present analytical investigation explains the dependence of these optical susceptibilities on controllable parameters such as pump intensity (I_0), doping concentration (via electron-plasma frequency, ω_p) and external dc magnetic field (via electron-cyclotron frequency, ω_c). Equations (20.12a–d) have been used to study NLO susceptibilities by varying controllable parameters: n_0, B_0 and I_0. Efforts have been directed towards:

(i) To determine suitable values of n_0, B_0 and I_0 to enhance second- and third-order nonlinearities, and
(ii) To search the feasibility of fast operating semiconductor NLO devices based on these nonlinearities.

Equations (20.12a, b) reveal that both $[\chi^{(2)}(\omega_s)]_\beta$ and $[\chi^{(2)}(\omega_s)]_{\beta,I}$ are finite if β is finite while (20.12c, d) reveal that $[\chi^{(3)}(\omega_s)]_{\beta,\gamma}$ and $[\chi^{(3)}(\omega_s)]_{\beta,\gamma,I}$ are finite if both β as well as γ are finite. Thus the finiteness of piezoelectricity is prerequisite for occurrence of second-order nonlinearity while finite if both piezoelectricity as well as electrostriction is essential condition for occurrence of third-order nonlinearity in piezoelectric semiconductor magneto-plasmas.

Using algebraic simplification, expressions can be obtained for real as well as imaginary parts of (intensity independent and dependent) second- and third-order optical susceptibilities. This is clearly established truth that real part of NLO susceptibilities accounts for nonlinear refraction while imaginary part give rise the

phenomena of nonlinear absorption in the medium. The knowledge of wave propagation characteristics in a nonlinear refractive medium provides the design of various optical devices such as filters, amplifiers, couplers and optical waveguides [14].

Figures 20.1 and 20.2 shows the nature of dependence of real parts of $[\chi^{(2)}(\omega_s)]_\beta$,$[\chi^{(3)}(\omega_s)]_{\beta,\gamma}$ and $[\chi^{(2)}(\omega_s)]_{\beta,I}$, $[\chi^{(2)}(\omega_s)]_{\beta,I}$ respectively.

In Fig. 20.1, the real parts of intensity-independent second- and third-order susceptibilities $[\chi^{(2)}(\omega_s)]_\beta$ and $[\chi^{(3)}(\omega_s)]_{\beta,\gamma}$ are plotted versus magnetic field B_0 for two different doping concentrations. It clearly shows the substantial enhancement of real parts of $[\chi^{(2)}(\omega_s)]_\beta$ and $[\chi^{(3)}(\omega_s)]_{\beta,\gamma}$ as well as alter of their sign. This distinctive behavior occurs because of two resonance conditions: (i) $\frac{(\nu^2+\omega_c^2)}{1-(\omega_p^2/4\omega_a^2)} \sim \omega_s^2$ (modified electron–electron collision frequency ~ Stokes wave frequency), and (ii) $\omega_c^2 \sim \omega_s^2$ (electron-cyclotron frequency ~ Stokes wave frequency). The situation at which real parts of $[\chi^{(2)}(\omega_s)]_\beta$ and $[\chi^{(3)}(\omega_s)]_{\beta,\gamma}$ changes their sign are termed as 'dielectric anomaly' and the excitation around resonance is known as 'anomalous dispersion' [22].

By adjusting values of n_0 (say 3×10^{19} m^{-3}) and B_0 (say 9.0 T), we obtained real part of $[\chi^{(2)}(\omega_s)]_\beta = 2.5 \times 10^{-9}$ m V^{-1} and real part of $[\chi^{(3)}(\omega_s)]_{\beta,\gamma} = 6.5 \times 10^{-17}$ m^2 V^{-2}. When B_0 is increased and n_0 is lowered, the change of sign of real parts of $[\chi^{(2)}(\omega_s)]_\beta$ as well as $[\chi^{(3)}(\omega_s)]_{\beta,\gamma}$ are observed between 0.0 and 10.5 T. This figure also manifests that when ω_p (through n_0) approaches to $2\omega_a$, the scattered Stokes wave frequency shifts in the direction of larger values of B_0 (i.e. blue shift). Interestingly, with further increasing ω_p, because of departure from resonance, the

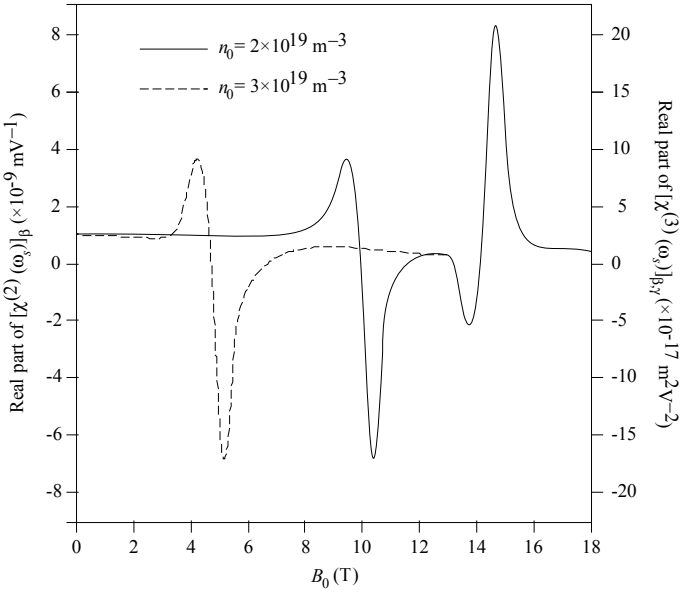

Fig. 20.1 Plot of real parts of $[\chi^{(2)}(\omega_s)]_\beta$, $[\chi^{(3)}(\omega_s)]_{\beta,\gamma}$ versus B_0

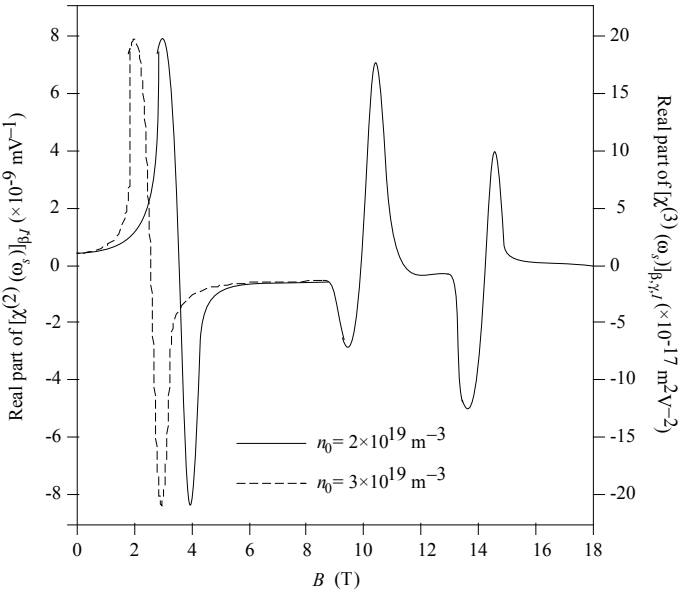

Fig. 20.2 Plot of real parts of $[\chi^{(2)}(\omega_s)]_{\beta,I}$, $[\chi^{(2)}(\omega_s)]_{\beta,I}$ versus B_0.

scattered Stokes wave frequency shifts in the direction of smaller values of B_0 (i.e. red shift).

For 10.5 T < B_0 < 14.2 T, the sign of real parts of $[\chi^{(2)}(\omega_s)]_{\beta}$ and $[\chi^{(3)}(\omega_s)]_{\beta,\gamma}$ both are negative. At $B_0 = 14.2$ T, the sign of real parts of $[\chi^{(2)}(\omega_s)]_{\beta}$ as well as $[\chi^{(3)}(\omega_s)]_{\beta,\gamma}$ become positive (because of the resonance condition (ii)) and their magnitudes are 8.4×10^{-9} m V^{-1} and 2.2×10^{-16} m^2 V^{-2}, respectively; which are about one order higher than reported in case of GaAlAs [23]. In particular, this result signifies that in the appearance of magnetic field (B_0 ~ 14.2 T), the effect of doping concentration on real parts of $[\chi^{(2)}(\omega_s)]_{\beta}$ and $[\chi^{(3)}(\omega_s)]_{\beta,\gamma}$ is weak because $\omega_p \ll \omega_c$. However, in the non-appearance of magnetic field ($B_0 = 0$ T), and $n_0 = 2 \times 10^{19}$ m^{-3}, the magnitude of real parts of $[\chi^{(2)}(\omega_s)]_{\beta}$ and $[\chi^{(3)}(\omega_s)]_{\beta,\gamma}$ are 0.8×10^{-9} m V^{-1} and 2.5×10^{-17} m^2 V^{-2} respectively; which are about one order lesser than the magnitudes obtained above near resonances. In the non-appearance of magnetic field, pump wave is scattered by induced acoustic field and electron-plasma wave in doped semiconductors.

The most important aspect of the result is the monitoring of real parts of $[\chi^{(2)}(\omega_s)]_{\beta}$ and $[\chi^{(3)}(\omega_s)]_{\beta,\gamma}$ by varying simultaneously/independently n_0 and B_0 and also attaining a large value of real parts of $[\chi^{(2)}(\omega_s)]_{\beta}$ and $[\chi^{(3)}(\omega_s)]_{\beta,\gamma}$ in piezoelectric semiconductor crystals. The results obtained in Fig. 20.1 allow the tuning of scattered Stokes wave over a broad frequency regime and opens up the opportunity of manufacture of frequency converters.

In Fig. 20.2, the real parts of intensity-dependent second- and third-order susceptibilities $[\chi^{(2)}(\omega_s)]_{\beta,I}$ and $[\chi^{(2)}(\omega_s)]_{\beta,I}$ are plotted versus magnetic field B_0 for two

different doping concentrations at pump intensity $I_0 = 2 \times 10^{12}$ W m^{-2}. This gives a picture of the enhancement of real parts of $[\chi^{(2)}(\omega_s)]_{\beta,I}$ and $[\chi^{(2)}(\omega_s)]_{\beta,I}$ as well as alter their sign. However, in this case the distinctive behavior of real parts of $[\chi^{(2)}(\omega_s)]_{\beta,I}$ and $[\chi^{(2)}(\omega_s)]_{\beta,I}$ occurs because of three resonance conditions: (i) $1 + \frac{\omega_p^2 \omega_c^2}{\nu^2} \sim \omega_s^2$, (ii) $2\omega_c^2 \sim \omega_s^2$, and (iii) $\omega_c^2 \sim \omega_s^2$. An exciting aspect of this case is an interaction between electron-plasmon oscillator and electron-cyclotron oscillator. Let we define this as hybrid-oscillator. As a consequence of interaction of pump electric field with the hybrid oscillator, electron-plasma and electron-cyclotron frequencies dependent coherent Stokes wave is generated. It is generally advantageous, moving the coherent Stokes wave frequency to an accessible spectral region in proportion to: (a) ω_c (or B_0) for fixed ω_p (or n_0), (b) ω_p (or n_0) for fixed ω_c (or B_0), and (c) combination of ω_c and ω_p both. For example, in n-InSb crystal ($n_0 = 2 \times 10^{19}$ m^{-3}), an external magnetic field (1.5 − 3.6 T) yield large values of real parts of $[\chi^{(2)}(\omega_s)]_{\beta,I}$ and $[\chi^{(2)}(\omega_s)]_{\beta,I}$ both, alter their sign, and shifts the coherent Stokes wave frequency in the direction of higher value (i.e. blue shift).

For 4.5 T < B_0 < 9 T, the sign of real parts of $[\chi^{(2)}(\omega_s)]_{\beta,I}$ and $[\chi^{(2)}(\omega_s)]_{\beta,I}$ both are negative and their values are nearly constant. This is because in this range of magnetic field, no resonance occurs. However, for 9.5 T < B_0 < 14.2 T, a sharp enhancement and alter of sign of real parts of $[\chi^{(2)}(\omega_s)]_{\beta,I}$ and $[\chi^{(2)}(\omega_s)]_{\beta,I}$ both at $B_0 = 10.5$ and 14.2 T occurs due to resonance conditions (ii) and (iii), respectively.

Here, it should be worth mentioning that apart from B_0 and n_0 dependence, intensity parameter may also be used in enhancing the real parts of $[\chi^{(2)}(\omega_s)]_{\beta,I}$ as well as $[\chi^{(2)}(\omega_s)]_{\beta,I}$. For fixed values of B_0 and n_0, the magnitude of real parts of $[\chi^{(2)}(\omega_s)]_{\beta,I}$ and $[\chi^{(2)}(\omega_s)]_{\beta,I}$ both increase linearly with rising pump intensity. However, practically it is not feasible to increase the excitation intensity in an arbitrary manner as it can cause the damage of semiconductor medium. Mayer et al. [24] concluded that when a sample of semiconductor crystal is illuminated by a laser beam having long pulse duration a repeated consequent is the production of heat. However, the damage threshold of semiconductor sample may be lowered either by illuminating the semiconductor sample with a pump wave having shorter pulse duration or by mechanism of free carrier nonlinear absorption.

These results also allow the tuning of scattered Stokes wave over a wide frequency regime and explore the manufacture of optical switches and frequency converters.

Figures 20.3 and 20.4 shows the nature of dependence of imaginary parts of $[\chi^{(2)}(\omega_s)]_{\beta}$, $[\chi^{(3)}(\omega_s)]_{\beta,\gamma}$ and $[\chi^{(2)}(\omega_s)]_{\beta,I}$, $[\chi^{(3)}(\omega_s)]_{\beta,\gamma,I}$ respectively.

In Fig. 20.3, the imaginary parts of intensity independent second- and third-order susceptibilities $[\chi^{(2)}(\omega_s)]_{\beta}$ and $[\chi^{(3)}(\omega_s)]_{\beta,\gamma}$ are plotted versus magnetic field B_0 for two different doping concentrations. It may be seen that for both concentrations initially imaginary parts of $[\chi^{(2)}(\omega_s)]_{\beta}$ and $[\chi^{(3)}(\omega_s)]_{\beta,\gamma}$ are positive and increase very slowly with increasing B_0. But, when $\omega_s^2 \sim \frac{(\nu^2+\omega_c^2)}{1-(\omega_p^2/4\omega_a^2)}$, imaginary parts of $[\chi^{(2)}(\omega_s)]_{\beta}$ and $[\chi^{(3)}(\omega_s)]_{\beta,\gamma}$ both rise abruptly and achieve their peak value and an alter of sign occurs at sharp resonance condition. Further because of departure from resonance, negative imaginary parts of $[\chi^{(2)}(\omega_s)]_{\beta}$ and $[\chi^{(3)}(\omega_s)]_{\beta,\gamma}$ both decreases sharply and achieve a comparatively smaller value. A further increase in magnetic

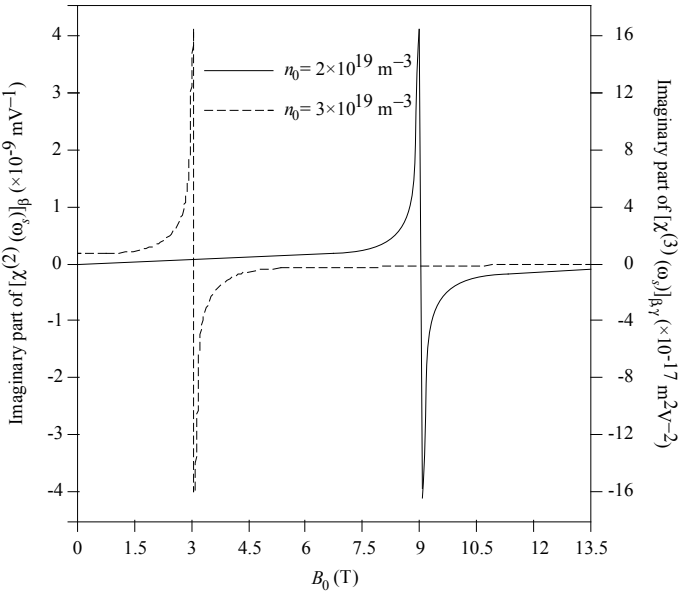

Fig. 20.3 Plot of imaginary part of $[\chi^{(2)}(\omega_s)]_\beta$, $[\chi^{(3)}(\omega_s)]_{\beta,\gamma}$ versus B_0

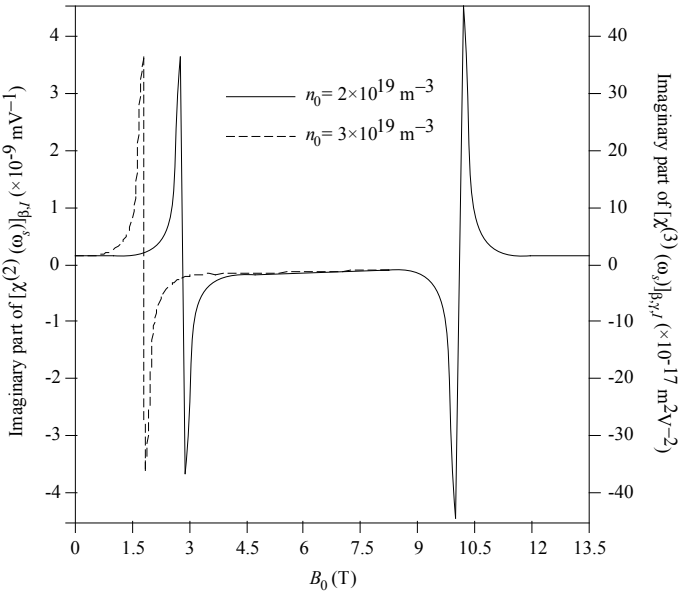

Fig. 20.4 Plot of imaginary part of $[\chi^{(2)}(\omega_s)]_{\beta,I}$, $[\chi^{(3)}(\omega_s)]_{\beta,\gamma,I}$ versus B_0

field causes an abrupt rise in imaginary parts of $[\chi^{(2)}(\omega_s)]_\beta$ and $[\chi^{(3)}(\omega_s)]_{\beta,\gamma}$ both occurs and an alter of sign is observed because of resonance condition: $\omega_s^2 \sim \omega_c^2$. These outcomes infer that when $\omega_p \sim 2\omega_a$, the alter of sign of imaginary parts of $[\chi^{(2)}(\omega_s)]_\beta$ and $[\chi^{(3)}(\omega_s)]_{\beta,\gamma}$ both can be achieved in low doped piezoelectric semiconductor crystals by an application of external magnetic field. Hence an external dc magnetic field dependent behavior of imaginary parts of $[\chi^{(2)}(\omega_s)]_\beta$ and $[\chi^{(3)}(\omega_s)]_{\beta,\gamma}$ in the case of piezoelectric semiconductor crystals can be utilized in designing optical switches because negative/positive imaginary parts of $[\chi^{(2)}(\omega_s)]_\beta$ and $[\chi^{(3)}(\omega_s)]_{\beta,\gamma}$ leads to loss/gain phenomena.

In Fig. 20.4, the imaginary parts of intensity dependent second- and third-order susceptibilities $[\chi^{(2)}(\omega_s)]_{\beta,I}$ and $[\chi^{(3)}(\omega_s)]_{\beta,\gamma,I}$ are plotted versus magnetic field B_0 for two different doping concentrations at pump intensity $I_0 = 2 \times 10^{12}$ W m^{-2}. For both the doping concentrations, initially imaginary part of $[\chi^{(2)}(\omega_s)]_{\beta,I}$ and $[\chi^{(3)}(\omega_s)]_{\beta,\gamma,I}$ both are positive and increase gradually with increasing B_0. When $\omega_c \sim \omega_s$, imaginary parts of $[\chi^{(2)}(\omega_s)]_{\beta,I}$ and $[\chi^{(3)}(\omega_s)]_{\beta,\gamma,I}$ both rises abruptly and attain their peak value. At sharp resonance condition: $\omega_s^2 \sim 1 + \frac{\omega_p^2 \omega_c^2}{\nu^2}$, alter of sign of imaginary parts of $[\chi^{(2)}(\omega_s)]_{\beta,I}$ and $[\chi^{(3)}(\omega_s)]_{\beta,\gamma,I}$ both occur. On further increasing B_0, sharp enhancement of imaginary parts of $[\chi^{(2)}(\omega_s)]_{\beta,I}$ and $[\chi^{(3)}(\omega_s)]_{\beta,\gamma,I}$ both is observed and alter of sign occur because of resonance condition: $\omega_s^2 \sim 2\omega_c^2$. Moreover, in this case, it can be observed that first resonance condition shifts toward smaller values of magnetic field with increasing doping concentration, while second resonance condition (near $B_0 = 10.0$ T) is independent of doping concentration. As an example, resonance occurs at 2.9 T when $n_0 = 2 \times 10^{19}$ m^{-3} and it shifts to smaller magnetic field ($B_0 = 1.9$ T) when $n_0 = 3 \times 10^{19}$ m^{-3}. Here, it should be noted that near the resonance conditions, the drift velocity of charge carriers, which strongly depends upon externally applied magnetic field, becomes much higher than acoustic wave velocity and consequently the rate of energy transfer from carrier-to-acoustic wave increases, and as a result the amplification of acoustic wave takes place. Subsequently, the amplified acoustic wave strongly interacts with the pump wave and the strength of the scattered Stokes mode enhances substantially.

20.4 Conclusions

In the present analysis, using the hydrodynamic (fluid) model for semiconductor magneto-plasma, the intensity independent/dependent second- as well as third-order NLO susceptibilities have been obtained in a piezoelectric semiconductor magneto-plasma, viz. *n*-InSb under off-resonant laser irradiation. The analysis deals with detailed incorporation of convective nonlinearity and explored the possibility of intensity dependence of second- and third-order NLO susceptibilities in piezoelectric semiconductor magneto-plasma. The analysis offer three achievable resonance conditions (by selecting controllable parameters such as external dc magnetic field and doping concentration): (i) electron-plasma frequency and acoustic wave

frequency, (ii) electron-cyclotron frequency and scattered Stokes wave frequency, and (iii) hybrid frequency and scattered Stokes wave frequency; at which an enhancement in magnitude and alter of sign of NLO susceptibilities occurs. The analysis lead to large tunable effects precisely in relation to frequency tuning and scattering phenomena which may be employed for frequency converters, spectroscopic measurement and design of optical switches. Hence, the proposed model opens up possibilities for the manufacture of efficient and high speed NLO devices.

References

1. H.J. Gerritsen, Appl. Phys. Lett. **10**, 239 (1967)
2. B.I. Stepanov, E.V. Ivakin, A.G. Rubanov, Dok. Acad. Nauk. SSSR **196**, 567 (1971)
3. A. Yariv, P. Yeh, *Optical Waves in Crystals* (Wiley, New York, 1984), p. 549
4. A.E. Willner, S. Khaleghi, M.R. Chitgarha, O.F. Yilmaz, J. Lightwave Technol. **32**, 660 (2014)
5. G. Banfi, V. Degiorgio, D. Ricard, Adv. Phys. **47**, 447 (1998)
6. H. Haug, S.W. Koch, *Quantum Theory of the Optical and Electronic Properties of Semiconductors*, 4th edn. (World Scientific, Singapore, 2004)
7. D.A.B. Miller, Laser Focus **19**, 61 (1983)
8. R.K. Jain, Opt. Eng. Bellingham **21**, 199 (1982)
9. S.D. Smith, Nature **316**, 319 (1982)
10. S.J. Sweeney, J. Mukherjee, Optoelectron. Dev. Mater., in *Springer Handbook of Electronic and Photonic Materials*, eds. by S. Kasap, P. Capper (Cham, Springer, 2017)
11. G. Lutz, *Semiconductor Radiation Detectors, Device Physics* (Springer, Berlin, 1999)
12. Y. Fu, M. Willander, *Physics Models of Semiconductor Quantum Devices* (Springer, Berlin, 1999)
13. E. Garmire, IEEE J. Quantum Electron. **6**, 1094 (2000)
14. G. Meinert, L. Banyai, P. Gartner, H. Haug, Phys. Rev. B **62**, 5003 (2000)
15. J.N. Heyman, P. Neocleous, D. Hebert, P.A. Crowell, T. Muller, K. Unterrainer, Phys. Rev. B **64**, 85202 (2001)
16. M.B. Johnston, D.M. Whittaker, A. Corchia, A.G. Davis, E.H. Linfield, J. Appl. Phys. **91**, 2004 (2001)
17. V.E. Gusev, A.A. Karabutov, *Laser Optoacoustics* (American Institute of Physics, New York, 1993), pp. 93–128
18. R.W. Boyd, *Nonlinear Optics San Diego* (Academic Press, 1992), Chap. 9
19. P.K. Kaw, J. Appl. Phys. **44**, 1497 (1973)
20. D.L. Rode, *Semiconductors and Semimetals*, vol. 10, eds. by R.K. Willardson, A.C. Beer (New York, Academic, 1975), p. 1
21. G.E. Stillman, C.M. Wolfe, J.O. Dimmock, J. Phys. Chem. Sol. **31**, 1199 (1970)
22. E.D. Palik, J.K. Furdyana, Rep. Prog. Phys. **33**, 1193 (1970)
23. X.H. Qu, H. Ruda, IEEE J. Quantum Electron. **31**, 228 (1995)
24. J.M. Mayer, F.J. Bartoli, M.R. Kruer, Phys. Rev. B **21**, 1559 (1980)

Chapter 21
Moving Ahead Towards Sustainable Development-AHWR, an Amicable Approach for Nuclear Reactors

Mahima Sachdeva, Ricardo B. Smith, and Astha Sachdeva

Abstract With a constant urge of digging the unraveled, India has come far ahead in taking an evolutionary step in the field of nuclear science. There has been a recent breakthrough in nuclear reactor advancements. India is using advanced heavy water reactors which function on thorium as one of its fuel components. It can be used in conjunction with plutonium or low enriched uranium. This has been a massive lead as it produces energy at commercial levels and leaves lesser residual actinides having long half-life and inert thorium oxide. This has optimized the energy production rate up to 50% with respect to its production of burnt fuels. This research focuses on bringing an insight on recent advancements in terms of researches and scientific projects that are being conducted in India and how its result would ascent with the current sustainability models such as "Green Chemistry", a program developed two decades ago in United States and England which defines its requirement for efficient transformation of reagents in obtaining desired results. This revolutionary uplift in nuclear science must reach global acceptance and execution. Considering the ample resources nature earth has bestowed us with, Brazil has remained away from the thorium fueled reactor project studied 50 years ago and there is no light put towards any future research prospects either. Being the second largest reserve of thorium on the entire planet, AHWR can become a mass advantage if explored and taken into deeper accounts.

M. Sachdeva
INO, Tata Institute of Fundamental Research, Mumbai, India

R. B. Smith (✉)
Nuclear and Energy Research Institute (IPEN/CNEN—SP), São Paulo, Brazil
e-mail: rbsmith@ipen.br

A. Sachdeva
Department of Anthropology, University of Delhi, New Delhi, India

V. K. Jain et al. (eds.), *Recent Trends in Materials and Devices*, Springer Proceedings in Physics 256, https://doi.org/10.1007/978-981-15-8625-5_21

21.1 Introduction

For more than 50 years, India is driving a nuclear programme known as the "Thorium Utilization Programme for Sustainable Energy". Due to abundance of thorium in the country and an increasing shortage of uranium, the efforts are being taken for definitive transition from uranium to thorium fuel cycle through three stages of the programme. The Advanced Heavy Water Reactor (AHWR) is the key component of the third stage. In its final stage, this reactor has proven to be a major contributor in reducing radioactive waste as it uses a fuel cycle with a smaller production of actinides. As thorium oxide has inert nature, it benefits in its prolonged storage. Therefore, safe disposal of spent fuel is achieved due to its inert matrix on completion of one fuel cycle mode.

As electricity needs are drastically increasing and fossil fuel reserves are on the verge of depletion, there is even greater concern of global warming and other environmental shifts. This unease in environment has brought nuclear power as a safe and important alternative to contribute substantially in addressing the global energy needs. As per the Human Development Report's per capita electricity consumption data, it is indicated that the world may need 3000–4000 nuclear reactors to meet the accelerating energy needs. Also, the concerns pertaining to human health and environmental changes by reducing pollution and waste production have taken a good leap since the mid-twentieth century and became more important after the long-term negative effects of human activities since the Industrial Revolution, which is an historical landmark of human's dominion over nature. It was clear that the search for cleaner production means and treatment of waste produced in the most diverse areas would be a matter not only of well-being but also of our bare survival. Therefore, in this paper, the main characteristics of Advanced Heavy Water Reactor will be presented as well as an analysis on how the Indian reactor seems consistent with these trends of increased safety and sustainability assurance in correlation with the twelve principles of the Green Chemistry and which of these principles can also be related to the nuclear area.

21.2 Sustainable Development

Sustainable development has been defined in many ways but the most frequently quoted definition is from Our Common Future, also known as the Brundtland Report: "Sustainable development is the one that serves the present needs without compromising the ability of future generations to meet their own needs" [1]. It is the economic, social, cultural and scientific development of societies ensuring more health, comfort and knowledge without depleting the planet's natural resources. Every form of relationship between man and nature must occur with the least possible damage to the environment. Policies, systems of trade, production, transformation and service, industry, tourism, agriculture, basic services, mining, and others must

exist to preserve biodiversity and the human being i.e. to protect the life of the planet [2].

Until 1982, data derived from thirteen most evolved countries working on nuclear reactors reveals that they dispose nuclear waste in drums and throw them into the deepest places in the ocean. According to an inventory organized by the International Atomic Energy Agency, approximately 85.0×10^{21} Bq of radioactive waste were discharged into the ocean [3]. The emission of radioactive gases and aerosols because of the atomic tests in the atmosphere was ceased in 1963 by the implication of Partial Nuclear Test Ban Treaty. An order of magnitude greater than 1.0×10^{21} Bq radioisotopes were estimated to be dispersed in the air by the 520 nuclear tests on Earth's surface [4].

21.2.1 Green Chemistry

Green chemistry is a design of chemical products and processes that reduces or eradicates the use or generation of hazardous substances. It is applied across the life cycle of a chemical product including its design, manufacture, use, and ultimate disposal [5]. The breadth of the concept of such chemistry is demonstrated in twelve principles which are as follows [6]:

1. Prevent waste.
2. Maximize atom economy.
3. Design less hazardous chemical synthesis.
4. Design safer chemicals and products.
5. Use Safer Solvents and Reaction Conditions.
6. Increase energy efficiency.
7. Use Renewable Feed Stocks.
8. Avoid chemical derivatives.
9. Use Catalysts and non-Stoichiometric Reagents.
10. Design chemicals and products for degradation after use.
11. Analyze in real time to prevent pollution.
12. Minimize the potential for accidents [5].

There is an amalgamation of green chemistry with nuclear energy utilization such as emerging separation techniques for nuclear fuel reprocessing and nuclear radioactive waste treatment [7, 8].

21.3 India's Nuclear Power Generation Programme

The nuclear power programme of India comprises of three stages. In first stage, India exerts the closed cycle mode in lieu of its phased expansion of nuclear power generation extending it through the second and third stages. Indigenous technology

for reprocessing of the spent fuel as well as the waste management programme has been developed by India through its own comprehensive research and development efforts and reprocessing plants were setup and are in operation, thereby attaining self-reliance in this domain. The second stage of nuclear power generation envisages the use of ^{239}Pu obtained from the first stage reactor (Pressurized Heavy Water Reactor) operation as a fuel core in Fast Breeder Reactors (FBR) and the byproduct formed namely ^{233}Uwill serve as a fuel for nuclear reactors of the third stage of India's Nuclear Power Programme. It is technically feasible to produce a sustained energy output of 420 GWe from the FBR.

Concurrently, it is proposed to use thorium-based fuel along with a small feed of plutonium-based fuel in Advanced Heavy Water Reactors (AHWRs). The AHWRs are expected to shorten the period of reaching the stage of large-scale thorium utilization.

21.3.1 Advanced Heavy Water Reactor

The Indian thorium-based nuclear energy systems are being developed in order to achieve sustainability in terms of fuel resources along with enhanced safety and reduction in waste generation. AHWR300-LEU is a 300 MWe, vertical, pressure-tube type reactor which uses boiling light water as coolant and heavy water as moderator. This reactor is particularly associated with a fuel cycle which has reduced environmental impact and also incorporates numerous passive safety features. Its fuel cluster contains 54 fuel pins which are arranged in three concentric circles surrounding a central displacer assembly (Fig. 21.1) and fuel cycle options are illustrated in Table 21.1 [9].

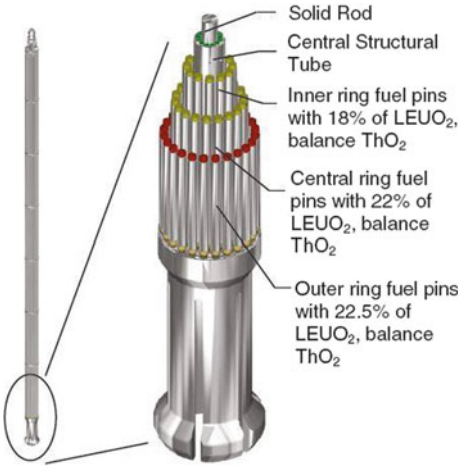

Fig. 21.1 AHWR300-LEU fuel cluster (*Source* [9])

Table 21.1 Fuel cycle options with AHWR

Fuel option with Pu + Th	Fuel option with LEU-Th
Inner ring: 3% ^{233}U + Th mixed oxide	**Inner ring**: 18.0% $LEUO_2$
Middle ring: 3.75% ^{233}U + Th mixed oxide	**Middle ring**: 22.0% $LEUO_2$
Outer ring: Pu (2.5% top, 4.0% bottom) + Th-mixed oxide	**Outer ring**: 22.5% $LEUO_2$

Source [9]

Several features of AHWR300-LEU which probably can reduce its capital and operating costs are listed below:

- Use of heavy water at low pressure can reduce the potential for leakage.
- Recovery of heat generated in the moderator for feed water heating.
- Inherent advantages of using high pressure boiling water as coolant: elimination of steam generators and the use of high-pressure stream.
- 500 m^3/day of demineralized water can be produced in multi-effect desalination plant by using steam from LP Turbine (for plants located on the sea coast).
- Design life of the reactor is hundred years [9].

Besides, an improved utilization of natural uranium resources in comparison with a modern LWR, AHWR300-LEU proposes remarkable advantages with respect to proliferation resistance. The 300MWe plant produces only 21% of the plutonium with reference to a modern LWR because of the use of mixed fuel (Fig. 21.2). Moreover, the plutonium obtained from the spent fuel of AHWR300-LEU consists of 56% of fissile isotopes approximately while the spent fuel from LWRs contains around 65% of fissile isotopes. Also, the fraction of ^{238}Pu is around 10% in total plutonium, which

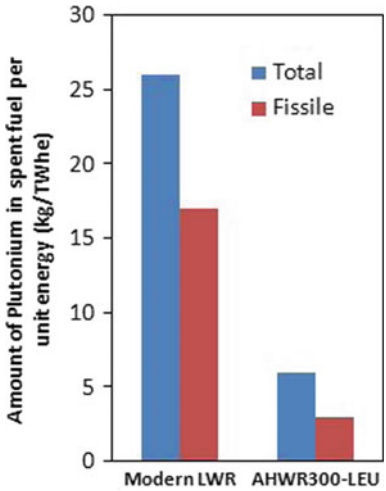

Fig. 21.2 Comparison of production of plutonium (*Source* [12])

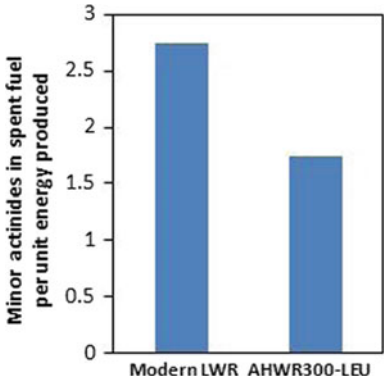

Fig. 21.3 Comparison of production of minor actinides (*Source* [12])

is much lower than modern LWRs. As it is responsible for generation of extensive amount of heat, the plutonium obtained from spent fuel of AHWR300-LEU serves as a less attractive source for proliferation. The appreciable quantities (approx. 200 ppm) of ^{232}U in uranium obtained from AHWR300-LEU's spent fuel are considered as one of the additional aspects of proliferation resistance. The daughter products of ^{232}U emit high-energy γ radiation. Thus, uranium can be re-used in other reactors in a proliferation resistant manner. It can also be noted that conventional approaches for dissolution are not efficient because of the significant percentage of thorium which makes the process of reprocessing more difficult [10, 11].

When compared to a modern LWR, AHWR300-LEU results in 37% lesser production of minor actinides for the same amount of energy output because of the higher periodicity of thorium (Fig. 21.3). Thus, burden on waste disposal requirements can be reduced. Further, the inert nature of the matrix makes thorium oxide suitable for prolonged storage and poses relatively complex challenges for reprocessing of AHWR300-LEU fuel as well [12].

21.4 Discussion

Out of twelve major principles of green chemistry, few of them are being discussed in context with the information gathered and reviewed on AHWR300-LEU:

Principle 1—Waste prevention: as AHWR300-LEU uses thorium as a fertile host, the quantity of minor actinides is significantly reduced. The thorium oxide produced as waste has an inert matrix which makes it suitable for long-term storage. It is important to recall here the convergence with the seventh principle of the radioactive waste management as adopted by IAEA [13] in 1995, which states that the generation of radioactive waste shall be maintained in the lowest level achievable. This can be understood as less waste volume and mass, lower activity, shorter half-lives and reduced radio toxicity of the radio nuclides contained in the waste.

Principle 2—Maximize atomic economy: although the principles of green chemistry were conceived for the production of substances with optimum use of chemical processes and expressed as the ratio of product mass and mass of reagents, it seems perfectly applicable to the generation of energy. Using the closed fuel cycle, the output of energy per unit mass of the primary fuel mined (kilograms of thorium or uranium) or raw material for the exploration of the energy source is much higher than any other fuel cycle including renewable, fossil fuels and other nuclear fuel cycles.

Principles 3 and 4—Designing less hazardous chemical synthesis, safer chemicals and products: the desirable characteristics of the discussed fuel cycle are intrinsically achieved by designing new systems for energy generation, thus meeting the idea behind the principle of safety by design.

Principle 6—Increase energy efficiency: this principle can be associated to the second principle, as pointed out earlier, in which the energy output per unit mass of mined and manufactured goods is much higher than the alternatives.

Principle 10—Design chemicals and products for optimum degradation after use: this is an intrinsic property of the waste that naturally decays the activity and reduces the associated danger. Although the time necessary for some radio nuclides present in the waste generated from fuel cycle to become harmless may exceed.

Principle 12—Minimize the potential for accidents: many passive systems which are incorporated in the reactor prevent the accident conditions to occur in case of forced shutdown and heat reduction. Also, the chance of leakage can be reduced with the use of heavy water at low pressures.

21.5 Conclusion (The Brazilian Experience)

In the 1960s, Brazil was in search of suitable nuclear reactor and the fuel to be used. According to the 2018 NEA/IAEA report, Brazil has the second largest thorium reserve on the planet after India [14]. It was up to the governing authorities to decide which system would be the most suitable. In 1965, in the city of Belo Horizonte, a team of nuclear engineers formed a thorium group aiming to make Brazil autonomous in the design and construction of a reactor based on thorium as nuclear fuel. The group's task was similar to that of India's Nuclear Programme. Researchers were sent to France for training and the first Brazilian research facilities related to power reactors were created. Several studies of heavy water reactor physics were performed in these laboratories with heavy water supplied by the United States. However, around 1968, the leaders of the country's electric sector started to defend the choice of a reactor with light water and enriched uranium, which was eventually accepted by the federal government. The thorium group broke shortly after this decision [15]. Fifty years ago, the idea of building a thorium-based power reactor was set aside, and three PWR (pressurized water) reactors were built using light water and enriched uranium. The thorium reserves remained idle. At some point in the future, the price of uranium will increase due to its decreasing availability which may cause the cost–benefit variable to tip in favor of thorium reactors.

This serves to be a high time for understanding the worth of thorium over uranium reserves and this concern needs more infrastructures and thinking minds to bring a revolutionary, economic and dynamic change in the game of nuclear energy production.

References

1. World Commission on Environment and Development, *Our Common Future (Brundtland Report)* (Oxford University Press, New York City, USA, 1987)
2. O Que É DesenvolvimentoSustentável. https://educacao.estadao.com.br/noticias/geral,o-que-desenvolvimento-sustentavel,20040728p8329 (2004)
3. International Atomic Energy Agency (IAEA), *Inventory of Radioactive Waste Disposals at Sea* (Vienna, Austria, IAEA, 1999)
4. United Nations Scientific Committee on the Effect of Atomic Radiation (UNSCEAR), *Sources and Effects of Ionizing Radiation.* https://www.unscear.org/docs/publications/1993/UNSCEAR_1993_Report.pdf (1993)
5. EPA, *Green Chemistry* (United States Environmental Protection Agency, 2019). https://www.epa.gov/greenchemistry.
6. P.T. Anastas, J.C. Warner, *Green Chemistry: Theory and Practice* (USA, Oxford University Press, New York City, 1998)
7. C.M. Wai, Green separation techniques for nuclear waste management. Amer Chem Soc Symp Ser **1046**, 53–63 (2010)
8. C.M. Wai, Emerging separation techniques: supercritical fluid and ionic liquid extraction techniques for nuclear fuel reprocessing and radioactive waste treatment, in *Advanced Separation Techniques for Nuclear Fuel Reprocessing and Radioactive Waste Treatment*, eds. by K.L. Nash, G.J. Lumetta (Woodhead Publishing, Cambridge, UK, 2011)
9. Bhabha Atomic Research Centre (BARC), *AHWR300-LEU: Advanced Heavy Water Reactor with LEU-Th MOX Fuel*. https://www.barc.gov.in/reactor/ahwr.pdf (2009)
10. Brookhaven National Laboratory, *The Indian Advanced Heavy Water Reactor (AHWR) and Non-Proliferation Attributes.* https://www.bnl.gov/isd/documents/79014.pdf (2012)
11. R.K. Sinha, The IAEA's contribution to the peaceful use of nuclear power. Nuclear Power Newslett. **3**(2) (2006)
12. R.K. Sinha, Advanced nuclear reactor systems—an Indian perspective. Energy Procedia **7**, 34–50 (2011)
13. International Atomic Energy Agency (IAEA), *Fundamental Safety Principles: Safety Fundamentals* (Vienna, Austria, IAEA, 2006)
14. NEA/IAEA, *Uranium 2018: Resources, Production and Demand* (OECD Publishing, Paris, France, 2019)
15. G. Camargo, *O Fogo dos Deuses* (Rio de Janeiro, Brazil, Contraponto, 2006)

Chapter 22
Review Article on Density Functional Theory

Jyoti Kapil, Pramila Shukla, and Ashish Pathak

Abstract Density Functional Theory (DFT), which is one of the most successful and popular quantum mechanical tools at present, to probe various properties of matter is reviewed. The two most important aspects on which DFT is based upon i.e. Hohenberg–Kohn Theorem and Kohn–Sham equations are discussed in brief. Different approximation schemes used in DFT; Local Density Approximation (LDA) Generalized Gradient Approximation (GGA) and Pseudopotential are also focused upon. Out of the numerous materials which are being explored through DFT, Heusler alloys and Titanium based alloys have proved to be forerunners due to their potential to be used as stronger, lighter and low-cost structural and functional materials of the future. Titanium based alloys are becoming popular mainly in aerospace, automobile, chemical, marine and medical industries due to their required and unique mechanical and chemical properties. The various phases and phase transformations in Ti- based alloys has made them a desirable functional material in various future applications. Heusler alloys have also gained importance in research in the past few years due to their fascinating and peculiar properties as compared to metals such as ferromagnetism and Half-metallicity, making them a potential candidate in the applications based on advanced spin based devices. The use of DFT is mainly focused upon the study of various electronic, mechanical and magnetic properties and phase stabilities of Titanium based alloys, half and Full-Heusler alloys. Developments and basics of DFT are also discussed.

22.1 Introduction

One of the major requirements of technology today is the invention, development and redevelopment of more and more structural and functional materials which are

J. Kapil (✉) · P. Shukla
Department of Physics, AIAS, Amity University, Noida, Uttar Pradesh, India
e-mail: jyoti.physics@gmail.com

A. Pathak
DMRL, Hyderabad, Telangana, India

V. K. Jain et al. (eds.), *Recent Trends in Materials and Devices*, Springer Proceedings in Physics 256, https://doi.org/10.1007/978-981-15-8625-5_22

stronger, lighter and cheaper; and which not only aid to the current technology but also a stepping stone for the future technological advancements. It can be said that the material science is currently one of the most popular field of research. It is known that for a particular application of a material we need to predict the arrangement of its constituents (atoms/molecules) and its various properties under different conditions. All the material properties are directly dependent on the chemical composition and the crystallographic structures of a material [1].

To know the electronic and structural properties of a material a full quantum mechanical treatment of the material is required. Quantum mechanically every information about the properties of a system is contained in it's wavefunction; which is found out by solving the Schrodinger equation for that system. But to solve a many-body Schrodinger equation with the current technology and computational power available is not computationally feasible and efficient. DFT comes handy in such a situation; as the basic variable used here is the electron density instead of the many-body wavefunction [2]. The kind of balance DFT strikes between the accuracy and computational efficiency makes it the most popular method at present to study the electronic and structural properties of a many-body correlated system [3].

The year 1964–65 can be considered as the time in which the foundation of Density Functional Theory (DFT) was laid by Hohenberg–Kohn through their first paper on DFT which established the fact that any property of a system in ground state is a unique functional of the ground state electron density [4]. However it did not specify the exact functional dependence. The Hohenberg theorem further made it firm that by minimizing the total energy of a system using electron density as a parameter, the ground state energy of the system can be found out.

In 1927 Thomas and Fermi were the first to propose the idea of a density-based calculations to find out the wavefunction of a many-body system of electrons [5, 6]. However they completely neglected the exchange and correlation among the electrons. In 1927 itself Hartree had proposed a method of finding the atomic wavefunction by considering a completely independent particle model in which he considered an atomic electron to be moving in an average "self-consistent" field of the remaining electrons [7]. In 1930 Fock and Slater extended this idea by incorporating Pauli's principle for spin half particles i.e. electrons and replaced the wavefunction, which was a simple product of individual wavefunction of electrons in Hartree theory by a more general wavefunction, a single Slater determinant [8]. They did not take into account the correlation among electrons. Considering linear combination of various possible determinants to write the total wavefunction further improvised the theory and came out to be known as Configuration Interaction [9]. But that made the calculations more complex and tedious. Present status of DFT or Modern DFT can be attributed to Kohn–Sham. Kohn–Sham simplified Hohenberg–Kohn theory by replacing a real interacting system of electrons in a many-body quantum system by an auxiliary system of non-interacting electrons with all the interaction related effects present in an exchange–correlation potential [10]. So in modern Density Functional Theory the approach is to find an appropriate energy functional corresponding to the non-interacting system and its effective potential that corresponds to the same electron density as that of the real many-body interacting system. This made the

calculations drastically simpler compared to any other approach and therefore is most popular at present in studying interactions in a many-body system.

Though there are innumerable materials which are being explored through DFT, Heusler alloys and Titanium based alloys have proved to be forerunners, given their potential to be used as stronger, lighter and low-cost structural and functional materials of the future.

Heusler alloys have gained importance over the past decades due to their unique properties such as half- metallicity, magnetic-shape memory effect, inverse magneto-caloric effect etc. Thin film form of these alloys showing half-metallic behavior has made them a potential candidate for applications in spintronics [11]. Various properties such as structural, electronic, magnetic, mechanical properties of Heusler Alloys have been studied over the years both theoretically and experimentally.

Titanium based alloys are becoming popular mainly in aerospace, automobile, chemical, marine and medical industries due to their required mechanical and chemical properties. Their high strength to weight ratio make them demanding in their applications in making stronger but lighter structures [12]. Titanium alloys have low density, high strength and high corrosion resistance. These properties of Ti-alloys are utilized as a structural material in aerospace industry. The Ti-alloys are categorized as α, near α, α + β and β alloys. The α-phase has hexagonal close pack (hcp) structure. The α-phase is stabilized by α stabilizer such as Al, Sn. The β phase has body centered cubic (bcc) structure. The β-phase is stabilized by a β stabilizer such as Mo, V, Cr etc. [13].

The article intends to review the role played by DFT in finding out the electronic, structural, elastic and various other properties of materials/alloys by taking the above-mentioned Alloys as examples. The article is organized in the following manner: In Sect. 22.2, we have briefly discussed the fundamentals of DFT and the various approximations used in it. Discussion on the usage of DFT in exploring various properties of Heusler Alloys and Ti-alloys by different researchers, will be presented in Sect. 22.3. Section 22.4 concludes the article.

22.2 Methods and Technical Details

The fundamental theorems on which DFT is based and the various approximations and approaches have been discussed in this section.

22.2.1 Hohenberg–Kohn Theorems

DFT is fundamentally based upon Hohenberg–Kohn Theorems:

Theorem I *Total ground state energy of a quantum mechanical system is a unique functional of the electron density* [4]*:*

$$E = E[n(\boldsymbol{r})] \tag{22.1}$$

$n(\boldsymbol{r})$ *is electron density.*

Theorem II *The electron density that minimizes the overall functional is the true ground state electron density* [4]*:*

$$E[n(\boldsymbol{r})] > Eo[n_o(\boldsymbol{r})] \tag{22.2}$$

where, $n_o(\mathbf{r})$ *is the ground state density.*

The Hamiltonian for the electronic structure of an atom/molecule can be written as:

$$\hat{H} = \hat{T} + \hat{v}_{ext} + \hat{v}_i \tag{22.3}$$

where, $\hat{v}_{ext}$ is the external potential on electrons due to nuclei, $\hat{T}$ is the kinetic energy operator, and $\hat{v}_i$ is the potential due to interaction between electrons.

According to Hohenberg–Kohn Theorems, once the total ground state energy is known or in other words the Hamiltonian is known one can in principle determine all the properties of the ground state. Thus all the ground state properties are the unique functional of the ground state electron density i.e. $n(\mathbf{r})$ uniquely determines the external potential v_{ext} [2].

For a given potential $v(\mathbf{r})$ the total energy as a unique functional of $n(\mathbf{r})$ is [2]:

$$E[n(\boldsymbol{r})] = \int v(\boldsymbol{r}) n(\boldsymbol{r}) dr + F[n(\boldsymbol{r})] \tag{22.4}$$

$F[n(\mathbf{r})]$ is the universal functional.

$$F[n(\boldsymbol{r})] = T[n(\boldsymbol{r})] + U[n(\boldsymbol{r})] \tag{22.5}$$

where, $T[n(\boldsymbol{r})]$ is Kinetic energy functional of electrons, and $U[n(\boldsymbol{r})]$ is the interaction energy of an electron with other electrons.

22.2.2 Kohn–Sham Approach

In Kohn–Sham (KS) approach a real interacting system of electrons in a many-body quantum system is replaced by an auxiliary system of non-interacting electrons with all the interaction related effects present in an exchange–correlation potential.

In KS –DFT [14]:

$$F[n(\boldsymbol{r})] = T_s[n(\boldsymbol{r})] + \frac{1}{2}\int \frac{n(\boldsymbol{r})n(\boldsymbol{r}')}{|\boldsymbol{r}-\boldsymbol{r}'|}\mathrm{d}r\mathrm{d}r' + E_{xc}[n(\boldsymbol{r})] \tag{22.6}$$

where, $T_s[n(\boldsymbol{r})]$ is the kinetic energy of a system of non-interacting electrons. Second term represents the Coulomb interaction energy. $E_{xc}[n(\boldsymbol{r})]$ is the exchange–correlation energy.

The exact expression for $E_{xc}[n(\boldsymbol{r})]$ in terms of $n(\boldsymbol{r})$ is not known; different approximations have been used to define it.

22.2.3 Local Density Approximation (LDA)

This is the simplest and most common approximation that is used in DFT. Under this approximation the concepts and formulation of a homogeneous electron gas are used [15]. The whole volume is divided into small areas and the density is assumed to be constant in each area i.e. locally.

In LDA [16–18]:

$$E_{xc}[n(\boldsymbol{r})] = \int \epsilon_{xc}[n(\boldsymbol{r})]n(\boldsymbol{r})\mathrm{d}r \tag{22.7}$$

where, ϵ_{xc} is exchange correlation energy per electron in a homogeneous electron gas of density $n(\mathbf{r})$.

LDA can be applied only when the variations in the electron density are not significant.

22.2.4 Generalized Gradient Approximation (GGA)

The more accurate type of approximation is Generalized Gradient Approximation, which in addition to the density, considers the gradient of electron density as well [19].

In GGA [14]:

$$E_{xc}[n(\boldsymbol{r})] = \int \mathrm{f}(n(\boldsymbol{r}),\ \nabla n(\boldsymbol{r}))\mathrm{d}r \tag{22.8}$$

where, $f(n(\boldsymbol{r}), \nabla n(\boldsymbol{r}))$ is a function of the density $(n(\boldsymbol{r}))$, and its gradient $(\nabla n(\boldsymbol{r}))$.

Some of the other approximations beyond GGA are meta-GGA and hybrid functionals. Meta-GGA is an approximation which depends on the Kohn–Sham kinetic-energy density, in addition to the density and its derivative [20]. Hybrid functionals

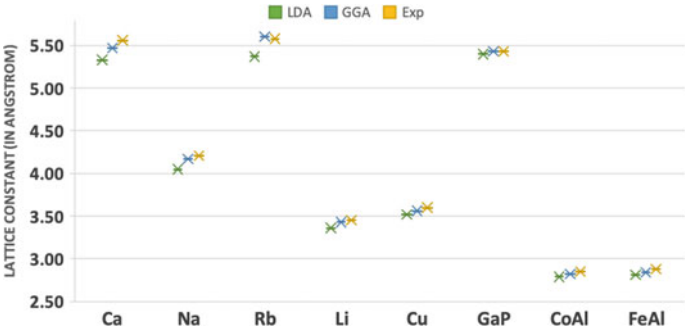

Fig. 22.1 Comparison of lattice constant of various elements and compounds determined using LDA and GGA with the experimentally obtained values (Phillips Hass et al. [23])

are the combination of different exchange and correlation functionals [21, 22]. GGA and meta-GGA can be considered as the extensions of LDA. LDA is a useful approximation in the cases where the density varies slowly; although the real systems do not have such a density. In finding the structural properties like lattice constant, cohesive energies etc. of a material, GGA shows better results than LDA.

Philipp Haas et al. [23] determined the lattice constants of various elements using LDA and GGA, as shown in the Fig. 22.1. LDA shows an overbinding trend [24]; and therefore, a smaller value of lattice constant for elements as well as for binary compounds.

22.2.5 Pseudopotential Approximation

The wavefunction of core electrons is quite oscillatory in nature as compared to the wavefunction of the valence electrons, which varies smoothly. The all electron potential (full-potential) varies as $1/r$ therefore diverges in core region. To overcome these problems we use pseudopotential approximation. In Pseudopotential approximation the actual potential of the core electrons is replaced by an effective potential and wavefunction of core region is replaced with symmetrical wave function of valence electrons which is less fluctuating. This reduces the number of plane waves used in the expansion of the wavefunction, making the calculations less complex and computationally feasible [25].

22.3 Discussions

A rational approach to ascertain the electronic and structural properties of a many-body correlated system, has led to the prolific usage of DFT by the researchers, as

a tool to find better materials to support present and future technical advancements. Heusler Alloys and Titanium based alloys have been the chosen materials for research in the field of material science given their differentiating properties.

22.3.1 Heusler Alloys

Heusler Alloys have garnered significant importance in research due to their unique properties such as half-metallicity, inverse magneto-caloric effect, thermoelectric effect, magnetic shape memory effect etc. Their ferromagnetic behavior even without any magnetic component makes them most desirable from the point of view of their application in magnetic shape memory. Using DFT with different basis sets under various approximations, electronic, mechanical, magnetic and thermoelectric properties of Heusler alloys have been studied in the past. Bala [26] observed spin polarized Density of States and band structure of Co_2MnSi using pseudopotential plane-wave method based on DFT with Perdew-Burke-Ernzerhof (PBE) generalized gradient approximation (GGA), showing half-metallic behavior. Amari et al. [27] observed the bulk modulus of Co_2YSi and its pressure derivative as 148.403 and 4.471 respectively in Ferromagnetic state using FP-LAPW + lo method with GGA.

Although based on various approximations related to the incorporation and accurate modelling of the exchange–correlation interactions involved among the many-body systems, DFT has proven to be an excellent tool in theoretical determination of the structural, electronic magnetic and elastic properties of the half-metallic ferromagnetic Heusler Alloys.

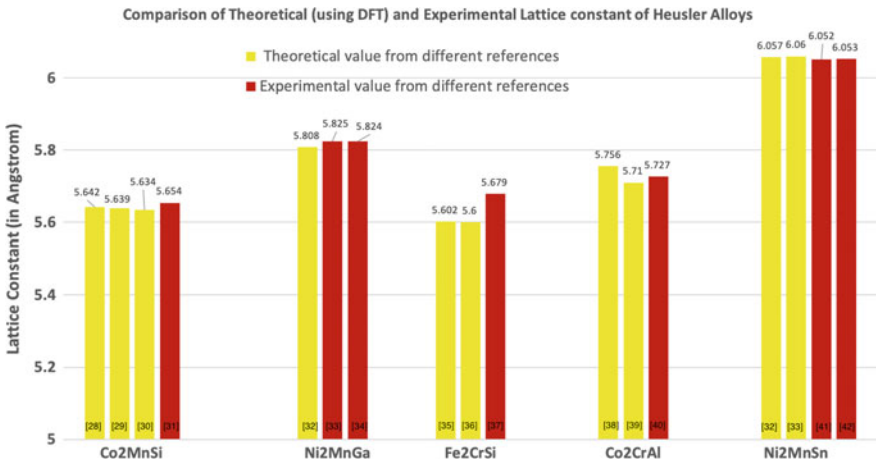

Fig. 22.2 Lattice constant of various Heusler alloys obtained using DFT and experimentally references [28–42] of the data obtained written in bars of the chart

In Fig. 22.2, the lattice constant of various Heusler alloys such as Co_2MnSi, Ni_2MnGa and Fe_2CrSi etc. calculated using DFT methods by different researchers has been compared with the experimentally available values in the literature references [28–42]. The percentage difference between the theoretical (DFT) and experimental values of the lattice constant is less than 2% showing the high level of accuracy with which DFT can produce results. Mechanical properties of Heusler alloys have not received their due importance which is an important property for the structural and functional application of a component.

22.3.2 Titanium Based Alloys

DFT technique is very useful for predicting the relative phase stability, electronic and mechanical properties of Ti-alloys.

The electronic, structural and mechanical properties of Ti_2AlX (X = Nb, Zr, Hf, Re) alloys in B2, $D0_{19}$ and O phases have been studied by using first principles density functional theory within generalized gradient approximation [43–45]. The equilibrium lattice constant values have been found to be in good agreement with the experimental values. The bonding, anisotropic and ductile to brittle behavior for all the alloys in different phases has been explained in their work. Further, Pathak [46] has studied the structural stability, electronic and mechanical properties of $Ti_3AlC_xN_{1-x}$ by relative variation of carbon to nitrogen using first principles pseudopotential plane -wave method. The structural stability along with their mechanical properties with C/N has been discussed in detail. Additionally, Pathak has studied the effect of site occupancy in Ti_2AlX (X = V, Cr, Fe, Mo, Ta, Nb, Zr, Hf and Re) alloys using first principles norm conserving pseudopotential plane -wave method [47]. In Ti_2AlX, the X atoms have been substituted at the Ti and/or Al sites and their stability have been checked and finally the mechanical properties of the stable alloys have been predicted on the basis of the value of the formation energy obtained. Recently, effect of transition metal Chromium on electronic and mechanical properties of chalcogenides such as Titanium di-sulphide compound has been studied using norm conserving pseudopotential within density functional theory (DFT) [48]. These chalcogenides are very relevant due to their layered and two-dimensional symmetric structures. These compounds are used as oxygen catalyst in fuel cells and are also promising material for future high-energy batteries.

22.4 Conclusions

Basics of DFT and its development have been discussed. Different approximation schemes used in DFT have also been focused upon depending upon their use in different situations according to the requirement. Properties of Heusler Alloys and Titanium based alloys have been explored from the point of view of the use of DFT

in determining these properties and their various applications. Mechanical properties of Heusler alloys have scope for future explorations; being the key element in determining the structural and functional applications of a material which will definitely lead to increased commercialization of such materials. γ Aluminide titanium based alloy is under the lens of the researchers at present to explore its various properties, as it could be a potential candidate in aerospace industry.

Acknowledgements We would like to acknowledge Amity Institute of Applied Sciences, Amity University, Noida and Defence Metallurgical Research Laboratory (DMRL), Telangana and Deshbandhu College, University of Delhi for their help and support.

References

1. S. Aitipamula, R.V. Vangala, J Indian Inst. Sci. **97**, 227 (2017)
2. R.M. Martin, *Electronic Structure, Basic Theory and Practical Methods* (Cambridge University Press, United Kingdom, 2004)
3. E.G. Parr, W. Yang, *Density Functional Theory of Atoms and Molecules* (Oxford University Press, New York, 1989)
4. P. Hohenberg, W. Kohn, Phys. Rev. B **136**, 864 (1964)
5. L.H. Thomas, Proc. Cambridge Phil. Soc. **23**, 542 (1926)
6. E. Fermi, Z. Phys. **48**, 73 (1928)
7. N.H. March, *Self-Consistent Fields in Atoms*, 1st edn. (Pergamon Press, Oxford, 1975)
8. J.C. Slater, Phys. Rev. **81**, 385 (1953)
9. *Recent Developments and Applications of Modern Density Functional Theory*, eds. by J.M. Seminario (Elsevier, Amsterdam, 1996)
10. W. Kohn, L.J. Sham, Phys. Rev. A **140**, 1133 (1965)
11. A. Hirohata, K. Takanashi, J. Phys. D Appl. Phys. **47**, 193001 (2014)
12. W. Sha, S. Malinov, *Titanium Alloys: Modeling of Microstructure, Properties and Applications*, 1st edn. (Elsevier Woodhead Publishing Ltd., Cambridge, England, 2009)
13. T.K. Nandy, A. Bhattacharjee, A.K. Singh, A.K. Gogia, Met. Mater. Processes **18**, 289 (2006)
14. W. Kohn, A.D. Becke, R.G. Parr, J. Phys. Chem. **100**, 12974 (1996)
15. *A Primer in Density Functional Theory*, eds. by C. Fiolhais, F. Nogueira, M. Marques (Springer, Berlin, 2003)
16. J.P. Perdew, A. Zunger, Phys. Rev. B **23**, 5048 (1981)
17. J.P. Perdew, Y. Wang, Phys. Rev. B **45**, 13244 (1992)
18. S.H. Vosko, L. Wilk, M. Nusair, Can. J. Phys. **58**, 1200 (1980)
19. J.P. Perdew, K. Burke, M. Ernzerhof, Phys. Rev. Lett. **77**, 3865 (1996)
20. J. Tao, J.P. Perdew, V.N. Staroverov, G.E. Scuseria, Phys. Rev. Lett. **91**, 146401 (2003)
21. A.D. Becke, J. Chem. Phys. **98**, 1372 (1993)
22. A.D. Becke, J. Chem. Phys. **98**, 5648 (1993)
23. P. Haas, F. Tran, P. Blaha, Phys. Rev. B **79**, 085104 (2009)
24. A.D. Becke, Phys. Rev. A **33**, 2786 (1986)
25. F. Giustino, *Materials Modeling Using Density Functional Theory, Properties and Predictions*, 1st edn. (Oxford University Press, United Kingdom, 2014)
26. R. Bala, *Material Today: Proceedings*, vol. 3, 1840 (RAINSAT2015, Elsevier, 2016)
27. S. Amari, B. Bouhafs, J. Supercond, Nov. Magn. **29**, 2311 (2016)
28. S. Amari, R. Mebsout, S. Mecabih, B. Abbar, B. Bouhafs, Intermetallics **44**, 26 (2014)
29. G. Gokoglu, O. Gulseren, Eur. Phys. J. B **76**, 321 (2010)
30. S. Picozzi, A. Continenza, A.J. Freeman, Lect. Notes Phys. **676**, 41 (2006)

31. P.J. Webster, J. Phys. Chem. Solids **32**, 1221 (1971)
32. A. Ayuela et al., J. Phys.: Condens. Matter. **11**, 2017 (1999)
33. P.J. Webster, Contemp. Phys. **10**, 559 (1969)
34. V.V. Martynov, V.V. Kokorin, J. Phys. III **2**, 739 (1992)
35. R. Jain, N. Lakshmi, V.K. Jain, A.R. Chandra, AIP Conf. Proc. **1942**, 090011 (2018)
36. H. Aly Samy, M. Shabara Reham, J. Magn. Magn. Mater. **360**, 143 (2014)
37. H.Z. Luo, Z.Y. Zhu, L. Ma, S.F. Xu, H.Y. Liu, Y.X. Li, G.H. Wu, J. Phys. D: Appl. Phys. **40**, 7121 (2007)
38. D.P. Rai, A. Shankar, Sandeep, M. P. Ghimire, R.K. Thapa, Int. J. Mod. Phys. B **26**, 1250071 (2012)
39. N. Arıkan, A. Iyigor, A. Candan et al., J. Mater. Sci. **49**, 4180 (2014)
40. A.W. Carbonari et al., **163**, 313 (1996)
41. B. Hamri et al., Comp. Cond. Matter. **3**, 14 (2015)
42. S. Plogmann et al., Phys. Rev. B **60**, 6428 (1999)
43. A. Pathak, A.K. Singh, Solid State Commun. **204**, 9 (2015)
44. A. Pathak, A.K. Singh, Intermetallics **63**, 37 (2015)
45. A. Pathak, J. Alloy. Compd. **695**, 35 (2017)
46. A. Pathak, Eur. Phys. J. Plus **132**, 190 (2017)
47. A. Pathak, Chin. J. Phys. **60**, 339 (2019)
48. A. Pathak, J. Appl. Res. Technol. **17**, 302 (2019)

Chapter 23
Preparation and Characterization of Influenza Virosomes Using Nonionic, Dialyazble Phospholipid for Efficient Membrane Solubilization and Reconstitution

Varun Kumar, Ramesh Kumar, V. K. Jain, and Suman

Abstract The present study aimed to formulate a novel strategy to prepare influenza A/H1N1 virosomes using 1,2-distearoyl-sn-glycero-3-phosphocholine (DSPC) as solubilizing agent and compared with that of known solubilizing agents like dipalmitoylphosphatidylcholine (DCPC), Dimyristoylphosphatidylcholine (DHPC), Octaethyleneglycol-mono-(*n* dodecyl) ether (OEG, $C_{12}E_8$), 1,2-dipalmitoyl-*sn*-glycero-3-phospho-*rac*-(1-glycerol) (PG) and Octaethyleneglycol-mono-(n dodecyl)ether (OEG, C12E8). The study involves solubilization and reconstitution of virus membrane with DSPC. DSPC is nonionic detergent with short chain lecithin, which makes it a suitable solubilizing and reconstituting agent. DSPC efficiently dissolve virus membrane and it is approximately 99.9% dialyzable from the virosome formulation without affecting fusion and membrane binding properties of prepared influenza virosomes. The prepared virosomes were characterized using blend of characterization tools like TEM, SEM and Bradford assay. The TEM and SEM results for prepared virosomes confirms the size ranging between 60 and 95 nm which is two times smaller than the size obtained with DCPC as solubilizing agent. Bradford's assay depicts the successful preparation of virosomes. Further the virosomes were used in encapsulation of herbal drug nanocurcumin, encapsulation efficiency and drug release profile was studied to evaluate its potential to be used in drug delivery.

V. Kumar · V. K. Jain · Suman (✉)
Amity Institute of Advanced Research and Studies (Materials and Devices), Amity University, Noida, Uttar Pradesh 201303, India
e-mail: snagpal@amity.edu

R. Kumar
Virology Section, Department of Microbiology, All India Institute of Medical Sciences (AIIMS), New Delhi, India

V. K. Jain et al. (eds.), *Recent Trends in Materials and Devices*, Springer Proceedings in Physics 256, https://doi.org/10.1007/978-981-15-8625-5_23

23.1 Introduction

Virosomal technology has shown promising results in the past as a means of both targeted and non-targeted drug delivery systems. Virosomes are essentially reconstituted viral envelopes, including both viral glycoproteins and membrane lipids, but are devoid of the viral genetic material. The outer surface of a virosome resembles that of the original virus, but the internal compartment is empty [1]. Virosomes are not capable of replication but can act as effective fusion vesicles and can be optimised to enable maximum incorporation of the drug molecules for best possible physiological outcomes simply by modifying the type or the content of membrane lipids. They are, the versatile drug delivery system, therefore, various ligands, such as, peptides, cytokines and even monoclonal antibodies, like those specific for tumour cells (Fab fragments) can be incorporated and made to be displayed on the virosomal membrane, thus making them tumour cell specific in nature [2].

Virosome delivery is generally founded for nanomedicine, which employ nanoparticle-mediated drug delivery in order to combat the downfalls associated with conventional drug delivery systems [3–5]. Influenza virosomes regarded as the most frequently used virosomes in drug delivery and their envelope comprises of a phospholipid bilayer along with the two viral glycoproteins, namely, hemagglutinin (HA) and neuraminidase (NA) protruding on the surface [6–8]. HA provides structural stability and homogeneity to virosomal-drug formulation whereas, NA is responsible for enhancing the viral entry into the targeted cell [9, 10] as well as the release of newly-formed virus particles during the budding stage by removal of terminal sialic acid from the saccharide chain on the surface of host cell [11].

A prerequisite for successful use of virosomes as vaccines or as delivery vehicles is the reconstitution of virus membrane proteins such that their immunogenic, receptor binding and membrane fusion properties retained unaltered. The overall process involved in virosomes production at lab as well as industrial scale required to maintain two critical parameters that are sterility and complete removal of detergent. Detergent choice is one of the main parameter in the preparation of functional virosome. Although several attempts to prepare functional virosomes has been performed earlier using various detergents like Octaethyleneglycol-mono(n-dodecyl)-ether and 1,2-diheptanoyl-sn-glycero-3 phosphocholine (DHPC) but these detergents required special treatments like absorbent hydro-phobic resin for their removal which add complexity to the overall process [2, 9].

Therefore, concept of dialysis for removal of detergent and also to maintain overall sterility was come into the picture which also leads to upscale of this technology towards industrial level. But the major limitation of dialysis is the use of detergents with relatively high critical micelle concentration (c.m.c.). The commonly used detergents in virosome membrane reconstitution are Triton X-100, OG and DHPC have low c.m.c. (<1 mM) and, therefore can't be easily removed by dialysis.

Similar studies have been conducted with 3-[(3-cholamidopropyl)-dimethylammonio]-1-propanesulfonate (CHAPS), cholate and deoxycholate having high c.m.c. but they resulted in fusion-inactive virosomes [2, 9].

Therefore, work is still going on for the search of new solubilizing agent with high cmc, which not only efficiently reconstitute viral membrane but also leads to fusion-active virosome. The present work describes the use of 1,2-distearoyl-sn-glycero-3-phosphocholine (DSPC) as solubilizing agent which belongs to the class of lecithin, nonionic detergent with high cmc and can be easily dialyzable. The study demonstrated that DSPC is more efficient in membrane solubilization and reconstitution for the preparation of influenza virosomes, as this having high cmc and can be completely removed by dialysis (approximately 99.9%). Further the prepared virosomes were used in an encapsulation of a herbal drug nanocurcumin, encapsulation and drug release profile was studied to evaluate its potential to be used in the targeted drug delivery [12–14].

23.2 Materials and Methodology

23.2.1 Materials

Viral Strain
The virosomes were prepared from influenza A/H1N1 (**inactive**) strain provided generously by Medical Hospital, New Delhi, India.

Chemicals
DSPC (1,2-Distearoyl-*sn*-glycero-3-phosphocholine) was purchased from Sigma Ltd., India. Hanks Buffered Saline solution (HBSS) was prepared in laboratory with analytical grade chemicals.

Instruments and Equipments
Scanning Electron Microscope (EVO-18, Carl Zeiss, Germany) and FEI Tecnai Transmission Electron Microscope, G2- series, USA were used to study the surface morphology of nanocurcumin and prepared virosome. Dynamic Light Scattering (DLS, Malvern Zetasizer S90 series) to carry the particle size analysis of the prepared nanocurcumin and virosome. Ultrasound device, ultrasonic cleaner TPC-25 from RoopTelesonic pvt ltd, India and Optima MAX-XP Ultracentrifuge, Beckman Coulter used in the preparation of curcumin nanoparticles. Rotavapour (R-210) equipped with heating bath (B-491) and vacuum pump (V-700), used to concentrate the nanocurcumin sample and to further breakdown the particle size. UV–visible spectrophotometer (Spectro UV–vis Dual beam and Auto Cell UVS-2700, Labomed, INC., Germany) was used to evaluate encapsulation efficiency and drug release studies.

23.2.2 Methodology

23.2.2.1 Preparation of Virosome and Encapsulation of Herbal Drug Nanocurcumin

Virosomes were prepared and encapsulated with drug as per our patented method for the preparation of nanocurcumin herbal hybrid virosome [15]. The herbal drug nanocurcumin was prepared by wet milling process as describe by Basniwal et al. [16], which is being utilized for encapsulation into virosomes.

Inactivation of Virus
Inactivation of Influenza A/H1N1 sample was performed by adding 0.02% formaldehyde in 1:2 ratio and sample was stored at −20 °C for three days for complete viral inactivation. 500 μL of inactived viral sample was transferred aspectically in three autoclaved eppendorfs and ultracentrifuge at 100,000 × *g* for 1 h at 4 °C. The supernatant was discarded (in 0.02% formaldehyde) and the pellet was dissolved in Hanks Buffered Saline solution (HBSS). The three eppendrofs were marked as follows:

(a) Inactive virus (control).
(b) Empty virosome (without nanocurcumin).
(c) Virosome for drug encapsulations.

Viral Membrane Solubilization
Eppendorfs *b* and *c* were subjected to membrane solubilization and reconstitution, DSPC was added into *b* and *c* eppendrofs and the suspension was incubated in ice for 30 min. Centrifuge the suspension for 1 h at 100,000 × *g* and the obtained pellet was resuspended in HBSS buffer.

Virosome Membrane Reconstitution
The virosome membrane reconstitutions were prepared in the following order: 130 μL 50% sucrose + 170 μL 10% sucrose + 200 μL virososme sample containing nanocurcumin; 130 μL 50% sucrose + 170 μL 10% sucrose + 200 μL empty virosome. Both the eppendrofs (B&C) were separately undergone discontinuous sucrose gradient centrifugation (10%/50% w/v sucrose in HBSS) at 100,000 × *g*for 1.5 h in 4 °C, The intermediate layer obtained after discontinuous centrifugation was collected and stored at 4 °C, to chill and then dialyze in PBS buffer pH 7.0 for 72 h with subsequent removal and addition of buffer at regular intervals.

23.2.2.2 Characterization of Reconstituted-Virosome

Bradford's Assay
The method of protein estimation which is based on the binding of Coomassie Brilliant Blue G-250 dye to the protein present in the sample. This bound form of the

dye has the maximum absorption spectrum at 595 nm of wavelength. Therefore, this assay was used to analyse the protein content of whole influenza virus sample (used as control), the prepared empty influenza virosomes and drug encapsulated virosomes, the readings obtained were marked against the standard protein curve prepared by serial dilution of Bovine Serum Albumin (BSA).

Scanning Electron Microscopy
The prepared samples of whole influenza virus (as control), reconstituted empty virosome and drug encapsulated virosome were subjected to Scanning Electron Microscopy analysis to determine their structure, surface topology and size. The results for all samples were compared and correlated.

Transmission Electron Microscopy
The Transmission Electron Microscopy was performed to obtain topographical, morphological, compositional and crystalline information of reconstituted empty virosome and drug encapsulated virosome. The results for all three samples were recorded and compared.

Encapsulation Efficiency of Reconstituted Virosome
The drug encapsulation efficiency of virosome was evaluated through centrifugation method [17]. The centrifugation was done with 1.5 mL of drug encapsulated virosome (with nanocurcumin) for 1.5 h at 14,000 rpm and supernatant was collected aspectically to remove untrapped nanocurcumin and their absorbance were checked at 435 nm. Encapsulation efficiency of virosome was calculated by using:

$$\text{Encapsulation efficiency} = \frac{\text{Drug total} - \text{Drug supernatant}}{\text{Drug total}}$$

where Drug total is the total amount of nanocurcumin added initially and Drug supernatant is the amount of encapsulated nanocurcumin in virosomes [18].

In-Vitro Drug Release Study of Virosome
The in-vitro drug release study of Virosome was determined through dissolution method at pH 2, 4, 6, 7 and 9 [1, 19]. The pretreatment of dialysis membrane was done by immersing dialysis membrane in 50 mL of PBS buffer of pH 7.0, for atleast 25–30 min prior to begun experiment. The dialysis membrane containing 0.5 mL of drug encapsulated virosome was placed in PBS buffer of pH 2, 4, 6, 7 and 9 individually at $37^{o} \pm 1$ °C with constant stirring at 400 rpm to check the drug release. 1 mL of sample was withdrawn at regular intervals i.e. 15 min, 30 min, 1, 2, 3, 6, 9, 12 and 24 h for the evaluation of nanocurumin release rate from Virosome. The concentration of nanocurcumin in the sample aliquot were examined at 435 nm using UV/VIS spectrophotometre and comparatively examined through the plotted standard graph of nanocurcumin, (absorption versus time) to draw release profile of the drug from Virosome.

Table 23.1 Comparitive study of the recovery of initial viral membrane protein by virosome prepared using DSPC with previously reported virosome using different solubilizing agents

Solubilizing agent	Protein concentration (μg/mL)	% Protein recovery	References
DSPC	168	53.2	Present work
DCPC	128	40.0	[21]
	150	37.5	[22]
DHPC	129.2	40	[20]

23.3 Results and Discussion

23.3.1 Characterization of Drug Encapsulated Virosomes

Bradford's Assay

The total protein concentration of the drug encapsulated virosome as well as that of the whole virus was determined by the Bradford's assay. The results showed that the purified virosomes prepared using DSPC contained approximately 51.1% or 165 μg/mL of the initial membrane protein (Table 23.1), which was found to be 11.56% higher protein comparing to virosome prepared from other solvent DCPC [20, 21].

The reconstituted drug encapsulated virosomes contained approximately 53.2% or 168 μg/mL protein as compared to the whole virus sample (Table 23.1). This was observed as the positive indication of virosomes preparation as the membrane protein concentration tends to reduce, approximately by 50–60% during reconstitution, since a considerable amount of membrane glycoproteins and lipids were lost during dialysis and ultracentrifugation. It is clear from the Table 23.1 that the recovery of initial viral membrane protein with DSPC is significantly higher among the widely used solubilizing agent for virus membrane solubilization and reconstitution.

Scanning Electron Microscopy (SEM)

The SEM results for the empty reconstituted virosome showed a slight variation in morphology, a shift from the normal circular/spherical morphology, as well as a reduction in particle size. The particles marked in the SEM result were 64.5, 60.5 and 48.4 nm in size (Fig. 23.1a). This reduction in size can be directly correlated with the considerable loss of membrane lipids and glycoproteins, also shown in Bradford's assay [10]. The reconstituted membranes, thus, have varied structural morphologies and reduced size ascribing to reduction in membrane protein concentrations.

Similarly, the SEM results for drug encapsulated virosomes, sample showed variation in structural morphology, with particle size ranging between 60 and 90 nm (Fig. 23.1b). The particles recorded for size gave the following results: 82.5, 70.2 and 66.0 nm in diameter. The average particle size of nanocurcumin being 51.2 nm, it may be regarded that the viral membrane could have been reconstituted with same

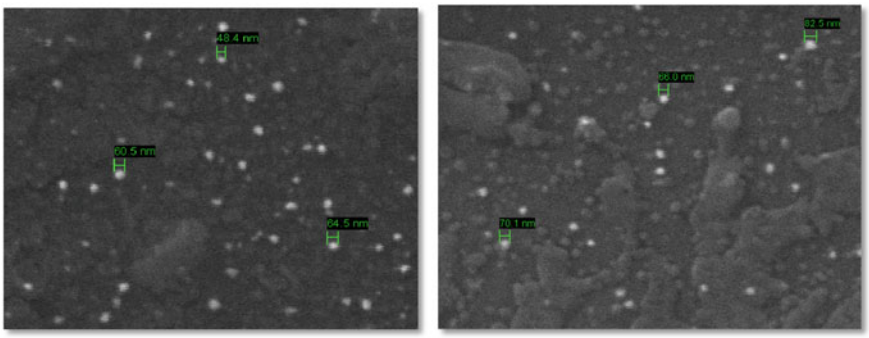

Fig. 23.1 **a** SEM result of an empty reconstituted virosome at 200 nm size scale, image depicts reduction in particle size of reconstituted virosome, with size ranging from 50 to 65 nm. **b** SEM result of nanocurcumin encapsulated virosome at 200 nm size scale showed circular morphology along with size ranging between 60 and 90 nm

amount of nanocurcumin with the viral membrane glycoproteins and lipids, thus, increasing the particle size of the resulting virosomes formed.

Transmission Electron Microscopy (TEM)

The results obtained for the formation of influenza virosome strongly asserted the formation of empty virosomes. The size obtained from the TEM image was found to be in range of 62.63–90.51 nm, was calculated from 50 representative virosomes (Fig. 23.2a), which is approximaely two times smaller than virosomes prepared with DCPC as solubilizing agent [21]. As far as shape is concerned, TEM images showed spherical shape of the prepared virosomes, which is approximately similar in shape of virosome prepared with DCPC [21]. The formation of virosomes, with their hollow interior and a faint, yet visible membrane outline further strengthens a part of this study. Whereas result obtained from the TEM analysis of drug encapsulated Virosome depicited the nanocurcumin encapsulation with size ranging between 65 and 95 nm (Fig. 23.2b).

Encapsulation Efficiency (EE) of Virosome

The absorbance at different concentration of nanocurcumin was calculated using UV/VIS spectrophotometer at 235 nm. The complete results of characterization and consequently encapsulation of drug by virosomes prepared using DSPC (our method) and it comparison with earlier reported virosome solubilizing agents is described (Table 23.2). The results showed that our virsomes encapsulation efficiency is nearly 80% which is far better than reported earlier, this might be their nano size and zeta potential which makes it very good for drug encapsulation.

In-Vitro Drug Release Study of Virosome

In-vitro drug release study of virosome was performed at pH 7.0. The results showed that 18.5% drug was release from nanocurcumin encapsulated virosome at pH 7.0

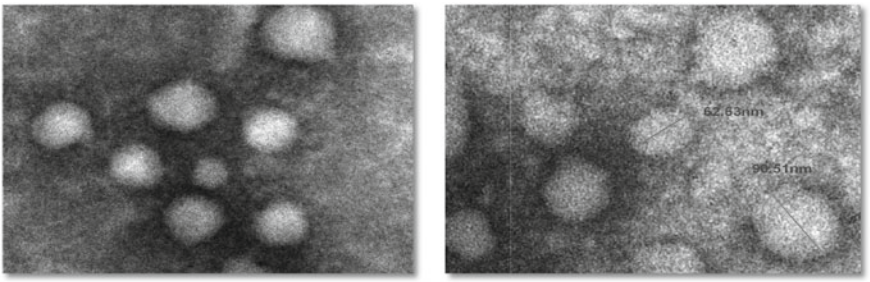

Figure 23.2 **a** TEM image for an empty influenza virosomes confirms the formation of empty virosome having spherical shape and size ranging between 50–65 nm with their reconstituted membranes. **b** TEM image of nanocurcumin encapsulated virosome confirms the formation of spherical shaped virosome with nanocurcumin (in white) encapsulation and size ranging between 60 and 90 nm

after 24 h (Fig. 23.3) i.e. nearly 50% more efficient in controlled release of drug compared to the liposome as drug delivery vehicle [4, 25]. There is no or negligible drug release from virosome were noticed at pH 2, 4, 6 and 9, hence making virosomes a good choice for delivering biological as well as synthetic drug by manifesting site specific release of the drug to targeted site at only specific pH that is 7.

23.4 Conclusion

In this manuscript we reported a new method to prepare Influenza A H1/N1 virosome using DSPC, a short-chain dialyzable phospholipid and characterized the same with blend of characterization tools. Removal of DSPC by dialysis resulted in reconstituted viral membrane vesicle.The size and homogeneity of reconstituted virosome varied accordingly to procedure employed, namely standard dialysis of solubilized membrane components and concentration of solubilizing agent. The membrane binding and fusion activity of reconstituted influenza virosome were recovered from DSPC solubilized viral membrane. In contrast, attempt to recover functionally active virosome using OG were often unsuccessful [21]. The virosome preparation obtained using DSPC with respect to average size and shape was efficiently observed through SEM and TEM analysis. According to the current observations self-assembly of amphiphiles like DSPC involves weak forces to strongly hold amphi-molecules together to ensure stability in the solution and the structure is more flexible due to weak interactions ensuring virosome to endure minor perturbation while conserving the reversibly of self assembled membrane molecules. Moreover the nanocurcumin encapsulation into the virosomes prepared using DSPC proved to be equally efficient in controlled release of drug also thus, offer an new solubilizing agent for virosome preparation in further application.

Table 23.2 Characteristics of prepared influenza virosome through DSPC in terms of size and encapsulation efficiency, and its comparison with previously reported virosome prepared using different solubilizing agents

Solubilizing agent	Mean particles size (nm)	Polydispersity index (PDI)	Zeta potential	Encapsulation efficiency (%)	References
DSPC	92 ± 3.06	0.512 ± 0.03	-61.0 ± 0.68	80.6	Present work
OEG, ($C_{12}E_8$) and PG	200	NA	NA	30–40	[23]
Octa(ethyleneglycol)-n-dodecyl monoether (C12E8)	100	NA	NA	0.5	[24]

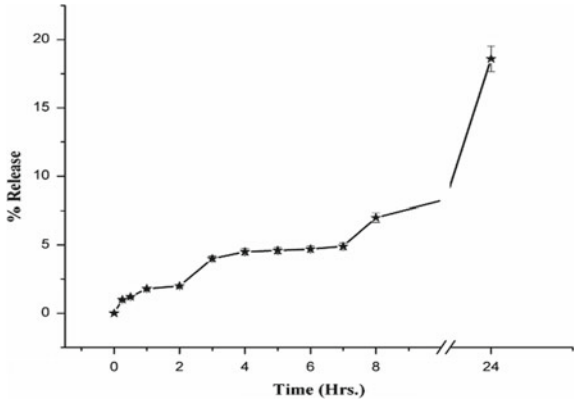

Fig. 23.3 Cumulative release of nanocurcumin from influenza virosome in 24 h at pH 7.0

Acknowledgements Authors would like to acknowledge the funding given to Varun Kumar, from the Department of Biotechnology [DBT/JRF/BET/I/2017/AL/319], New Delhi, Government of India. We would also like to show our gratitude to Dr. Ashok Chauhan, Founder President Amity University for their continuous encouragement and support.

Conflict of Interest There is no conflict of interest in the present study.

Human and Animal Rights No Humans and animals were used for studies.

Consent for Publication Not applicable.

References

1. R.H. Müller, C.M. Keck, Drug delivery to the brain–realization by novel drug carriers. J. Nanosci. Nanotechnol. **4**(5), 471–483 (2004)
2. S. Bhattacharya, B. Mazumder, Virosomes: a novel strategy for drug delivery and targeting. BioPharm. Int. **24**, s9–s14 (2011)
3. R. Langer, Biomaterials in drug delivery and tissue engineering: one laboratory's experience. Acc. Chem. Res. **33**(2), 94–101 (2000)
4. A. Huckriede et al., Influenza virosomes: combining optimal presentation of hemagglutinin with immunopotentiating activity. Vaccine **9**(21), 925–931 (2003)
5. P. Sapra, T.M. Allen, Improved outcome when B-cell lymphoma is treated with combinations of immunoliposomal anticancer drugs targeted to both the CD19 and CD20 epitopes. Clin. Cancer Res. **10**(7), 2530–2537 (2004)
6. Y. Sun et al., RGD peptide-based target drug delivery of doxorubicin nanomedicine. Drug Dev. Res. **78**(6), 283–291 (2017)
7. S. Soni et al., Pharmacoscintigraphic evaluation of polysorbate80-coated chitosan nanoparticles for brain targeting. Am. J. Drug Delivery **3**(3), 205–212 (2005)
8. N. Singh et al., Virosomes as novel drug delivery system: an overview. PharmaTutor **5**(9), 47–55 (2017)
9. H. Maeda, T. Sawa, T. Konno, Mechanism of tumor-targeted delivery of macromolecular drugs, including the EPR effect in solid tumor and clinical overview of the prototype polymeric drug SMANCS. J. Control. Release **74**(1–3), 47–61 (2001)

10. R.A. Lamb, S.L. Zebedee, C.D. Richardson, Influenza virus M2 protein is an integral membrane protein expressed on the infected-cell surface. Cell **40**(3), 627–633 (1985)
11. K. Metsikkö, G. van Meer, K. Simons, Reconstitution of the fusogenic activity of vesicular stomatitis virus. EMBO J. **5**(13), 3429–3435 (1986)
12. G.M. Cragg, D.J. Newman, Plants as a source of anti-cancer agents. J. Ethnopharmacol. **100**(1–2), 72–79 (2005)
13. M.M. Babar, et al., in *Antivirals and Antiretrovirals* (2013)
14. B. Mazumder, *Virosomes: A Novel Strategy for Drug Delivery and Targeting*, vol. 24, pp. S9–S14 (2011)
15. Suman, et al., *Preparation and Characterization of Nanocurcumin Encapsulated Virosome for Cancer Treatment*. Indian patent Application no. 201711001264
16. R.K. Basniwal et al., Curcumin nanoparticles: preparation, characterization, and antimicrobial study. J. Agric. Food Chem. **59**(5), 2056–2061 (2011)
17. Z.Y. Ng et al., Assessing the potential of liposomes loaded with curcumin as a therapeutic intervention in asthma. Colloids Surf. B **172**, 51–59 (2018)
18. S.S. Jana et al., Targeted cytosolic delivery of hydrogel nanoparticles into HepG2 cells through engineered Sendai viral envelopes. FEBS Lett. **515**(1–3), 184–188 (2002)
19. R. Singh, J.W. Lillard Jr., Nanoparticle-based targeted drug delivery. Exp. Mol. Pathol. **86**(3), 215–223 (2009)
20. A. Homhuan, S. Prakongpan, Use of a dialyzable shortchain phospholipid for efficient preparation of virosome vaccines against newcastle disease. Thai J. Pharm. Sci. **31**(3–4), 63–106 (2007)
21. J. De Jonge, et al., Use of a dialyzable short-chain phospholipid for efficient solubilization and reconstitution of influenza virus envelopes. Biochim. Biophys. Acta (BBA) Biomembr. **1758**(4), 527–536 (2006)
22. M. Noori, et al., *Construction of Influenza A/H1N1 Virosomal Nanobioparticles* (2011)
23. M. Amacker et al., Peptide-loaded chimeric influenza virosomes for efficient in vivo induction of cytotoxic T cells. Int. Immunol. **17**(6), 695–704 (2005)
24. A. Arkema et al., Induction of cytotoxic T lymphocyte activity by fusion-active peptide-containing virosomes. Vaccine **18**(14), 1327–1333 (2000)
25. M. Kawai et al., Dynamics of different-sized solid-state nanocrystals as tracers for a drug-delivery system in the interstitium of a human tumor xenograft. Breast Cancer Res. **11**(4), R43 (2009)

Chapter 24
Studies on Rheological Properties of Magneto-Rheological Fluid as a Function of Particle Size and Concentration

Arti Maan, Bhuvneshwar Rai, Vinay Tyagi, and Praveen Kumar Kaicker

Abstract Magneto-rheological (MR) Fluids are colloidal suspensions of magnetic particles in carrier fluid. MR Fluids shows unique rheological behavior on application of magnetic field. When magnetic field is applied these fluids change their viscosity drastically within milliseconds. The rheological behavior of fluid typically depends on the properties of magnetic particles like size, shape, density, saturation magnetization value and also on the concentration of particles in the fluid. In this study, we have investigated the influence of particle size and concentration of magnetic particles on the rheological properties of MR Fluid. MR Fluids were prepared by using two different sized carbonyl iron particles (i.e. 3–5 and 7–9 μm). Concentration of carbonyl iron particles were varied from (25 to 40) % by volume in silicon oil as carrier fluid. Experimental results show that on increasing the volume fraction of carbonyl iron particles shear stress and viscosity increases in both the cases. However, MR Fluid with large sized particles shows higher shear stress value and lower viscosity compared to the MR Fluid containing smaller sized particles.

24.1 Introduction

Magneto-rheological fluids are the suspension of magnetizable particles in base fluid. The rheological properties of these fluids varied within milliseconds on application of magnetic field [1]. Under influence of magnetic field the suspended magnetic particles gets aligned in the direction of the applied magnetic field and interacts to form a structure that can resists shear deformation or flow [2]. This change results in a rapid increase in the viscosity of fluid that restricts the flow and thereby improving shock absorbing properties of MR fluid [3]. On the removal of the magnetic field from the system, the suspended particles get free for the movement which results in the reduction of viscosity. The rheological properties of a fluid can vary depending

A. Maan (✉) · B. Rai · V. Tyagi · P. K. Kaicker
Shriram Institute for Industrial Research, New Delhi, Delhi 110007, India
e-mail: artimaan8@gmail.com

V. K. Jain et al. (eds.), *Recent Trends in Materials and Devices*, Springer Proceedings in Physics 256, https://doi.org/10.1007/978-981-15-8625-5_24

upon the particle size, shape, density, concentration and saturation magnetisation value [4].

Magneto-rheological fluids are the suspensions of micro/nano-sized, magnetic particles dispersed in a carrier liquid such as mineral oil, synthetic oil, water or ethylene glycol [5]. The carrier fluid acts as a dispersed medium and ensures the homogeneity of particles in the fluid. Whereas, carbonyl iron is frequently used as dispersed phase due to its high magnetic permeability, high magnetisation value, low coercivity, small remnance and common availability [6]. Various additives like stabilizers, thixotropic agents and surfactants are used to minimise gravitational settling, enhanced suspension stability and for low off-state viscosity of MR fluids. The stabilizers are used to suspend particles in the fluid, whereas, the surfactants get adsorbed on the outer layer of magnetic particles to promote polarization induced in the suspended particles on the application of a magnetic field [7].

Key challenge in the development of MR fluid is its lower viscosity in the absence of magnetic field, higher yield stress and stability against sedimentation. Different materials, methods and formulations have been used to overcome these challenges. Many attempts have been made to minimise particle settling in MR fluid by introducing different additives like lithium grease [8], fumed silica [9], nanoclay [10], guar gum [11], iron oxide nanowires [12], carbon nanotubes [13, 14] etc. Some researchers have also studied the effect of polymer coating on magnetic particles on the sedimentation rate of MR fluid [15, 16]. Moreover, a few researchers have studied the effect of adding flake shaped (electrolytic iron particles) [17, 18], needle shaped (CrO_2) particles [19] in the suspension to reduce settling. It was claimed that the combination of spherical carbonyl iron particles and magnetic wires or rods exhibits higher yield stress and stability against sedimentation.

From the available literature it is evident that rheological properties and stability of MR fluid typically depends on the nature of magnetic particles. Therefore, it is of great importance to first choose an appropriate size and shape of a magnetic particle. Past literature does not provide any information that which size of magnetic particle should be used to develop an MR fluid that possesses low viscosity, high shear stress and uniform dispersion.

In view of above, aim of the present work is to investigate the effect of particle size and concentration on the rheological behavior of MR Fluids. MR Fluids were synthesized by using two different sized carbonyl iron particles i.e. large size (7–9) μm and small size (3–5) μm separately. Concentrations of carbonyl iron particles were varied from (25–40) % by volume. Developed MR fluids were studied for rheological properties.

24.2 Materials and Methods

24.2.1 Materials

Silicon oil has been selected as a carrier fluid because it is the most commonly available carrier fluid that possesses good temperature stability, high flash point and very low freezing point. Whereas carbonyl iron was used as dispersed phase due to its high saturation magnetization and small remanence. Carbonyl iron of two sizes i.e. 3–5 and 7–9 μm having density 7.8 g/ml was procured from Sigma Aldrich, Germany and was used as such without any further purification. AP3 Lithium Grease was used as an additive to improve dispersion of magnetic particles and reduce particle agglomeration and aggregation in silicone oil was procured from local supplier.

24.2.2 Methods

24.2.2.1 Preparation of MR Fluid

Initially AP 3 Lithium grease (6 wt% of CI particles) was added to silicone oil and was mixed for 4 h using overhead mechanical stirrer at 400 rpm to make uniform solution. Required quantity of carbonyl iron particles of different sizes were added slowly in the respective formulations. After addition of carbonyl iron particles in the solution, stirring was continued for 12 h at 800 rpm followed by an ultra-sonication for 30 min to form homogeneous fluid.

24.2.2.2 Characterization

Carrier Fluid
Silicone oil was characterized for different properties, such as viscosity, flash point and freezing point, which directly affect the performance of MR fluid. The viscosity was carried out by using Brookfield Viscometer (Make: DV-II + Pro) at 25 ± 2 °C. Flash point and freezing point are the key properties of carrier fluid which affects the end application of MR fluid. Flash point was determined as per ASTM D 92-18 using open cell cup and the freezing point was carried-out as per ASTM D 2386-03.

Magnetic Particles
Carbonyl iron particles were characterized for properties such as particle size, shape and magnetic property which influence the rheological properties of MR Fluid. Particle size analysis was carried out by Particle Size Analyser (S3500, M/S Microtec Inc. US) using laser diffraction techniques. The shape of particles was analyzed by Scanning Electron Microscope (SEM) (EVO 18 Special Edition, Zeiss, Germany). Magnetic properties of carbonyl iron particles have been performed

by using Vibrating sample magnetometer (VSM). The hysteresis curve has been obtained to determine the saturation magnetization.

MR Fluid

The developed MR fluids were investigated for properties such as yield stress and viscosity using parallel plate rheometer (Anton Paar, GmbH, Germany). Viscosity of samples was evaluated in both OFF state and On state modes at 313 K. In the presence and absence of a magnetic field, the fluid is being stirred to homogenize at constant shear rate of 100 s^{-1} for 30 s. The fluid was then kept stable for 30 s before varying the shear rate from 1 to 600 s^{-1}. In this study, we have reported shear stress values at 300 s^{-1} and viscosity values at 600 s^{-1}.

24.3 Results and Discussion

Carrier Fluid: Viscosity of carrier fluid is one of the important parameter to be considered during preparation of MR fluid because carrier fluid having high viscosity will result in high off-state viscosity and low volume of suspended magnetic particle. Viscosity of silicon oil was measured as 10 cPs using Brookfield Viscometer. Flash point and freezing point are the key properties of a carrier fluid which affects the service temperature of MR Fluid. Flash point and freezing point of silicon oil was determined and found as −70 and 168 ℃, respectively, shows that the MR fluid prepared by using silicon oil will exhibit wide range of service temperature.

Magnetic Particle: Magnetic particles were characterized for size, shape and saturation magnetization, Fig. 24.1a presents the particle size distribution curve of large size carbonyl iron particles (7–9) μm. From the results, it was found that D10, D50 and D90 values of these particles are 2.7, 7.8 and 22.7, indicating 10%, 50% and 90% of the particles lie below this particle size respectively. Whereas, Fig. 24.1b shows the particle size distribution curve of small size carbonyl iron particles (3–5) μm particles. The D10, D50 and D90 values of (3–5) μm particles are 1.3, 3.5 and 8.2, respectively.

Shape of particle is an important property that must be considered before selection of magnetic particle for the development process as it governs the suspension stability and rheology of the MR fluid. Morphological properties of the magnetic particles also affect the yield strength of the final MR fluid. The MR fluid prepared using spherical particles possess high yield strength compared to flake shaped particles because spherical shape particles helps in minimizing the magnetic shape anisotropy leading to better property [20]. The low magnetic shape anisotropy of magnetic particles helps in the formation of strong bond between magnetic particles leading to high yield strength of the fluid [7]. Shape of the carbonyl iron particles is studied using SEM and the SEM micrographs of large size (7–9) μm and small size (3–5) μm are shown in Fig. 24.2a, b. From the micrographs one can observe that both particles are spherical in shape.

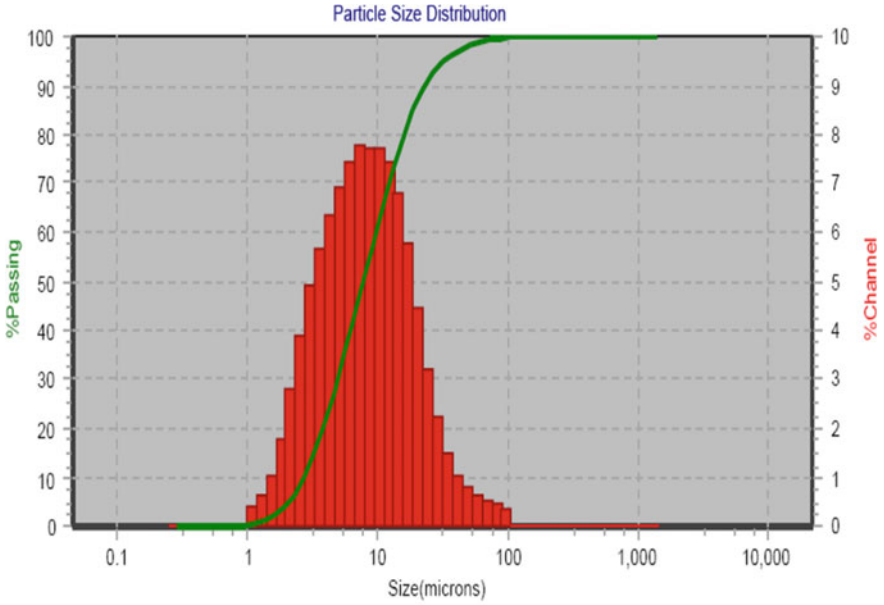

a) 7-9 µ

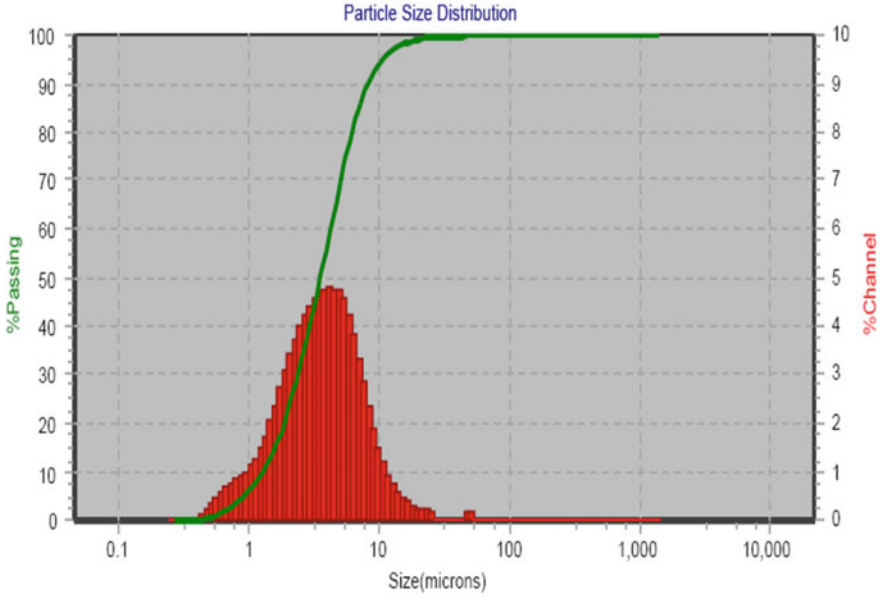

b) 3-5 µ

Fig. 24.1 Particle size distribution curves of carbonyl iron particles

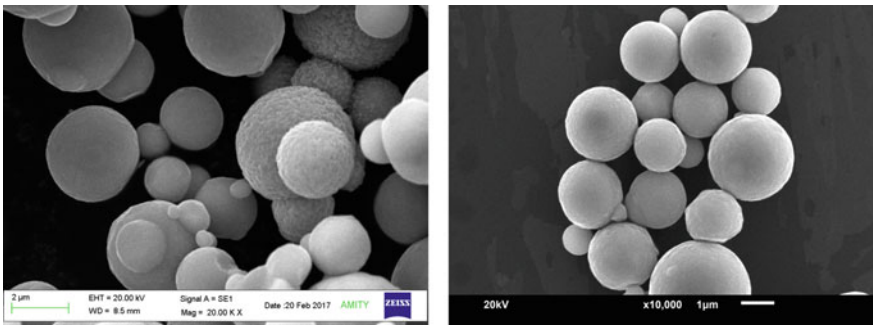

a) 7-9 µ **b) 3-5 µ**

Fig. 24.2 SEM micrographs of carbonyl iron particles

Magnetic property of the magnetic particle is one of the important parameter needed to be considered during selection of it, which can be measure with the help of hysteresis loop. The magnetic particles with small hysteresis loop are the material of choice for making MR fluid as these particles possess low retentivity and coercivity, high saturation magnetization, permeability and small remanence.

Magnetic property of both the carbonyl iron particles in terms of M–H curve have been measured by Vibrating Sample Magnetometer (VSM) at room temperature and the hysteresis curve obtained is shown in Fig. 24.3a, b. On application of magnetic field, carbonyl iron particles showed a strong response and the saturation magnetization reached to 198 and 191 (emu/g) for large size (7–9) µm and small size (3–5) respectively. MR fluid developed by adding magnetic particles having high saturation magnetization value will sustain up to higher magnetic field strength that lead to an increase in the final yield stress value.

24.3.1 Magneto-Rheological Fluid

Magneto-rheological fluids were prepared by varying concentration (i.e. from 25 to 40% by volume) of large size carbonyl iron particles and small size carbonyl iron particles separately. Results shown in Tables 24.1 and 24.2 shows that viscosity of the MR fluids at 600 shear rate increases as the concentration of particles increases in carrier fluid whereas decreases with MR fluid with large particles for same concentration. On comparing the results, MR fluid prepared using small particles shows maximum shear stress 43 kPa and viscosity 395 mPa s at 40 vol%, and MR fluid prepared using large particles shows maximum shear stress 55 kPa and viscosity 240 mPa s at 40 vol%, The MR fluid prepared using larger particles shows higher shear stress value and far less viscosity than smaller particles based MR fluid. It could

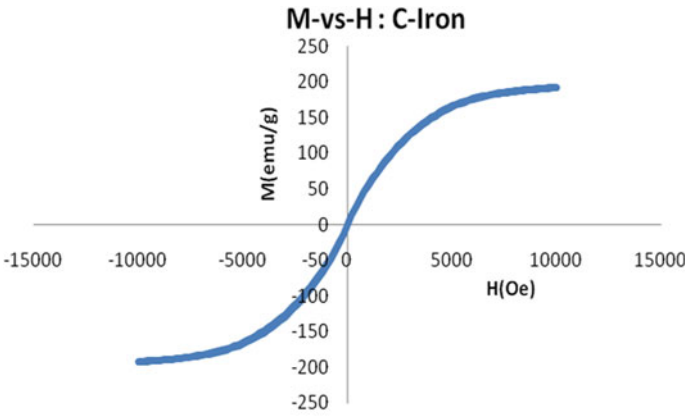

a) 7-9 µ

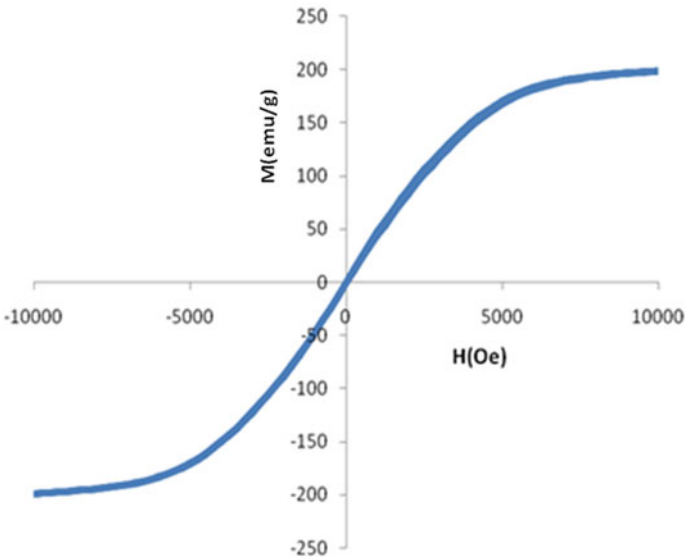

b) 3-5 µ

Fig. 24.3 Hysteresis curves of carbonyl iron particles

Table 24.1 Properties of MR fluid based large size carbonyl iron particles (7–9) µm

S. No.	CI (vol%)	Shear stress (kPa)@300 s^{-1}	Viscosity (mPa s)@600 s^{-1}	Relaxation time (mS)
1	25	28	43	40
2	30	38	120	40
3	35	50	191	40
4	40	55	240	40

Table 24.2 Properties of MR fluid based small size carbonyl iron particles (3–5) μm

S. No.	CI (vol%)	Shear stress (kPa)@300 s^{-1}	Viscosity (mPa s)@600 s^{-1}	Relaxation time (mS)
1	25	15	94	40
2	30	32	183	40
3	35	36	246	40
4	40	43	395	40

be due the particles with larger in size will create high dipolar—dipolar structure and stronger chain interaction compared to small particles.

OFF State Measurements

Shear rate versus viscosity graph of the different samples are shown in Figs. 24.4 and 24.5. As shown in Figs. 24.4 and 24.5 viscosity decreases with increase in the shear rate. Further viscosity of MR fluid prepared using same size of magnetic particles increases as the concentration of magnetic particles increases in carrier fluid. Whereas viscosity of MR fluid prepared using different size of particle having same concentration decreases as the particle size of the magnetic particles increases in carrier fluid. This study shows that the size and concentration both of magnetic particles as well as shear rate affects the restriction in movement of the disc by fluid i.e. it will increase with increase in the concentration of magnetic particles whereas decreases with increasing the size of the particles and shear rate.

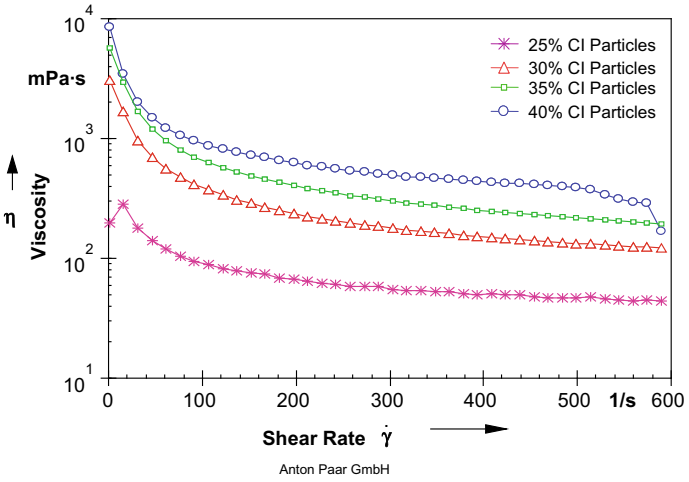

Fig. 24.4 Shear rate versus viscosity curves of MR fluid based on carbonyl iron particle (7–9) μm

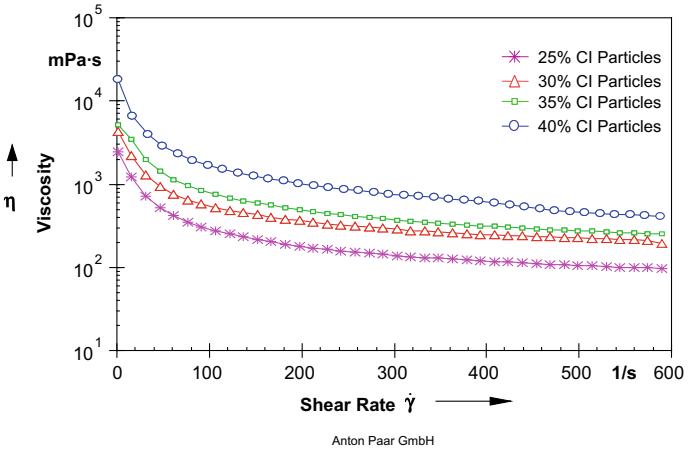

Fig. 24.5 Shear rate versus viscosity curves of MR fluid based on carbonyl iron particles (3–5) μm

ON State Measurements

The rheological property of the developed MR fluids measured on application of magnetic field is known as ON state. The rheological properties such as viscosity and yield stress as the function of current was evaluated and given in graph shown in Figs. 24.6, 24.7, 24.8 and 24.9.

Current versus viscosity graph of the different samples shows that viscosity of MR fluid increases with increasing the current. Further viscosity of MR fluid prepared using same size of magnetic particles increases as the concentration of magnetic particles increases in carrier fluid. Whereas viscosity of MR fluid prepared using

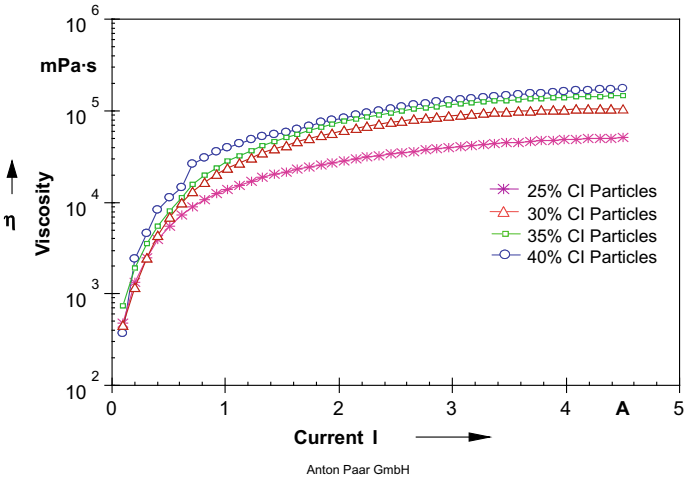

Fig. 24.6 Current versus viscosity curves of MR fluid based on carbonyl iron particles (7–9) μm

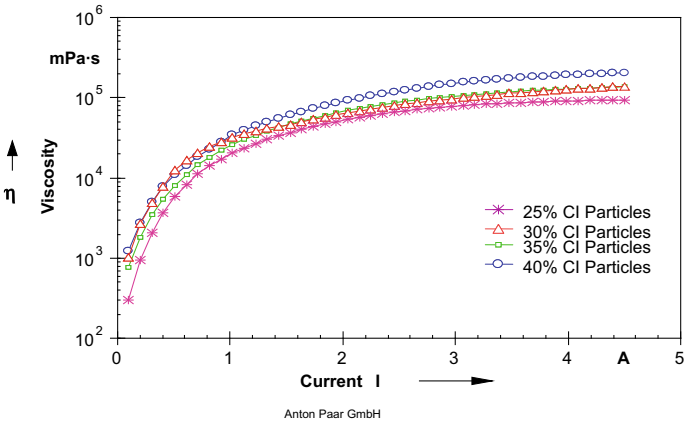

Fig. 24.7 Current versus viscosity curves of MR fluid based on carbonyl iron particles (3–5) μm

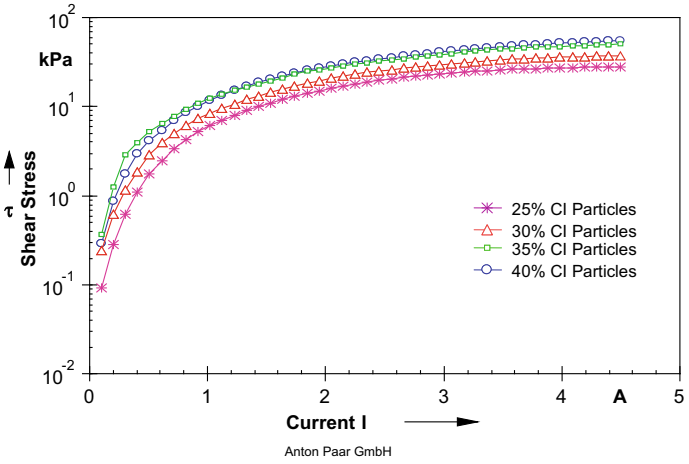

Fig. 24.8 Current versus shear stress curves of MR fluid based on carbonyl iron particles (7–9) μm

different size of particle having same concentration increases as the particle size of the magnetic particles increases in carrier fluid.

24.4 Conclusion

Magneto-rheological (MR) Fluids were prepared by dispersing two different sizes of carbonyl iron particles (i.e. 3–5 and 7–9 μm) in silicon oil. The concentration of

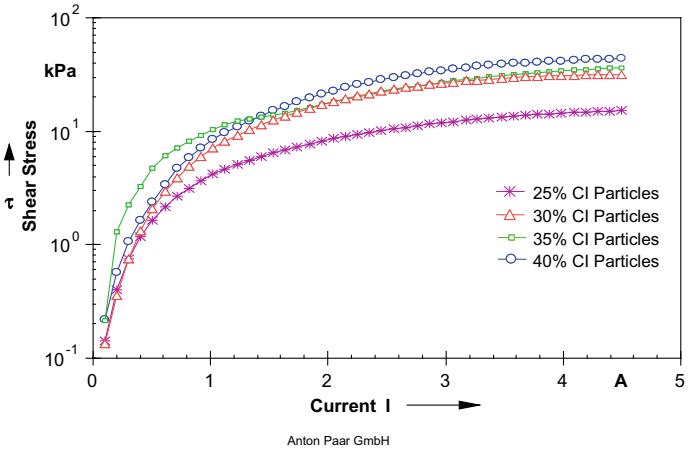

Fig. 24.9 Current versus shear stress curves of MR Fluid based on carbonyl iron particles (3–5) μm

carbonyl iron particles were varied from 25 to 40% by volume in silicon oil. Results show that the concentration and particle size of carbonyl iron particles affects the off-state as well as on-state rheological properties of the prepared MR fluid. Shear stress and viscosity of the MR fluid increases with increasing the volume fraction of carbonyl iron particles in the base fluid. MR Fluid prepared with large sized particles shows higher shear stress value and lower viscosity compared to the MR Fluid containing smaller sized particles.

Acknowledgements The authors are thankful to the Defence Research and Development Organization, DRDO, India, for funding this project. Authors would also like to thank management, Shriram Institute for Industrial Research, Delhi for their continuos support and encouragement.

References

1. A.G. Olabi, A. Grunwald, Design and application of magneto-rheological fluid. Mater. Des. **36**, 2658–2664 (2007)
2. S. Odenbach, Recent progress in magnetic fluid research. J. Phys. Condens. Matter. **16**(32), 1135–1150 (2004)
3. J.S. Kumar, P.S. Paul, G. Raghunathan, D.G. Alex, A review of challenges and solutions in the preparation and use of magneto-rheological fluids. Int. J. Mech. Mater. Eng. **14**(13), 1–18 (2019)
4. R.V. Upadhyay, Steady shear rheology and magnetic properties of flake-shaped iron particle based MR fluid; before and after tribology study. Braz. J. Phys. **49**, 820–828 (2019)
5. M. Kciuk, R. Turczyn, Properties and application of magnetorheological fluids. J. Achiev. Mater. Manuf. Eng. **18**(1–2), 127–130 (2006)
6. A.J. Margida, K.D. Weiss, J.D. Carlson, Magnetorheological materials based on iron alloy particles. Int. J. Mod. Phys. B **10**(23), 3335–3341 (1996)

7. B.K. Kumbhar, S.R. Patil, S.M. Sawant, Synthesis and characterization of magneto-rheological (MR) fluids for MR brake application. Eng. Sci. Technol. Int. J. **18**(3), 432–438 (2015)
8. H. Singh, H.S. Gill, S.S. Sehgal, Synthesis and sedimentation analysis of magneto-rheological fluid. Ind. J. Sci. Tech. **9**(S1), 1–5 (2016)
9. J. Xu, J. Li, J. Cao, Effect of fumed silica weight fraction on rheological properties of magnetorheological polishing fluid. Colloid. Polym. Sci. **296**(5), 1–12 (2018)
10. H.S. Chae, S.H. Piao, A. Maity, H.J. Choi, Additive role of attapulgite nanoclay on carbonyl iron-based magnetorheological suspension. Colloid. Polym. Sci. **293**(1), 89–95 (2014)
11. C. Fang, B.Y. Zhao, L.S. Chen, Q. Wu, N. Liu, K.A. Hu, The effect of green additive guar gum on the rheological properties of MR fluid. Smart Mater. Struct. 14(1) (2004)
12. S.P. Rwei, L.Y. Wang, M.J. Chen, The study of magnetorheology of iron oxide nanowires. J. Nanomater. **2013**, 1–8 (2013)
13. S. Samouhos, G. Mckinley, Carbon nanotube-magnetite composites, with applications to developing unique magnetorheological fluids. J. Fluids Eng. **129**(4), 429–437 (2007)
14. H.T. Pu, F.J. Jiang, Z. Yang, B. Yan, X. Liao, Effects of polyvinylpyrrolidone and carbon nanotubes on magnetorheological properties of iron based magnetorheological fluids. J. App. Poly. Sci. **102**(2), 1653–1657 (2006)
15. Y.H. Kim, B.J. Park, H.J. Choi, Y. Seo, Coating of magnetic particle with polystyrene and its magnetorheological characterization. Phys. Status Solidi A **204**(12), 4178–4181 (2007)
16. J.W. Lee, K.P. Hong, S.H. Kwon, H.J. Choi, M.W. Cho, Suspension rheology and magnetorheological finishing characteristics of biopolymer coated carbonyl iron particles. Ind. Eng. Chem. Res. **59**(9), 2416–2424 (2017)
17. R. Jinaga, T. Jagadeesha, S. Kolekar, S.B. Choi, The synthesis of organic oils blended magnetorheological fluids with the field dependent material characterization. Int. J. Mol. Sci. **20**(22), 5766–5779 (2019)
18. S. Vinod, R. John, J. Philip, Magnetorheological properties of sodium sulphonate capped electrolytic iron based MR fluid: a comparison with CI based MR fluid. Smart Mater. Struct. **26**(2), 025003 (2016)
19. B. Chin, J.H. Park, M.H. Kwon, O.O. Park, Rheological properties and dispersion stability of magnetorheological suspensions. Rheol. Acta **40**, 211–219 (2001)
20. R.V. Upadhyay, Z. Laherisheth, K. Shah, Rheological properties of soft magnetic flake shaped iron particle based magnetorheological fluid in dynamic mode. Smart Mater. Struct. **23**(1), 1–8 (2014)

Chapter 25
Graphene Doped Ferric Oxide Nanoparticles as a Competent Adsorbent for Water Purification

Rohit Babu Aniyery, Anita Gupta, Bharti Sharma, Nahar Singh, H. Kaur, Tania Banerjee, and Anjali Tyagi

Abstract Heavy metals and ionic contamination in drinking and surface water have been reported in many parts of the world and it is considered as one of the major global issues. It is significant and challenging to remove undesirable metals from the water system. Their exposure is quite hazardous to human health. Till date, numerous methods have been suggested for effective removal of heavy metals from water, like chemical precipitation, ion exchange, adsorption, membrane filteration, and electrochemical technologies. The low-cost adsorbent has been studied as a substitute for current costly methods. The present investigation was carried out for adsorption of heavy metals using magnetic graphene doped nanosized ferric oxide (nFeO). The experiment included their wet chemical synthesis and characterization [using X-ray diffraction (XRD), Scanning Electron Microscope (SEM) and Atomic absorption spectroscopy (AAS)] followed by the study of adsorption behaviour of heavy metals [e.g. Pb(II), Cd(II)] from aqueous systems under varying experimental conditions. It is found that nFeO is a very good adsorbent towards the removal of Pb and Cd. Almost all the toxic elements have been adsorbed at neutral pH, the maximum absorption of cadmium occurred at 35 min at pH 6.3–7.6 and maximum absorption of lead occurred at 35 min at pH 6.6–7.7. The results were further substantiated by sample analysis.

R. B. Aniyery (✉) · A. Gupta · A. Tyagi
Amity Institute of Applied Sciences, AUUP, Noida, India
e-mail: rohit7rba1992@gmail.com

B. Sharma · N. Singh
Department of Analytical Chemistry, CSIR-NPL, New Delhi, India

H. Kaur
Department of Applied Sciences, PEC University of Technology, Chandigarh, India

T. Banerjee
University of Delhi, South Campus, New Delhi, India

V. K. Jain et al. (eds.), *Recent Trends in Materials and Devices*, Springer Proceedings in Physics 256, https://doi.org/10.1007/978-981-15-8625-5_25

25.1 Introduction

Water plays an important role in sustaining plants, animals, and humans in many aspects of life, but due to increasing industrial pollutants such as inorganic chemicals (viz., As, Cd, Pb, Cr, F, Hg, Se, NO_3^- etc.) and other contaminations like agricultural/organic chemicals (viz., pesticides, detergents, insecticides etc.) used for controlling the pest in crops and biological pollutants (viz., Fungi, algae, gram-positive/gram-negative bacteria etc.) effluents [1–3] like toxic heavy metals is increasing in water resources, tends to accumulate in living organisms, and causes several diseases and disorders [4–6]. Heavy metals are non-biodegradable as well as carcinogenic in nature that even trace amount (exceeding 5 g/cm^3) present in water can cause severe damage to human health and the ecosystem. Pollution caused by heavy metals has become a major environmental issue worldwide [7–10]. Keeping this in view the World Health Organization(WHO)/Environmental Protection Agency (EPA) has proposed a guideline according to that maximum permissible amount in water, like total pesticides, should not be more than 0.3 ppm, arsenic <0 ppb, chromium < 50 ppb, nitrites 50 ppm. To protect water resource from contamination, wastes must be treated properly before they are released to conduits [11–13]. So it is crucial to develop a drinking water treatment having a potential for removing undesirable concentration present in drinking water. As we know that water is the basic requirement for mankind existence and environmental fate and toxicity of any material are critical issues in the choice of material for water purification, therefore, we did a study on synthesis and characterization of intrinsic and graphene doped ferric oxide nanoparticles and its application as water purification was undertaken. Graphene oxide has an excellent electronic, thermal, optical, mechanical and adsorptive properties [14, 15] so it can be used as an adsorbent material for removing the heavy metals and dyes [16] from the aqueous solution [17–19]. Iron oxide-based nanomaterial has more application in removal of heavy metals due to its small size, large surface area, magnetic property [20–25] and the most important thing is that it is eco-friendly. The strong magnetic property of Iron oxide nanoparticles empower it to adsorb the heavy metals effectively from the heavy metal contaminated water [26], it also makes facile separation of adsorbents from the system thus it could be reused for any further application. The sustainability of iron oxide based nanomaterial could decrease the pollution and economic burden. Ferric oxides nanoparticles (Fe_3O_4, γ-Fe_2O_3) show exceptional potential in water purification with its exclusive features like low toxicity, chemical inertness, biocompatibility and superparamagnetism [27]. Nanoparticle material possesses a high surface-to-volume ratio, enhanced magnetic property, special catalytic properties and eco-friendly technology.

Keeping the advantages and disadvantages of the above methods and material, an attempt has been made by synthesizing oxides of iron by the wet chemical route and their utilization for water purification [28]. Graphene is basically a two dimensional (2D) one atom thick nanomaterial having of sp^2-hybridised carbon atom. Graphene has gained credibility because of its important physical property which has a large surface area of 2600 m^2 g^{-1} making it highly porous and presence of

functional group like –O, −OH, −COOH form complexes with the metal ions are implemented to replace heavy metal ions [29]. We have tried to combine both properties of graphene and iron oxide by doping the graphene with the iron oxides nanoparticle thus making the properties of adsorbing material twice the time greater than the individual material. Many techniques [30, 31] are used to remove heavy metals from the water. Among these nano-based adsorbents are the more efficient technologies for the removal of heavy metals from the water [32–35].

25.2 Experimental Process

25.2.1 Material/Chemicals Details

All the chemicals used for the synthesis of intrinsic ferric oxides, graphene doped ferric hydroxide and determination of lead and cadmium by AAS like sodium borohydride ($NaBH_4$), ethanol (C_2H_5OH), ferrous sulphate ($FeSO_4$), polyvinylpyrrolidone (PVP), ferric chloride ($FeCl_3$), methanol (CH_3OH), ammonium hydroxide (NH_4OH), graphite flakes and ammonium chloride (Fisher Scientific Excelar) used were of the analytical grade and received from E. Merck. 35% of HCl of the GR grade was also used. All the chemicals were prepared in distilled water. Calibration of AAS instrument was done by using standard stock solutions after subsequent dilutions. The two standard stock solutions are 1000 mg/L of cadmium and 1000 mg/L of lead. All these solutions were used after subsequent dilutions. The pipettes, beakers, volumetric flask of various capacities were made of Borosil glass. All the acid dissolution, dilutions work was carried out in laminar flow bench with ventilation system. An oven (SE Heatech silgomelt pizautovens), a hot plate (Ambassador), centrifuge (Remi C-24 plus), ultra-Sonicator (Elma Transonic T700/H) and magnetic stirrer (Remi equipment's Pvt. Ltd.) and heating furnace (METREX) have been used to dry the precipitate at 120 °C and to digest the test sample respectively. The weighing work was done using Ohaus make, GD 200 model balance. The synthesized nanoparticles of ferric oxide and graphene functionalised ferric hydroxide were characterized using powder XRD using Bruker AXS D8 Advance Diffractometer. Data analysis was carried out using Diffracplus software. Diffractograms were recorded using CuK radiation with a graphite monochromator in the diffracted beam. The morphology of synthesized material was examined by using SEM/TEM, Netherland, F-30 G2 STWIN, FEI make TEM, field emission gun (FEG) operated at 300 kV. Particle size of as synthesized graphene doped ferric hydroxide nanostructure was measured by Malvern particle size analyzer (Model Micro-P, range 0.05–550 μm) at University of Delhi. Atomic Absorption Spectrometer-Graphite Furnace Atomic Absorption Spectrometer (GFAAS) was utilized for the determination of low concentration of cadmium and lead using argon as the carrier gas.

25.2.2 Material Synthesis

25.2.2.1 Preparation of Intrinsic (Pure) Ferric Oxide

For the synthesis of pure iron oxide, 8 g of ferric chloride ($FeCl_3$) and 1.5 g of PVP was taken in a flask containing 200 mL of distilled water. The beaker was kept on a magnetic stirrer and solution was stirred up to boiling, 70–80 °C for 1 hour, then after 1 hour the ammonia solution was poured into the beaker for the neutralization. After that, solution was cooled at room temperature and centrifuged at 6000 rpm, boiled to remove the ammonia smell and finally dried in an oven at 105 °C. After that the sample was divided into two parts one-half part remain as it is and the other half part was kept in the heating furnace at 895 °C and finally weighed.

25.2.2.2 Preparation of Fe_2O_3 Iron Oxide

Iron solution was prepared by dissolving 20 g of ferrous sulphate, 10 g PVP and 10 g of sodium oleate poured into a flask containing 200 mL of distilled water. The chemicals was emulsified and stirred on the magnetic stirrer for half an hour. While stirring the mixture, it was separated into two layers, one layer of sodium oleate and another layer of ferrous sulphate and PVP. After that a small amount of sulphuric acid and sodium hydroxide was added to solubilize the mixture. Then the whole mixture was stirred for 15 hour at 45 °C. After that solution had been cooled at room temperature and centrifuged at 7500 rpm for 4 min and finally dried in an oven maintained the temperature at 105 °C for the whole day. The dried sample was then ground in the pestle mortar and again placed in the oven and finally weighed after drying.

25.2.2.3 Preparation of Graphene Doped Iron Hydroxide

For the synthesis of graphene doped iron oxide, 8 g of $FeCl_3$, 1.5 g of PVP and 0.5 g of graphene was taken in a flask containing 200 mL of distilled water. The beaker was kept on a magnetic stirrer and solution was stirred up to boiling say 70–80 °C for 1 hour, then after 1 hour the ammonia solution was poured into the beaker for the neutralization. After that solution had been cooled at room temp and centrifuged at 6000 rpm, boiled to remove the ammonia smell then again centrifuged and finally dried in an oven maintained the temperature at 105 °C for the whole day. The dried sample was then ground in the pestle mortar and again placed in the oven and finally weighed.

25.2.3 Experimental Work of AAS

For cadmium extraction experiment a cadmium stock solution of 1000 ppm was prepared by dissolving 1.73 g cadmium chloride (Analytical reagent grade) in one litre of distilled water. For lead extraction experiment a lead stock solution of 1000 ppm was prepared by dissolving 1.6 g of lead nitrate (Analytical reagent grade) in one litre of distilled water. Two sets (six each) of intrinsic ferric oxide (Fe_3O_4) for cadmium and lead and two sets (six each) of graphene doped $Fe(OH)_3$ of different pH were taken in separate clean and dried beakers. The pH of each set was measured using a calibrated pH meter. The pH of the solutions were adjusted around; 3.5, 4.8, 6, 7.5, 8.5, and 10 using 0.001 HCl and 0.001 M ammonium hydroxide. To each solution, 100 mg of synthesized intrinsic as well as graphene doped $Fe(OH)_3$ were added in each beaker. The solutions were ultra-sonicated and kept at room temperature. The solutions were then tested for the left over concentration of cadmium and lead after 5, 10, 20, 30, 35 and 40 min. The determination of cadmium and lead has been done up to mg/L level by FAAS using a mixture of air (5 L/min) and acetylene (1.5 L/min; flame rich) at 217 nm (Pb) and 228.8 nm (Cd) wavelength and 0.5 nm slit.

25.3 Result and Discussion

25.3.1 Characterization Using Powder-XRD

The diffraction patterns for intrinsic ferric hydroxide and graphene doped ferric hydroxide were recorded in the 2θ range from 20° to 80°. All observed diffraction peaks correspond to $Fe(OH)_3$ (PDF). The identification of phases of pure ferric hydroxide and graphene doped ferric oxide was carried out using X-ray diffraction with scanning speed of 2°/min with graphite Monochromator. The XRD pattern reveals pure phase of ferric hydroxide is given in Fig. 25.1a, while Fig. 25.1b represents XRD of graphene functionalized ferric hydroxide nanomaterial. The average crystallite approximates 55 nm for pure ferric hydroxide and 75 nm for graphene functionalized ferric hydroxide. We found that our synthesized materials are in nanometer range and the peaks broadening reveals that the synthesized materials are amorphous in nature. The XRD results demonstrates the formation of pure ferric hydroxide nanoparticles and the graphene doped ferric hydroxide nanoparticles, hence justifies the synthesis of material.

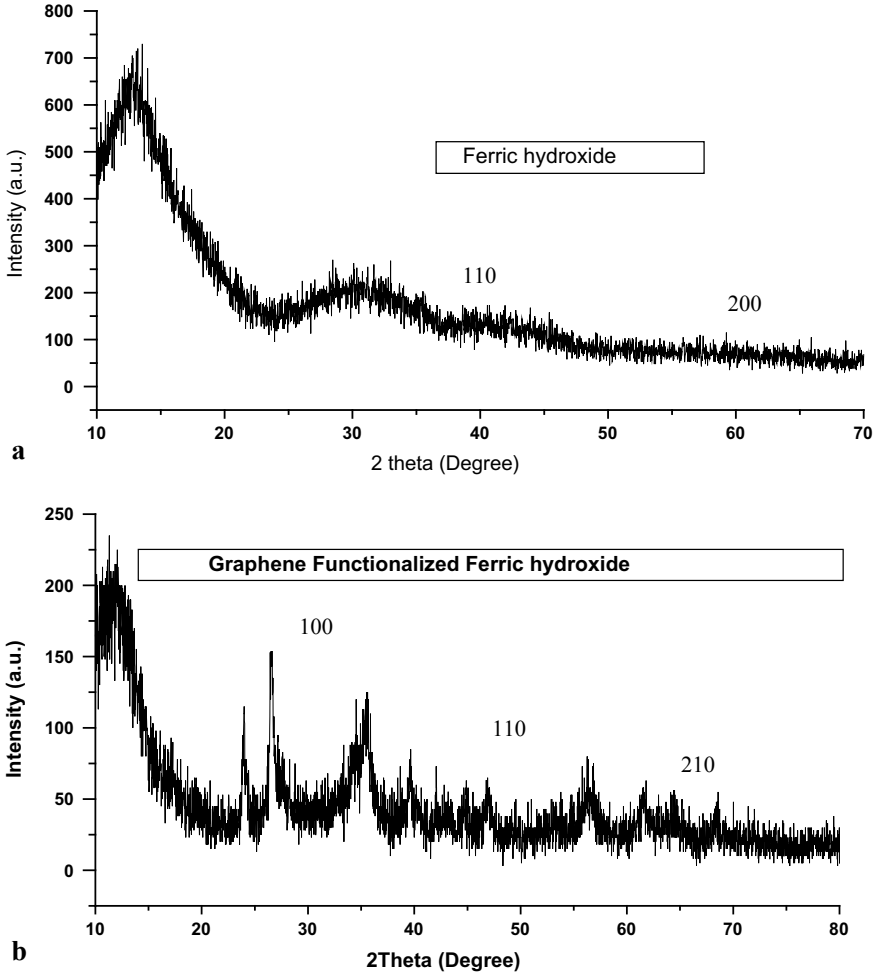

Fig. 25.1 **a** XRD of pure ferric hydroxide, **b** XRD of graphene doped ferric hydroxide

25.3.2 Characterization Using Powder Using SEM

The SEM studies were also done. Figure 25.2a represents the SEM micrograph of ferric hydroxide as synthesized with a lattice spacing of about 0.278 nm [approx. 2.8 Aχ for the (111)] plane in the cubic $Fe(OH)_3$. The micrograph shows that the product is composed of the microsphere with diameter of 15–20 nm. There is clear agglomeration in the sample but the entire sphere has a distinct boundary. The SEM of graphene doped ferric hydroxide is given in Fig. 25.2b.

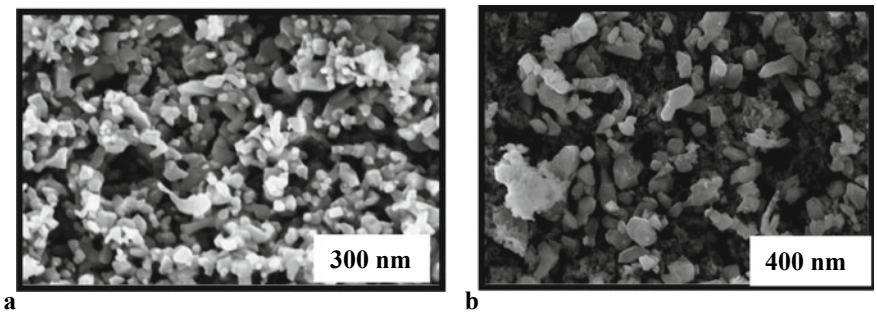

Fig. 25.2 **a** SEM of ferric hydroxide, **b** SEM of graphene doped ferric hydroxide

25.3.2.1 Characterization Using Particle Size Distribution

Photon correlation spectroscopy (PCS) was used to measure the average nanoparticles size and size distribution (polydispersity index) of graphene doped ferric hydroxide nanoparticles. The mean particle size of the graphene doped ferric hydroxide was determined at 25 °C using the Zetasizer Nano ZS (Malvern Instruments, Malvern, UK). The average size of graphene doped ferric hydroxide nanoparticles was found to be 210.9 nm (Fig. 25.3; Table 25.1).

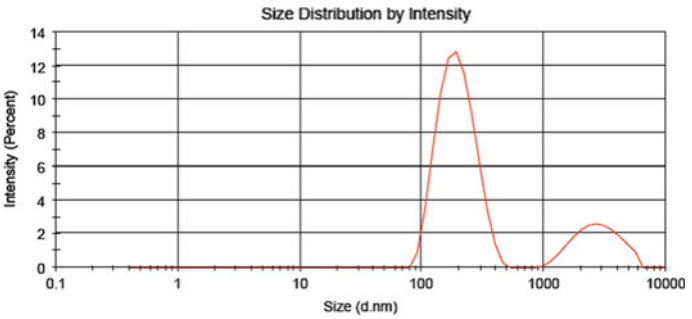

Fig. 25.3 The particle size distribution of chemically synthesized graphene doped ferric hydroxide

Table 25.1 Particle size distribution by intensity of graphene doped ferric hydroxide is shown in Fig. 25.3

Sample	Z average size (d nm)	PDI	Peak	Size (d nm)	Width (d nm)	Intensity (%)
Graphene doped ferric hydroxide	210.9	0.387	1	200.1	68.44	79.1

25.3.2.2 Characterization Using AAS

The determination of cadmium and lead has been done up to mg/L level by FAAS using mixture of air (5 L/min) and acetylene (1.5 L/min; flame rich) at 217 nm (Pb) and 228.8 nm (Cd) wavelength and 0.5 nm slit.

To study the effect of pH on cadmium adsorption using graphene doped ferric hydroxide, we varied the pH from 3.3 to 10.2 and noted the adsorption at different pH. From Table 25.2 it was observed that maximum adsorption took place at pH range 6.3–7.6. Hence, it was concluded that 6.3–7.6 range is the best range for cadmium removal. So the next experiment has been done for to study the effect of time on cadmium adsorption using graphene doped ferric hydroxide at same concentration (1000 ppm) keeping the pH constant (Fig. 25.4).

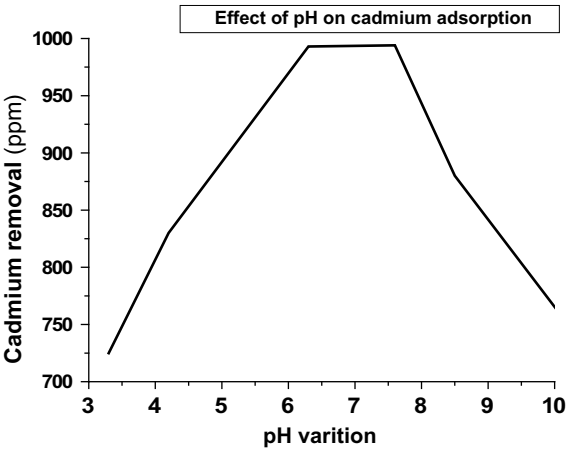

Fig. 25.4 Effect of pH on cadmium removal using graphene functionalized ferric hydroxide

Table 25.2 The effect of pH on cadmium adsorption using graphene doped ferric hydroxide

Material used	pH variation	Cadmium taken (ppm)	Cadmium removal (ppm)
Graphene doped ferric hydroxide	3.3	1000	725
	4.2	1000	830
	6.3	1000	993
	7.6	1000	994
	8.5	1000	880
	10.2	1000	780

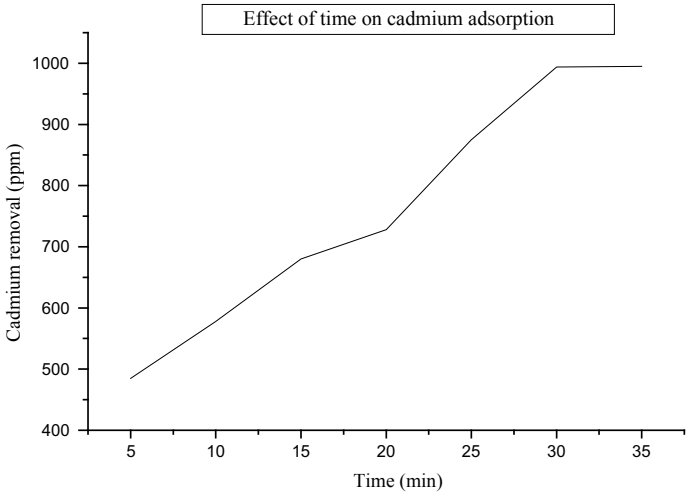

Fig. 25.5 Effect of time on cadmium removal using graphene doped ferric hydroxide at pH 6.3–7.6

From Table 25.3 it is evident that maximum absorption of cadmium occurred at 35 min at pH 6.3–7.6. On further maximization of time no significant changes was observed (Fig. 25.5).

To study the effect of pH on lead adsorption using graphene doped ferric hydroxide, we varied the pH from 3.4 to 10.3 and noted the adsorption at different pH. From Table 25.4 it was observed that maximum adsorption took place at pH range 6.6–7.7. Hence, it was concluded that 6.6–7.7 range is the best range for lead removal. So the next experiment has been done for to study the effect of time on cadmium adsorption using graphene doped ferric hydroxide at same concentration (1000 ppm) keeping the pH constant (Fig. 25.6).

From Table 25.5 it is evident that maximum absorption of lead occurred at 35 min at pH 6.6–7.7. On further maximization of time no significant changes was observed (Fig. 25.7).

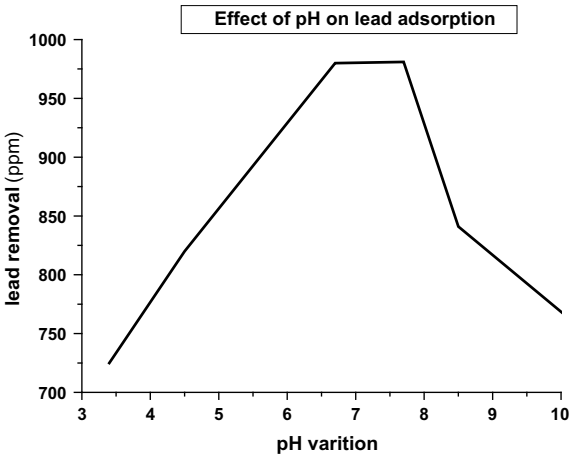

Fig. 25.6 Effect of pH on lead removal using graphene doped ferric hydroxide

Table 25.3 The effect of time on cadmium removal using graphene doped ferric hydroxide at pH 6.3–7.6

Material used	pH variation	Time (min)	Initial concentration of cadmium (ppm)	Cadmium removal (ppm)
Graphene doped ferric oxide	6.3–7.6	5	1000	485
	6.3–7.6	10	1000	578
	6.3–7.6	15	1000	680
	6.3–7.6	20	1000	728
	6.3–7.6	25	1000	875
	6.3–7.6	30	1000	994
	6.3–7.6	35	1000	995
	6.3–7.6	40	1000	995

Table 25.4 The effect of pH on lead removal using graphene doped ferric hydroxide

Material used	pH variation	Lead taken (ppm)	Lead removal (ppm)
Graphene doped ferric oxide	3.4	1000	750
	4.5	1000	838
	6.6	1000	994
	7.7	1000	992
	8.5	1000	854
	10.3	1000	754

Table 25.5 The effect of time on lead removal using graphene doped ferric hydroxide at pH 6.6–7.7

Material used	pH variation	Time (min)	Initial concentration of lead (ppm)	Lead removal (ppm)
Graphene doped ferric hydroxide	6.6–7.7	5	1000	442
	6.6–7.7	10	1000	548
	6.6–7.7	15	1000	659
	6.6–7.7	20	1000	720
	6.6–7.7	25	1000	863
	6.6–7.7	30	1000	992
	6.6–7.7	35	1000	993
	6.6–7.7	40	1000	993

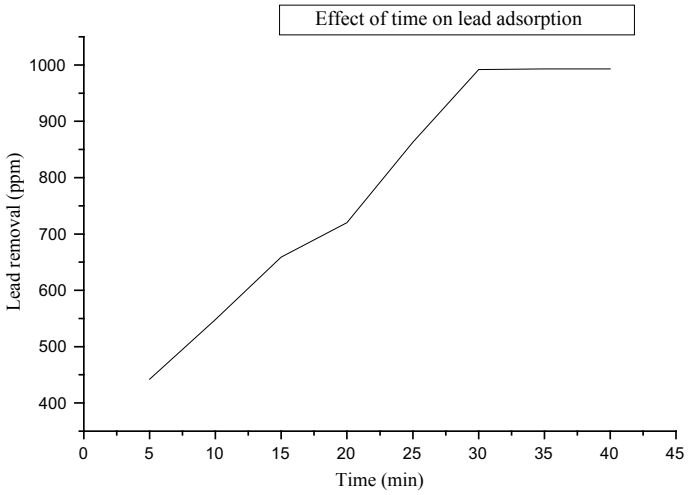

Fig. 25.7 Effect of time on lead removal using graphene doped ferric hydroxide at pH 6.7–7.7

25.4 Conclusion

It was concluded from the research that the synthesized graphene doped ferric hydroxide nanoparticle can be used for the purification of water contaminated by cadmium and lead. Since pH is the most resolving factor for quality of water, the proposed material don't altered it even after adding or removal of toxic contaminants like cadmium and lead. The maximum absorption of cadmium occurred at 35 min at pH 6.3–7.6 and maximum absorption of lead occurred at 35 min at pH 6.6–7.7. On further maximization of time no major changes has been observed. So the proposed material removes cadmium and lead within 35 min effectively and efficiently. So the proposed material can be safely used for water purification. This material can also be impregnated in membrane form to make it commercialize in sophisticated water

purification system. But the material which we have identified can also be beneficial in army troops as it needed few grams for purifying the water of drain, pond and river. Magnetic nanoparticles possess an important magnetic property which helps to remove easily within magnetic field. The reuse of magnetic nanoadsorbent will decrease production cost burden. Magnetic nanoadsorbent technology for water remediation is the more helpful and appropriate for removing and separating heavy metals. Prior to their mass application health effect and fate into the environment of magnetic base nanomaterial should be addressed.

Acknowledgements The authors would like to thank CSIR-National Physical Laboratory, New Delhi, India and Amity University, Noida, India for their kind support in providing the facilities for successful conduction of this research work.

Funding This research did not receive any specific grant from funding agencies in the public, commercial, or not-for-profit sectors.

References

1. R. Baby, B. Saifullah, M.Z. Hussein, Carbon nanomaterials for the treatment of heavy metal-contaminated water and environmental remediation. Nanoscale Res. Lett. **14**, 341 (2019). https://doi.org/10.1186/s11671-019-3167-8
2. J. Edogi, Economic impacts of effluent composition of a process industry on the receiving environment: a study of Port Harcourt refining company 1. Adv. J. Econ. Market. Res. Bassey Enya Ndem (Ph.D.), 3 Unuafe, Blessing Omokaro (Ph.D. In View)
3. M.D. Hladilek, K.F. Gaines, J.M. Novak et al., Microbial community structure of a freshwater system receiving wastewater effluent. Environ. Monit. Assess. **188**2016. https://doi.org/10.1007/s10661-016-5630-7
4. L. Järup, Hazards of heavy metal contamination. Br. Med. Bull. **68**(1), 167–182 (2003). https://doi.org/10.1093/bmb/ldg032
5. P.B. Tchounwou, C.G. Yedjou, A.K. Patlolla et al., Heavy metal toxicity and the environment. Mol. Clin. Environ. Toxicol. **101**, 133–164 (2012). https://doi.org/10.1007/978-3-7643-8340-4_6
6. N. Newton, Preparation and properties of granular ferric hydroxide as an adsorbent in potable water treatment, a doctoral thesis submitted in partial fulfilment of the requirements for the award of Doctor of Philosophy of Loughborough University (2002)
7. M. Fujita, Y. Ide, D. Sato et al., Heavy metal contamination of coastal lagoon sediments: Fongafale Islet, Funafuti Atoll, Tuvalu. Chemosphere **95**, 628–634 (2013). https://doi.org/10.1016/j.chemosphere.2013.10.023
8. S.K. Al-Musharsfi, I.Y. Mahmoud, S.N. Al-Bahry, Heavy metal pollution from treated sewage effluent. APCBEE Proc. **5**, 344–348 (2013). https://doi.org/10.1016/j.apcbee.2013.05.059
9. H.A. Naser, Assessment and management of heavy metal pollution in the marine environment of the Arabian Gulf: a review. Mar. Pollut. Bull. **72**(1), 6–13 (2013). https://doi.org/10.1016/j.marpolbul.2013.04.030
10. G. Akinci, D.E. Guven, S.K. Ugurlu, Assessing pollution in Izmir Bay from rivers in western Turkey: heavy metals. Environ. Sci. **15**(12), 2252–2262 (2013). https://doi.org/10.1039/C3EM00333G
11. A. Byers,ed., *Reader's Digest Atlas of Canada. Montreal* (The Reader's Digest Association (Canada) Ltd., 1995)

12. C. Chambers, M. Winfield, *Mining's Many Faces: Environmental Mining Law and Policy in Canada* (Canadian Institute for Environmental Law and Policy, Toronto, 2000)
13. E. Canada, *Threats to Sources of Drinking Water and Aquatic Ecosystem Health in Canada* (National Water Research Institute, Burlington, 2001)
14. K.S. Novoselov, A.K. Geim, S.V. Morozov et al., Electric field effect in atomically thin carbon films. Am. Assoc. Adv. Sci. **306**(5696), 666–669 (2004). https://doi.org/10.1126/science.1102896
15. E.C. Kennedy, Effect of Corrosion on Bond between Steel and Concrete of Corroded and Inhibitive Reinforcement Embedded in Reinforced Concrete Structures in Accelerated Corrosive medium View Project Improvement of Expansive Soils with Blended Composite Materials as Stabilizers View project (2020)
16. M. Çakmakci, V. Bali, B. Özkaya et al., Treatment processes based on the molecular weight distribution of textile dyeing wastewater. Environ. Prot. Eng. **44**, 147–158 (2018). https://doi.org/10.5277/epe180210
17. Deng, L. Lü, H. Li, F. Luo, The adsorption properties of Pb(II) and Cd(II) on doped graphene prepared by electrolysis method. J. Hazard. Mater. **183**(1–3), 923–930. https://doi.org/10.1016/j.jhazmat.2010.07.117
18. G.K. Ramesha, A.V. Kumara, H.B. Muralidhara et al., Graphene and graphene oxide as effective adsorbents toward anionic and cationic dyes. J. Colloid Interface Sci. **361**(1), 270–277 (2011). https://doi.org/10.1016/j.jcis.2011.05.050
19. S.T. Yang, S. Chen, Y. Chang et al., Removal of methylene blue from aqueous solution by graphene oxide. J. Colloid Interface Sci. **359**(1), 24–29 (2011). https://doi.org/10.1016/j.jcis.2011.02.064
20. P. Xu, G.M. Zeng, D.L. Huang et al., Use of iron oxide nanomaterials in wastewater treatment: a review. Sci. Total Environ. **424**, 1–10 (2012). https://doi.org/10.1016/j.scitotenv.2012.02.023
21. C.L. Warner, W. Chouyyok, K.E. Mackie et al., Manganese doping of magnetic iron oxide nanoparticles: tailoring surface reactivity for a regenerable heavy metal sorbent. Langmuir **28**(8), 3931–3937 (2012). https://doi.org/10.1021/la2042235
22. A.E. Karatapanis, D.E. Petrakis, C.D. Stalikas, A layered magnetic iron/iron oxide nanoscavenger for the analytical enrichment of ng-L(-1) concentration levels of heavy metals from water. Anal. Chim. Acta. **726**, 22–27 (2012). https://doi.org/10.1016/j.aca.2012.03.018
23. H. Yang, Z. Tian, J. Wang, S. Yang, A magnetic resonance imaging nanosensor for Hg (II) based on thymidine-Doped supermagnetic iron oxide nanoparticles. Sens. Actuators B Chem. **161**(1), 429–433 (2012). https://doi.org/10.1016/j.snb.2011.10.055
24. A.S. Teja, P.-Y. Koh, Synthesis, properties, and applications of magnetic iron oxide nanoparticles. Prog. Cryst. Growth Charact. Mater. **55**, 22–45 (2009). https://doi.org/10.1016/j.pcrysgrow.2008.08.003
25. Z. Liu, H. Wang, C. Liu, Y. Jiang et al., Magnetic cellulose-chitosan hydrogels prepared from ionic liquids as reusable adsorbent for removal of heavy metal ions. Chem. Commun. (Camb) **48**(59), 7350–7352 (2012). https://doi.org/10.1039/C2CC17795A
26. N. Idrees, B. Tabassum, E.F. Abd Allah et al., Groundwater contamination with cadmium concentrations in some West U.P. Regions, India. Saudi J. Biol. Sci. **25**, 1365–1368 (2018). https://doi.org/10.1016/j.sjbs.2018.07.005
27. R.-P. Ostovar, F. Saberi et al., Versatile sulfathiazole-doped magnetic nanoparticles as catalyst in oxidation and alkylation reactions. Catalysts **9**, 348. https://doi.org/10.3390/catal9040348
28. M.E. McHenry, D.E. Laughlin, Nano-scale materials development for future magnetic applications. Acta Mater. **48**(1), 223–38 (2000). https://doi.org/10.1016/S1359-6454(99)00296-7
29. R. Amann, H. Lemmer, M. Wagner, Monitoring the community structure of wastewater treatment plants: a comparison of old and new techniques. FEMS Microbiol. Ecol. **25**, 205–215 (1998). https://doi.org/10.1111/j.1574-6941.1998.tb00473.x
30. M. Zhao, Y. Xu, C. Zhang et al., New trends in removing heavy metals from wastewater. Appl. Microbiol. Biotechnol. **100**, 6509–6518 (2016)

31. M.D. Márquez-Medina, D. Rodríguez-Padrón, A.M. Balu et al., Mechanochemically synthesized supported magnetic fe-nanoparticles as catalysts for efficient vanillin production. Catalysts **9**, 290 (2019). https://doi.org/10.3390/catal9030290
32. M. Hua, S. Zhang, B. Pan et al., Heavy metal removal from water/wastewater by nanosized metal oxides: a review. J. Hazard Mater. **211–212**, 317–331 (2012). https://doi.org/10.1016/j.jhazmat.2011.10.016
33. B.I. Kharisov, H.V.R. Dias, O.V. Kharissova et al., Iron-containing nanomaterials: synthesis, properties, and environmental applications. RSC Adv. **2**(25), 9325–9358 (2012). https://doi.org/10.1039/C2RA20812A
34. Z. Feng, S. Zhu, D.R. Martins de Godoi et al., Adsorption of Cd^{2+} on carboxyl-terminated superparamagnetic iron oxide nanoparticles. Anal. Chem. **84**(8), 3764–3770 (2012). https://doi.org/10.1021/ac300392k
35. E. Blessing, C. Kennedy, E.N. Ezekiel, Predicting the migration of aluminium inhibited by industrial effluents in Trans Amadi Streams, Port Harcourt, Rivers State